UNIVERSITY OF CALIFORNIA
SANTA CRUZ

EXPLORING THE GRAPHENE/HEXAGONAL BORON NITRIDE HETEROSTRUCTURE FROM THE BOTTOM TO THE TOP

A dissertation submitted in partial satisfaction
of the requirements for the degree of

DOCTOR OF PHILOSOPHY

in

PHYSICS

by

Eberth Arturo Quezada-López

September 2020

The Dissertation of Eberth Arturo Quezada-López is approved:

_____
Professor Jairo Velasco Jr., chair

_____
Professor David Lederman

_____
Professor Sergey Syzranov

_____
Quentin Williams
Interim Vice Provost and Dean of Graduate Studies

TABLE OF CONTENTS

LIST OF ABREVIATIONS

1D	One dimension/dimensional
2D	Two dimensions/dimensional
3D	Three dimensions/dimensional
AC	Alternating current
AFM	Atomic force microscope/microscopy
ARPES	Angle resolved photoemission spectroscopy
BE	Binding energy
BLG	Bilayer graphene
BZ	Brillouin zone
CNP	Charge neutrality point
DC	Direct current
$\boldsymbol{dI/dV_s}$	Differential conductance
DIC	Differential interference contrast
DOS	Density of states
DT	Direct tunneling
$\boldsymbol{E_F}$	Fermi energy/level
EBL	Electron beam lithography
FET	Field effect transistor
FFT	Fast Fourier transform
FZP	Fresnel zone plate
hBN	Hexagonal boron nitride
HEB	High energy band
LDOS	Local density of states
LEB	Low energy band
MLG	Monolayer graphene
MMA	Methyl methacrylate
n-doped	Negatively doped
p-doped	Positively doped
PAT	Phonon assisted tunneling

PF	Poole-Frenkel
PMMA	Poly-methyl methacrylate
Pt-Ir	Platinum iridium
QD	Quantum dot
Si^{+}	Positively doped silicon
SiO_2	Silicon dioxide
STM	Scanning tunneling microscope/microscopy
STS	Scanning tunneling spectroscopy
TB	Tight binding
UHV	Ultra-high vacuum
$\boldsymbol{V_G}$	Backgate voltage
$\boldsymbol{V_S}$	Sample bias voltage
VHS	Van Hove singularity
W	Tungsten

LIST OF FIGURES

TABLE

Abstract

Exploring the Graphene/hexagonal Boron Nitride Heterostructure from the Bottom to the Top

by

Eberth Arturo Quezada-López

The wide range of applications and promising possibilities of stacked 2D materials highlight the importance of studying heterostructures. The works presented in this dissertation tell a comprehensive story about the heterostructure composed of graphene and hexagonal boron nitride (hBN). Through the use of established characterization techniques such as transport and scanning tunneling microscopy, we will explore phenomena in the graphene/hBN heterostructure from the bottom up in three vertical stages. Stage 1 is the bottommost part of the heterostructure and deals with the accumulation of charged defects in hBN induced by an exposure to high electric fields. Stage 2 focuses on the graphene/hBN interface and how these layered materials work together to enable the corralling of relativistic charge carriers. Finally, stage 3 probes the exposed surface of a double-layered graphene system which is decoupled from hBN while still benefiting from its structural support. The interplay between these materials yields high quality and atomically resolved tunneling spectroscopy results that suggest the emergence of correlated phenomena in naturally occurring double-layered graphene.

Acknowledgements

I feel extremely fortunate and borderline ashamed to have had the chance to work in a lab with state-of-the-art equipment, in one of the most beautiful towns in the world, and with the brightest and friendliest of people. In the following paragraphs, I want to offer my deepest gratitude to those whose dedication, guidance, and positivity have contributed to the work I present here.

First and foremost, I want to acknowledge the people directly responsible for the work presented in this dissertation. During my time in Santa Cruz, my adviser Prof. Jairo Velasco Jr.'s relentless guidance and support taught me the value and rewards of hard work. He also made me a better presenter, communicator, and writer. I hope he'll be fine if I break some conventions here. I was very fortunate to have John Davenport as my fellow lab mate (and brother) from day one. I hope to have osmotically gained some of his fearless optimism and infectious sense of humor after these fun five years. Everything I learned about STM and UHV was thanks to Fred Joucken who was a great friend and a brutally honest mentor. I am excited to continue seeing his little boys grow up. Zhehao Ge not only worked tirelessly with us to keep the STM up and running but also provided valuable insights. I eagerly look forward to riding bikes around Santa Cruz with him again.

Our group was very lucky to count with faculty and staff at UC Santa Cruz that were willing to help and share equipment during the beginning stages of our lab. Professor Sue Carter and her student Katie Hellier kindly trained and shared their fabrication facilities with us. Tom Yuzvinsky trained and advised us on all things SEM. Professors David Belanger and Zack Schlesinger shared their lab spaces, equipment, and priceless experience when we had nothing but a microscope and lots of scotch tape. Professor Art Ramirez and his students and my good friends Patrick LaBarre and Maverick McLanahan provided guidance, equipment, and from time to time let us borrow some liquid nitrogen. And finally, Joe "the machinist" Cox who taught me how

to work metal using WWII era machines and helped me build many crucial components and parts for my experiments.

I also want to thank my professors from Los Angeles Valley College who jumpstarted my fascination with science. Professors Teresa Sutcliffe, Luz Shin, Mary Hito, and Luke Haley, I will never forget your passion for teaching and friendly encouragement.

Finally, I want to thank my family. To my sister and brother, thank you for your love, support, and making me and my parents very proud. To Melissa, thank you for your boundless amounts of patience and making me smile every day. I can't imagine riding out a pandemic with anyone else but you. And to my parents, who left their country, family, and lives behind in search of a better future for their three children. No amount of work will ever compare to the sacrifices you have made. Here is my best attempt.

Dedicado a Eber y Enma
(Mis padres)

Chapter 1 – Introduction

The story of graphene begins even before it was conceivable for it to exist in stable form. Before Novoselov and Geim[1,2] demonstrated that single atomic sheets of carbon could be isolated in the laboratory, theorists studied graphene's properties as a steppingstone to understanding graphite[3,4]—a crystal made up of stacked graphene layers. A decade and a half after Novoselov and Geim's 2004 historical achievement, the field of two-dimensional (2D) materials has expanded well beyond graphene. Developments in industrial and technological applications,[5–13] the assembly and study of novel heterojunctions,[5,14–17] and the rise of twisted graphene layers[18–23] are proof that the world of 2D materials continues to expand.

1.1 The Current State of Graphene

Graphene is a one-atom thick film of carbon atoms in a honeycomb arrangement. Graphene was shown to have an abundance of unique mechanical, electrical, chemical, and thermal properties. These properties were largely explored in the years following its isolation in 2004. Currently, the mature field of graphene is branching out into a wide array of applications, ranging from bio-medical sensors to energy storage. No joint effort embodies the development of applied graphene research better than the Graphene Flagship. Started in 2013, this 10-year project funded by the

European Union seeks to expedite the transition of graphene from research to commercialization.[6] This multinational effort has even released products containing graphene to the market. Some of these include graphene-based inks,[7,8] polymer-graphene composites,[9,10] thin-film coating,[11,12] and even earphones.[13]

The projects promoted by the Graphene Flagship are exciting and crucial for the realization of future technologies. All of the products soon-to-be or currently in the market rely on graphene's high mechanical strength, chemical stability, and high thermal conductivity. This is evident from the fact that most of these products integrate graphene in composites or use graphene as an added ingredient onto existing technology. The use of graphene's unique and novel electrical properties, however, are largely lacking in current marketable applications. Scaling the production of graphene to fit industrial demand while maintaining its relativistic electron behavior continues to present a challenge. One possible solution for such challenge is offered by graphene's ability to interface with other layered materials. Research efforts in recent years have explored the properties of other single to few atom thick materials that when combined with graphene lead to exciting physical phenomena.

1.2 Graphene as Part of the Whole

Van der Waals forces that hold together single graphene layers in graphite can also hold together heterostructures that incorporate a wide variety of 2D materials. The family of 2D materials has expanded beyond semi-metallic graphene to include metals

like $NbSe_2$, semiconductors like MoS_2, and insulators like hBN. The creation of heterojunctions by mixing type III-V semiconductors are restricted by material compatibility such as lattice mismatch, crystal plane orientation, and difference in growth recipes. However, van der Waals heterostructures do not have such limitations. The large and growing number of members in the 2D materials family offers a far greater number of combinations. Moreover, the complexity of heterostructures that can be created is boundless and has proven to result in viable electrical components for future technologies.

Stacking different 2D crystals into a heterostructure can improve the quality and performance of its individual components. However, the effects arising from one material's influence on the other have become more important as they have provided new and exciting insights. For example, when stacked on hBN (an insulator), graphene's electronic and mechanical properties were initially shown to vastly improve.[24] More recently, studies have shown that hBN does more than just improve graphene's qualities. For example, graphene's surface can undergo reconstruction,[25,26] its band structure can form a gap and satellite Dirac points,[27,28] and defects in hBN can be used to corral electrons in graphene.[29,30] Moreover, researchers have produced a wide range of electronic and optoelectronic devices by mixing graphene with a variety of layered materials. Such devices include logic gates and circuits,[31,32] radio-frequency oscillators,[33] resonant tunneling diodes,[34] photodetectors,[35] phototransistors,[36] light-emitting diodes,[37] and plasmonic devices.[38] In addition to all this progress, the field of 2D materials has undergone a rebirth in the past two years after superconductivity was

discovered by stacking twisted graphene sheets. This twist was achieved by rotating two graphene sheets with respect to each other's out-of-plane axes. Researchers have shown that the modulation of the crystallographic alignment between individual graphene layers by a "magic" angle leads to correlated insulating and unconventional superconducting states.[18,20,39–41]

1.3 Outline of the Thesis

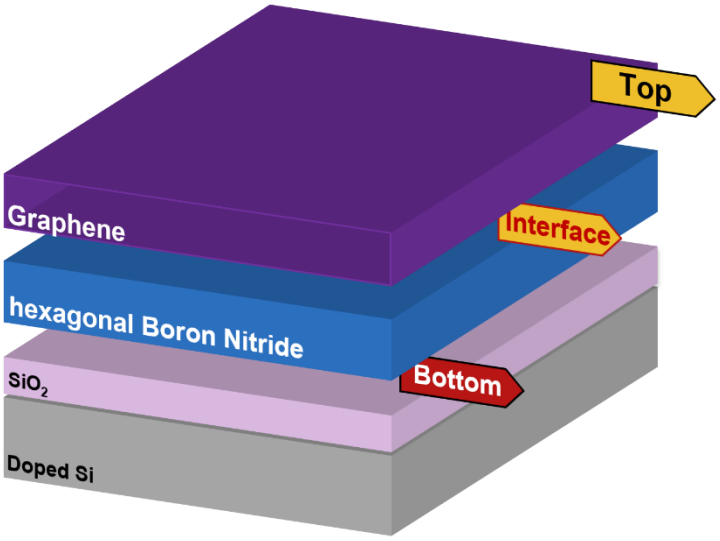

Figure 1.1| Sectors of the graphene/hexagonal boron nitride (hBN) heterostructure. Schematic of a graphene/hBN heterostructure resting on standard SiO_2/doped Si substrate. The stages of the heterostructure discussed in this thesis are label accordingly. "Bottom": the interface between hBN and SiO_2. "Interface": the interface between hBN and graphene. "Top": the surface of graphene.

The wide range of applications and promising possibilities of stacked 2D materials highlight the importance of studying heterostructures. The works I will

present in this thesis tell a comprehensive story of the heterostructure composed of graphene and hBN. Through the use of established characterization techniques such as electrical transport, photoemission spectroscopy, and scanning tunneling microscopy, we will explore phenomena in the graphene/hBN heterostructure from the bottom up in 3 vertical stages (see Fig. 1.1). Stage 1, the "Bottom", is the bottommost part of the stack and deals with the accumulation of charged defects in hBN. Stage 2, the "Interface", focuses on the interface of graphene and hBN and how these layered materials work together to create superlattices and enable the corralling of graphene electrons. Finally stage 3, the "Top", uses the benefits of fully decoupling graphene from hBN to yield high quality tunneling spectroscopic results in a double-layered graphene system enabling us to probe correlated phenomena.

Chapter 2 introduces the band structure theory of monolayer graphene (MLG) and bilayer graphene (BLG) calculated using tight-binding theory. Using this single particle approach, I will show how the high degree of symmetry in MLG and BLG's lattice lead to their unique band structures. After applying a low energy approximation in both graphene and BLG, I will obtain their respective characteristic zero-gap bands located at high symmetry points in the Brillouin zone. The acquired band structure knowledge will be used in the subsequent chapters as we explore the electrical properties of both MLG and BLG while on hBN.

Chapter 3 contains the theory of the major characterization techniques used in this thesis: scanning tunneling microscopy (STM) and nanospot angle resolved photoemission spectroscopy (nano-ARPES). The experimental application of these

techniques on graphene will also be covered. Chapter 4 contains relevant experimental procedures that enable the application of the techniques discussed in Ch. 3. These procedures include graphene/hBN device fabrication, mechanical cleaning of graphene's surface, electrochemical etching of STM probes, and the calibration of STM tips with Au(111).

The stages of our exploration of the graphene/hBN heterostructure will begin in Ch. 5 with the "Bottom". This stage explores the effect of strong electric fields on hBN. By applying electric fields on the order of $1\ \mathrm{V/nm}$, we will demonstrate that charge accumulation can occur inside hBN through the excitation of its defects. Using electrical transport measurements, the charge build-up inside hBN will be tracked by changes in the electronic signature of MLG under different conditions.

The "Interface" stage will be covered by Ch. 6 and 7. Chapter 6 will introduce a technique that uses charge accumulation in hBN to pseudo-confine electrons into a graphene quantum dot (QD). This chapter will demonstrate that an STM tip interacts electrostatically with the graphene QD during spectroscopic characterization. Chapter 7 will explore variations in the crystallographic alignment between BLG and hBN using spatially resolved photoemission spectroscopy.

Finally, the "Top" stage is covered by Ch. 8. After having explored the "Bottom" and "Interface" stages of the graphene/hBN heterostructure, we focus solely on the "Top" stage (see Fig. 1.1). This chapter provides a comprehensive characterization of BLG's band structure using scanning tunneling spectroscopy. Any

possible electronic coupling between hBN and BLG is eliminated with a sufficiently large crystallographic misalignment between them. Despite decoupling from hBN, BLG still benefits from the structural support and electronic isolation from substrate induced disorder that hBN provides. These advantages of decoupled BLG on hBN enable us to map the atomically resolved distribution and evolution of electronic structure features such as the Van Hove singularity and high energy bands in BLG.

The last chapter (Ch. 9) will summarize and highlight the results discussed in Ch. 5-8 which explore the graphene/hBN heterostructure in three different, yet interconnected, stages. This chapter will end with an outlook and possible directions for future studies that can stem from the works presented in this thesis.

Chapter 1 - References

(1) Novoselov, K. S.; Geim, A. K.; Morozov, S. V.; Jiang, D.; Zhang, Y.; Dubonos, S. V.; Grigorieva, I. V.; Firsov, A. A. Electric Field in Atomically Thin Carbon Films. *Science (80-.).* **2004**. https://doi.org/10.1126/science.1102896.

(2) Novoselov, K. S.; Geim, A. K.; Morozov, S. V.; Jiang, D.; Katsnelson, M. I.; Grigorieva, I. V.; Dubonos, S. V.; Firsov, A. A. Two-Dimensional Gas of Massless Dirac Fermions in Graphene. *Nature* **2005**. https://doi.org/10.1038/nature04233.

(3) Wallace, P. R. The Band Theory of Graphite. *Phys. Rev.* **1947**. https://doi.org/10.1103/PhysRev.71.622.

(4) McClure, J. W. Diamagnetism of Graphite. *Phys. Rev.* **1956**. https://doi.org/10.1103/PhysRev.104.666.

(5) Novoselov, K. S.; Mishchenko, A.; Carvalho, A.; Castro Neto, A. H. 2D

Materials and van Der Waals Heterostructures. *Science*. 2016. https://doi.org/10.1126/science.aac9439.

(6) Graphene Flagship http://www.graphene-flagship.eu/.

(7) GrapheneTech S.L.: GraphInk http://www.graphene-tech.net/product/conductive-ink/.

(8) Cambridge Graphene: Graphene Inks http://www.cambridgegraphene.com/#what-we-do.

(9) Vittoria: GRAPHENE 2.0 https://www.vittoria.com/eu/graphene-technology.

(10) Avanzare: graphene http://www.avanzarematerials.com/graphene/.

(11) Graphene-xt https://www.graphene-xt.com/en/.

(12) AIXTRON: Deposition System for Carbon Nanomaterials https://www.aixtron.com/en/products/2d-nanotechnology-pecvd/bm-pro.

(13) MediaDevil Artisanphonics CB-01 Nanene® Graphene-Enhanced Luxury Wood Earphones https://mediadevil.com/products/artisanphonics-cb-01-nanene-graphene-wood-earphones.

(14) Geim, A. K.; Grigorieva, I. V. Van Der Waals Heterostructures. *Nature*. 2013. https://doi.org/10.1038/nature12385.

(15) Schaibley, J. R.; Yu, H.; Clark, G.; Rivera, P.; Ross, J. S.; Seyler, K. L.; Yao, W.; Xu, X. Valleytronics in 2D Materials. *Nature Reviews Materials*. 2016. https://doi.org/10.1038/natrevmats.2016.55.

(16) Feng, Y. P.; Shen, L.; Yang, M.; Wang, A.; Zeng, M.; Wu, Q.; Chintalapati, S.; Chang, C. R. Prospects of Spintronics Based on 2D Materials. *Wiley Interdisciplinary Reviews: Computational Molecular Science*. 2017. https://doi.org/10.1002/wcms.1313.

(17) Cui, C.; Xue, F.; Hu, W. J.; Li, L. J. Two-Dimensional Materials with Piezoelectric and Ferroelectric Functionalities. *npj 2D Materials and Applications*. 2018. https://doi.org/10.1038/s41699-018-0063-5.

(18) Cao, Y.; Fatemi, V.; Fang, S.; Watanabe, K.; Taniguchi, T.; Kaxiras, E.; Jarillo-Herrero, P. Unconventional Superconductivity in Magic-Angle Graphene Superlattices. *Nature* **2018**. https://doi.org/10.1038/nature26160.

(19) Chen, G.; Sharpe, A. L.; Gallagher, P.; Rosen, I. T.; Fox, E. J.; Jiang, L.; Lyu, B.; Li, H.; Watanabe, K.; Taniguchi, T.; Jung, J.; Shi, Z.; Goldhaber-Gordon, D.; Zhang, Y.; Wang, F. Signatures of Tunable Superconductivity in a Trilayer Graphene Moiré Superlattice. *Nature* **2019**. https://doi.org/10.1038/s41586-019-1393-y.

(20) Lu, X.; Stepanov, P.; Yang, W.; Xie, M.; Aamir, M. A.; Das, I.; Urgell, C.; Watanabe, K.; Taniguchi, T.; Zhang, G.; Bachtold, A.; MacDonald, A. H.; Efetov, D. K. Superconductors, Orbital Magnets and Correlated States in Magic-Angle Bilayer Graphene. *Nature* **2019**. https://doi.org/10.1038/s41586-019-1695-0.

(21) Wong, D.; Wang, Y.; Jung, J.; Pezzini, S.; Dasilva, A. M.; Tsai, H. Z.; Jung, H. S.; Khajeh, R.; Kim, Y.; Lee, J.; Kahn, S.; Tollabimazraehno, S.; Rasool, H.; Watanabe, K.; Taniguchi, T.; Zettl, A.; Adam, S.; Macdonald, A. H.; Crommie, M. F. Local Spectroscopy of Moiré-Induced Electronic Structure in Gate-Tunable Twisted Bilayer Graphene. *Phys. Rev. B - Condens. Matter Mater. Phys.* **2015**. https://doi.org/10.1103/PhysRevB.92.155409.

(22) He1, M.; Li1, Y.; Cai1, J.; Liu1, Y.; Watanabe2, K.; Taniguchi2, T.; , Xiaodong Xu1, 3†; and Matthew Yankowitz. Tunable Correlation-Driven Symmetry Breaking in Twisted Double Bilayer Graphene. **2020**.

(23) Yuan Cao, 1, ∗ Daniel Rodan-Legrain, 1 Oriol Rubies-Bigorda, 1 Jeong Min; Park, 1, 2 Kenji Watanabe, 3 Takashi Taniguchi, 3 and Pablo Jarillo-Herrero. Electric Field Tunable Correlated States and Magnetic Phase Transitions in Twisted Bilayer-Bilayer Graphene. **2019**.

(24) Dean, C. R.; Young, A. F.; Meric, I.; Lee, C.; Wang, L.; Sorgenfrei, S.; Watanabe, K.; Taniguchi, T.; Kim, P.; Shepard, K. L.; Hone, J. Boron Nitride Substrates for High-Quality Graphene Electronics. *Nat. Nanotechnol.* **2010**. https://doi.org/10.1038/nnano.2010.172.

(25) Woods, C. R.; Britnell, L.; Eckmann, A.; Ma, R. S.; Lu, J. C.; Guo, H. M.; Lin, X.; Yu, G. L.; Cao, Y.; Gorbachev, R. V.; Kretinin, A. V.; Park, J.; Ponomarenko, L. A.; Katsnelson, M. I.; Gornostyrev, Y. N.; Watanabe, K.; Taniguchi, T.; Casiraghi, C.; Gao, H. J.; Geim, A. K.; Novoselov, K. S. Commensurate-Incommensurate Transition in Graphene on Hexagonal Boron Nitride. *Nat. Phys.* **2014**. https://doi.org/10.1038/nphys2954.

(26) Woods, C. R.; Withers, F.; Zhu, M. J.; Cao, Y.; Yu, G.; Kozikov, A.; Ben Shalom, M.; Morozov, S. V.; Van Wijk, M. M.; Fasolino, A.; Katsnelson, M. I.; Watanabe, K.; Taniguchi, T.; Geim, A. K.; Mishchenko, A.; Novoselov, K. S. Macroscopic Self-Reorientation of Interacting Two-Dimensional Crystals. *Nat. Commun.* **2016**. https://doi.org/10.1038/ncomms10800.

(27) Yankowitz, M.; Xue, J.; Cormode, D.; Sanchez-Yamagishi, J. D.; Watanabe, K.; Taniguchi, T.; Jarillo-Herrero, P.; Jacquod, P.; Leroy, B. J. Emergence of Superlattice Dirac Points in Graphene on Hexagonal Boron Nitride. *Nat. Phys.* **2012**. https://doi.org/10.1038/nphys2272.

(28) Hunt, B.; Sanchez-Yamagishi, J. D.; Young, A. F.; Yankowitz, M.; LeRoy, B. J.; Watanabe, K.; Taniguchi, T.; Moon, P.; Koshino, M.; Jarillo-Herrero, P.;

Ashoori, R. C. Massive Dirac Fermions and Hofstadter Butterfly in a van Der Waals Heterostructure. *Science (80-.).* **2013**. https://doi.org/10.1126/science.1237240.

(29) Lee, J.; Wong, D.; Velasco, J.; Rodriguez-Nieva, J. F.; Kahn, S.; Tsai, H. Z.; Taniguchi, T.; Watanabe, K.; Zettl, A.; Wang, F.; Levitov, L. S.; Crommie, M. F. Imaging Electrostatically Confined Dirac Fermions in Graphene Quantum Dots. *Nat. Phys.* **2016**. https://doi.org/10.1038/nphys3805.

(30) Ghahari, F.; Walkup, D.; Gutiérrez, C.; Rodriguez-Nieva, J. F.; Zhao, Y.; Wyrick, J.; Natterer, F. D.; Cullen, W. G.; Watanabe, K.; Taniguchi, T.; Levitov, L. S.; Zhitenev, N. B.; Stroscio, J. A. An on/off Berry Phase Switch in Circular Graphene Resonators. *Science (80-.).* **2017**. https://doi.org/10.1126/science.aal0212.

(31) Yang, H.; Heo, J.; Park, S.; Song, H. J.; Seo, D. H.; Byun, K. E.; Kim, P.; Yoo, I. K.; Chung, H. J.; Kim, K. Graphene Barristor, a Triode Device with a Gate-Controlled Schottky Barrier. *Science (80-.).* **2012**. https://doi.org/10.1126/science.1220527.

(32) Sup Choi, M.; Lee, G. H.; Yu, Y. J.; Lee, D. Y.; Hwan Lee, S.; Kim, P.; Hone, J.; Yoo, W. J. Controlled Charge Trapping by Molybdenum Disulphide and Graphene in Ultrathin Heterostructured Memory Devices. *Nat. Commun.* **2013**. https://doi.org/10.1038/ncomms2652.

(33) Mishchenko, A.; Tu, J. S.; Cao, Y.; Gorbachev, R. V.; Wallbank, J. R.; Greenaway, M. T.; Morozov, V. E.; Morozov, S. V.; Zhu, M. J.; Wong, S. L.; Withers, F.; Woods, C. R.; Kim, Y. J.; Watanabe, K.; Taniguchi, T.; Vdovin, E. E.; Makarovsky, O.; Fromhold, T. M.; Fal'ko, V. I.; Geim, A. K.; Eaves, L.; Novoselov, K. S. Twist-Controlled Resonant Tunnelling in Graphene/Boron Nitride/Graphene Heterostructures. *Nat. Nanotechnol.* **2014**. https://doi.org/10.1038/nnano.2014.187.

(34) Lin, Y. C.; Ghosh, R. K.; Addou, R.; Lu, N.; Eichfeld, S. M.; Zhu, H.; Li, M. Y.; Peng, X.; Kim, M. J.; Li, L. J.; Wallace, R. M.; Datta, S.; Robinson, J. A. Atomically Thin Resonant Tunnel Diodes Built from Synthetic van Der Waals Heterostructures. *Nat. Commun.* **2015**. https://doi.org/10.1038/ncomms8311.

(35) Koppens, F. H. L.; Mueller, T.; Avouris, P.; Ferrari, A. C.; Vitiello, M. S.; Polini, M. Photodetectors Based on Graphene, Other Two-Dimensional Materials and Hybrid Systems. *Nature Nanotechnology*. 2014. https://doi.org/10.1038/nnano.2014.215.

(36) Roy, K.; Padmanabhan, M.; Goswami, S.; Sai, T. P.; Ramalingam, G.; Raghavan, S.; Ghosh, A. Graphene-MoS 2 Hybrid Structures for Multifunctional Photoresponsive Memory Devices. *Nat. Nanotechnol.* **2013**. https://doi.org/10.1038/nnano.2013.206.

(37) Cheng, R.; Li, D.; Zhou, H.; Wang, C.; Yin, A.; Jiang, S.; Liu, Y.; Chen, Y.; Huang, Y.; Duan, X. Electroluminescence and Photocurrent Generation from Atomically Sharp WSe2/MoS2 Heterojunction p-n Diodes. *Nano Lett.* **2014**. https://doi.org/10.1021/nl502075n.

(38) Grigorenko, A. N.; Polini, M.; Novoselov, K. S. Graphene Plasmonics. *Nature Photonics*. 2012. https://doi.org/10.1038/nphoton.2012.262.

(39) Xie, Y.; Lian, B.; Jäck, B.; Liu, X.; Chiu, C. L.; Watanabe, K.; Taniguchi, T.; Bernevig, B. A.; Yazdani, A. Spectroscopic Signatures of Many-Body Correlations in Magic-Angle Twisted Bilayer Graphene. *Nature* **2019**. https://doi.org/10.1038/s41586-019-1422-x.

(40) Stepanov, P.; Das, I.; Lu, X.; Fahimniya, A.; Watanabe, K.; Taniguchi, T.; Koppens, F. H. L.; Lischner, J.; Levitov, L.; Efetov, D. K. Untying the Insulating and Superconducting Orders in Magic-Angle Graphene. *Nature* **2020**. https://doi.org/10.1038/s41586-020-2459-6.

(41) Arora, H. S.; Polski, R.; Zhang, Y.; Thomson, A.; Choi, Y.; Kim, H.; Lin, Z.; Wilson, I. Z.; Xu, X.; Chu, J. H.; Watanabe, K.; Taniguchi, T.; Alicea, J.; Nadj-Perge, S. Superconductivity in Metallic Twisted Bilayer Graphene Stabilized by WSe2. *Nature* **2020**. https://doi.org/10.1038/s41586-020-2473-8.

Chapter 2 – Band Structure Theory of Monolayer and Bilayer Graphene

2.1 Introduction

One of the most frequently quoted facts about graphene is that it has massless electrons. In this chapter we will show how this result is obtained by using the tight-binding (TB) model. We will begin by introducing the TB model for a general crystal with translational symmetry. Then, we will apply this model to monolayer graphene (MLG) to obtain insights about its quasiparticle scattering behavior which is a significant mechanism for the phenomena presented in Ch. 6. In a similar manner, we will apply the TB model to calculate bilayer graphene's (BLG's) band structure and discuss its bandgap tunability—a crucial feature discussed in Ch. 8. Finally, we will introduce a TB computational package used to simulate the local density of states for MLG and BLG in Ch. 6 and 8, respectively.

2.2 The Tight-Binding (TB) Model

The TB model is an approach used to calculate the electronic band structure of a wide range of solids. As indicated in the name, this approach has increased accuracy for solids where atoms have atomic orbitals "tightly-bound" to their nuclei. By being "tightly-bound", atoms in the solid have less overlap between themselves and are thus considered to be "non-interacting". This enables us to approximate a material's wave

functions by linear combinations of Bloch functions of isolated atoms in a crystal lattice. Despite being a single-electron approach, the TB model can provide insights necessary to describe many-body phenomena[1] as we will see in Ch. 8. However, to calculate the band structure of MLG and BLG that is commonly used in the literature, such adaptations to the TB model are not necessary.

The starting point of the TB model is to assume a system of translational invariant sites—each having n orbitals ϕ_j. An appropriate description for such system can be given by a linear combination of these orbitals, i.e. Bloch functions:

$$\Phi_j(\boldsymbol{k},\boldsymbol{r}) = \frac{1}{\sqrt{N}} \sum_{l=1}^{N} e^{i\boldsymbol{k}\cdot\boldsymbol{R}_{jl}}\, \phi_j\,(\boldsymbol{r}-\boldsymbol{R}_{jl}) \tag{2.1}$$

This expression is the linear combination of the jth orbital of N unit cells, where R_{jl} denotes the position of the jth orbital at the lth unit cell.

Once we have the modes Φ_j across the crystals lattice, we can approximate the crystal's wave function $\Psi_i(k,r)$ as follows:

$$\Psi_i(\boldsymbol{k},\boldsymbol{r}) = \sum_{j=1}^{n} c_{ij}\Phi_j(\boldsymbol{k},\boldsymbol{r}) \tag{2.2}$$

So far, the wave function $\Psi_i(\boldsymbol{k},\boldsymbol{r})$ can apply to any crystal with some form of translational symmetry. The specificity of the energy distribution and interaction between atoms in a crystal is encoded in the Hamiltonian H. So, assuming we have H for some crystal, from the Schrödinger equation we can express the eigenvalue $E_i(\boldsymbol{k})$ as:

$$E_i(\boldsymbol{k}) = \frac{\langle \Psi_i | H | \Psi_i \rangle}{\langle \Psi_i | \Psi_i \rangle} \tag{2.3}$$

By plugging in the expanded expression of the wave functions in (2.2), we obtain

$$E_i(\boldsymbol{k}) = \frac{\sum_{j,l}^{n} c_{ij}^* c_{il} H_{jl}}{\sum_{j,l}^{n} c_{ij}^* c_{il} S_{jl}} \tag{2.4}$$

Here, H_{jl} are referred to as the transfer integral's matrix elements $H_{jl} = \langle \Phi_j | H | \Phi_l \rangle$ and S_{jl} are the overlap integral's matrix elements $S_{jl} = \langle \Phi_j | \Phi_l \rangle$.

In principle we can compute the transfer and overlap integrals assuming we know the ϕ_j orbitals at each unit cell. However, to obtain the energy $E_i(\boldsymbol{k})$ we still need to address the unknown coefficients c_{ij}. This requires minimizing the energy expression in (2.4) with respect to c_{ij}^*. This process leads to the consolidation of the coefficients c_{ij}^* in (2.4) which results in

$$\sum_{j=1}^{n} c_{ij} H_{lj} = E_i(\boldsymbol{k}) \sum_{j=1}^{n} c_{ij} S_{lj} \tag{2.5}$$

E_i can now be obtained by a standard matrix diagonalization process, or equivalently by solving the characteristic equation:

$$\det (H - E_i S) = 0 \tag{2.6}$$

There will be as many solutions for E_i as there are atoms within a unit cell. Equation (2.6) is the starting point of TB calculations. In the upcoming sections we will apply this result to MLG and BLG.

2.3 Band Structure Theory of Monolayer Graphene

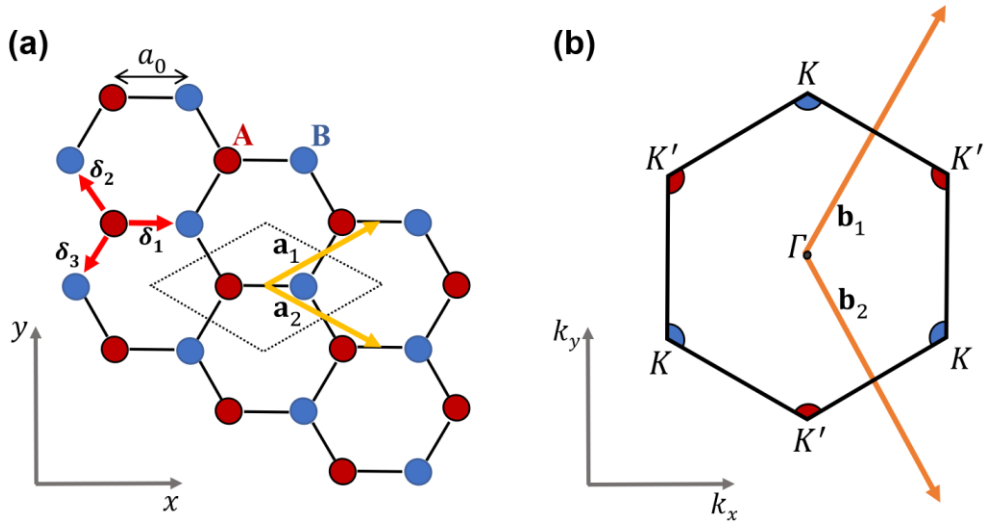

Figure 2.3.1| Real and reciprocal space lattices of monolayer graphene (MLG). (a) Schematic of graphene's lattice with lattice constant a_0. The triangular sublattices A and B are colored red and blue, respectively. The primitive lattice vectors $\mathbf{a}_1$ and $\mathbf{a}_2$ are shown as yellow arrows. The nearest neighbors δ_i are indicated by the red arrows. **(b)** Schematic of the reciprocal lattice of graphene showing the first Brillouin zone. There are two sets of equivalent high-symmetry points K and K'. The reciprocal lattice vectors $\mathbf{b}_1$ and $\mathbf{b}_2$ are shown as the orange arrows.

In graphene, carbon atoms use up their in-plane sp^2 orbitals to form σ-bonds between them. This leaves us with their out-of-plane and "tightly-bound" $2p_z$ orbitals which are used as the building blocks for graphene's Bloch functions which form π-bonds. To assemble these, we define the parameters that encode graphene's lattice information—the primitive and reciprocal lattice vectors.

Figure 2.3.1a shows a schematic of graphene's lattice. Graphene's lattice can be thought of as two interlocking triangular lattices made up of atoms labeled A and B. For this reason, it is instructive to color each sublattice differently. The primitive unit

cell in this lattice is delineated by the dotted rhomboid in Fig. 2.3.1a. Each carbon atom is separated by a distance a_0 = 1.4 Å. Thus, the primitive lattice vectors $\mathbf{a}_1$ and $\mathbf{a}_2$ are given by:

$$\mathbf{a}_1 = a_0\left(\frac{3}{2}, \frac{\sqrt{3}}{2}\right) \quad ; \quad \mathbf{a}_2 = a_0\left(\frac{3}{2}, -\frac{\sqrt{3}}{2}\right) \tag{2.7}$$

The primitive lattice vectors enable us to obtain the reciprocal lattice vectors $\mathbf{b}_1$ and $\mathbf{b}_2$, which in turn enables us to construct graphene's reciprocal lattice. The first Brillouin zone (BZ) of this space is depicted in Fig. 2.3.1b where the reciprocal lattice vectors $\mathbf{b}_i$ satisfy $\mathbf{b}_i \cdot \mathbf{a}_j = 2\pi\boldsymbol{\delta}_{ij}$, and are given by:

$$\mathbf{b}_1 = \frac{1}{a_0}\left(\frac{2\pi}{3}, \frac{2\pi}{\sqrt{3}}\right) \quad ; \quad \mathbf{b}_2 = \frac{1}{a_0}\left(\frac{2\pi}{3}, -\frac{2\pi}{\sqrt{3}}\right) \tag{2.8}$$

As mentioned above, we will only consider the out-of-plane $2p_z$ orbitals which lead to two low energy bands π and π^*.[2,3] With this consideration we can express the 2D Bloch function for graphene as:

$$\Phi(\boldsymbol{k}, \boldsymbol{r}) = \sum_{\boldsymbol{R}} e^{i\boldsymbol{k}\cdot\boldsymbol{R}}\left(c_A\phi_A^{2p_z}(\boldsymbol{r} - \boldsymbol{R}) + c_B\phi_B^{2p_z}(\boldsymbol{r} - \boldsymbol{R} - a_0\hat{\boldsymbol{x}})\right) \tag{2.9}$$

The orbitals $\phi_A^{2p_z}$ and $\phi_B^{2p_z}$ correspond to the $2p_z$ orbitals for each carbon atom within the unit cell. The translation vector $\boldsymbol{R}$ is understood to be any integer combination of the primitive lattice vectors $\mathbf{a}_1$ and $\mathbf{a}_2$. The equivalent coefficients c_A and c_B are introduced to ensure the normalization of the Bloch function; i.e. $|c_A|^2 + |c_B|^2 = 1$.

Referring to (2.6), to solve for graphene's bands we need to identify the components H_{ij} and S_{ij} in the sublattice basis, where

$$H = \begin{pmatrix} H_{AA} & H_{AB} \\ H_{BA} & H_{BB} \end{pmatrix} \quad ; \quad S = \begin{pmatrix} S_{AA} & S_{AB} \\ S_{BA} & S_{BB} \end{pmatrix} \tag{2.10}$$

It is convenient to first address the diagonal components for each matrix. The components H_{AA} and H_{BB} represent the ionization energies of the $2p_z$ orbitals for the A and B atoms in the unit cell, respectively. Thus, we define $H_{AA} = H_{BB} \equiv \varepsilon_{2p_z}$. The components S_{AA} and S_{BB} simplify to 1 given that these are expressed in terms of the normalized Bloch function (2.9) as $S_{AA} = \langle \Phi(\mathbf{r} = \boldsymbol{R}_A) | \Phi(\mathbf{r} = \boldsymbol{R}_A) \rangle = 1$ and $S_{BB} = \langle \Phi(\mathbf{r} = \boldsymbol{R}_B) | \Phi(\mathbf{r} = \boldsymbol{R}_B) \rangle = 1$, where $\boldsymbol{R}_A$ and $\boldsymbol{R}_B$ are the displacement vectors that span the A and B sublattices, respectively. To summarize these considerations thus far, we have:

$$H = \begin{pmatrix} \varepsilon_{2p_z} & H_{AB} \\ H_{AB}^* & \varepsilon_{2p_z} \end{pmatrix} \quad ; \quad S = \begin{pmatrix} 1 & S_{AB} \\ S_{AB}^* & 1 \end{pmatrix} \tag{2.11}$$

To obtain expressions for the off-diagonal elements in the H and S matrices, it is adequate to only consider interactions between nearest neighbors.[2] That is to say, we only consider the three B atoms surrounding each A atom, and vice versa. The vectors indicating the nearest neighbors of the sublattice atom A are depicted by the red arrows in Fig. 2.3.1a and given by:

$$\boldsymbol{\delta}_1 = (a_0, 0) \; ; \; \boldsymbol{\delta}_2 = a_0 \left(-\frac{1}{2}, \frac{\sqrt{3}}{2} \right) \; ; \; \boldsymbol{\delta}_3 = a_0 \left(-\frac{1}{2}, -\frac{\sqrt{3}}{2} \right) \tag{2.12}$$

Thus, the off-diagonal element H_{AB} can be written as:

$$H_{AB} = 2 \sum_{\boldsymbol{R}_{Ai}, \boldsymbol{R}_{Bj}} \frac{1}{2} e^{i\boldsymbol{k}\cdot(\boldsymbol{R}_{Bi} - \boldsymbol{R}_{Aj})} \langle \phi_A^{2p_z}(\boldsymbol{r} - \boldsymbol{R}_{Ai}) | H | \phi_B^{2p_z}(\boldsymbol{r} - \boldsymbol{R}_{Bj}) \rangle \quad (2.13)$$

In this expression, the factors 2 and $1/2$ account for spin and double counting of nearest neighbors, respectively. The factor in the bra-ket notation is the hopping energy between atoms A and B, and will hereby be expressed as $-\gamma_0$. Optical spectroscopy and transport experiments have determined this parameter to be $\gamma_0 \sim 3$ eV.[4]

After limiting each atom's influence to its three nearest neighbors by using the vectors from (2.12), we obtain:

$$H_{AB} = -\gamma_0 \sum_j e^{i\boldsymbol{k}\cdot\boldsymbol{\delta}_j} = -\gamma_0 \, f(\boldsymbol{k}) \quad (2.14)$$

$$\text{where} \qquad f(\boldsymbol{k}) = e^{ik_x a_0} + 2e^{-ik_x a_0/2} \cos\left(k_y a_0 \sqrt{3}/2\right) \quad (2.15)$$

A similar treatment follows for the off-diagonal elements of the *S* matrix:

$$S_{AB} = 2 \sum_{\boldsymbol{R}_{Ai}, \boldsymbol{R}_{Bj}} \frac{1}{2} e^{i\boldsymbol{k}\cdot(\boldsymbol{R}_{Bi} - \boldsymbol{R}_{Aj})} \langle \phi_A^{2p_z}(\boldsymbol{r} - \boldsymbol{R}_{Ai}) \big| \phi_B^{2p_z}\big(\boldsymbol{r} - \boldsymbol{R}_{Bj}\big) \rangle$$

$$= \sum_j e^{i\boldsymbol{k}\cdot\boldsymbol{\delta}_j} \, s_0 = s_0 \, f(\boldsymbol{k}) \quad (2.16)$$

here $s_0 = \langle \phi_A^{2p_z} \big| \phi_B^{2p_z} \rangle = \langle \phi_B^{2p_z} \big| \phi_A^{2p_z} \rangle$. s_0 is an experimentally determined constant

with finite values for overlapping orthogonal orbitals between adjacent atoms.

We have now identified all the elements needed to solve the characteristic equation (2.6) which can be expressed as:

$$\det\begin{pmatrix} \varepsilon_{2p_z} - E & -(\gamma_0 + s_0)f(\boldsymbol{k}) \\ -(\gamma_0 + s_0)f^*(\boldsymbol{k}) & \varepsilon_{2p_z} - E \end{pmatrix} = 0 \tag{2.17}$$

$$\Rightarrow \left(E - \varepsilon_{2p_z}\right)^2 - \left(\left[E - \varepsilon_{2p_z}\right]s_0 + \varepsilon_{2p_z}s_0 + \gamma_0\right)^2 |f(\boldsymbol{k})|^2 = 0 \tag{2.18}$$

Finally, the eigenvalue solutions $E(\boldsymbol{k})$ that relate a charge carrier's energy to its momentum in graphene are given by:

$$E_{\pm}(\boldsymbol{k}) = \frac{\varepsilon_{2p_z} \pm \gamma_0 |f(\boldsymbol{k})|}{1 \mp s_0 |f(\boldsymbol{k})|} \tag{2.19}$$

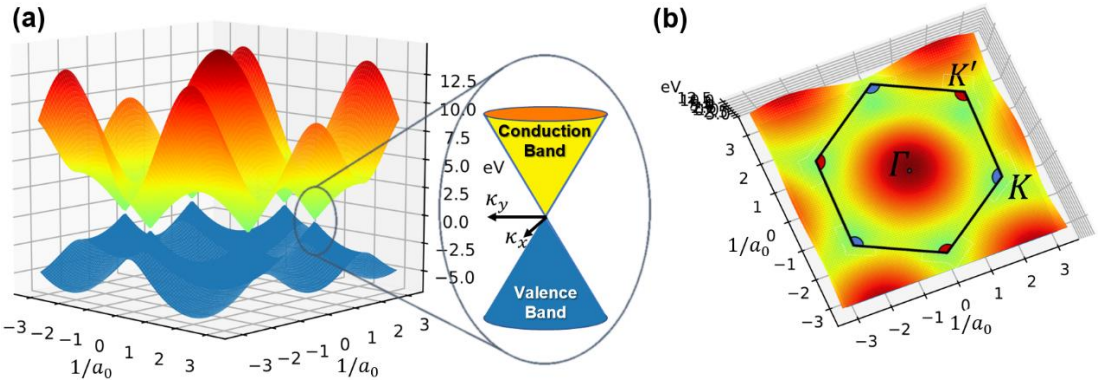

Figure 2.3.2| Low energy band structure of MLG. (a) Surface plot of graphene's low energy bands from (2.19) using the following parameters: $\gamma_0 = 2.8$ eV; $s_0 = 0.13$; and $\varepsilon_{2p_z} = 0$. The valence and conduction bands are colored blue and green-to-red, respectively. These bands touch at six corners of the Brillouin zone—points K and K'. Inset to the right shows a schematic of the zoomed in conical valence and conduction bands around a K point. **(b)** Top-view of the bands in (a) where the first BZ is outlined using the color gradient from the conduction band.

A plot of these bands near the first BZ is shown in Figs. 2.3.2a-b. These plots display some of graphene's unique band structure features. For example, the valence and conduction bands meet at the six vertices of the first BZ. These inequivalent points are labeled K and K' and are also referred to as valleys (akin to band minima in semiconductors). Near these points and within ~ 1 eV, the valence and conduction bands have linear dispersion which implies that graphene electrons behave as massless particles. By letting $\varepsilon_{2p_z} = 0$, the zero-energy point in Fig. 2.3.2a resides at the intersection of the valence and conduction bands—called the Dirac point. This means that for pristine graphene, the Fermi level is located at these points. As a consequence, changing the onsite energy ε_{2p_z} changes the Fermi level, which in turn changes the amount of available states. This property will be employed in Ch. 6 to simulate pseudo-confinement in graphene by spatially varying the onsite energies ε_{2p_z} across a sheet of graphene. Finally, we note that a clear asymmetry between the maxima and minima at the Γ point can be observed in Fig. 2.3.2a. This asymmetry arises due to a finite overlap parameter s_0, which in most cases can be ignored given that it does not change the bands near the K points and Fermi level.

2.3.1 Low energy states in MLG

To study the low energy states in graphene near the Dirac point, we start by redefining the reciprocal lattice parameters k_x and k_y so that they become centered

around the point, expressed as $\boldsymbol{K} = \frac{1}{a_0}\left(0, \frac{4\pi}{3\sqrt{3}}\right)$ in the $\boldsymbol{k}$-basis . Let

$$\kappa_x \equiv k_x \quad ; \quad \kappa_y \equiv k_y - \frac{4\pi}{3a_0\sqrt{3}} \tag{2.20}$$

This substitution and subsequent drop of higher order terms lead to an approximation of (2.15) given by:

$$f(\boldsymbol{k}) \approx \frac{\sqrt{3}}{2} a_0(-\kappa_y + i\kappa_x) \tag{2.21}$$

This allows us to obtain a compact Dirac-like Hamiltonian for low-energy states near K:

$$H_K \cdot \vec{\boldsymbol{c}} = \frac{\sqrt{3}}{2}\gamma_0 a_0 \begin{pmatrix} 0 & \kappa_y + i\kappa_x \\ \kappa_y - i\kappa_x & 0 \end{pmatrix} \cdot \begin{pmatrix} c_A \\ c_B \end{pmatrix} = E \begin{pmatrix} c_A \\ c_B \end{pmatrix} \tag{2.22}$$

The eigenvalue solutions for this equation represent the valence (E_-) and conduction (E_+) bands in MLG:

$$E_\pm = \pm\frac{\sqrt{3}}{2}\gamma_0 a_0 |\boldsymbol{\kappa}| \equiv \pm\hbar v_f |\boldsymbol{\kappa}| \tag{2.23}$$

In this expression, the vector $\boldsymbol{\kappa}$ represents small excursions in reciprocal space around the vicinity of the K point. We have also introduced the Fermi velocity as $v_f = \frac{3}{2\hbar}\gamma_0 a_0$. This quantity has been determined to be $\sim c/300$, where c is the speed of light.[5,6]

The band structure in this low energy regime is depicted in the inset of Fig.2.3.2a by the cones whose apices touch at the Dirac point. Graphene is thus referred

to as a semi-metal because despite having no bandgap, it has a density of states (DOS) minimum at the Dirac point. The simple result in (2.23) is extremely profound. The linear energy dispersion near the K point suggests that electrons in graphene behave much like massless particles in vacuum that travel at about $1/100^{\text{th}}$ the speed of light. Note that to arrive to this result we employed two approximations: (1) only nearest neighbor interactions, and (2) $|\boldsymbol{\kappa}|a_0 \ll 1$ near the K-point. However, despite these approximations, graphene's linear dispersion near K has been shown to hold when next nearest neighbors are considered or even when calculations more advanced than the TB model are used.[7]

We will now shift focus to the eigenvectors that result from (2.22). First, we define an angle θ between $\boldsymbol{\kappa}$ and the κ_x-axis such that:

$$\kappa_y \pm i\kappa_x = \pm i|\boldsymbol{\kappa}|e^{\mp i\theta} \tag{2.24}$$

We note that a similar treatment for the K' point leads to a similar relation after substituting $\kappa_y \to -\kappa_y$. Thus, taking these expressions into account, the eigenstates for the K and K' valleys are found by solving for c_A and c_B in:

$$H_K \cdot \boldsymbol{c} = \hbar v_F|\boldsymbol{\kappa}| \begin{pmatrix} 0 & ie^{-i\theta} \\ -ie^{i\theta} & 0 \end{pmatrix} \cdot \begin{pmatrix} c_A \\ c_B \end{pmatrix} = E_{\pm} \begin{pmatrix} c_A \\ c_B \end{pmatrix} \tag{2.25}$$

$$H_{K'} \cdot \boldsymbol{c} = \hbar v_F|\boldsymbol{\kappa}| \begin{pmatrix} 0 & ie^{i\theta} \\ -ie^{-i\theta} & 0 \end{pmatrix} \cdot \begin{pmatrix} c_A \\ c_B \end{pmatrix} = E_{\pm} \begin{pmatrix} c_A \\ c_B \end{pmatrix} \tag{2.26}$$

By choosing $c_A = 1$, the eigenvector solutions are:

$$\psi_{\pm}^{K} = \frac{1}{\sqrt{2}} \begin{pmatrix} 1 \\ \mp i e^{i\theta} \end{pmatrix} e^{i\boldsymbol{\kappa}\cdot\boldsymbol{r}} \quad ; \quad \psi_{\pm}^{K'} = \frac{1}{\sqrt{2}} \begin{pmatrix} 1 \\ \pm i e^{-i\theta} \end{pmatrix} e^{i\boldsymbol{\kappa}\cdot\boldsymbol{r}} \tag{2.27}$$

In these expressions, ψ_+ and ψ_- correspond to the eigenvectors for the conduction and valence bands, respectively. A plane wave term $e^{i\boldsymbol{\kappa}\cdot\boldsymbol{r}}$ has been attached to provide spatial dependence . The vectors in (2.27) are expressed in the basis of the A and B sublattices. Thus, there is a strong dependence between a state's momentum direction and its probability of being in the A or B sublattice. This binary behavior resembles an electron's spin in a magnetic field and is thus referred to as *pseudospin*. However, instead of saying that electrons are spin up or down, we may think of pseudospin as the quality of electrons being localized either in the A or B sublattice.

In addition, by arranging the Pauli matrices as $\hat{\boldsymbol{\sigma}} = (\sigma_y, -\sigma_x)$, we can express the effective Dirac-like Hamiltonian in (2.22) as $H_K = v_F \hat{\boldsymbol{\sigma}} \cdot \mathbf{p}$**;** where $\mathbf{p} = \hbar\boldsymbol{\kappa}$. For the K' valley we just substitute $\sigma_y \rightarrow (-\sigma_y)$. This expression highlights the fact that the pseudospin of graphene's fermions is intimately linked to their momenta. From conservation of energy, the projection of an electron or hole's momentum onto their pseudospin must be conserved. This conservation rule gives rise to exotic scattering properties of charge carriers in graphene which will be discussed in the following section.

2.3.2 Scattering properties of charge carriers in MLG

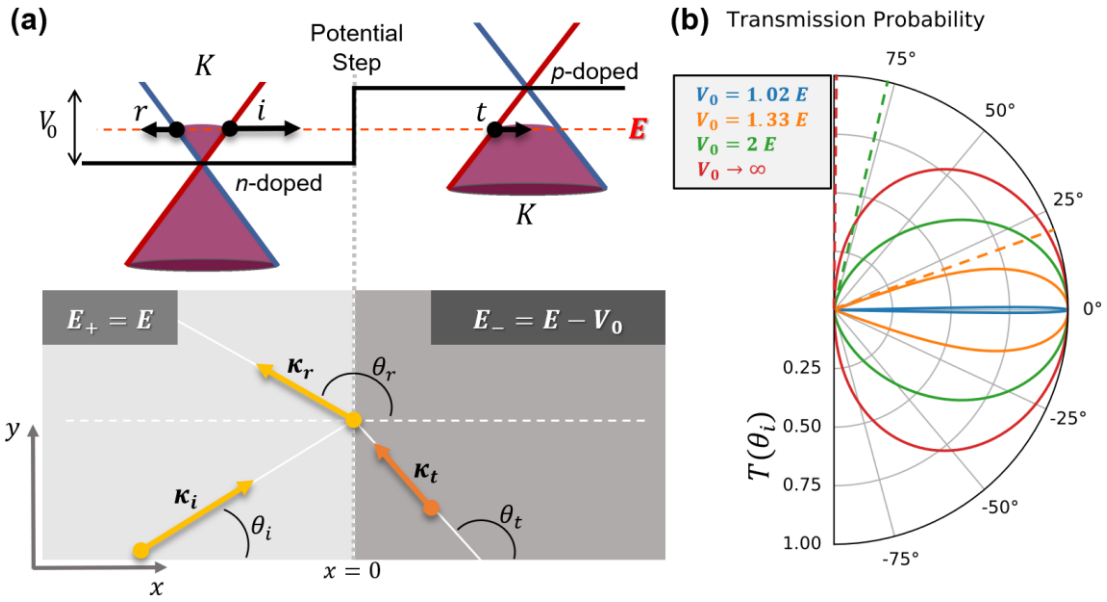

Figure 2.3.3| MLG charge carrier scattering across a step potential. (a) Schematic showing electron scattering off a sharp step potential in MLG which separates *n*-doped and *p*-doped regions. Top: Side-view of scattering potential where an electron in the conduction band moves transmits through with amplitude t onto the valence band and reflects with amplitude r. The black arrows depict electron velocities. Bottom: Top-view of scattering process depicting an electron's incident ($\boldsymbol{\kappa}_i$), transmitted ($\boldsymbol{\kappa}_t$), and reflected ($\boldsymbol{\kappa}_r$) wave vectors. **(b)** Plots of the transmission probability T as a function of the incident angle θ_i for different values of the potential height V_0 with respect to electron's energy E. Regardless of potential height, an electron can be fully transmitted at normal incidence.

The eigenvectors in (2.27) display unique scattering behavior akin to relativistic particles.[8,9] The scattering properties of quasiparticles in graphene are crucial to explain the mechanism behind the pseudo-confinement of graphene electrons discussed in Ch. 6.

As a first simple example, consider a state in the conduction band propagating

along the $\theta = 0$ direction near the K point. In the conduction band, the pseudospin part in (2.27) results in $\begin{pmatrix} 1 \\ -i \end{pmatrix}$. Now, consider a state that propagates in the opposite direction; i.e. $\theta = \pi$. Such state has a pseudospin of $\begin{pmatrix} 1 \\ i \end{pmatrix}$. The inner product of these oppositely propagating states results in zero. This implies that there is no overlap between backscattered states. In the absence of A-B sublattice symmetry breaking, this property manifests experimentally in the form of weak backscattering which leads to enhanced mean free paths.[10]

Now, we will consider a more complex scenario and come up with an expression for the transmission probability of an electron across a sharp potential as done by Allain and Fuchs.[11] Consider an electron in the K valley impinging on a sharp step potential V_0 with incident angle θ_i shown in Fig. 2.3.3a. This schematic depicts two regions separated by a sharp step potential. In the left region, the electron in the conduction band has energy $E_+ = E$ with respect to the Dirac point. In the right region, the electron propagates in the valence band and has energy $E_- = E - V_0$. The fact that $E_- < 0$ implies that the wave vector points in the opposite direction to the wave propagation. Additionally, backscattering in y across the step potential is not allowed since the potential is a function of x only. Unlike familiar optics behavior, these considerations result in the depiction of the transmitted orange arrow pointing towards the left region and appearing below the normal line (see Fig. 2.3.3a).

First, we write out the expressions for the three wave vectors in Fig. 2.3.3a. For

sake of simplicity, we will let $\hbar v_F = 1$, so that (2.23) becomes:

$$E_{\pm} = \pm|\boldsymbol{\kappa}| \tag{2.28}$$

With this in mind, we can express the wave vectors from Fig. 2.3.3a as:

$$\boldsymbol{\kappa}_i = E(\cos\theta_i\,, \sin\theta_i) \equiv \left(\kappa_x, \kappa_y\right) \tag{2.29}$$

$$\boldsymbol{\kappa}_r = E(\cos(\pi - \theta_i)\,, \sin(\pi - \theta_i)) = \left(-\kappa_x, \kappa_y\right) \tag{2.30}$$

$$\boldsymbol{\kappa}_t = -(E - V_0)(\cos\theta_t\,, \sin\theta_t) \equiv \left(\kappa_x', \kappa_y\right) \tag{2.31}$$

where $\theta_r = \pi - \theta_i$ in (2.30) results from translational symmetry between the incident and reflected wave vectors along y, i.e. $\boldsymbol{\kappa}_i \cdot \hat{\boldsymbol{y}} = \boldsymbol{\kappa}_r \cdot \hat{\boldsymbol{y}}$. The same condition applied to the transmitted wave $\boldsymbol{\kappa}_i \cdot \hat{\boldsymbol{y}} = \boldsymbol{\kappa}_t \cdot \hat{\boldsymbol{y}}$ leads to an expression for θ_t which was applied to (2.31):

$$\sin\theta_t = \frac{-E}{V_0 - E}\sin\theta_i \tag{2.32}$$

Second, we write out the wavefunctions corresponding to the *n* and *p*-doped regions in Fig. 2.3.3a. Let r and t be the coefficients for the reflected and transmitted eigenstates, respectively. If we ignore normalization coefficients, account for symmetry arguments, and use (2.27) at the K point, we can express these wavefunctions as:

$$\psi_n = \left[\begin{pmatrix} 1 \\ -e^{i\theta_i} \end{pmatrix} e^{i\kappa_x x} + r\begin{pmatrix} 1 \\ -e^{i(\pi-\theta_i)} \end{pmatrix} e^{-i\kappa_x x}\right] e^{i\kappa_y y} \tag{2.33}$$

$$\psi_p = t\begin{pmatrix}1\\ e^{i\theta_t}\end{pmatrix} e^{i\kappa'_x x} e^{i\kappa_y y} \tag{2.34}$$

Ensuring continuity of these wavefunctions at $x = 0$ leads to:

$$r = \frac{e^{i\theta_t} + e^{i\theta_i}}{e^{-i\theta_i} - e^{i\theta_t}} \;\; ; \;\; t = \frac{e^{i\theta_i} + e^{-i\theta_i}}{e^{-i\theta_i} - e^{i\theta_t}} \tag{2.35}$$

Now, we consider conservation of current probability along the x direction. This means the following:

$$\left\langle \psi_i \left| \frac{\boldsymbol{\kappa}_i}{|\boldsymbol{\kappa}_i|} \right| \psi_i \right\rangle + \left\langle \psi_r \left| \frac{\boldsymbol{\kappa}_r}{|\boldsymbol{\kappa}_r|} \right| \psi_r \right\rangle + \left\langle \psi_t \left| \frac{\boldsymbol{\kappa}_t}{|\boldsymbol{\kappa}_t|} \right| \psi_t \right\rangle = 0 \tag{2.36}$$

where the wavefunctions ψ_i, ψ_r, and ψ_t correspond to the incident, reflected, and transmitted components in (2.33) and (2.34). If we consider R and T to be the reflection and transmission probabilities, respectively, the law of conservation of probability states that $1 = R + T$. Consequently, from (2.36) we obtain:

$$1 = |r|^2 + \left(-|t|^2 \frac{\cos\theta_t}{\cos\theta_i}\right) = R + T \tag{2.37}$$

Finally, using (2.35) we can express the transmission and reflection probabilities as:

$$T = -\frac{\cos\theta_i \cos\theta_t}{\sin^2\left(\frac{\theta_i + \theta_t}{2}\right)} \tag{2.38}$$

$$R = \frac{\cos^2\left(\frac{\theta_i - \theta_t}{2}\right)}{\sin^2\left(\frac{\theta_i + \theta_t}{2}\right)} \tag{2.39}$$

where θ_t can be expressed in terms of θ_i with (2.32).

Figure 2.3.3b shows a plot of the transmission probability T as a function of the incident angle θ_i. The curves are plotted for $-\pi/2 < \theta_i < \pi/2$ and θ_t has been shifted by π to fit within this range. The case for four magnitudes of the potential step V_0 with respect to E are plotted. From this plot we gather that as $V_0 \to E$; a particle can cross the potential step only if it travels at normal incidence ($\theta_i = 0°$). As V_0 increases, particles have higher transmission probabilities for angles near normal incidence. Additionally, particles become fully reflected past certain critical angles for different values of V_0. These minimum angles of total internal reflection are indicated by the dashed lines in Fig. 2.3.3b. In the limit $V_0 \to \infty$; only particles with $\kappa_x = 0$ become fully reflected. Regardless of the relative height of V_0 it is apparent that at normal incidence particles have a 100% probability of being transmitted through the step potential. This bizarre result is known as Klein tunneling. The unconventional scattering properties of graphene electrons have led to the realization of novel electron-optics phenomena like negative index of refraction.[12,13] Moreover, in Ch. 6 we will discuss a circular electrostatic potential where the primary trapping and escape mechanism relies on the scattering results we have presented here. For further discussion of different scattering scenarios such as smoothly varying potentials, see the work by Allain and Fuchs.[11]

2.4 Band Structure Theory of Bilayer Graphene

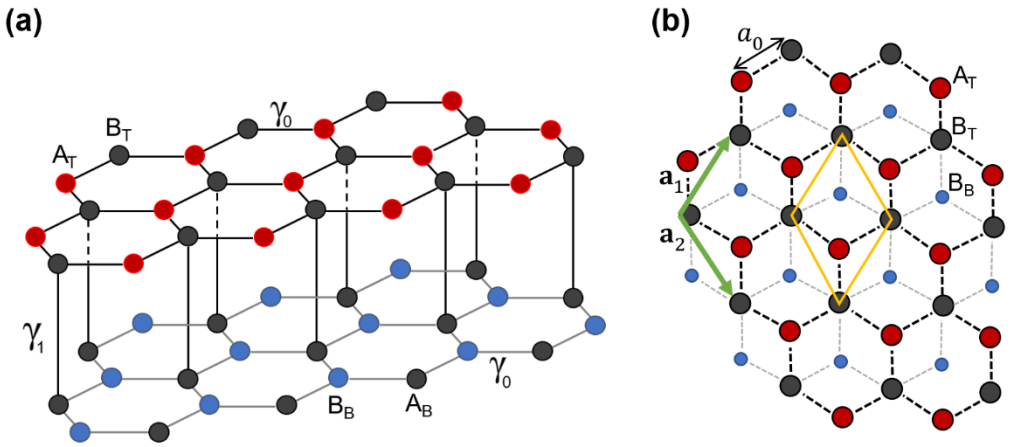

Figure 2.4.1| Lattice of Bernal stacked bilayer graphene (BLG). (a) Schematic of the lattice of Bernal stacked BLG. The top layer atoms are labeled as A_T (red circles) and B_T (gray circles). The bottom layer atoms are labeled as A_B (gray circles) and B_B (blue circles). The intralayer hopping term γ_0 between $A_{T(B)}$ and $B_{T(B)}$ atoms and the interlayer hopping term γ_0 between B_T and A_B atoms are indicated. **(b)** Top view of Bernal stacked BLG. The unit cell is outlined by the orange rhomboid. The unit cell in BLG encloses 4 atoms in total. The primitive lattice vectors $\mathbf{a}_1$ and $\mathbf{a}_2$ are illustrated by the green arrows.

In this section we will calculate the band structure of Bernal stacked bilayer graphene (BLG) using the TB model and following a similar procedure as done for MLG. However, we will only highlight the main points of the calculation. We will apply the nearest neighbor approximation early on to acquire expressions for the low energy band structure of BLG.

The lattice in BLG is composed of two layers of graphene stacked on top of each other. Figure 2.4.1a depicts BLG's lattice in the Bernal stacking configuration where the A_B atom is right below the B_T atom. This configuration is also known as AB-

stacked. BLG's band structure will be calculated using the intralayer and interlayer hopping terms γ_0 and γ_1, respectively. The term γ_0 is the same as in monolayer graphene. The term γ_1 indicates the coupling between the A_B and B_T atoms, which approximates the coupling between the top and bottom layers. More advanced calculations may employ higher order hopping terms[4] such as γ_3 and γ_4. However, assuming that $\gamma_3 = \gamma_4 = 0$ appropriately describes the results I will discuss in Ch. 7 and 8. Figure 2.4.1b shows the top view of BLG's lattice with the primitive lattice $\mathbf{a}_1$ and $\mathbf{a}_2$ vectors indicated by the green arrows. The unit cell is outlined by the orange rhomboid. For BLG, this unit cell extends in the z direction such that it encloses a total of 4 atoms: A_T, B_T, A_B, and B_B.

Similar to the procedure demonstrated for MLG, we will use BLG's unit cell atoms to indicate the basis for the matrices in the characteristic equation $\det(H_{ij} - ES_{ij}) = 0$. Thus, assuming the basis $\{A_T, B_T, A_B, B_B\}$

$$H = \begin{pmatrix} \varepsilon_{2p_z} & -\gamma_0 f^*(\boldsymbol{k}) & 0 & 0 \\ -\gamma_0 f^*(\boldsymbol{k}) & \varepsilon_{2p_z} & \gamma_1 & 0 \\ 0 & \gamma_1 & \varepsilon_{2p_z} & -\gamma_0 f^*(\boldsymbol{k}) \\ 0 & 0 & -\gamma_0 f^*(\boldsymbol{k}) & \varepsilon_{2p_z} \end{pmatrix} \tag{2.40}$$

$$S = \begin{pmatrix} 1 & -s_0 f(\boldsymbol{k}) & 0 & 0 \\ -s_0 f^*(\boldsymbol{k}) & 1 & 0 & 0 \\ 0 & 0 & 1 & -s_0 f(\boldsymbol{k}) \\ 0 & 0 & -s_0 f^*(\boldsymbol{k}) & 1 \end{pmatrix} \tag{2.41}$$

where

$$f(\boldsymbol{k}) = e^{ik_y a_0} + 2e^{-ik_y a_0/2}\cos\left(k_x a_0\sqrt{3}/2\right) \tag{2.42}$$

Note that this expression is slightly different from (2.15) since we arbitrarily chose the unit cell such that the BZ is rotated by 30° with respect to the MLG case. The composition of BLG by two single layers of graphene is apparent from these matrices. If subdivided by layers, we see that each of the top and bottom sub-bases form the same matrices as (2.11) coupled by a single "hopping" matrix $\begin{pmatrix} 0 & 0 \\ \gamma_1 & 0 \end{pmatrix}$.

At this point, the characteristic equation $\det\left(H_{ij} - ES_{ij}\right) = 0$ may be solved. However, we can simplify our calculations by applying the low energy restrictions. Like in MLG, these restrictions imply that we can assume; $s_0 \to 0$ at low energies and define $\varepsilon_{2p_z} \equiv 0$. These considerations simplify the characteristic equation to:

$$\det\begin{pmatrix} -E & -\gamma_0 f(\boldsymbol{k}) & 0 & 0 \\ -\gamma_0 f^*(\boldsymbol{k}) & -E & \gamma_1 & 0 \\ 0 & \gamma_1 & -E & -\gamma_0 f(\boldsymbol{k}) \\ 0 & 0 & -\gamma_0 f^*(\boldsymbol{k}) & -E \end{pmatrix} = 0 \tag{2.43}$$

the four eigenvalue solutions are:

$$E_{\pm}^{\alpha}(\boldsymbol{k}) = \pm\frac{\gamma_1}{2}\left(\sqrt{1 + \frac{4\gamma_0^2|f(\boldsymbol{k})|^2}{\gamma_1^2}} + \alpha\right) \quad ; \quad \alpha = \pm 1 \tag{2.44}$$

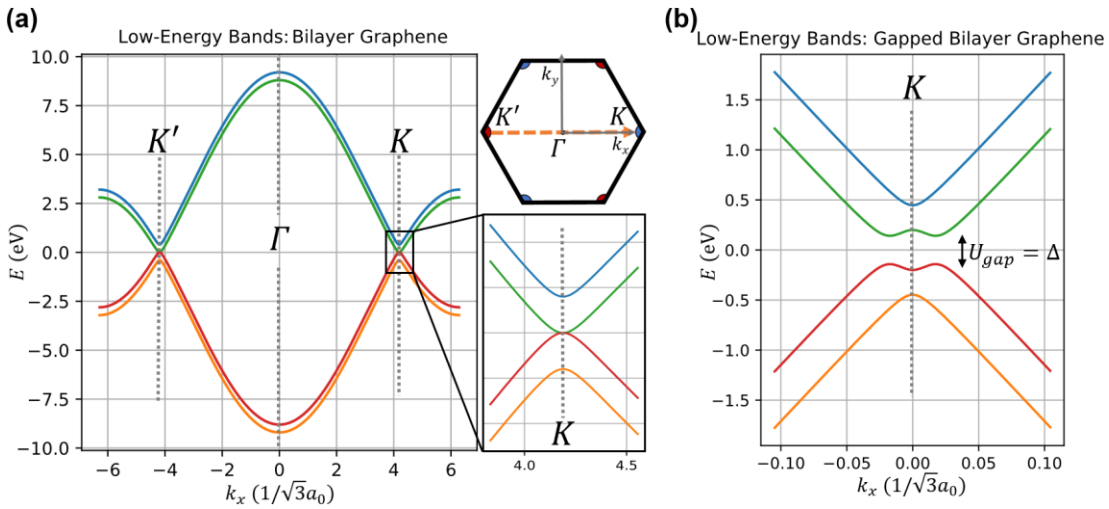

Figure 2.4.2| Low energy band structure of BLG. (a) Plot of the low energy bands of BLG considering only nearest neighbor interactions and $s_0 = 0$. Parameters used: $\gamma_0 = 3$ eV; $\gamma_1 = 0.4$ eV; and $\varepsilon_{2p_z} = 0$. The conduction and valence bands touch at six corners of the BZ as shown by the inset around the K point. **(b)** Plot of the low energy bands of BLG near K considering only nearest neighbor interactions, $s_0 = 0$, and finite layer asymmetry Δ. Parameters used: $\gamma_0 = 3$ eV; $\Delta = \gamma_1 = 0.4$ eV. Finite layer asymmetry Δ induces a band gap at the K and K' points in the BZ.

These solutions are plotted in Fig. 2.4.2a. This plot shows that two bands touch at six high symmetry points; akin to what we obtained for MLG. These points are also labeled K and K'. However, unlike MLG, the bands touching at the CNP are not linear. From this we infer that BLG does not have massless light-like electrons. However, we will shortly see that BLG electrons still have their own version of pseudospin and are therefore considered massive Dirac fermions.

To obtain the low energy eigenvectors in BLG near the K point, we further assume that $|E| \ll |\gamma_1|$ and $|\gamma_0 f(\boldsymbol{k})| \ll |\gamma_1|$. The latter assumption is justified given that at the K points $f(\boldsymbol{K}) = 0$. Applying these conditions to (2.43) reduces the

dimensionality of the problem such that only the coefficients representing the A_T and B_B atoms have non-zero components[4]. Similar to (2.22) for MLG, we can restructure the characteristic equation (2.43) about the K point as:

$$-\frac{\hbar^2}{2m}\begin{pmatrix} 0 & \left(\kappa_x - i\kappa_y\right)^2 \\ \left(\kappa_x + i\kappa_y\right)^2 & 0 \end{pmatrix}\begin{pmatrix} c_{\mathrm{A_T}} \\ c_{\mathrm{B_B}} \end{pmatrix} = E\begin{pmatrix} c_{\mathrm{A_T}} \\ c_{\mathrm{B_B}} \end{pmatrix} \tag{2.45}$$

here $m = \gamma_1/(2v_f^2)$ acts as an effective mass term. Solutions to E yield the valence (E_-) and conduction (E_+) bands:

$$E_\pm = \pm\frac{\hbar^2}{2m}|\boldsymbol{\kappa}|^2 \tag{2.46}$$

We will now shift focus to the eigenvectors that result from (2.45). First, we define an angle θ between $\boldsymbol{\kappa}$ and the κ_x-axis such that:

$$\kappa_x \pm i\kappa_y = |\boldsymbol{\kappa}|e^{\pm i\theta} \tag{2.47}$$

We note that a similar treatment for the K' point leads to a similar relation after substituting $\kappa_x \to -\kappa_x$. Thus, taking these expressions into account, we find the eigenstates for the K and K' valleys by solving for c_A and c_B in:

$$H_K \cdot \boldsymbol{c} = \frac{\hbar^2}{2m}|\boldsymbol{\kappa}|^2\begin{pmatrix} 0 & e^{-2i\theta} \\ e^{2i\theta} & 0 \end{pmatrix}\cdot\begin{pmatrix} c_{A_T} \\ c_{B_B} \end{pmatrix} = E_\pm\begin{pmatrix} c_{A_T} \\ c_{B_B} \end{pmatrix} \tag{2.48}$$

$$H_{K'} \cdot \boldsymbol{c} = \frac{\hbar^2}{2m}|\boldsymbol{\kappa}|^2\begin{pmatrix} 0 & e^{2i\theta} \\ e^{-2i\theta} & 0 \end{pmatrix}\cdot\begin{pmatrix} c_{A_T} \\ c_{B_B} \end{pmatrix} = E_\pm\begin{pmatrix} c_{A_T} \\ c_{B_B} \end{pmatrix} \tag{2.49}$$

By choosing $c_{A_T} = 1$, the eigenvectors are given by:

$$\psi_{\pm}^{K} = \frac{1}{\sqrt{2}} \begin{pmatrix} 1 \\ \mp e^{2i\theta} \end{pmatrix} e^{i\boldsymbol{\kappa}\cdot\boldsymbol{r}} \quad ; \quad \psi_{\pm}^{K'} = \frac{1}{\sqrt{2}} \begin{pmatrix} 1 \\ \mp e^{-2i\theta} \end{pmatrix} e^{i\boldsymbol{\kappa}\cdot\boldsymbol{r}} \tag{2.50}$$

Much like MLG, BLG also displays pseudospin properties. However, they do not exactly mirror the scattering properties discussed in section 2.3.2. Regardless, we can draw an analogy between MLG and BLG. In MLG's case, the pseudospin degree of freedom corresponds to charge carriers being localized in the A or B sublattice. In BLG, given that we decoupled from the dimer site atoms B_T and A_B, the pseudospin degree of freedom corresponds to an electron or hole's localization in either the A_T or B_B sublattice. In simpler terms, a particle's pseudospin in BLG can be thought of as being localized in the top or bottom layer. BLG chirality will not be considered in the rest of the thesis, but for further reading on its consequences in scattering see the works by McCann,[4] Shytov,[14] and Allain and Fuchs.[11]

2.4.1 Bandgap tunability in BLG

The ability to tune a material's band gap is of paramount importance in the development of electronic and optoelectronic components such as transistors, diodes, and photodetectors. In conventional semiconductors, band gap tunability is set in a material during fabrication through careful tuning of stoichiometric ratios and strain engineering. However, real-time *in*-situ tunability has not been realized. This limitation in conventional semiconductors can be overcome in BLG.

The semi-metallic nature of MLG arises from the symmetry between the A and B sublattices. In order to induce a gap, these two sublattices would need to have unequal on-site energies. Although a precise and controllable change of these sublattice energies in MLG has not been experimentally achieved, recent studies have shown that graphene can be gapped with strain and substrate-induce symmetry breaking.[15,16] Thankfully, band gap tunability is feasible in BLG due to the primary sublattice symmetry existing between the top and bottom layers. This section will provide an overview of BLG's band gap tunability achieved by braking layer symmetry which will be experimentally demonstrated in Ch. 8.

Inducing layer asymmetry in BLG amounts to changing the $2p_z$ orbital energies of the top layer atoms with respect to the bottom ones. Experimentally, this is achieved by applying a perpendicular electric field on BLG. As an electric field emanates from a remote conducting substrate, the layer in BLG closest to such substrate experiences enhanced changes to its charge density when compared to the layer furthest away. This is the case for a uniform electric field E since a change in electric potential ΔV only depends on a change in distance Δd from the plate electrode, i.e. $\Delta V = E \cdot \Delta d$. I will cover the experimental process to achieve this change in more detail in Ch. 8. However, for our TB model calculations, layer asymmetry can be adapted into (2.40) by shifting the onsite energies between the layers by Δ, such that $\left(\varepsilon_{2p_z}\right)^{\mathrm{A_T}} = \left(\varepsilon_{2p_z}\right)^{\mathrm{B_T}} = -\frac{1}{2}\Delta$; and $\left(\varepsilon_{2p_z}\right)^{\mathrm{A_B}} = \left(\varepsilon_{2p_z}\right)^{\mathrm{B_B}} = +\frac{1}{2}\Delta$. These considerations yield:

$$H_{\Delta} = \begin{pmatrix} -\frac{1}{2}\Delta & -\gamma_0 f(\boldsymbol{k}) & 0 & 0 \\ -\gamma_0 f^*(\boldsymbol{k}) & -\frac{1}{2}\Delta & \gamma_1 & 0 \\ 0 & \gamma_1 & +\frac{1}{2}\Delta & -\gamma_0 f(\boldsymbol{k}) \\ 0 & 0 & -\gamma_0 f^*(\boldsymbol{k}) & +\frac{1}{2}\Delta \end{pmatrix} \tag{2.51}$$

Applying the same restrictions as done for the layer symmetric case, we can assume the overlap matrix S to be a unit matrix. Thus, to calculate the bands in this layer-asymmetric case, one needs to solve the characteristic equation $\det(H_{\Delta} - E\mathbf{I}) = 0$, where $\mathbf{I}$ is a 4x4 unit matrix. There are four eigenvalue solutions for E which are given by[4]:

$$E_{\pm}^{\alpha}(\boldsymbol{k}) = \pm\left[\frac{\Delta^2}{4} + v_F^2 p^2 + \frac{\gamma_1^2}{2} + \alpha\frac{\gamma_1^2}{2}\sqrt{1 + \frac{4v_F^2 p^2}{\gamma_1^2} + \frac{4\Delta^2 v_F^2 p^2}{\gamma_1^4}}\right]^{1/2} \tag{2.52}$$

where $\alpha = \pm 1$, and the linear approximation from (2.21) was applied such that $\gamma_0|f(\boldsymbol{k})| \sim v_F p = v_F \hbar|\boldsymbol{k}|$.

Figure 2.4.2b shows a plot of the solutions for (2.52) where the asymmetry term used is $\Delta = \gamma_1 = 0.4$ eV. Far from the K and K' points, the bands in BLG remain largely unchanged after layer symmetry has been broken. However, as shown in Fig. 2.4.2b we see that within a few eV around the K point, the conduction and valence bands no longer touch. In fact, an effective bandgap $U_{gap} = \Delta$ has opened up.

In Ch. 8 we will use scanning tunneling spectroscopy to map the evolution of

this gap as we change the strength of a perpendicular electric field. Additionally, we will demonstrate that appropriate tuning of the layer asymmetry in BLG leads to a clear spectroscopic signature of the valence band edge which is mapped spatially.

2.5 Pybinding: a TB Computational Package

The TB model results obtained in section 2.2 have general applicability to crystals with translational symmetry. Those results are applied and can be expanded upon by a computational package written in Python called Pybinding[17]. Essentially, this method computes (2.6) after the user has defined the unit cell, primitive lattice vectors, and hopping parameters γ_i. Conveniently, this package comes with predefined models for MLG and BLG which can be called with the commands `graphene.monolayer()` and `graphene.bilayer()`, respectively.

Below is a sample script that computes the bands in MLG assuming translational symmetry by using a standard eigenvalue solver[17]

```
"""Calculate and plot the band structure of monolayer graphene"""
import pybinding as pb
import matplotlib.pyplot as plt
from math import sqrt, pi
from pybinding.repository import graphene

pb.pltutils.use_style()


model = pb.Model(
    graphene.monolayer(),  # predefined lattice from the material repository
    pb.translational_symmetry()    # creates an infinite sheet of graphene
)
solver = pb.solver.lapack(model)  # eigensolver from the LAPACK library

# significant points in graphene's Brillouin zone
a_cc = graphene.a_cc  # carbon-carbon distance
Gamma = [0, 0]
```

```
K1 = [-4*pi / (3*sqrt(3)*a_cc), 0]
M = [0, 2*pi / (3*a_cc)]
K2 = [2*pi / (3*sqrt(3)*a_cc), 2*pi / (3*a_cc)]

# plot the bands through the desired points
bands = solver.calc_bands(K1, Gamma, M, K2)
bands.plot(point_labels=['K', r'$\Gamma$', 'M', 'K'])
plt.show()
```

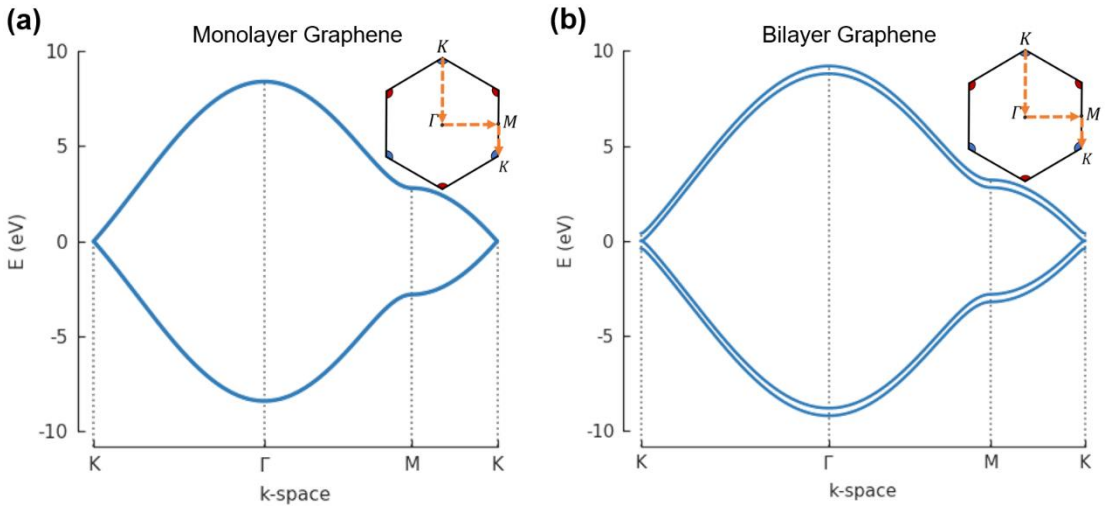

Figure 2.5| Computed MLG and BLG bands using Pybinding. (a) Plot of MLG's bands considering only nearest neighbor interactions. Parameters used: $\gamma_0 = 2.8$ eV; and $\varepsilon_{2p_z} = 0$. **(b)** Plot of BLG's bands considering only nearest neighbor interactions. Parameters used: $\gamma_0 = 2.8$ eV; $\gamma_1 = 0.4$ eV.

The result of this script is the plot shown in Fig. 2.5a where the band structure of MLG is plotted along the dashed orange arrows indicated in the BZ. The bands of BLG can also be calculated by calling `graphene.bilayer()` from the material repository. The result for BLG's bands calculation is shown in Fig. 2.5b. Note that these bands are also shown in Fig. 2.4.2a which were obtained analytically. The Pybinding package will be used in Ch. 6 and 8. In Ch. 6 we will calculate the spatial dependence of the local density of states (LDOS) of MLG within a parabolic electrostatic potential. In Ch. 8, we will simulate layer asymmetry in BLG to calculate

its LDOS for specific atoms in the unit cell.

Chapter 2 - References

(1) Aguilera, I.; Friedrich, C.; Blügel, S. Many-Body Corrected Tight-Binding Hamiltonians for an Accurate Quasiparticle Description of Topological Insulators of the Bi2Se3 Family. *Phys. Rev. B* **2019**. https://doi.org/10.1103/PhysRevB.100.155147.

(2) Saito, R.; Dresselhaus, G.; Dresselhaus, M. S. *Physical Properties of Carbon Nanotubes*; 1998. https://doi.org/10.1142/p080.

(3) Wallace, P. R. The Band Theory of Graphite. *Phys. Rev.* **1947**. https://doi.org/10.1103/PhysRev.71.622.

(4) McCann, E.; Koshino, M. The Electronic Properties of Bilayer Graphene. *Reports Prog. Phys.* **2013**. https://doi.org/10.1088/0034-4885/76/5/056503.

(5) Novoselov, K. S.; Geim, A. K.; Morozov, S. V.; Jiang, D.; Zhang, Y.; Dubonos, S. V.; Grigorieva, I. V.; Firsov, A. A. Electric Field in Atomically Thin Carbon Films. *Science (80-.).* **2004**. https://doi.org/10.1126/science.1102896.

(6) Martin, J.; Akerman, N.; Ulbricht, G.; Lohmann, T.; Smet, J. H.; Von Klitzing, K.; Yacoby, A. Observation of Electron-Hole Puddles in Graphene Using a Scanning Single-Electron Transistor. *Nat. Phys.* **2008**. https://doi.org/10.1038/nphys781.

(7) Reich, S.; Maultzsch, J.; Thomsen, C.; Ordejón, P. Tight-Binding Description of Graphene. *Phys. Rev. B - Condens. Matter Mater. Phys.* **2002**. https://doi.org/10.1103/PhysRevB.66.035412.

(8) Cheianov, V. V.; Fal'ko, V. I. Selective Transmission of Dirac Electrons and Ballistic Magnetoresistance of N-p Junctions in Graphene. *Phys. Rev. B - Condens. Matter Mater. Phys.* **2006**. https://doi.org/10.1103/PhysRevB.74.041403.

(9) Katsnelson, M. I.; Novoselov, K. S.; Geim, A. K. Chiral Tunnelling and the Klein Paradox in Graphene. *Nat. Phys.* **2006**. https://doi.org/10.1038/nphys384.

(10) Banszerus, L.; Schmitz, M.; Engels, S.; Goldsche, M.; Watanabe, K.; Taniguchi, T.; Beschoten, B.; Stampfer, C. Ballistic Transport Exceeding 28 Mm in CVD Grown Graphene. *Nano Lett.* **2016**. https://doi.org/10.1021/acs.nanolett.5b04840.

(11) Allain, P. E.; Fuchs, J. N. Klein Tunneling in Graphene: Optics with Massless Electrons. *Eur. Phys. J. B* **2011**. https://doi.org/10.1140/epjb/e2011-20351-3.

(12) Lee, G. H.; Park, G. H.; Lee, H. J. Observation of Negative Refraction of Dirac Fermions in Graphene. *Nat. Phys.* **2015**. https://doi.org/10.1038/nphys3460.

(13) Chen, S.; Han, Z.; Elahi, M. M.; Habib, K. M. M.; Wang, L.; Wen, B.; Gao, Y.; Taniguchi, T.; Watanabe, K.; Hone, J.; Ghosh, A. W.; Dean, C. R. Electron Optics with P-n Junctions in Ballistic Graphene. *Science (80-.).* **2016**. https://doi.org/10.1126/science.aaf5481.

(14) Shytov, A. V. Cloaked Resonant States in Bilayer Graphene. **2015**.

(15) Hunt, B.; Sanchez-Yamagishi, J. D.; Young, A. F.; Yankowitz, M.; LeRoy, B. J.; Watanabe, K.; Taniguchi, T.; Moon, P.; Koshino, M.; Jarillo-Herrero, P.; Ashoori, R. C. Massive Dirac Fermions and Hofstadter Butterfly in a van Der Waals Heterostructure. *Science (80-.).* **2013**. https://doi.org/10.1126/science.1237240.

(16) Woods, C. R.; Britnell, L.; Eckmann, A.; Ma, R. S.; Lu, J. C.; Guo, H. M.; Lin, X.; Yu, G. L.; Cao, Y.; Gorbachev, R. V.; Kretinin, A. V.; Park, J.; Ponomarenko, L. A.; Katsnelson, M. I.; Gornostyrev, Y. N.; Watanabe, K.; Taniguchi, T.; Casiraghi, C.; Gao, H. J.; Geim, A. K.; Novoselov, K. S. Commensurate-Incommensurate Transition in Graphene on Hexagonal Boron Nitride. *Nat. Phys.* **2014**. https://doi.org/10.1038/nphys2954.

(17) Moldovan, D.; Anđelković, M.; Peeters Francois. pybinding v0.9.4: a Python package for tight-binding calculations http://doi.org/10.5281/zenodo.826942.

Chapter 3 - Scanning Tunneling Microscopy and Angle-Resolved Photoemission Spectroscopy

3.1 Introduction

In this chapter I will discuss two techniques used to characterize graphene—scanning tunneling microscopy (STM) and angle-resolved photoemission spectroscopy (ARPES). These techniques are surface sensitive and are generally limited to probing a crystal's surface properties.[1–7] However, graphene is a true 2D crystal that hosts an exposed 2D electron gas.[8,9] This fact makes both STM and ARPES extremely valuable tools to explore graphene's unique electronic properties. Moreover, STM and ARPES are complimentary techniques. For example, ARPES is only able to probe occupied states while STM can probe occupied and unoccupied states.[4] ARPES can probe a material's band structure with momentum resolution and an energy range of $\sim$10 eV, but with limited energy resolution ($\sim$10 meV).[3] On the other hand, STM can probe a sample's density of states without momentum resolution over a narrower energy range ($\sim$1 eV) but with higher energy resolution ($\sim$0.5 meV).

In the following sections, I will outline the theory behind STM with detailed emphasis on results that are necessary to explain spectroscopic features in Ch. 6 and Ch. 8. The last section will cover the general principle of ARPES which will be used to characterize BLG in Ch. 7.

3.2 The Scanning Tunneling Microscopy Technique

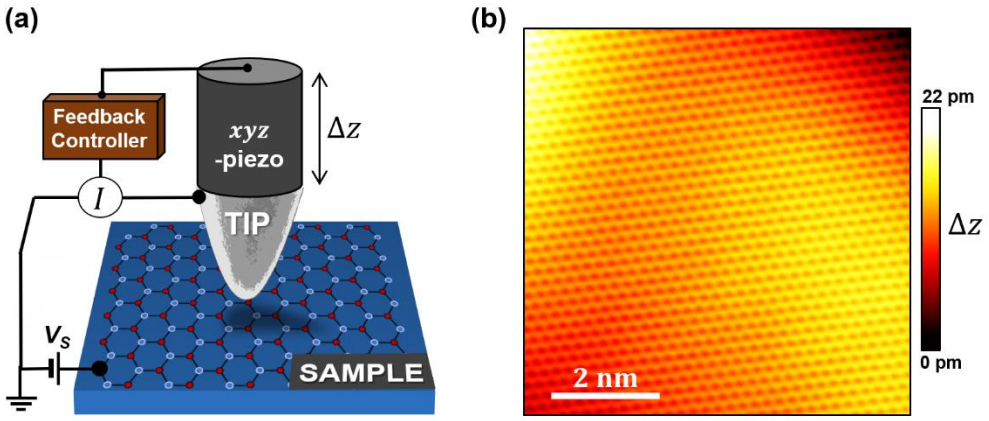

Figure 3.2.1| Scanning Tunneling Microscopy on graphene. (a) Schematic of an STM showing the main components used in constant-current topography scans. During a constant-current scan the tip hovers over the sample by a distance Δz regulated by the z-piezo. The tunneling current can be tuned by changing the bias voltage V_S between the tip and sample. **(b)** Constant-current topographic image of monolayer graphene (MLG). Variations of the intensity in this image corresponds to changes of the z-piezo height to keep I constant while the tip tracks the surface in the xy plane. Tunneling parameters used in this scan: $I = 0.5$ nA; $V_S = -200$ mV.

Before discussing the theory behind the tunneling phenomena that is at the heart of STM, it is important to become acquainted with the STM's basic experimental operation. An STM can be thought of as the interaction between two electrodes: a tip and a sample. The schematic of an STM is depicted in Fig. 3.2.1a. A voltage bias (V_S) is applied between a metallic tip and a conductive sample while the tip hovers over the sample's surface sufficiently close ($\sim 5 - 10$ Å). Once the tip's apex and sample's surface are in close proximity, electrons may hop from the tip onto the sample, or vice versa. The steady flow of these electrons registers as a current I. This is the quantum mechanical tunneling current.

When a sample's surface topography is scanned, we engage the feedback controller (see Fig. 3.2.1a) in "constant-current" mode. For this mode, we select a constant value for I that is maintained by the z-piezoelectric motor which self-regulates the tip's distance from the sample's surface. A resolution of $\sim 1\,\mathrm{pm}$ at $\sim 4.8\,\mathrm{K}$ is achieved by the z-piezoelectric motor which responds to electrical stimuli by expanding and contracting as a result of the piezoelectric effect.[10,11] This sequence of procedures describes the feedback loop used in the STM measurements presented in this thesis. As an example, Fig. 3.2.1b shows a topographic map of monolayer graphene (MLG) in "constant-current" mode. Once a constant current I is engaged, the x and y-piezoelectric motors track along the sample's surface plane while the z-piezo changes the tip's height (Δz) so that I remains constant. A computer then compiles the Δz values and plots them as a function of (x, y) as shown in Fig. 3.2.1b where the hexagonal lattice of graphene is clearly displayed.

The STM measurements discussed for the remainder of this thesis are performed in a low-temperature ultra-high vacuum STM manufactured by Createc.[10] A photograph of the STM system is shown in Fig. 3.2.2a where the main sections have been highlighted and labeled. When a sample is introduced into the system, it enters through the loading-lock (highlighted in orange). This chamber is pumped with a turbomolecular pump down to $\sim 10^{-7}$ Torr before introducing the sample into the preparation-chamber (prep-chamber) highlighted in yellow. Once inside the prep-chamber, the sample may be annealed to remove excess adsorbates from it's surface. Once the pressure in the prep-chamber drops to $\sim 10^{-10}$ Torr, it is introduced into the

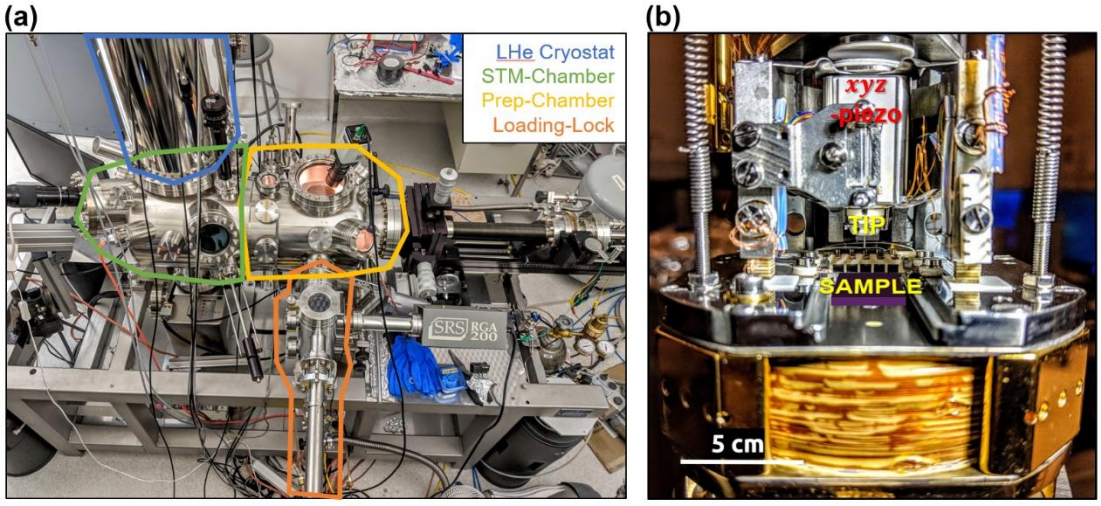

Figure 3.2.2| Low-temperature ultra-high vacuum STM. (a) Photograph of the Createc[10] STM used to characterize graphene field effect transistors. Some of the STM's components crucial to its operation in ultra-high vacuum and low-temperature operation are indicated. **(b)** Photograph of the STM head. This part contains the relevant components sketched in Fig. 3.2.1.

STM-chamber (highlighted green) where the pressure can drop down to 10^{-11} Torr. The sample is then placed into the STM's head pictured in Fig. 3.2.2b. The STM head is maintained at ~4.8 K by being in contact with a liquid helium cryostat (highlighted blue in Fig. 3.2.2a) via a thin metallic wire with high thermal conductivity. Figure 3.2.2b also labels the main components (sample, tip, and piezoelectric motors) depicted and discussed on Fig. 3.2.1a.

3.2.1 The theory of scanning tunneling microscopy

Now that the basic experimental procedures to operate the STM have been discussed, I will present the theoretical treatment of the tunneling phenomena that enables the STM to probe a material's density of states (DOS). First, we will obtain an expression for the tunneling current between the tip and sample in 1D. Then, we will transition to 3D space by approximating the tip's apex to be an atom with a spherically symmetric wavefunction. Finally, we will apply these tunneling theory results to the case for tunneling onto surface states. The topics discussed here have been adapted from previous works and discussions[4,12–14] to present the most relevant details for the studies covered in this thesis.

3.2.1.1 Tip-to-sample tunneling in 1D

To understand tunneling between the STM tip and a sample, it is convenient to simplify the geometry and dimensionality of the problem by assuming a 1D system. The formalism introduced by Bardeen[15] assumes both the tip and sample to be two 1D electrodes separated by a vacuum gap as depicted in the diagram in Fig. 3.2.3a, where the vacuum potential energy $U_V = 0$. It is also assumed that both the tip and sample have eigenstates $\{\Psi_{T_i}(t)\}$ and $\{\Psi_{S_j}(t)\}$, respectively, each of which satisfies the time dependent Schrödinger equation under their respective potentials:

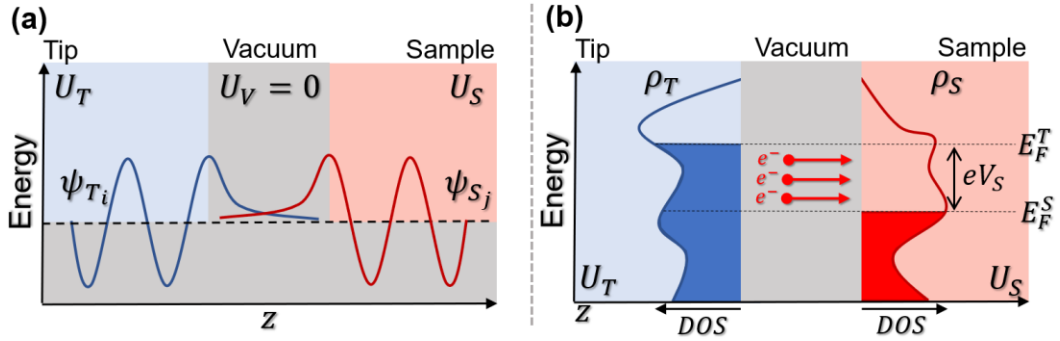

Figure 3.2.3| Schematic representations of tunneling phenomena between a tip and sample. (a) A tip (U_T) and sample (U_S) are separated by a region of empty space (U_V). General eigenstates of the tip (ψ_{T_i}) and sample (ψ_{S_j}) are depicted such that they extend and decay into the vacuum. The overlap and transitions between these eigenstates determine the rate of electron hoping events which leads to a measurable tunneling current. **(b)** Schematic depicting tunneling between two electrodes (tip and sample) with defined density of states $\rho_T(E)$ and $\rho_S(E)$. By applying a bias V_S between the sample and tip, *elastic* tunneling occurs when occupied states in the tip tunnel into unoccupied states in the sample with the same energy.

$$i\hbar\frac{\partial\Psi_{T_i}}{\partial t} = \left[-\frac{\hbar^2}{2m}\frac{\partial^2}{\partial z^2} + U_T\right]\Psi_{T_i} = H_T\Psi_{T_i} \tag{3.1}$$

$$i\hbar\frac{\partial\Psi_{S_j}}{\partial t} = \left[-\frac{\hbar^2}{2m}\frac{\partial^2}{\partial z^2} + U_S\right]\Psi_{S_j} = H_S\Psi_{S_j} \tag{3.2}$$

The respective time independent Schrödinger equations are also satisfied by their stationary components $\{\psi_{T_i}\}$ and $\{\psi_{S_j}\}$, i.e.:

$$\Psi_{T_i}(t) = \psi_{T_i}e^{-i(E_{T_i})t/\hbar} \quad \text{where} \quad H_T\psi_{T_i} = E_{T_i}\psi_{T_i} \tag{3.3}$$

$$\Psi_{S_j}(t) = \psi_{S_j}e^{-i(E_{S_j})t/\hbar} \quad \text{where} \quad H_S\psi_{S_j} = E_{S_j}\psi_{S_j} \tag{3.4}$$

Now that the eigenstates for both the tip and sample have been properly defined, we need to impose the condition that an eigenstate from the tip (or sample) may

temporally evolve into eigenstates of the sample (or tip). Imposing this condition implies that $\langle \psi_{S_j} | \psi_{T_i} \rangle = 0$ for all i, j. If this were not the case, it would open the possibility for an electron to be both in the tip and sample simultaneously at $t = 0$. Thus, a wavefunction that starts as the ith eigenstate of the tip (ψ_{T_i}) and evolves into eigenstates of the sample is written as:

$$\Psi_{T_i \to S}(t) = \psi_{T_i} e^{-i(E_{T_i})t/\hbar} + \sum_j c_{S_j}(t) \psi_{S_j} e^{-i(E_{S_j})t/\hbar} \tag{3.5}$$

with $c_j(0) = 0$. This wavefunction is defined for the complete system which includes the tip, vacuum, and sample. Thus, we can apply it to the complete system's Schrödinger equation

$$i\hbar \frac{\partial \Psi_{T_i \to S}}{\partial t} = \left[-\frac{\hbar^2}{2m} \frac{\partial^2}{\partial z^2} + U_T + U_V + U_S \right] \Psi_{T_i \to S} \tag{3.6}$$

Plugging (3.5) into (3.6) results in:

$$\begin{aligned} i\hbar \sum_j \frac{\partial c_{S_j}(t)}{\partial t} \psi_{S_j} e^{-i(E_{S_j})t/\hbar} \\ = U_S \, \psi_{T_j} e^{-i(E_{T_j})t/\hbar} + \sum_j c_{S_j}(t) U_T \psi_{S_j} e^{-i(E_{S_j})t/\hbar} \end{aligned} \tag{3.7}$$

We then operate on the left with $\langle \psi_{S_i} |$ to obtain:

$$
\begin{aligned}
i\hbar \sum_j \frac{\partial c_{S_j}(t)}{\partial t} \delta_{ij}\, e^{-i(E_{S_j})t/\hbar} \\
&= \langle \psi_{S_i} | U_S | \psi_{T_j} \rangle e^{-i(E_{T_j})t/\hbar} \\
&+ \sum_j c_{S_j}(t) \langle \psi_{S_i} | U_T | \psi_{S_j} \rangle e^{-i(E_{S_j})t/\hbar}
\end{aligned}
\tag{3.8}
$$

Recalling our previous discussion, eigenstates in the sample should not exists in the tip, thus $\langle \psi_{S_i} | U_T | \psi_{S_j} \rangle \sim 0$. Therefore, (3.8) becomes:

$$
i\hbar \frac{\partial c_{S_i}(t)}{\partial t} = M_{S_i,T_j}\, e^{-i(E_{T_j} - E_{S_i})t/\hbar} \tag{3.9}
$$

where the tunneling matrix element is defined as $M_{S_i,T_j} = \langle \psi_{S_i} | U_S | \psi_{T_j} \rangle$. After integrating (3.9) over time, we have:

$$
c_{S_j}(t) = M_{S_j,T_i} \frac{2 \sin\left[\left(E_{T_i} - E_{S_j}\right) t/2\hbar\right]}{E_{T_i} - E_{S_j}} \tag{3.10}
$$

where the indices i and j have been exchanged to the coefficient defined in (3.5).

Based on the way we defined the time-evolving wavefunction (3.5), the probability rate of the *i*th tip eigenstate tunneling into the *j*th sample eigenstate is given by:

$$
p_{T_i \to S_j} = \frac{d}{dt} |c_{S_j}(t)|^2 = \frac{2\pi}{\hbar} |M_{S_j,T_i}|^2 \frac{\sin\left[\left(E_{T_i} - E_{S_j}\right) t/\hbar\right]}{\pi \left(E_{T_i} - E_{S_j}\right)} \tag{3.11}
$$

Equation (3.11) has been written in a manner such that the last factor resembles the Dirac delta function:

$$\frac{\sin\left[\left(E_{T_i}-E_{S_j}\right)t/\hbar\right]}{\pi\left(E_{T_i}-E_{S_j}\right)} \to \delta\left(E_{T_i}-E_{S_j}\right) \quad \text{in the limit} \quad \hbar/t \to 0 \tag{3.12}$$

Considering the time-energy relation $\Delta E\,\Delta t \sim \hbar$, the requirement that $\hbar/t \to 0$ is equivalent to the elastic tunneling condition $E_{T_i} \sim E_{S_j}$, i.e. this applies for sufficiently long tunneling times. This implies that to tunnel into the jth sample eigenstate, the ith tip eigenstate must have the same energy. Thus, the tunneling probability rate from the ith tip eigenstate to sample eigenstates of energies within the elastic tunneling range is:

$$p_{T_i \to S} = \frac{d}{dt}|c_S(t)|^2 = \frac{2\pi}{\hbar}|M_{S_j,T_i}|^2 \sum_{S_j} \delta\left(E_{T_i}-E_{S_j}\right) \tag{3.13}$$

The quantity inside the sum counts the number of sample eigenstates with energy E_{T_i}. Thus, this quantity can be interpreted as the density of states of the sample at such energy. With this consideration, we can express (3.13) as follows:

$$p_{T_i \to S} = \frac{d}{dt}|c_S(t)|^2 = \frac{2\pi}{\hbar}|M_{S_j,T_i}|^2\, \rho_S\left(E_{T_i}\right) \tag{3.14}$$

Finally, to relate the transition probability rate (3.14) to our experimental procedures, we apply a voltage bias V_S between the sample and the tip, depicted in Fig. 3.2.3b. For electrons to hop from the tip to the sample, states in the sample have to be unoccupied. A finite V_S voltage makes this possible by emptying sample states accessible to tip states within the energy range $eV_S = E_F^T - E_F^S$, where E_F^T and E_F^S are

tip and sample Fermi energies, respectively. The tunneling current I can therefore be expressed as the compilation of all such tip eigenstates that overlap with sample eigenstates within eV_S:

$$I = \frac{4\pi e}{\hbar}\int_0^{eV_S} \rho_T(E_F^T + \epsilon)\, \rho_S(E_F^T - eV_S + \epsilon)|M_{TS}|^2 d\epsilon \tag{3.15}$$

In this expression, I omit the broadening from the Fermi distribution functions under the assumption that the energy resolution of our experimental probe is larger than thermal broadening. This is the case experimentally since we can achieve a resolution of ~ 1 meV, whereas our thermal broadening is ~ 0.4 meV at a temperature of 5 K. Equation (3.15) provides a generalized approximation for the tunneling current I between two electrodes under an applied V_S voltage.

Finally, we can apply experimentally reasonable restrictions on (3.15) to acquire the sample's density of states $\rho_S(E)$. First, we use a metallic tip like tungsten or platinum-iridium. Since metals' DOS stay relatively constant within energy ranges of a few hundred meV, we can assume: $\rho_T(E) \to \rho_T$. Second, the tunneling matrix M_{TS} can be assumed to be energy independent within a few hundred meV. In fact, in the next section we will see that M_{TS} approximately depends on the out-of-plane reach of the sample's wave functions. Third, by coupling V_S to an AC signal, we can extract the derivative of the tunneling current with respect to V_S. These considerations lead to:

$$\frac{dI}{dV_S} = \frac{4\pi e^2}{\hbar}|M_{TS}|^2 \rho_T\, \rho_S(V_S) \tag{3.16}$$

This important result is the foundation of scanning tunneling spectroscopy (STS). The interpretation of the STS results presented in Ch. 6, and Ch. 8 rely on the fact that $dI/dV_S \propto \rho_S(V_S)$. Thus, we can expect a dI/dV_S signal to provide information about a sample's DOS.

3.2.1.2 Decoding the tunneling matrix elements in 3D: the s-wave approximation

The expression for the tunneling current I (3.15) obtained in the previous section holds for the 3D case despite having been derived in 1D. In this section we will adapt the real-world implications of tunneling between a 3D tip and a surface. Information regarding the geometry of a tip is encoded in the tunneling matrix $|M_{TS}|$ [see (3.15)]. By generalizing Eqts. (3.1)-(3.4) to 3D, we can express the tunneling matrix as:

$$M_{TS} = \langle \psi_S | U_S | \psi_T \rangle = \langle \psi_S | \left(E_S + \frac{\hbar^2}{2m} \nabla_S^2 \right) | \psi_T \rangle \tag{3.17}$$

where ∇_S^2 is the second spatial derivative applied to eigenstates of the sample.

We must now invoke the elastic tunneling condition ($E_S = E_T$) in the vacuum region where the tip and sample eigenstates overlap. Thus, we can substitute:

$$E_S \rightarrow E_T = -\frac{\hbar^2}{2m} \nabla_T^2 + U_T \tag{3.18}$$

where ∇_T^2 is the second spatial derivative applied to eigenstates of the tip. After plugging (3.18) into (3.17) we obtain:

$$M_{TS} = -\frac{\hbar^2}{2m}\langle\psi_S|\nabla_T^2|\psi_T\rangle + \frac{\hbar^2}{2m}\langle\psi_S|\nabla_S^2|\psi_T\rangle + \cancel{\langle\psi_S|U_T|\psi_T\rangle} \tag{3.19}$$

The third term in this equation has been crossed out because the tip's potential approaches zero in the vacuum. The tunneling matrix can be expressed in integral form as:

$$M_{TS} = -\frac{\hbar^2}{2m}\int_{\Omega_S}(\psi_S^*\nabla^2\psi_T - \psi_T\nabla^2\psi_S^*)\,d^3\boldsymbol{r} \tag{3.20}$$

where Ω_S represents a volume around the sample such that $\psi_S \neq 0$. This expression is further simplified by noting that the integrand equals $\nabla\cdot(\psi_S^*\nabla\psi_T - \psi_T\nabla\psi_S^*)$. This enables us to apply Green's theorem and integrate over a surface Σ between the tip and sample. This results in:

$$M_{TS} = -\frac{\hbar^2}{2m}\int_{\Sigma}(\psi_S^*\nabla\psi_T - \psi_T\nabla\psi_S^*)\cdot d\boldsymbol{S} \tag{3.21}$$

We have thus far, expressed the tunneling matrix M_{TS} in a way that excludes the sample's potential U_S. Now, we apply Green's theorem again to (3.21) to obtain:

$$M_{TS} = -\frac{\hbar^2}{2m}\int_{\Omega_T}(\psi_S^*\nabla^2\psi_T - \psi_T\nabla^2\psi_S^*)\,d^3\boldsymbol{r} \tag{3.22}$$

It may appear that the progression from (3.20) to (3.22) has circular reasoning. However, the ability to switch the space we integrate over from the sample to tip is a profound consequence of the elastic tunneling condition. Namely, the eigenstates with energies E_T and E_S overlap somewhere in the region between the tip and the sample. This enables us to choose a surface Σ such that the second application of Green's

theorem changes the integrable volume to enclose the tip. These steps completely decouple the tunneling matrix from the sample and can be summarized as:

$$\int_{\Omega_S} d^3\boldsymbol{r} \rightarrow \int_{\Sigma} d\boldsymbol{S} \rightarrow \int_{\Omega_T} d^3\boldsymbol{r} \tag{3.23}$$

Finally, I shall take this one step further and assume that the tip's apex is represented by an atom. If this is the case, it is logical to assume that ψ_T can be expressed by an s-wave function much like the ground state of the hydrogen atom

$$\psi_T \propto \frac{e^{\kappa|\mathbf{r}-\mathbf{r}_0|}}{4\pi|\mathbf{r}-\mathbf{r}_0|} \tag{3.24}$$

where $\mathbf{r}_0$ is the radius of the electron cloud for the atom at the tip's apex and κ is known as the screening or decay length. Importantly, this expression is a solution to the screened Poisson equation such that:

$$(\nabla^2 - \kappa^2)\psi_T = -\delta(\mathbf{r}-\mathbf{r_0}) \tag{3.25}$$

Invoking once again the elastic tunneling condition ($E_T = E_S$), it is reasonable to expect both ψ_S and ψ_T to the decay at the same rate into the vacuum. Thus, with the sample's surface located at z_0, $\psi_S \sim e^{\kappa|z-z_0|}$ implies that:

$$\nabla^2\psi_S = \kappa^2\psi_S \tag{3.26}$$

We apply this expression to (3.22) and use (3.25) to obtain:

$$M_{TS} \propto -\int_{\Omega_T} \psi_S^*(\nabla^2 - \kappa^2)\psi_T \, d^3\boldsymbol{r} \propto \int_{\Omega_T} \psi_S^*\delta(\mathbf{r}-\mathbf{r}_0)\, d^3\boldsymbol{r} \tag{3.27}$$

Lastly, the application of the 3D delta function leads to one of the main results:

$$M_{TS} \propto \psi_S^*(\mathbf{r}_0) \tag{3.28}$$

We recall that $\mathbf{r}_0$ indicates the radial extent of the atom at the tip's apex. Thus, (3.28) implies that sample eigenstates with a larger overlap with this atom will have an increased tunneling probability. This is the case given that the weighing coefficients $|M_{TS}|^2$ in (3.15) modulate the contribution of sample eigenstates to the tunneling current. In other words, sample states that extend further into the vacuum contribute the most to the tunneling current.

3.2.1.3 Tunneling into a 2D crystal

I will now expand upon the insights from the previous section by approximating ψ_S as a 2D Bloch function with onsite s-wave orbitals:

$$\psi_S = \sum_{\mathbf{R}} f(\mathbf{r}-\mathbf{R}) e^{i\boldsymbol{k}_\parallel \cdot \mathbf{R}} \tag{3.29}$$

where $\mathbf{R}$ is the 2D Bravais lattice vector, $\boldsymbol{k}_\parallel$ is the in-plane momentum, and

$$f(\mathbf{r}-\mathbf{R}) = \frac{e^{-\lambda(\mathbf{r}-\mathbf{R})}}{\lambda(\mathbf{r}-\mathbf{R})} \tag{3.30}$$

with λ representing the "decay" length of the atomic s-wave state. Considering that the onsite s-wave should decay in the out-of-plane direction z, we can perform a Fourier expansion on (3.30) as done by Tersoff and Hamann[12]

$$f(\mathbf{r}-\mathbf{R}) = \int b(\boldsymbol{q})\, e^{-(\lambda^2+q^2)^{1/2}|z|}\, e^{i\boldsymbol{q}\cdot(\mathbf{r}_\parallel - \mathbf{R})}\, d^2q \tag{3.31}$$

where $b(\boldsymbol{q})$ is a real valued function with no spatial dependence, and $\mathbf{r}_{\parallel}$ is the in-plane position vector. By applying (3.31) to (3.29) we obtain:

$$\psi_S = \int b(\boldsymbol{q})\, e^{-\left(\lambda^2+q^2\right)^{1/2}|z|}\; e^{i\boldsymbol{q}\cdot\mathbf{r}_{\parallel}} \sum_{\mathbf{R}} e^{i\left(\boldsymbol{k}_{\parallel}-\boldsymbol{q}\right)\cdot\mathbf{R}}\, d^2q \tag{3.32}$$

Next, we note that the quantity being summed over, **R** in (3.32), is a collection of plane waves in real space. Thus, we can express it as a sum of singularities in reciprocal space

$$\sum_{\mathbf{R}} e^{i\left(\boldsymbol{k}_{\parallel}-\boldsymbol{q}\right)\cdot\mathbf{R}} = \sum_{\boldsymbol{G}} \delta(\boldsymbol{k}_{\parallel} - \boldsymbol{q} + \boldsymbol{G}) \tag{3.33}$$

with $\boldsymbol{G}$ as the reciprocal lattice vectors that span the Brillouin zone (BZ). Applying this to (3.32) leads to:

$$\psi_S = \sum_{\boldsymbol{G}} b(\boldsymbol{k}_{\parallel} + \boldsymbol{G})\, e^{-\left(\lambda^2+k_{\parallel}^2+\mathrm{G}^2\right)^{1/2}|z|} e^{i(\boldsymbol{k}_{\parallel}+\boldsymbol{G})\cdot\mathbf{r}_{\parallel}} \tag{3.34}$$

By restricting the extent of the sample wave function to the first BZ (i.e. $\boldsymbol{G} = 0$) we can simplify (3.34) as:

$$\psi_S \propto e^{-\left(\lambda^2 + k_{\parallel}^2\right)^{1/2}|z|} e^{i\boldsymbol{k}_{\parallel}\cdot\mathbf{r}_{\parallel}} \tag{3.35}$$

This result indicates that states with large in-plane momentum rapidly decay into the vacuum. This fact is significant for graphene since the Fermi level lies at the corners of the BZ, which have large in-plane momenta. In Ch. 6, I will discuss the implication of this result when analyzing graphene's tunneling spectroscopy.

In summary we apply the results (3.35) and (3.28) to the experimentally measured tunneling current I to obtain:

$$I \propto \exp\left(-2\left(\lambda^2 + k_{\parallel}^2\right)^{1/2}|z|\right) \tag{3.36}$$

This relation shows that states with large in-plane momentum contribute much less to the measured tunneling current. Furthermore, this result indicates that the contribution of the strong in-plane momentum states can be modulated by changes in the tip height z. I will apply this concept to measurements performed in Ch. 6 and Ch. 8 to increase the contribution of large in-plane momentum states.

3.3 Angle Resolved Photoemission Spectroscopy

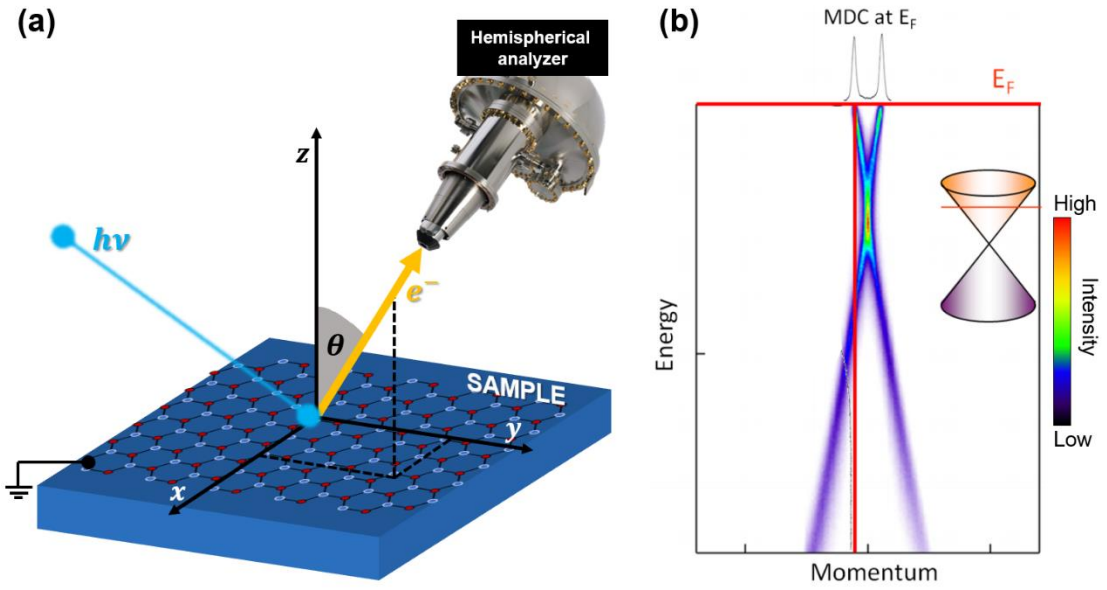

Figure 3.3| Photoemission spectroscopy of graphene. (a) Schematic depicting the photoemission process. A beam of light with energy $h\nu$ (typically from a laser, helium lamp, or synchrotron source) ejects electrons from graphene's surface. These electrons are collected by a hemispherical analyzer (Image credit: Rowaco[16]) which maps the emitted photoelectron's kinetic energy E_K as a function of the photoemission angle θ. **(b)** Angle resolved photoemission spectra of n-doped MLG. The inset depicts MLG's bands with E_F in the conduction band. A momentum distribution curve (MDC) taken at the Fermi level is shown at the top of the plot. These pair of peaks correspond to the Lorentz distributions predicted by the single-particle spectral function applied to MLG. This plot was adapted from D. Siegel.[17]

In this section, I will provide a summarized overview of angle resolved photoemission spectroscopy (ARPES) adapted from various works.[17–19] A spatially-resolved version of this technique will be used in Ch. 7 to map spatial inhomogeneities and their effects on BLG's band structure.

ARPES is a widely used surface characterization technique in condensed matter physics.[1,2,20] It uses the photoelectric effect to directly probe a material's band structure with energy and momentum resolution. The schematic in Fig. 3.3a depicts the photoemission spectroscopy process. A focused beam of light with energy $h\nu$ shines upon the sample's surface. As a result of the photoelectric effect, a photoelectron is ejected from the sample's surface with kinetic energy E given by:

$$E = h\nu - \phi - |E_B| \tag{3.37}$$

where ϕ is the sample's work function and E_B is the binding energy of the ejected photoelectron. Photons impart negligible momentum onto electrons in the sample. Thus, in-plane momentum is conserved for a crystal with translational invariance. This suggests that the emitted photoelectron has in-plane momentum given by:

$$\mathbf{p}_{\parallel} = \hbar \boldsymbol{k}_{\parallel} = \sqrt{2mE}\sin(\theta) \tag{3.38}$$

where θ is the angle between the ejected electron and the out-of-plane axis.

Equations (3.37) and (3.38) outline the principle of photoemission spectroscopy. Namely, by knowing the photoelectron's kinetic energy E and angle θ, we can deduce the emitted electron's binding energy and in-plane momentum. Conveniently, due to graphene's 2D nature, its electrons do not have out-of-plane momentum. Thus, photoemission spectroscopy is able to fully map graphene's band structure. Experimentally, E and θ can be determined by a hemispherical analyzer such as that shown in Fig. 3.3a. This analyzer maps the intensity I of ejected photoelectrons as a function of E and $\boldsymbol{k}_{\parallel}$ by electrostatically deflecting their path onto a charge-coupled

device. However, the signal intensity measured by the analyzer contains more information than just E.

Assuming that when excited, a photoelectron does not interact with the system it originated from,[21] the experimentally obtained photoemission intensity $I(E, \boldsymbol{k})$ can be expressed as follows:

$$I(E, \boldsymbol{k}) = I_0(E, \boldsymbol{k}) f(E) A(E, \boldsymbol{k}) \tag{3.39}$$

where E and $\boldsymbol{k}$ are the photoelectron's energy and momentum vector, respectively. The first term in the expression above, $I_0(E, \boldsymbol{k})$, is the transition matrix element which suppresses the photoemission intensity based on interference phenomena or experimentally controlled parameters such as polarization[2,17,20,22]. The second term, $f(E)$, is the Fermi occupation function. The inclusion of this function highlights the fact that photoemission spectroscopy only probes occupied states, i.e. states with energy $E < E_F$. Finally, the third term, $A(E, \boldsymbol{k})$, is the single-particle spectral function given by:

$$A(E, \boldsymbol{k}) = -\frac{1}{\pi} \frac{\Sigma''(E, \boldsymbol{k})}{\left(E - \epsilon(\boldsymbol{k}) - \Sigma'(E, \boldsymbol{k})\right)^2 + \left(\Sigma''(E, \boldsymbol{k})\right)^2} \tag{3.40}$$

In this expression, $\epsilon(\boldsymbol{k})$ is the bare band energy dispersion. Σ' and Σ'' are the real and imaginary parts of the electron self-energy, respectively. Physically, Σ' is the photoelectron's excitation screening energy and Σ'' is proportional to the inverse lifetime of the states with energy $\epsilon(\boldsymbol{k})$.

In general, the self-energy Σ is assumed to be independent or negligibly dependent on the photoelectron's momentum.[23–25] This approximation implies that only $\epsilon(\boldsymbol{k})$ carries momentum dependence in (3.40). Furthermore, if we consider graphene's dispersion relation $\epsilon(\boldsymbol{k}) = \nu_F|\boldsymbol{k}|$, the experimentally obtained photoemission intensity $I(E, \boldsymbol{k})$ becomes a Lorentzian distribution centered at $\nu_F|\boldsymbol{k}| + \Sigma'(E)$, with a characteristic width $\Sigma''(E)$. This result is beautifully illustrated by D. Siegel's plot[17] in Fig. 3.3b, where the horizontal trace taken at E_F for *n*-doped MLG clearly shows two Lorentzian distributions at $\pm|\boldsymbol{k}|$. This experimental result displays the capability of photoemission spectroscopy at resolving bandstructure features with momentum resolution. In Ch. 7, I will show the application of this technique on BLG using a highly focused incident light beam which enables us to extract crucial tight-binding parameters.

Chapter 3 - References

(1) Reinert, F.; Nicolay, G.; Schmidt, S.; Ehm, D.; Hüfner, S. Direct Measurements of the L-Gap Surface States on the (111) Face of Noble Metals by Photoelectron Spectroscopy. *Phys. Rev. B - Condens. Matter Mater. Phys.* **2001**. https://doi.org/10.1103/PhysRevB.63.115415.

(2) Bostwick, A.; Ohta, T.; Seyller, T.; Horn, K.; Rotenberg, E. Quasiparticle Dynamics in Graphene. *Nat. Phys.* **2007**. https://doi.org/10.1038/nphys477.

(3) Mo, S.-K. Angle-Resolved Photoemission Spectroscopy for the Study of Two-Dimensional Materials. *Nano Converg.* **2017**. https://doi.org/10.1186/s40580-017-0100-7.

(4) Chen, C. J. *Introduction to Scanning Tunneling Microscopy: Second Edition*;

2007. https://doi.org/10.1093/acprof:oso/9780199211500.001.0001.

(5) Crommie, M. F.; Lutz, C. P.; Eigler, D. M. Imaging Standing Waves in a Two-Dimensional Electron Gas. *Nature* **1993**. https://doi.org/10.1038/363524a0.

(6) Crommie, M. F.; Lutz, C. P.; Eigler, D. M. Confinement of Electrons to Quantum Corrals on a Metal Surface. *Science (80-.).* **1993**. https://doi.org/10.1126/science.262.5131.218.

(7) Zhang, Y.; Tang, T. T.; Girit, C.; Hao, Z.; Martin, M. C.; Zettl, A.; Crommie, M. F.; Shen, Y. R.; Wang, F. Direct Observation of a Widely Tunable Bandgap in Bilayer Graphene. *Nature* **2009**. https://doi.org/10.1038/nature08105.

(8) Novoselov, K. S.; Geim, A. K.; Morozov, S. V.; Jiang, D.; Zhang, Y.; Dubonos, S. V.; Grigorieva, I. V.; Firsov, A. A. Electric Field in Atomically Thin Carbon Films. *Science (80-.).* **2004**. https://doi.org/10.1126/science.1102896.

(9) Novoselov, K. S.; Geim, A. K.; Morozov, S. V.; Jiang, D.; Katsnelson, M. I.; Grigorieva, I. V.; Dubonos, S. V.; Firsov, A. A. Two-Dimensional Gas of Massless Dirac Fermions in Graphene. *Nature* **2005**. https://doi.org/10.1038/nature04233.

(10) CreaTec Fischer & Co. GmbH https://createc.de/Contact/.

(11) CTS Corporation https://www.ctscorp.com/resource-center/tutorials/piezo-basics/.

(12) Tersoff, J.; Hamann, D. R. Theory of the Scanning Tunneling Microscope. *Phys. Rev. B* **1985**. https://doi.org/10.1103/PhysRevB.31.805.

(13) Brar, V. W. Scanning Tunneling Spectroscopy of Graphene and Magnetic Nanostructures. PhD Thesis, University fo California, Berkeley, 2010.

(14) Wong, D. Tuning Electrostatic Potentials for Imaging the Quantum Properties of Massless Dirac Fermions in Graphene. PhD Thesis, University of California, Berkeley, 2017.

(15) Bardeen, J. Tunnelling from a Many-Particle Point of View. *Phys. Rev. Lett.* **1961**. https://doi.org/10.1103/PhysRevLett.6.57.

(16) DA30-L: Hemispherical analyser. Rowaco. https://rowaco.se/en/item/da30-l-hemispherical-analyser/.

(17) Siegel, D. A. The Electronic Structure of Single-Layer Graphene. PhD. Thesis., University of California, Berkeley, 2012.

(18) Zhou, S. Dirac Fermions in Graphene and Graphite — a View from Angle-Resolved Photoemission Spectroscopy. PhD. Thesis., University of California, Berkeley, 2007.

(19) Joucken, F. Graphene and Nitrogen-Doped Graphene Studied by Local Probe and Photoemission. PhD. Thesis., Universite de Namur, Belgium, 2015.

(20) Damascelli, A.; Hussain, Z.; Shen, Z. X. Angle-Resolved Photoemission Studies of the Cuprate Superconductors. *Reviews of Modern Physics*. 2003. https://doi.org/10.1103/RevModPhys.75.473.

(21) Chang, J. J.; Langreth, D. C. Deep-Hole Excitations in Solids. I. Fast-Electron-Plasmon Effects. *Phys. Rev. B* **1972**. https://doi.org/10.1103/PhysRevB.5.3512.

(22) Damascelli, A. Probing the Electronic Structure of Complex Systems by ARPES. *Phys. Scr. T* **2004**. https://doi.org/10.1238/Physica.Topical.109a00061.

(23) Valla, T.; Fedorov, A. V.; Johnson, P. D.; Wells, B. O.; Hulbert, S. L.; Li, Q.; Gu, G. D.; Koshizuka, N. Evidence for Quantum Critical Behavior in the Optimally Doped Cuprate Bi2Sr2CaCu2O(8+δ). *Science (80-.).* **1999**. https://doi.org/10.1126/science.285.5436.2110.

(24) Kordyuk, A. A.; Borisenko, S. V.; Koitzsch, A.; Fink, J.; Knupfer, M.; Berger, H. Bare Electron Dispersion from Experiment: Self-Consistent Self-Energy Analysis of Photoemission Data. *Phys. Rev. B - Condens. Matter Mater. Phys.* **2005**. https://doi.org/10.1103/PhysRevB.71.214513.

(25) Pletikosić, I.; Kralj, M.; Milun, M.; Pervan, P. Finding the Bare Band: Electron Coupling to Two Phonon Modes in Potassium-Doped Graphene on Ir(111). *Phys. Rev. B - Condens. Matter Mater. Phys.* **2012**. https://doi.org/10.1103/PhysRevB.85.155447.

Chapter 4 - Experimental Methods

4.1 Graphene/hBN Field Effect Transistor Fabrication

The studies discussed in this thesis use 2D material heterostructures that were fabricated with specific experiments in mind. In this section we present the fabrication techniques for a graphene/hBN field effect transistor (FET). These techniques and recipes were adapted from and inspired by multiple fabrication works[1–4] and were perfected after intensive trial-and-error.

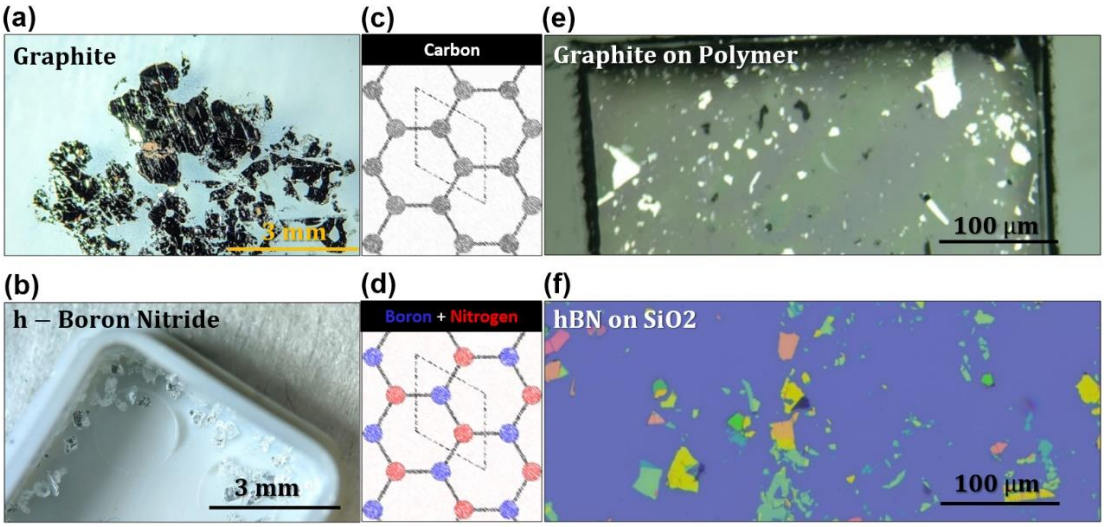

Figure 4.1.1| Ingredients for a graphene/hexagonal boron nitride heterostructure. **(a)** Crystals of highly oriented pyrolytic graphite. **(b)** Crystals of hexagonal-boron nitride. **(c)** Lattice schematic of a single layer of graphene where the unit cell containing two carbon atoms is enclosed by the dashed rhomboid. **(d)** Lattice schematic of a single layer of hBN where the unit cell containing a nitrogen and a boron atom is enclosed by the dashed rhomboid. **(e)** Optical image of exfoliated graphite placed onto a substrate MMA. **(f)** Optical image of exfoliated hBN placed onto an SiO_2 substrate. Approximately, light blue flakes have 10 to 60 layers, yellow flakes have 60 to 120 layers. Other flake colors have higher layer counts and are not typically used.

In our experiments, the heterostructures consist of a combination of single and multi-layers of graphene and hBN held together by interlayer van der Waals forces. We obtain graphene and hBN layers by mechanically exfoliating parent crystals of highly oriented pyrolytic graphite and hBN,[5] respectively. Mechanical exfoliation of these crystals is performed using the same Scotch tape technique from the seminal work by K. Novoselov and A. Geim.[6] Figures 4.1.1a and 4.1.1b shown optical images of the parent crystals from which we obtain thin films of graphene and hBN, respectively.

The use of hBN is ubiquitous in all the experiments discussed in this thesis and the majority of studies that involve 2D materials in the last few years. The combination of hBN's electronic and mechanical properties make it an ideal substrate for graphene-based heterostructures. Figures 4.1.1c and 4.1.1d show schematics of the lattices for graphene and hBN, respectively. The unit cell in graphene is delineated by the dashed rhomboid in Fig. 4.1.1c. Graphene gets its semi-metallic properties from the presence of inversion symmetry between the carbon atoms in this unit cell. In contrast, hBN does not have a similar inversion symmetry given that its unit cell (dashed rhomboid in Fig. 4.1.1d) is composed of two unequal atoms (boron and nitrogen). Similar to a 1D dimer with unequal atoms in the unit cell,[7] hBN has a bandgap. Optical and electric characterization of hBN have reported its bandgap to be between 5 and 6 eV.[5,8,9] As an insulator, hBN serves as a substrate for graphene without interfering with its electrical transport properties. Additionally, Fig. 4.1.1d shows that hBN has a honeycomb structure similar to graphene. In fact, the boron-to-nitrogen bonds in hBN are only ~1.7% longer than the carbon-to-carbon bonds in graphene.[1] This mechanical

similarity, together with Van der Waals attraction, enables sharp interfaces and ultra-flat surfaces on graphene/hBN heterostructures.[10,11] Additionally, charge inhomogeneity is drastically reduced as compared to graphene that is supported by substrates with dangling bonds such as SiO_2.[1,12]

Before mechanically assembling our graphene/hBN heterostructure, we place each of these exfoliated materials onto appropriate substrates. For the case of graphene, we place the exfoliated graphite crystal onto a polymer stack. Figure 4.1.1e shows an optical image of a polymer substrate after placing scotch tape with exfoliated graphite onto it. (See appendix for polymer preparation recipe). The polymer used is methyl methacrylate (MMA) resting on top of clear Scotch tape stuck onto a glass slide. The bright white regions in Fig. 4.1.1e correspond to thick (up to hundreds of layers) pieces of graphite. Careful optical survey is necessary in order to find faint mono and bilayer graphene flakes. We identify few-layer graphene flakes by measuring the contrast between them and the background. A contrast of 3% and 6% indicate we have located mono and bilayer graphene, respectively.[13,14] Next, we place down exfoliated hBN crystals onto a SiO_2/Si^+ wafer. An optical image of the result is shown in Fig. 4.1.1f. In this image the SiO_2 substrate appears purple in color. The hBN flakes are the multicolored islands seen on the image. The variations in color, a product of thin film interference, roughly indicate the thickness of the hBN flakes. Flakes between purple and blue colors are a few to tens of nanometers, whereas green and yellow flakes can be hundreds of nanometers thick. From this multitude of islands, we choose an appropriately sized hBN with a flat and damage-free surface. Flat and damage free

surfaces can be identified by using the differential interference contrast (DIC) mode on an optical microscope. DIC mode enhances variations in image contrast caused by surface roughness.

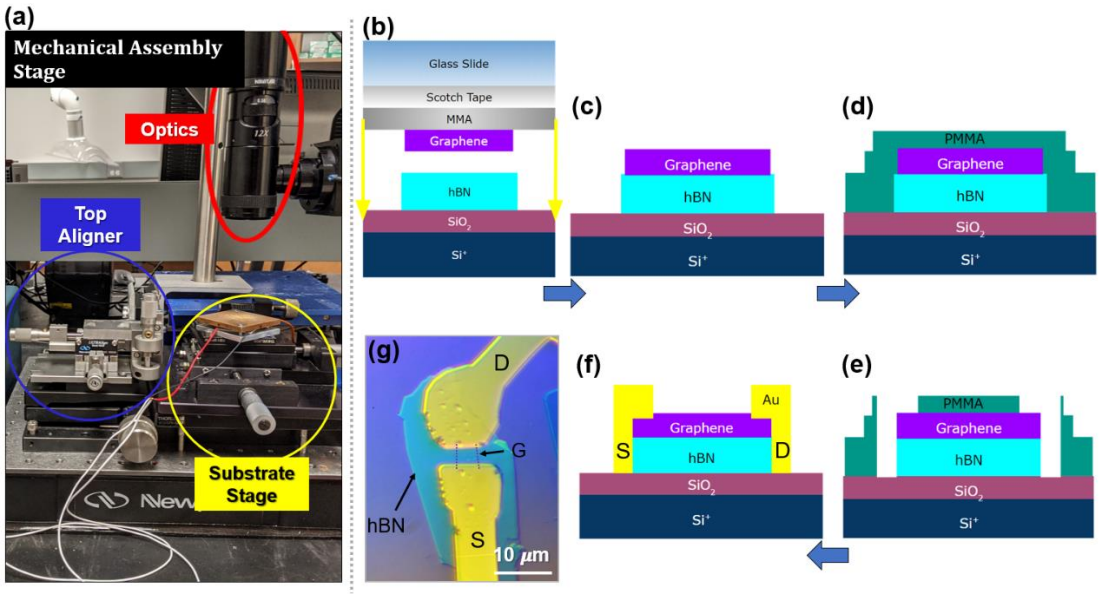

Figure 4.1.2| Assembly and fabrication of graphene/hBN Field Effect Transistors (FETs). (a) Picture of the tabletop setup used to assemble heterostructures. A substrate containing graphene is attached facing down onto the Top Aligner. The substrate hBN is placed onto the Substrate Stage. The optic attachments are used to align the graphene and hBN flakes as they approach contact. **(b)** Schematic of the placement of graphene onto hBN. The Substrate Stage in (a) can be tuned to achieve optimal tilt. **(c)** Completed graphene/hBN heterostructure after dissolving MMA substrate. **(d)** Heterostructure with PMMA resist spin-coated onto it. **(e)** Source and drain electrode pattern cavities following electron beam lithography (EBL) and resist development. **(f)** Completed graphene/hBN FET after Au/Cr thermal evaporation. **(g)** Optical image of completed graphene/hBN FET where graphene is outlined by the purple lines. The source and drain electrodes serve to inject charge carriers onto graphene, while a voltage applied to Si^+ controls the back-gate.

Once we have identified both graphene and hBN crystals on their respective substrates, we proceed with their mechanical interfacing. After identifying and choosing a suitable graphene flake, we mount the polymer substrate facing down on

the Top Aligner, pictured in Fig. 4.1.2a. The selected hBN flake on the SiO_2/Si^+ wafer is placed onto the Substrate Stage, also pictured in Fig. 4.1.2a. The home-built assembly stage has multiple micromanipulator controls that enable us to tune the tilt of both the Top Aligner and Substrate stage. By controlling the height of the Top Aligner with a *z*-micromanipulator, we slowly place graphene onto hBN as depicted by the schematic in Fig. 4.1.2b. Once graphene has contacted hBN, we gradually raise the Substrate Stage's temperature to ~65 ℃. This gentle increase in temperature allows us to regulate the speed at which the polymer spreads across the SiO_2 substrate. After mechanically placing graphene onto hBN, the stack is placed in dichloromethane for 45 minutes to dissolve the polymer stack. Figure 4.1.2c shows a complete heterostructure schematic after mechanical assembly and solvent treatment.

To make a field effect transistor (FET) out of the graphene/hBN heterostructure, we proceed by placing down source and drain electrodes onto it, noting that the underlying doped silicon (Si^+) acts as a tunable gate. Figures 4.1.2d-f depict the process of placing down electrodes. First, we spin coat a double layer of poly-methyl methacrylate (PMMA) resists (495-PMMA/950-PMMA) onto the heterostructure and substrate wafer (Fig. 4.1.2d). The resist is then cured for 5 minutes at 180 ℃. We use electron beam lithography (EBL) to alter the polymer structure in the resist which exposes cavities with small regions of exposed graphene as illustrated in Fig 4.1.2e. (See appendix for EBL parameters used). The final step of the FET fabrication is the evaporation of contact metals. First, we thermally evaporate a sticky metal layer (~5 nm) of chromium (Cr) immediately followed by 50 to 200 nm of gold (Au). The

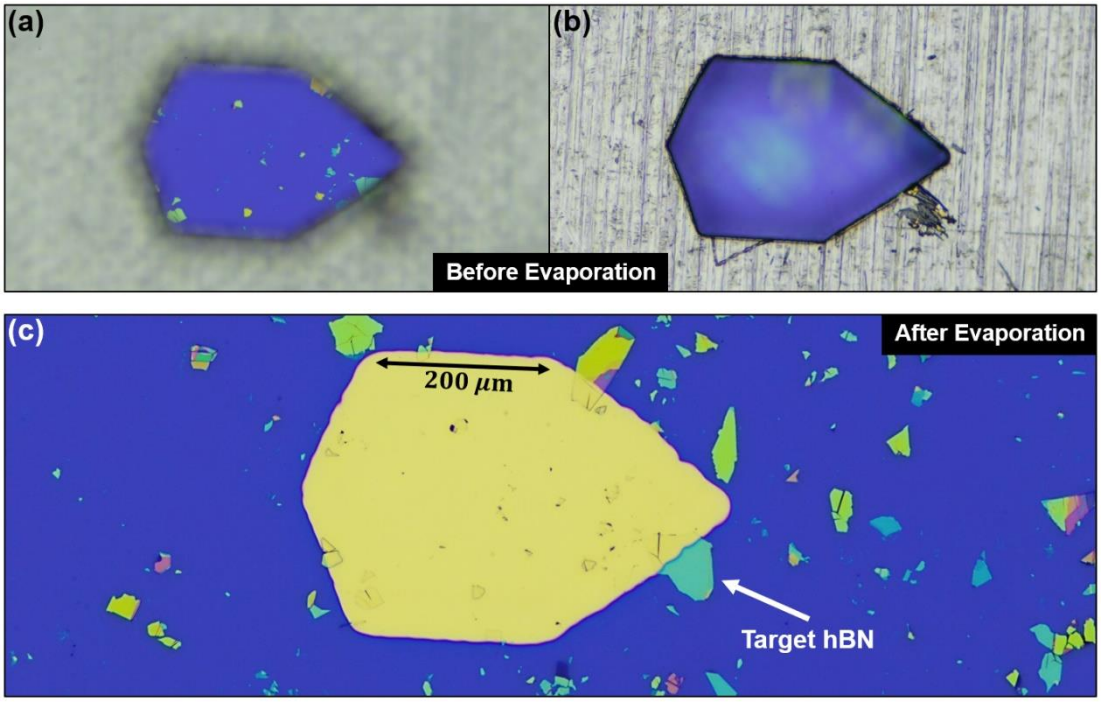

Figure 4.1.3| Stencil mask for single-electrode evaporation. (a-b) Optical images of a stainless-steel stencil mask placed over an hBN flake shown at different focus lengths prior to evaporation. **(c)** Optical image of the stencil mask evaporation result showing the desired overlap with a chosen hBN.

thickness of Au evaporated depends on the thickness of the hBN crystal in the heterostructure. The Au thickness needs to be at least 10 nm thicker than the hBN substrate to ensure successful electrical contact. After dissolving the PMMA resist in acetone, we obtain a completed graphene/hBN FET depicted in Fig. 4.1.2f. The Au electrodes act as the source and drain for the FET, and a back-gate voltage is connected to the p-doped Si layer below the insulating SiO_2 dielectric. Some devices discussed in this thesis implement a graphite layer underneath hBN and serve as a back-gate to allow for stronger capacitive coupling and reduce charge inhomogeneity on the graphene layer. Figure 4.1.2g shows an optical image of a completed graphene/hBN FET where

the graphene flake has been purposefully chosen to be narrow in order to minimize the channel area and improve electrical transport characteristics.

As an alternative to EBL, we also placed a contact electrode using a stencil mask method. The device in Ch. 7 was fabricated using this technique in order to ensure a clean surface for photoemission characterization. For this evaporation technique we use a laser etched stainless steel stencil mask[15] (see Figs. 4.1.3a-b). This mask is aligned so that a corner of the polygon shape overlaps with a flake before being evaporated using the same metal combination discussed above. Figure 4.1.3c shows the final result of a stencil mask evaporation which required no polymer contact or solvent rinsing.

4.2 Mechanical Cleaning of Graphene Using Atomic Force Microscopy

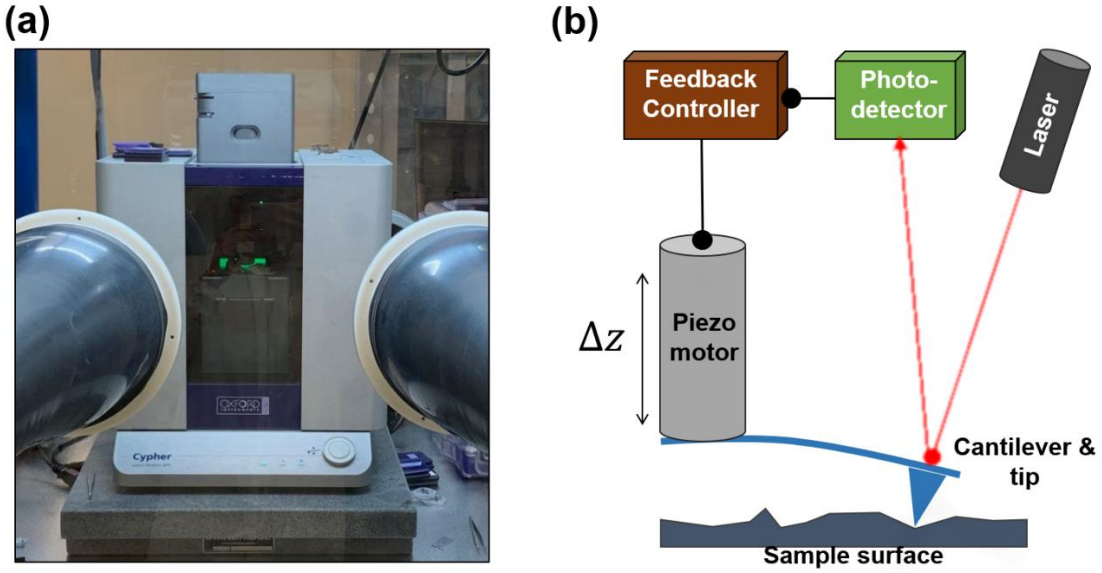

Figure 4.2.1| Atomic force microscope (AFM) inside a glovebox. (a) Picture of the Cypher-S AFM used to characterize and treat the surface of 2D materials. This AFM is operated inside a glovebox filled with nitrogen or argon gas. **(b)** Schematic of an AFM showing the basic components used during sample surface characterization. A laser shines light onto a highly reflective cantilever while a photodiode converts the reflected light into an electrical signal. This signal is used to modulate the deflection (contact AFM mode) or oscillation amplitude (tapping AFM mode) of the cantilever by varying the tip-sample distance.

During the mechanical assembly and EBL of the graphene/hBN heterostructure, the surface of graphene is exposed to polymers. In this section I will present a technique for clearing off polymer residue from the surface of graphene using an atomic force microscope (AFM). This technique has been adapted from an earlier work.[16] We improve upon this work by scanning in an inert environment and minimizing the damaging effect of the AFM tip onto graphene's surface, thus, making it compatible with scanning tunneling microscopy studies.

The mechanical cleaning of graphene's surface is performed with an Asylum Research Cypher-S AFM from Oxford Instruments. The AFM is operated at room temperature inside a glovebox filled with nitrogen or argon gas and is pictured in Fig. 4.2.1a. Two AFM modes are primarily used: (1) tapping mode for surface characterization and (2) contact mode for mechanical cleaning. Both of these modes use the same components depicted in Fig. 4.2.1b. In tapping mode, the cantilever oscillates around its natural frequency as the photodiode acquires an oscillating signal from the laser reflection near the end of the cantilever. As the tip tracks along the sample surface, changes in the oscillation amplitude are picked up by the detector. The feedback controller then commands the cantilever to change height in order to restore the oscillation amplitude of the cantilever to a pre-determined value. Contact mode operates in a similar but simpler manner. In contact mode, the tip touches the sample surface until the cantilever bends by an amount determined by the laser signal's deflection. As the tip tracks the surface of the sample, the feedback controller varies the height of the cantilever to keep a constant laser signal deflection. Both of these methods enable us to construct an image of the sample surface's height, height variations, and stiffness as the tip tracks along the x and y directions.

We use tapping mode AFM to characterize the coverage of graphene's surface by polymer residue, given that it is less damaging to soft surfaces. Figure 4.2.2a shows an optical image of a graphene/hBN/graphite heterostructure after completing the fabrication steps discussed in section 4.1. Figure 4.2.2b shows a tapping mode AFM

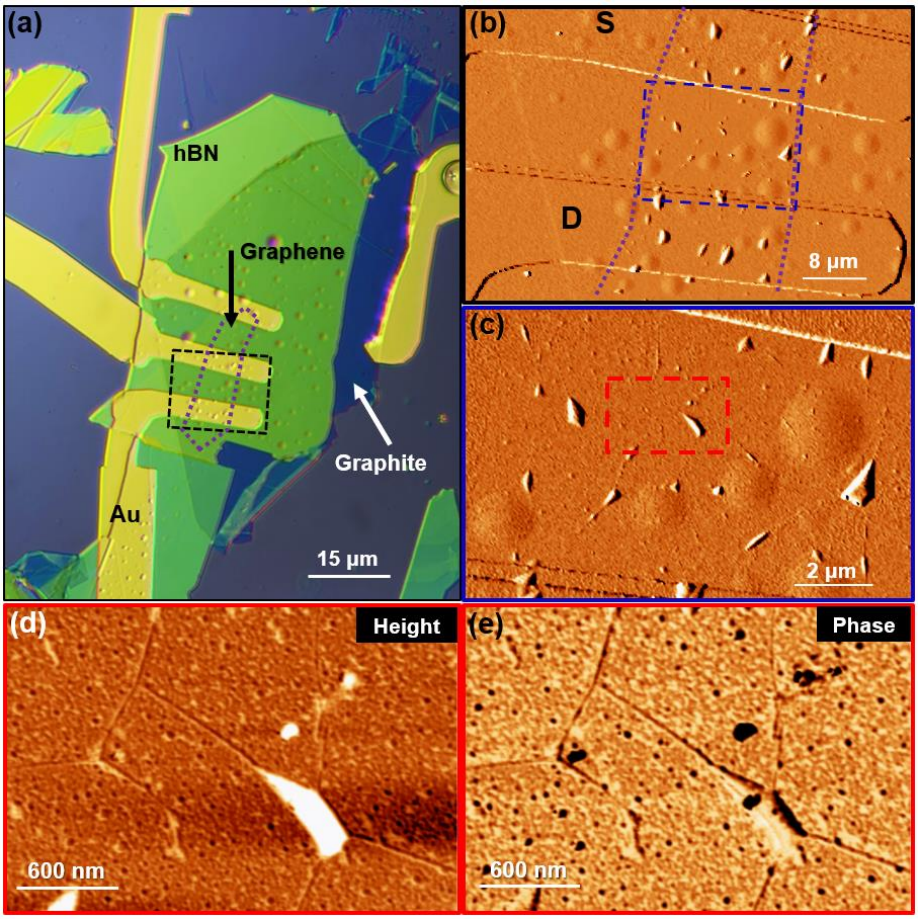

Figure 4.2.2| Initial characterization of the surface of graphene using an AFM. (a) Optical image of a graphene/hBN/graphite heterostructure after the placement of gold (Au) electrodes. **(b)** AFM amplitude image of the black dashed rectangle in (a). The region where graphene lays on top of hBN is enclosed by the purple dotted lines. **(c)** Close-up AFM amplitude image of the blue dashed rectangle in (b). Regions of higher amplitude are bubbles in the interface of graphene and hBN. In this scan, residual polymer evenly coats graphene's surface and appears as granularity in the AFM image. **(d)** Close-up AFM height image of red dashed rectangle in (c). Small alternating dark and bright circles indicating contaminants, evenly cover graphene's surface. **(e)** AFM phase image of the same region in (d). Bright regions in this image indicate stiff areas while dark regions indicate soft areas. The dark circles (soft areas) in (c) indicate the accumulation of polymer residue.

amplitude scan of the region enclosed by the dashed black rectangle in Fig. 4.2.2a. The bright and dark regions indicate changes in the amplitude of oscillation of the

cantilever as the tip is tracked over the sample surface. The smooth and round bubbles on Fig. 4.2.2b are formed during the placement of hBN on top of graphite. The sharper and elongated bubbles are formed during the placement of graphene onto hBN. The region consisting of exposed graphene is outlined by the purple dashed lines in Fig. 4.2.2b. Figure 4.2.2c shows a close-up tapping mode AFM amplitude scan of the graphene FET channel corresponding to the blue dashed box in Fig. 4.2.2b. This image displays some granularity (appearance of roughness). On occasion, these features may be caused by AFM image artefacts caused by an enlarged radius of the AFM tip, resulting from wear. However, we will see that this apparent roughness is due to the presence of contaminants uniformly covering graphene's surface. We can see this more clearly in the close-up scan in Fig. 4.2.2d. This image shows the variations in height across the surface of graphene. Moreover, we can obtain the signal for the phase of the oscillation of the cantilever. Figure 4.2.2e shows the AFM phase image of the same region in Fig. 4.2.2d. The dark and bright regions on this image correspond to relative changes in stiffness on the surface.[17] For our case, the darker regions correspond to softer material than the bright regions. Thus, we attribute these dark spots to accumulations of polymer residue left during the FET fabrication process.

Now that the presence of contaminants on graphene's surface has been identified, I demonstrate how to remove them. We use the AFM in contact mode to clear polymer off graphene's surface. We use an AFM cantilever with relatively low spring constant, specifically the Econo-ESP-Au tips with spring constant $k \sim 0.2\ \mathrm{N/m}$. By using a tip with a small k value, we are able to gently contact the surface of graphene

without causing damage. Figures 4.2.3a-c show a progression of contact mode AFM amplitude scans taken at the second, fifth, and twentieth pass using a force of 3.5 nN. From these images, it is evident that material is moved aside until no more is left to be moved; such is the case in Fig. 4.2.3c. In Figs. 4.2.3d and 4.2.3e we compare tapping mode AFM phase scans taken before and after the mechanical cleaning process. This comparison clearly shows that the soft material evenly coating graphene's surface (Fig. 4.2.3d) no longer appears after the cleaning process. Instead, Fig. 4.2.3e shows a clear surface without soft/stiff variations. Finally, we demonstrate that this AFM cleaning method does not damage the atomic structure of graphene. In Fig. 4.2.3f we show an STM topographic scan of a bilayer graphene FET that underwent the mechanical cleaning process with AFM. As is evident from this STM image, no small-scale damage is imparted by the AFM cleaning procedure.

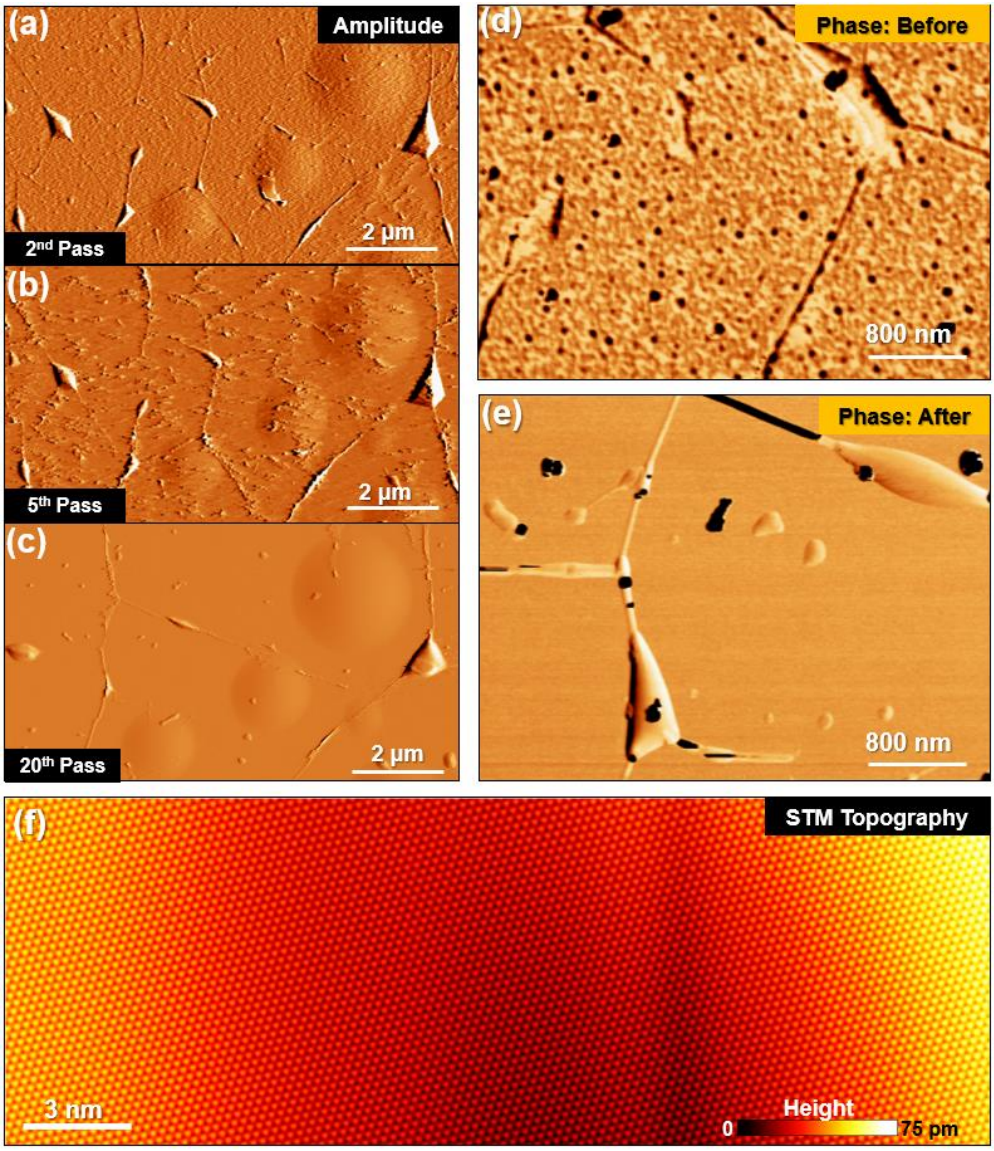

Figure 4.2.3| Mechanical cleaning of graphene's surface with AFM. (a)-(c) AFM amplitude images acquired during the second, fifth, and twentieth AFM scan in contact mode was performed, respectively. (b) shows polymer in the process of being moved aside by the AFM tip. After twenty passes (c), polymer streaks are no longer observed which indicates the removal of polymer residue on this region. **(d)** Tapping mode AFM phase image of graphene's surface before the AFM mechanical cleaning process. **(e)** Tapping mode AFM phase image of graphene's surface after the AFM mechanical cleaning process. The clear reduction of dark spots from (d) to (e) indicates a successful removal of polymer residue from graphene's surface. **(f)** STM topographic scan of the surface of a bilayer graphene sample that underwent the mechanical cleaning process with AFM. The lack of damage at the atomic level highlights the gentle nature of our adapted mechanical cleaning technique.

4.3 Electrochemical Etching of Metallic Probes for Scanning Tunneling Microscopy

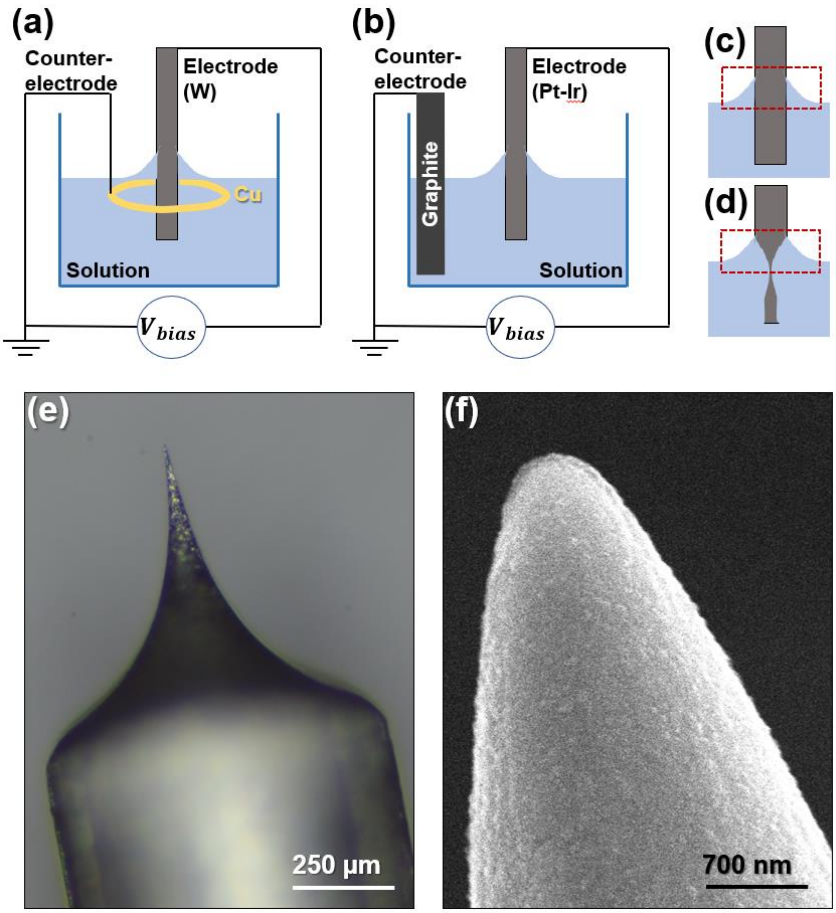

Figure 4.3.1| Electrochemically etching of STM tips. (a-b) Schematics for the tip etching setup using tungsten (a) and platinum-iridium (b) consisting an electrode and a counter-electrode submerged in an ionic solution while connected to opposite ends of a power supply (V_{bias}). **(c)** Schematic of the tip (gray) submerged in the solution before starting the etching process. The shape of the tip primarily depends on the formation of a proper meniscus (enclosed by red rectangle). **(d)** Schematic of the tip (gray) submerged in the solution near the end of the etching process. Once the bottom part of the tip electrode falls off, V_{bias} is turned off immediately. **(e)** Optical image of a tungsten tip after the process of electrochemical etching. **(f)** SEM image of the apex of a tungsten tip demonstrating the sharpness of the apex.

Landing a metallic STM tip onto a graphene sample measuring a few tens of micrometers across presents numerous challenges. However, using a telescoping lens mounted on an optical port at the side of the STM, we manage to view our sample substrates with a resolution of ~3 μm. To land on a graphene sample under these conditions, a sharp, mechanically robust, and oxidation-free tip is needed. Diagrams for the electrochemical etching process for making tungsten (W) and platinum-iridium (Pt-Ir) tips are shown in Figs. 4.3.1a and 4.3.1b, respectively. The experiments presented in this thesis use these two tip materials. Below we outline the process and components to electrochemically etch each tip material:

(i) Tungsten Tip:

- Electrode: High purity tungsten wire (~ 0.6 mm in diameter).
- Counter-electrode: circular loop of copper wire.
- Solution: 4 g of NaOH in 50 mL of DI water.
- V_{bias} starts at 8 V DC and may vary as needed so that current stays around 15 mA.

(ii) Platinum-iridium Tip:

- Electrode: High purity PtIr wire (~ 0.6 mm in diameter).
- Counter-electrode: artist-grade water-soluble graphite block.
- Solution: 14 g of $CaCl_2$ in 40 mL of DI water
- V_{bias} starts at 20 V AC with a current of ~ 800 mA. The tip may be sunk deeper into the solution to maintain a similar current.

- A few drops of acetone may be added to reduce large bubble formation during the etching process.

During the etching process, it is crucial to maintain a well-formed meniscus at the interface of the electrode and solution to ensure a tip shape with a proper aspect ratio. This meniscus is indicated by the red box in Figs. 4.3.1c-d and may need to be readjusted during the etching process. Figure 4.3.1d depicts the state of the electrode towards the end of the etching processes. After the bottom dangling piece of the tip electrode drops, V_{bias} is turned off immediately. The tip is then rinsed with acetone and isopropanol. We proceed to mount the newly etched tip onto the STM's tip holder, immediately introduce it into the STM's high vacuum load-lock chamber and pump it down. This rapid introduction into the vacuum system minimizes the buildup of oxidants on the tip's apex. Figure 4.3.1e shows an optical image of a successfully etched W tip. The gradual reduction in width ensures mechanical stability of the tip. Tips with high aspect ratios are more likely to become unstable during STM scans. A close-up of the tip's apex is shown by the SEM image in Fig. 4.3.1f. We are able to obtain tips with apex radii down to $\sim$150 nm.

Finally, before a tip can be used in the STM, it must first undergo treatment under UHV. After being introduced into the preparation chamber of the STM, the tip is sputtered with Argon gas at 1.7 kV and an emission current of 10 mA for 30 to 60 minutes. It is then briefly annealed for 1 minute at $\sim$550 ℃. This UHV treatment

ensures the removal of any oxidants that may have formed on the surface of the newly etched tip. Once this is done, the STM tip is ready for calibration.

4.4 STM Tip Calibration on Au(111)

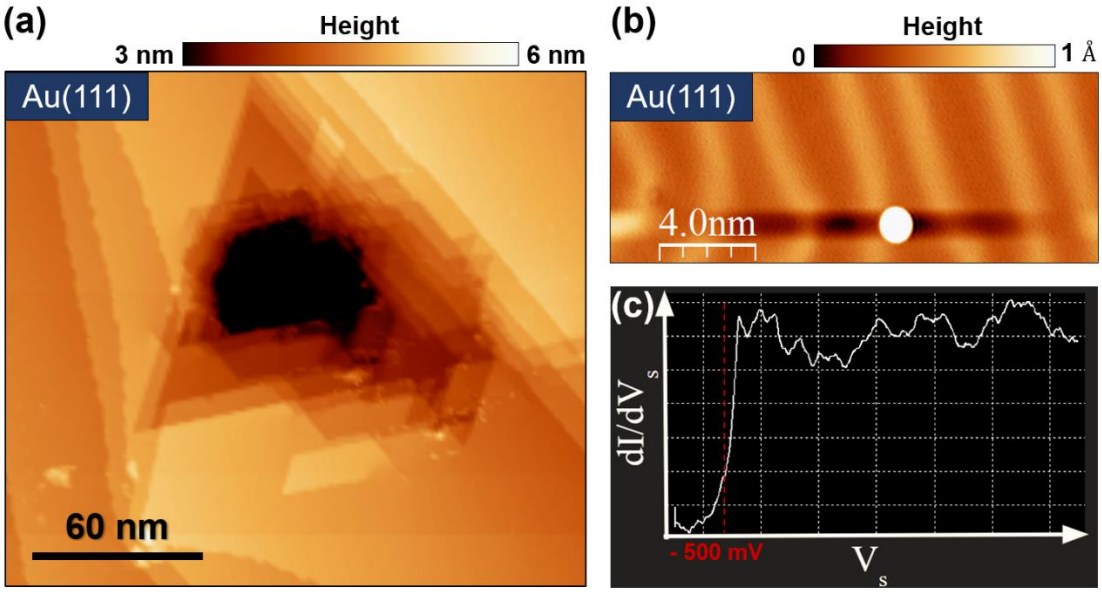

Figure 4.4.1| Scanning tunneling microscope (STM) tip calibration on Au(111). (a) Topography of Au(111) after aggressively poking the STM tip 5 nm onto the surface while applying a sample bias $V_S = -5$ V. The triangular cavity left by the aggressive poke suggests the tip was coated with Au. **(b)** Topography of Au(111). After lightly poking the STM tip 8 Å onto the surface, a small circular protrusion is left behind. The vertical ridges correspond to Au(111)'s surface reconstruction.[18] **(c)** Differential conductance (dI/dV_S) of Au(111) displays the expected surface-state spectrum[18]. Tunneling parameters used: $V_S = -0.7$ V, $I = 1$ nA, $V_{ac} = 10$ mV.

The most important factor in any experiment is the ability to obtain reproducible results. When performing STM characterization, reproducibility of spectroscopic measurements is key. To this end, whenever a sample is under study inside the STM, we follow a careful STM tip calibration procedure. This procedure enables us to obtain

a stable STM tip that provides reproducible spectroscopic data and clear atomic resolution.

The STM experiments presented in this thesis used electrochemically etched W and PtIr tips. Using tips of different materials can create variability in spectroscopic data due to differences in work function between the tip and graphene or BLG. Reproducibility, regardless of tip material, is still attained when proper calibration is followed. The first step of our calibration process is to coat the tip with gold by aggressively poking the STM tip onto the surface of a single crystal of Au(111). To perform an aggressive poke, we bring the STM tip ~ 5 nm into the gold surface. In some cases, we found that applying a sample bias of $V_S \leq -5\,V$ during the poke left behind a cavity. One such cavity left by an aggressive poke is shown in Fig. 4.4.1a. The triangular shaped cavity left behind suggests that the STM tip's apex became coated by gold atoms.[19]

After coating the STM tip with gold, we gently poke the STM tip 8 Å into the surface of Au(111). Figure 4.4.1b shows an example of a successful gentle poke that leaves behind a small circular protrusion. We perform an average of 50 gentle pokes before we find a protrusion with the desired characteristics. These characteristics include a diameter of < 2 nm, circular symmetry, and an absence of residue surrounding the protrusion. Finally, to ensure reproducible spectroscopic measurements, we obtain a differential conductance (dI/dV_S) spectrum of the surface of Au(111). An example of an acceptable dI/dV_S spectrum is shown in Fig. 4.4.1c

where the expected surface-state signature of Au(111)[18] can be seen at $V_S \sim -500\ \mathrm{m}V$.

Chapter 4 - References

(1) Dean, C. R.; Young, A. F.; Meric, I.; Lee, C.; Wang, L.; Sorgenfrei, S.; Watanabe, K.; Taniguchi, T.; Kim, P.; Shepard, K. L.; Hone, J. Boron Nitride Substrates for High-Quality Graphene Electronics. *Nat. Nanotechnol.* **2010**. https://doi.org/10.1038/nnano.2010.172.

(2) Zomer, P. J.; Dash, S. P.; Tombros, N.; Van Wees, B. J. A Transfer Technique for High Mobility Graphene Devices on Commercially Available Hexagonal Boron Nitride. *Appl. Phys. Lett.* **2011**. https://doi.org/10.1063/1.3665405.

(3) Zomer, P. J.; Guimarães, M. H. D.; Brant, J. C.; Tombros, N.; Van Wees, B. J. Fast Pick up Technique for High Quality Heterostructures of Bilayer Graphene and Hexagonal Boron Nitride. *Appl. Phys. Lett.* **2014**. https://doi.org/10.1063/1.4886096.

(4) Pizzocchero, F.; Gammelgaard, L.; Jessen, B. S.; Caridad, J. M.; Wang, L.; Hone, J.; Bøggild, P.; Booth, T. J. The Hot Pick-up Technique for Batch Assembly of van Der Waals Heterostructures. *Nat. Commun.* **2016**. https://doi.org/10.1038/ncomms11894.

(5) Taniguchi, T.; Watanabe, K. Synthesis of High-Purity Boron Nitride Single Crystals under High Pressure by Using Ba-BN Solvent. *J. Cryst. Growth* **2007**. https://doi.org/10.1016/j.jcrysgro.2006.12.061.

(6) Novoselov, K. S.; Geim, A. K.; Morozov, S. V.; Jiang, D.; Zhang, Y.; Dubonos, S. V.; Grigorieva, I. V.; Firsov, A. A. Electric Field in Atomically Thin Carbon Films. *Science (80-.).* **2004**. https://doi.org/10.1126/science.1102896.

(7) Kittel, C. Introduction to Solid State Physics, 8th Edition. *Wiley Sons, New York, NY* **2004**.

(8) Watanabe, K.; Taniguchi, T.; Kanda, H. Direct-Bandgap Properties and Evidence for Ultraviolet Lasing of Hexagonal Boron Nitride Single Crystal. *Nat. Mater.* **2004**. https://doi.org/10.1038/nmat1134.

(9) Museur, L.; Feldbach, E.; Kanaev, A. Defect-Related Photoluminescence of Hexagonal Boron Nitride. *Phys. Rev. B - Condens. Matter Mater. Phys.* **2008**. https://doi.org/10.1103/PhysRevB.78.155204.

(10) Haigh, S. J.; Gholinia, A.; Jalil, R.; Romani, S.; Britnell, L.; Elias, D. C.; Novoselov, K. S.; Ponomarenko, L. A.; Geim, A. K.; Gorbachev, R. Cross-Sectional Imaging of Individual Layers and Buried Interfaces of Graphene-Based Heterostructures and Superlattices. *Nat. Mater.* **2012**. https://doi.org/10.1038/nmat3386.

(11) Geim, A. K.; Grigorieva, I. V. Van Der Waals Heterostructures. *Nature*. 2013. https://doi.org/10.1038/nature12385.

(12) Rutter, G. M.; Jung, S.; Klimov, N. N.; Newell, D. B.; Zhitenev, N. B.; Stroscio, J. A. Microscopic Polarization in Bilayer Graphene. *Nat. Phys.* **2011**. https://doi.org/10.1038/nphys1988.

(13) Rahman, S. F. A.; Hashim, A. M.; Kasai, S. Graphene Layer Number Determination from Red-, Green-, and Blue-Channel of Optical Images; 2012. https://doi.org/10.1109/escinano.2012.6149702.

(14) Bing, D.; Wang, Y.; Bai, J.; Du, R.; Wu, G.; Liu, L. Optical Contrast for Identifying the Thickness of Two-Dimensional Materials. *Opt. Commun.* **2018**. https://doi.org/10.1016/j.optcom.2017.06.012.

(15) Photo Etch Technology http://stencil.com/.

(16) Goossens, A. M.; Calado, V. E.; Barreiro, A.; Watanabe, K.; Taniguchi, T.; Vandersypen, L. M. K. Mechanical Cleaning of Graphene. *Appl. Phys. Lett.* **2012**. https://doi.org/10.1063/1.3685504.

(17) Brandsch, R.; Bar, G.; Whangbo, M. H. On the Factors Affecting the Contrast of Height and Phase Images in Tapping Mode Atomic Force Microscopy. *Langmuir* **1997**. https://doi.org/10.1021/la970822i.

(18) Chen, W.; Madhavan, V.; Jamneala, T.; Crommie, M. F. Scanning Tunneling Microscopy Observation of an Electronic Superlattice at the Surface of Clean Gold. *Phys. Rev. Lett.* **1998**. https://doi.org/10.1103/PhysRevLett.80.1469.

(19) Oliver, D. J.; Paul, W.; El Ouali, M.; Hagedorn, T.; Miyahara, Y.; Qi, Y.; Grütter, P. H. One-to-One Spatially Matched Experiment and Atomistic Simulations of Nanometre-Scale Indentation. *Nanotechnology* **2014**. https://doi.org/10.1088/0957-4484/25/2/025701.

Chapter 5 - Persistent and Reversible Electrostatic Control of Doping in Graphene/hexagonal Boron Nitride Heterostructures

5.1 Introduction

Since its first application as a substrate for graphene field effect transistors (FETs),[1] hexagonal Boron Nitride (hBN) has become a prominent component in 2D material devices. In addition, hBN has been shown to host defects that can be manipulated to change the electronic properties of adjacent 2D materials.[2–9] Despite the wide use of such defect manipulations, no focused efforts have been made to further the understanding of defect excitations and their influence in graphene/hBN FETs. In this chapter, we explore the effect of high electric fields ($\sim 1\ \mathrm{V/nm}$) on graphene/hBN FETs and find persistent and reversible shifts in graphene's charge neutrality point (CNP). By increasing the applied electric field and temperature of our device, we find that this CNP shift is enhanced. With this insight, we propose a mechanism that explains these observations based on Pool-Frenkel emissions from defects in hBN. Finally, we show that such effect may be suppressed by using graphite as a backgate, thus preventing any unintended changes in the electrical properties of graphene/hBN FETs.

5.2 Basics of Monolayer Graphene (MLG) Electrical Transport

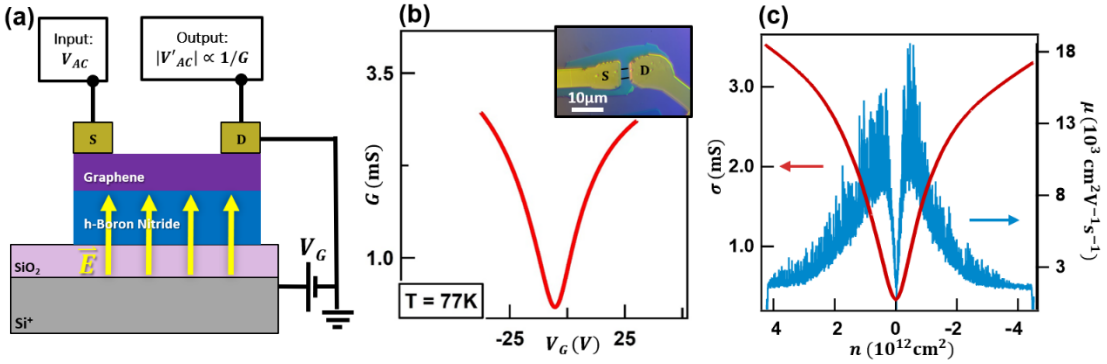

Figure 5.1| Device schematic and conductance measurement for a graphene/hBN Field Effect Transistor (FET). (a) Graphene/hBN heterostructure supported by SiO_2/Si^+ substrate (not drawn to scale). Graphene is contacted by Cr/Au electrodes and a gate voltage (V_G) is applied to the *p*-doped silicon substrate. **(b)** Conductance (G) plotted as a function of V_G for a graphene/hBN FET. The CNP is close to 0 V, indicating low levels of pre-existing doping. Inset: optical micrograph of device. The scale bar shown is 10 μm. **(c)** Re-scaled axes from conductance curve in (b) after employing a parallel plate capacitor geometry and the Drude model. Conductivity σ as a function of charge density n is shown by the red curve. The corresponding field effect mobility $\mu(n)$ is shown by the blue curve.

Before discussing the effects of high electric fields (E-fields) on graphene/hBN FETs, it is worth taking a closer look at the primary characterization technique used in this chapter.

The electrical transport measurements presented in this chapter were primarily performed on two-terminal graphene/hBN FETs. The fabrication steps for these FETs is provided in Ch. 4. We apply a $5\,\mu V$ AC signal between the source and drain electrodes as depicted in Fig. 5.1a. In this circuit arrangement, graphene acts as a resistor with conductance G which is inversely proportional to the amplitude of the

output AC signal. Next, due to graphene's 2D nature, we modulate the amount of filled states by changing the Fermi level with a perpendicular E-field. This field emanates from the Si^+ substrate by application of a backgate voltage V_G. Figure 5.1b shows a plot obtained by measuring the two-terminal conductance G while varying V_G. This conductance curve was obtained at 77 K with the FET device shown in the inset of Fig. 5.1b. From this curve we see that as V_G is tuned, the amount of mobile charges changes manifesting as variation in conductance G. The minimum of conductance in this curve corresponds to the Fermi level crossing the Dirac point and is referred to as the CNP.

The curve obtained in Fig. 5.1b can be re-scaled using a parallel plate capacitor model and the Drude model to approximate physically relevant quantities. We note that our approximations neglect contact resistance and quantum capacitance. Our analysis in this chapter relies on quantifying relative changes of the CNP, thus given that contact resistance contributes a constant reduction to conductance, we may ignore it. Additionally, we are not concerned with higher order contributions to the device capacitance by MLG's density of states, thus we can also ignore quantum capacitance. For a more rigorous treatment that considers contact resistance and quantum capacitance, see the review by Das Sarma *et al*[10] and the thesis by Jilin[11].

First, we consider a parallel plate capacitor geometry with insulating hBN/SiO_2 dielectric layers. This simple electrostatic configuration enables us to express the charge carrier density n induced on graphene by the Si^+ backgate as:

$$n = C_G(V_G - V_0)/e \qquad \text{where} \qquad (5.1)$$

$$\frac{1}{C_G} = \frac{1}{\epsilon_0}\left(\frac{d_{\mathrm{SiO_2}}}{\epsilon_{\mathrm{SiO_2}}} + \frac{d_{h\mathrm{BN}}}{\epsilon_{h\mathrm{BN}}}\right) \tag{5.2}$$

and C_G is the backgate capacitance per unit area with dielectric thicknesses $d_{\mathrm{SiO_2}} = 285$ nm and $d_{h\mathrm{BN}} = 10$ nm. The relative permittivity used for these layers are $\epsilon_{\mathrm{SiO_2}} = \epsilon_{h\mathrm{BN}} = 4$.[12,13] The value V_0 is the offset between the CNP and $V_G = 0$. For the curve in Fig. 5.1b this value is $V_0 = -5$ V. In general, the quantity V_0 accounts for the intrinsic doping of an FET device due to the presence of charged impurities.[11,14,15] Thus, pristine graphene FETs are expected to have $V_0 = 0$. This value can be heavily influenced by the substrate underneath MLG (tens of volts for MLG/SiO_2). However, since we use hBN as a substrate, we often find graphene FET devices with $V_0 < 5$ V.

An additional quantity that can be extracted from conductance curves is the device's field effect mobility μ. This quantity gives an indication for the quality and cleanliness of the device. However, it is important to note that unlike metals, graphene's carrier concentration is not constant. As a consequence, the mobility μ is not an accurate representation of sample cleanliness at vanishing charge carrier concentration near the CNP. Regardless, we can use μ as an indication of sample quality for sufficiently large carrier concentrations.[10,16,17] High values of μ indicate low rates of charge carrier scattering events during electrical transport. State-of-the-art graphene FET fabrication techniques[18] can achieve mobilities of up to ~10^5 $\mathrm{cm^2 V^{-1} s^{-1}}$. We can approximate a value for μ on our device by using an expression for electrical conductivity σ from the Drude model:

$$\sigma \sim ne\mu \tag{5.3}$$

The FETs characterized in this chapter were assembled such that the channel width W and length L are both ~3 μm. Thus, since $G = (W/L)\sigma$; we can approximate $G \sim \sigma$. Using this estimate and (5.1) we replot the conductance curve as $\sigma(n)$ shown by the red curve in Fig. 5.1c. From (5.3), the slope of this curve enables us to extract μ:

$$\mu \sim \frac{1}{e}\frac{d\sigma}{dn} \tag{5.4}$$

The field effect mobility μ is plotted in blue in Fig. 5.1c where it displays maximum mobilities of ~18 000 $\text{cm}^2V^{-1}\text{s}^{-1}$, but for higher charge carrier densities the mobility stays roughly constant at ~3 000 $\text{cm}^2V^{-1}\text{s}^{-1}$. We note that in our estimates we have not accounted for contact resistance from the thermally evaporated electrodes. However, in this chapter we primarily rely on relative qualitative differences between curves of the same device and changes in CNP. Thus, the added contact resistance may be ignored. Now that we have a general idea of electrical transport characterization in MLG/hBN FETs, we will explore the effect of strong electric fields on MLG's CNP.

5.3 The Versatility of Defects in hBN

Thin sheets of hBN are prominent components in 2D material devices because they are insulating and exhibit atomically flat surfaces. In addition, hBN has been shown to enable manipulation of the electronic properties of adjacent 2D materials. Early studies that incorporated hBN into graphene FETs showed that the electronic

properties of these devices vastly improved due to hBN's characteristic inertness and flatness.[1,19] Since then, many techniques have been developed to mechanically place graphene on top of hBN. This has resulted in the continued improvement of graphene FET electron mobilities.[18,20–22] A second wave of studies used hBN as a vehicle to induce electronic changes in graphene FETs, such as control of crystallographic alignment between graphene and hBN[23–25] and the excitation of defects in the supporting hBN.[2] In regards to the latter, numerous experiments have utilized light and localized electric fields to manipulate defects in hBN,[2,3] realize rewritable *p-n* junctions,[4] image and control chiral bound states,[5,6] and develop Berry phase switches.[7] Despite the wide use of these techniques based on the manipulation of defects in graphene/hBN FETs, no focused efforts have been made to understand such defect excitation process. In particular, the role of high E-fields and variable temperatures on the excitation of hBN defects in these FETs remains largely unexamined. Such parameters should be crucial for the onset and nature of defect excitations in hBN.

5.4 High E-Field Induced CNP Shifts in Graphene/hBN FETs

In this section, we discuss the effects of applying high E-fields on the order of $\sim 1\ \mathrm{V/nm}$ on graphene/hBN heterostructures at different temperatures. Figure 5.1a shows a schematic for a graphene FET transistor used in our study. Before we expose the FETs to high E-fields, we obtain their intrinsic behavior by sweeping an applied gate voltage (V_G) while recording the two-terminal conductance (G). Figure 5.1b shows

one such conductance curve where the minima corresponds to the CNP in graphene's band structure.[26] As discussed above, the close proximity of the CNP to $V_G = 0$, indicates a low level of intrinsic doping V_0 for this device. This is expected for heterostructures composed of graphene and hBN.[1]

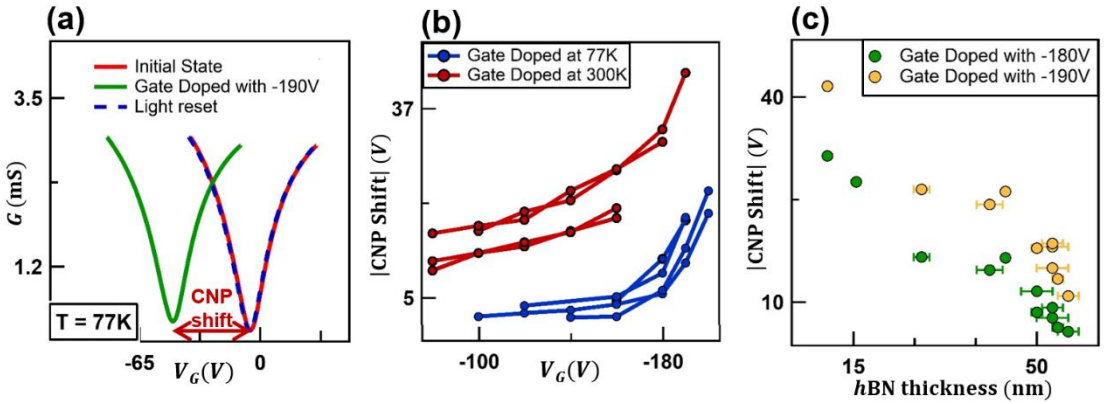

Figure 5.2| Graphene/hBN FETs exposed to high electric fields. (a) $G(V_G)$ curves display the changes of electrical properties in graphene/hBN FETs after application of a high electric field emanating from the backgate. The red curve was obtained before high E-field exposure. The green curve was obtained after applying $V_G = -190$ V for 8 minutes. The dashed blue line was obtained after shining light on the FET for 5 minutes while maintaining $V_G = 0$ V. **(b)** Dependence of charge neutrality point (CNP) shifts on applied V_G of 4 devices with similar hBN thickness (~55 nm) at 77 K (blue) and 300 K (red). **(c)** Dependence of CNP shifts on substrate hBN thickness for $V_G = -180$ V (green circles) and $V_G = -190$ V (orange circles).

We induce large E-fields in our FET devices by applying V_G from -80 V to -210 V between the p-doped silicon (Si^+) substrate and monolayer graphene (MLG) for 8 minutes (see section 5.5 for details on time dependence). Immediately after, we reduce V_G to zero and obtain a conductance curve $G(V_G)$. Figure 5.2a shows conductance curves taken before and after high E-fields are applied. The red curve corresponds to an initial state (before high E-field exposure), while the green curve

corresponds to a state after the sample was exposed to $V_G = -190$ V. Evidently, the high E-field exposure has shifted the CNP of the device to the left by 40 V. We note that only negative values of V_G were applied since changes to the CNP for positive V_G were slow and nearly imperceptible. Additionally, we observed negligible changes in the field effect mobility μ after high E-field exposures as demonstrated by the slopes of the before (red) and after (green) curves in Fig. 5.2a. Finally, by exposing the same device to light while maintaining $V_G = 0$ V, we find that the initial state of our FET device is recovered. This effect was studied in depth by L. Ju *et al*.[2] For details on the experimental setup used for the light-induced recovery, see the published article's supplement.[27] The hBN defects' sensitive response to light provides an additional mechanism for tuning 2D material's electrical properties beyond graphene.[28,29] The result of the light-mediated resetting process is shown by the dashed blue curve in Fig. 5.2a, where the CNP has returned to its original value.

5.4.1 CNP shifts dependence on V_G and temperature

We further explore the behavior of graphene/hBN FETs under high E-fields by varying gate voltage intensities V_G for samples with similar hBN thicknesses. Figure 5.2b shows a plot of the CNP shifts for four different devices with hBN substrates of similar thicknesses ($\sim$55 nm) measured after multiple high E-field exposures by V_G. We observe that the magnitude of the CNP shifts are generally greater after the FETs have been exposed to higher gate voltages. Figure 5.2b also shows that the CNP shift

behaves similarly for each temperature that was examined, 300 K and 77 K. This is evident from the clustering of the CNP shift points for each temperature, as shown by the grouping of the red and blue curves. At 300 K, the CNP shifts become more pronounced after applying $V_G = -150$ V. At 77 K, the CNP shift becomes greater after applying $V_G = -180$ V. The overall magnitude of the CNP shifts are also higher at 300 K. For example, with an applied gate voltage of -160 V a CNP shift of 5 V is achieved at 77 K, whereas at 300 K, the same device achieves a CNP shift of 20 V.

5.4.2 CNP shifts dependence on substrate hBN thickness

We also consider the role of hBN thickness in CNP shifts for graphene/hBN FETs under high E-field exposures. We measured shifts in CNP for various hBN thicknesses after applying two different gate voltages. The thicknesses of our FETs were determined using atomic force microscopy. We find that the thickness of the substrate hBN also influences the level of CNP shift after a high E-field exposure. Figure 5.2c shows CNP shifts achieved for multiple FET devices that have different thicknesses of hBN substrates. The data indicates that devices with hBN substrates that are thin achieve higher levels of CNP shift when exposed to the same gate voltage as devices with thicker hBN substrates. The thicknesses of the hBN substrates in our FET devices range from 10 nm to 56 nm. We also note, in Fig. 5.2c, that although CNP shifts are different between V_G exposures of -180 V and -190 V, the incremental change in CNP shift for each gate exposure (with different hBN thicknesses) increases

by similar amounts. Finally, we found that devices with hBN thinner than 10 nm did not respond to resetting with light. For this reason, we did not include these devices in Fig. 5.2c, nor in the rest of our experiments.

5.4.3 CNP shifts dependence on exposure time

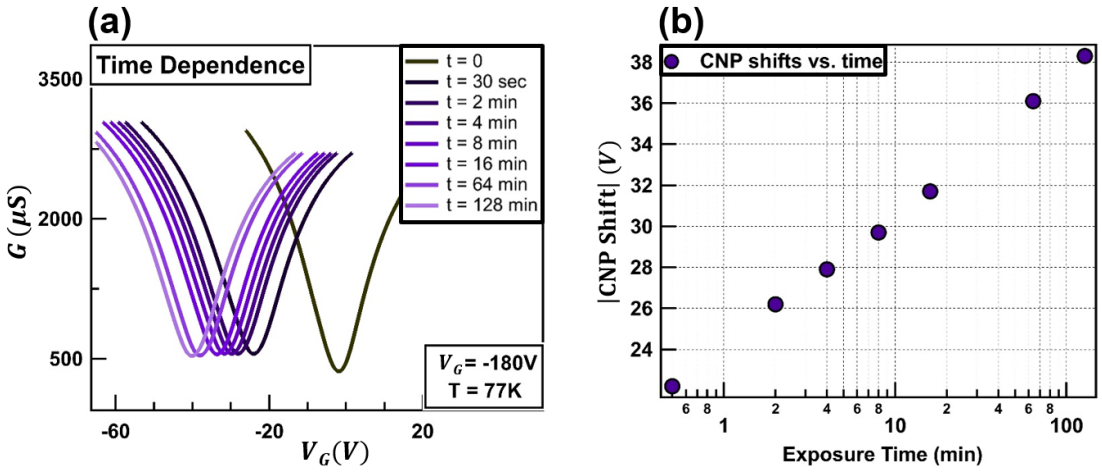

Figure 5.3| Time dependence of CNP shifts in graphene/hBN FET under a high E-field exposure. (a) Conductance curves (G) as a function of backgate voltage V_G for a graphene/hBN FET. Curves were obtained for different exposure times to a backgate voltage of -180 V. **(b)** CNP shifts obtained from (a) are plotted as a function of time. The time axis has been scaled logarithmically. Given the logarithmic behavior of CNP shift magnitudes, the arbitrary choice of an 8 minute high E-field exposure time was made.

Shifts in CNP were also measured as a function of high E-field exposure time. Figure 5.3a shows conductance (G) traces as a function of gate voltage V_G for different exposure times at $V_G = -180$ V and 77 K. These traces were obtained using a graphene/hBN FET with an hBN thickness of 10 nm. It is evident from Fig. 5.3a that

the CNP (minima in each curve) shifts towards increasingly negative values as the exposure time increases. Figure 5.3b shows the magnitude of the CNP shifts from Fig 5.3a as a function of exposure time. The time (horizontal) axis is scaled logarithmically. Figure 5.3b shows that within the range of the CNP shifts plotted, the magnitude of CNP shifts increases with time. This increment in CNP shift is pronounced at first, and then diminishes as the exposure time increases.

In the following section we will establish a link between CNP shifts and hBN defect ionization events. With this in mind, we can make an analogy between the time dependence of CNP shifts and charge buildup in a parallel plate capacitor. Like charges populating a capacitor, CNP shifts should continue to gradually but slowly increase until a maximum number of ionized defects is reached at $t = \infty$. For the case of defect ionization in bulk hBN, the intensity of the electric field diminishes due to screening from charged hBN defects. Therefore, the CNP shift's rate of increase should continue to decrease until the potential from the applied V_G matches the potential from the charged defects in bulk hBN. For the FET used in Figs. 5.3a-b, at $t = \infty$ the CNP shift magnitude should in principle reach -180 V. As a side note, this limit is more easily attained when using photo-excitations, as observed in previous works.[2,28,29]

5.5 Heuristic Model for High E-Field Defect Ionization in hBN

We believe that the observed pronounced CNP shifts in our graphene FETs can be explained by the manipulation of defects in the supporting hBN substrate. Negligible

hysteresis observed in conductance curves allows us to dismiss the presence of dipolar adsorbates on graphene's surface.[30] In addition, the leakage current between the backgate and graphene stayed constant at the noise floor of our voltage supply ($\sim$1 pA) while the high E-fields were being applied. These observations hence allow us to rule out electrochemical doping. Furthermore, the existence of defects in bulk hBN has been experimentally verified and even utilized to alter the electronic properties of 2D materials. Initially, bulk hBN was shown to have defects such as carbon and oxygen impurities through studies that used averaged ensemble techniques, such as secondary ion mass spectroscopy and photo-luminescence.[31–33] Individual defects have also been observed at the atomic scale via scanning tunneling and transmission electron microscopy studies.[3,34,35] In addition, numerous previous works have demonstrated manipulation of hBN defects. One set of studies realized manipulation of hBN defects at the micron scale by exposing 2D material/hBN heterostructures to visible light.[2,28,29] Another set of studies achieved manipulation by using localized electrostatic excitations from a scanning tunneling microscope tip to modulate the charge state of individual defects and small ensembles of defects.[3,6,7,9,36] In these works, it was also shown that no irreversible changes are made to graphene's surface after the application of strong localized E-fields.

To explain the CNP shift observed in our experiments we utilize the existence/manipulation of hBN defects and the Poole-Frenkel (PF) model.[37] This model puts forth that at finite temperature, an E-field enables the flow of charges that originate from the ionization of defect traps in insulating and semi-conducting

materials. Other models that describe charge flow through an insulator such as Fowler-Nordheim tunneling and space charge limited current were not considered because they are not defect-based and do not account for simultaneous temperature and E-field modulation.[38] Previous experiments on thin insulating/semiconducting films have measured a flow of charges due to defect traps, known as the PF current (j_{PF}). For semiconducting films, such traps come from dopant impurities.[39,40] In the case of insulators, growth and synthesis parameters determine the number of charge carrier traps.[41,42] These works have shown that j_{PF} increases with increasing temperature and increasing applied E-field.[43] Thus, within the PF model, a measurement of larger j_{PF} (coincident with increased temperature or E) corresponds to a greater number of defect ionization events. In our experiment with graphene/hBN FETs, we observe CNP shifts after our samples have been exposed to high E-fields and increased temperatures (see Figs. 5.2b-c). Because the CNP shifts in our experiments and j_{PF} in prior works both increase with large applied E and increasing temperature, we believe that these two share the same origin.

Now that we have established a basis for invoking the PF model to describe our experimental observations, we apply it to explain the mechanism behind the CNP shifts. Single donor-like defects within the hBN are modeled as an $1/r$ potential (black solid line) with a trap charge (red circle) in Fig. 5.4. Only donor-like defects are considered since CNP shifts were mostly absent when applying positive V_G. Initially (Fig. 5.4a), when no gate voltage is applied, the defects in hBN are neutral; the trapped charge remains within an unaltered potential. Moreover, the FET can be modeled as a

parallel plate capacitor with an electric potential that is linear with respect to the distance between the electrodes. As a result, once a sufficiently large and uniform field $\vec{E}$ (Fig. 5.4b) is applied, a linear potential is added onto the attractive Coulomb potential. This addition causes a tilt which lowers the barrier that confines the trapped charge,[37] allowing the charge to escape.

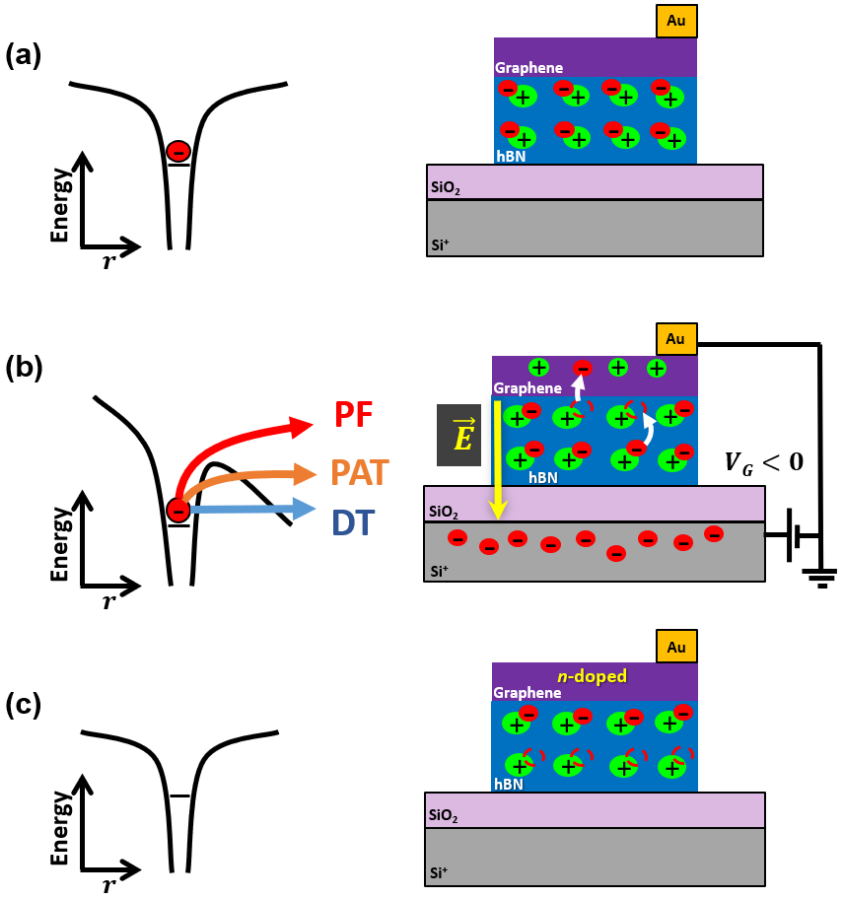

Figure 5.4| Heuristic model for the persistent electrostatic doping due to high *E*-fields. (a) Initial state of a graphene/hBN FET. Neutral hBN defects are represented by a trap potential (black line) with a charge inside (red circle). **(b)** Intermediate state. When a large electric field is applied with the gate, defect charges are excited out of the trap potential via three different pathways: direct tunneling (DT), phonon assisted tunneling (PAT), thermal emission (PF). These pathways are depicted by the blue, orange, and red arrows respectively. **(c)** Final state. After some period of time, defects remain ionized and remotely *n*-dope graphene.

Generally, three different charge escape pathways from Frenkel type defects can occur; direct tunneling (DT), phonon assisted tunneling (PAT), and thermal emission (PF).[44] Thermal emission via the Poole-Frenkel effect is the simplest mechanism of ionization given that it only considers over-the-barrier emissions. PAT considers trapped charges tunneling out of the potential after the ionization energy has been lowered due to lattice vibrations around the defect traps. Notably, DT dominates when E-fields are high enough that phonon interactions are not necessary for defects to tunnel out of the trap. Determination of which of these mechanisms dominates is out of the scope of the device geometry of this work. Future investigations can be pursued that measure the ionization current directly as a function of E-field and temperature.[45] Nonetheless, we do observe that at higher temperatures, defect ionization events increase. We believe this to be a result of an enhancement of the thermally excitable pathways PF and PAT.

After the trapped charges escape their confining potential, they eventually reach the graphene layer and leave a net positive charge in hBN. Guidance of these charges is enabled by the applied E-field, which allows them to gradually migrate towards graphene by hoping onto vacant defects within adjacent hBN layers. This process is depicted in the right panel of Fig. 5.4b. Once they reach the top layer of hBN, these charges exit the heterostructure through the grounded graphene. Eventually, this process leads to a layer of positive ionized defects close to the interface of hBN and SiO_2 resulting in the partial screening of negative charges from the Si^+ backgate. As depicted in Figs. 5.4b-c, the separation distance between the ionized defect layer and

graphene approximately equals the supporting hBN thickness. As a result, in FETs with thinner hBN, an increase in capacitive coupling between the slab of charged defects and graphene (considering a parallel plate capacitor model) enhances CNP shifts (see Fig. 5.2c). In Fig. 5.4c, the electric field $\vec{E}$ is turned off and the charged defect traps near the hBN/SiO_2 interface remain. These charged traps persistently gate the entire graphene flake remotely and make it *n*-doped. Such doping results in the CNP shift shown in Fig. 5.2a.

5.6 Suppression of Charge Accumulation in hBN

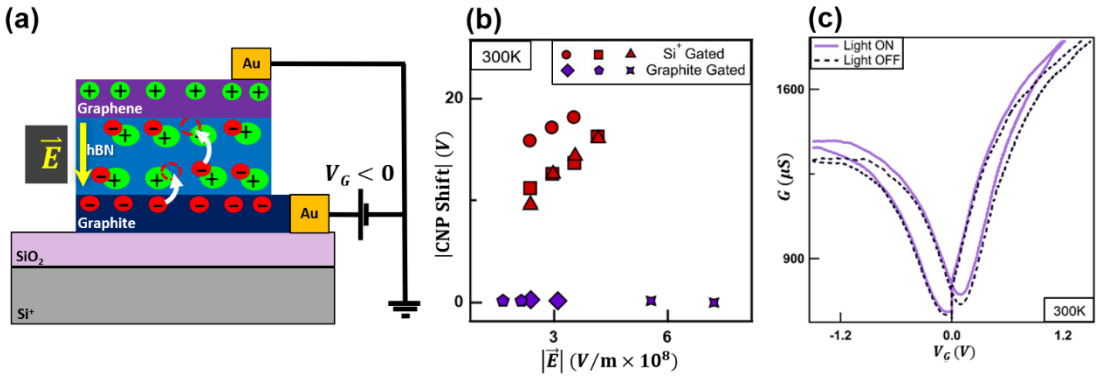

Figure 5.5| Suppression of high *E*-field and light induced CNP shifts. (a) Schematic of hBN defect de-activation. Charges in Graphite repopulate emptied hBN defect traps. **(b)** Comparison of CNP shifts between silicon gated (red polygons) and graphite gated (purple polygons) FETs after exposure to similar electric field intensities. **(c)** Suppression of light-induced doping in a graphene/hBN/graphite FET. Conductance curves (G) as a function of backgate voltage V_G for a graphene/hBN/graphite FET. For both curves, the backgate voltage V_G was swept from zero towards negative values, back to positive values, and finally back to 0 V. Traces were obtained while exposing the FET to light and no light as represented by the purple and dashed black curves, respectively. This plot demonstrates the resilience of a graphite gated FET against photo-induced CNP changes.

The PF model and electric field guided charge hopping within hBN discussed above provides insight on how to suppress the CNP shifts observed in our experiments. Such suppression is crucial for experiments that require controllable doping of 2D materials supported by hBN such as angle resolved photoemission spectroscopy (ARPES)[46,47] and high temperature electrical transport.[48,49] Based on the discussion for Fig. 5.4, the neutralization of the ionized traps near the hBN/SiO_2 interface should suppress high E-field induced CNP shifts. To this end, we have implemented a graphite flake as a backgate for our graphene/hBN heterostructure. A schematic for one such device is shown in Fig. 5.5a. To explain how this device will suppress high E-field induced CNP shifts, we adapt the process described in Figs. 5.4b-c to include free charges from a graphite layer between hBN and SiO_2. As we expose the hBN traps to strong E-fields, released charges migrate towards graphene and eventually to ground (similar to Fig. 5.4b). For the graphene/hBN/graphite heterostructure, however, free electrons in semi-metallic graphite populate the activated traps in hBN. This flow of electrons between graphite, hBN, and ultimately graphene prevents the build-up of charged traps near the hBN and graphite interface. Without this buildup, a persistent CNP shift cannot emerge.

In Fig. 5.5b we show the results of several transport experiments that validate our proposed solution for suppressing CNP shifts due to high E-fields. Specifically, we measured the two-terminal conductance (G) for three graphene/hBN/graphite FETs after exposing them to large E-field intensities, similar to our measurements in Figs. 5.1b and 5.2a. The hBN thicknesses for these devices were 20 nm, 40 nm, and 60 nm.

From these conductance measurements we extract the shift in CNP and plot them with the corresponding electric field used during the exposure. This data is shown in Fig. 5.5b, where the measured response for each device is denoted by a purple colored polygon. As a comparison, we replot the room temperature data from graphene/hBN FETs supported by Si^+ from Fig. 5.2b. These data points are indicated as red colored polygons. Evidently, for the graphene/hBN/graphite FETs we did not observe shifts in the CNP for E-field intensities of up to ~ $0.8\ \mathrm{V/nm}$; while for the graphene/hBN FETs, clear shifts were observed.

To further test the resilience of graphite-gated FETs against doping from ionized hBN defects, we applied the photoinduced doping technique on a graphene/hBN/graphite FET. This technique applies light onto 2D material/hBN FETs[2,4,28] to create doped region on graphene by exciting hBN defects, as is done with high electric fields in this chapter. The results of this test are shown in Fig. 5.5c. The purple curve in Fig. 5.5c shows conductance (G) as a function of gate voltage V_G of a graphite-gated FET while exposing it to light from a purple diode laser.[27] We also measured the FET's conductance against V_G without exposing the sample to any light. This is shown by the dashed black curve in Fig 5.5c. For the case of graphene/hBN FETs, the inclusion of photo-excitations increases the rate at which hBN defects are ionized.[2] Despite the possible increase of ionization events provided by light, Fig. 5.5c demonstrates the complete suppression of electrostatic changes in our graphene/hBN/graphite FET. Both curves in Fig. 5.5c show a small hysteresis with V_G. However, $G(V_G)$ traces do not change significantly between the trials when the sample

was and was not exposed to light.

5.7 Conclusion

In conclusion, we have demonstrated that high E-field exposures emanating from a Si^+ backgate can induce a reversible change in the electronic properties of graphene/hBN heterostructures. A range of E-field intensities and different temperatures were examined in our study. We found that CNP shifts in graphene increase as both the electric field intensity and temperature are increased. Due to the similarities between CNP shifts in our study and prior works on Poole-Frenkel emissions, we applied the Poole-Frenkel model to explain the mechanism by which high E-fields induce persistent doping in our graphene/hBN FETs. Using insight from our proposed mechanism, we assembled an FET heterostructure that eliminates persistent unintended doping. This FET contains an additional layer of graphite underneath the graphene/hBN stack. Here, graphite acts as a backgate and, importantly, prevents charge buildup in the hBN. The suppression of charge buildup in hBN is important for ARPES and high temperature electrical transport studies because it recovers controllable device doping.[29,48] Nonetheless, studies that utilize doping in 2D materials can incorporate the doping technique we presented here to enhance *n*-doping in a given 2D material. Finally, this doping technique can be used to quantify deliberate defect incorporation in hBN, which has been employed by several quantum emitter studies.[50–52] Synthesis processes that deliberately increase defect densities in hBN may

utilize high E-field exposure to attain an approximate measure of defect densities based on the magnitude of CNP shifts.

Chapter 5 - References

(1) Dean, C. R.; Young, A. F.; Meric, I.; Lee, C.; Wang, L.; Sorgenfrei, S.; Watanabe, K.; Taniguchi, T.; Kim, P.; Shepard, K. L.; Hone, J. Boron Nitride Substrates for High-Quality Graphene Electronics. *Nat. Nanotechnol.* **2010**. https://doi.org/10.1038/nnano.2010.172.

(2) Ju, L.; Velasco, J.; Huang, E.; Kahn, S.; Nosiglia, C.; Tsai, H.-Z.; Yang, W.; Taniguchi, T.; Watanabe, K.; Zhang, Y.; Zhang, G.; Crommie, M.; Zettl, A.; Wang, F. Photoinduced Doping in Heterostructures of Graphene and Boron Nitride. *Nat. Nanotechnol.* **2014**, *9* (5), 348–352. https://doi.org/10.1038/nnano.2014.60.

(3) Wong, D.; Velasco, J.; Ju, L.; Lee, J.; Kahn, S.; Tsai, H.-Z.; Germany, C.; Taniguchi, T.; Watanabe, K.; Zettl, A.; Wang, F.; Crommie, M. F. Characterization and Manipulation of Individual Defects in Insulating Hexagonal Boron Nitride Using Scanning Tunnelling Microscopy. *Nat. Nanotechnol.* **2015**, *10* (11), 949–953. https://doi.org/10.1038/nnano.2015.188.

(4) Velasco, J.; Ju, L.; Wong, D.; Kahn, S.; Lee, J.; Tsai, H. Z.; Germany, C.; Wickenburg, S.; Lu, J.; Taniguchi, T.; Watanabe, K.; Zettl, A.; Wang, F.; Crommie, M. F. Nanoscale Control of Rewriteable Doping Patterns in Pristine Graphene/Boron Nitride Heterostructures. *Nano Lett.* **2016**. https://doi.org/10.1021/acs.nanolett.5b04441.

(5) Zhao, Y.; Wyrick, J.; Natterer, F. D.; Rodriguez-Nieva, J. F.; Lewandowski, C.; Watanabe, K.; Taniguchi, T.; Levitov, L. S.; Zhitenev, N. B.; Stroscio, J. A. Creating and Probing Electron Whispering-Gallery Modes in Graphene. *Science (80-.).* **2015**. https://doi.org/10.1126/science.aaa7469.

(6) Lee, J.; Wong, D.; Velasco, J.; Rodriguez-Nieva, J. F.; Kahn, S.; Tsai, H. Z.; Taniguchi, T.; Watanabe, K.; Zettl, A.; Wang, F.; Levitov, L. S.; Crommie, M. F. Imaging Electrostatically Confined Dirac Fermions in Graphene Quantum Dots. *Nat. Phys.* **2016**. https://doi.org/10.1038/nphys3805.

(7) Ghahari, F.; Walkup, D.; Gutiérrez, C.; Rodriguez-Nieva, J. F.; Zhao, Y.; Wyrick, J.; Natterer, F. D.; Cullen, W. G.; Watanabe, K.; Taniguchi, T.; Levitov, L. S.; Zhitenev, N. B.; Stroscio, J. A. An on/off Berry Phase Switch in Circular Graphene Resonators. *Science (80-.).* **2017**. https://doi.org/10.1126/science.aal0212.

(8) Gutiérrez, C.; Walkup, D.; Ghahari, F.; Lewandowski, C.; Rodriguez-Nieva, J. F.; Watanabe, K.; Taniguchi, T.; Levitov, L. S.; Zhitenev, N. B.; Stroscio, J. A. Interaction-Driven Quantum Hall Wedding Cake–like Structures in Graphene Quantum Dots. *Science (80-.).* **2018**. https://doi.org/10.1126/science.aar2014.

(9) Walkup, D.; Ghahari, F.; Gutiérrez, C.; Watanabe, K.; Taniguchi, T.; Zhitenev, N. B.; Stroscio, J. A. Tuning Single-Electron Charging and Interactions between Compressible Landau Level Islands in Graphene. *Phys. Rev. B* **2020**. https://doi.org/10.1103/PhysRevB.101.035428.

(10) Das Sarma, S.; Adam, S.; Hwang, E. H.; Rossi, E. Electronic Transport in Two-Dimensional Graphene. *Rev. Mod. Phys.* **2011**. https://doi.org/10.1103/RevModPhys.83.407.

(11) Xia, J. Charge Transport and Quantum Capacitance of Graphene. PhD Thesis., Arizona State University, 2010.

(12) Laturia, A.; Van de Put, Maarten L. . Vandenberghe, W. G. Dielectric Properties of Hexagonal Boron Nitride and Transition Metal Dichalcogenides: From Monolayer to Bulk. *npj 2D Mater. Appl. Vol.* **2018**, *2* (6). https://doi.org/https://doi.org/10.1038/s41699-018-0050-x.

(13) El-Kareh, B. *Fundamentals of Semiconductor Processing Technologies*; Kluwer Academic Publishers, 1995.

(14) Freitag, F. Graphene: From Diffusive to Ultraclean-Interacting Systems. PhD Thesis., University of Basel, Switzerland, 2012.

(15) Handschin, C. J. Quantum Transport in Encapsulated Graphene P-N Junctions. PhD Thesis., University of Basel, Switzerland., 2017.

(16) Tan, Y. W.; Zhang, Y.; Bolotin, K.; Zhao, Y.; Adam, S.; Hwang, E. H.; Das Sarma, S.; Stormer, H. L.; Kim, P. Measurement of Scattering Rate and Minimum Conductivity in Graphene. *Phys. Rev. Lett.* **2007**. https://doi.org/10.1103/PhysRevLett.99.246803.

(17) Jang, C.; Adam, S.; Chen, J.; Williams, E.; Das Sarma, S.; Fuhrer, M. Tuning the Effective Fine Structure Constant in Graphene: Opposing Effects of Dielectric Screening on Short- and Long-Range Potential Scattering. *Phys. Rev. Lett.* **2008**, *101* (146805). https://doi.org/https://doi.org/10.1103/PhysRevLett.101.146805.

(18) Pizzocchero, F.; Gammelgaard, L.; Jessen, B. S.; Caridad, J. M.; Wang, L.; Hone, J.; Bøggild, P.; Booth, T. J. The Hot Pick-up Technique for Batch Assembly of van Der Waals Heterostructures. *Nat. Commun.* **2016**. https://doi.org/10.1038/ncomms11894.

(19) Yang, W.; Chen, G.; Shi, Z.; Liu, C. C.; Zhang, L.; Xie, G.; Cheng, M.; Wang, D.; Yang, R.; Shi, D.; Watanabe, K.; Taniguchi, T.; Yao, Y.; Zhang, Y.; Zhang, G. Epitaxial Growth of Single-Domain Graphene on Hexagonal Boron Nitride. *Nat. Mater.* **2013**. https://doi.org/10.1038/nmat3695.

(20) Zomer, P. J.; Dash, S. P.; Tombros, N.; Van Wees, B. J. A Transfer Technique for High Mobility Graphene Devices on Commercially Available Hexagonal Boron Nitride. *Appl. Phys. Lett.* **2011**. https://doi.org/10.1063/1.3665405.

(21) Wang, L.; Meric, I.; Huang, P. Y.; Gao, Q.; Gao, Y.; Tran, H.; Taniguchi, T.; Watanabe, K.; Campos, L. M.; Muller, D. A.; Guo, J.; Kim, P.; Hone, J.; Shepard, K. L.; Dean, C. R. One-Dimensional Electrical Contact to a Two-Dimensional Material. *Science (80-.).* **2013**. https://doi.org/10.1126/science.1244358.

(22) Zomer, P. J.; Guimarães, M. H. D.; Brant, J. C.; Tombros, N.; Van Wees, B. J. Fast Pick up Technique for High Quality Heterostructures of Bilayer Graphene and Hexagonal Boron Nitride. *Appl. Phys. Lett.* **2014**. https://doi.org/10.1063/1.4886096.

(23) Yankowitz, M.; Xue, J.; Cormode, D.; Sanchez-Yamagishi, J. D.; Watanabe, K.; Taniguchi, T.; Jarillo-Herrero, P.; Jacquod, P.; Leroy, B. J. Emergence of Superlattice Dirac Points in Graphene on Hexagonal Boron Nitride. *Nat. Phys.* **2012**. https://doi.org/10.1038/nphys2272.

(24) Geim, A. K.; Grigorieva, I. V. Van Der Waals Heterostructures. *Nature*. 2013. https://doi.org/10.1038/nature12385.

(25) Woods, C. R.; Britnell, L.; Eckmann, A.; Ma, R. S.; Lu, J. C.; Guo, H. M.; Lin, X.; Yu, G. L.; Cao, Y.; Gorbachev, R. V.; Kretinin, A. V.; Park, J.; Ponomarenko, L. A.; Katsnelson, M. I.; Gornostyrev, Y. N.; Watanabe, K.; Taniguchi, T.; Casiraghi, C.; Gao, H. J.; Geim, A. K.; Novoselov, K. S. Commensurate-Incommensurate Transition in Graphene on Hexagonal Boron Nitride. *Nat. Phys.* **2014**. https://doi.org/10.1038/nphys2954.

(26) Novoselov, K. S.; Geim, A. K.; Morozov, S. V.; Jiang, D.; Zhang, Y.; Dubonos, S. V.; Grigorieva, I. V.; Firsov, A. A. Electric Field in Atomically Thin Carbon Films. *Science (80-.).* **2004**. https://doi.org/10.1126/science.1102896.

(27) Quezada-Lopez, E. A.; Joucken, F.; Chen, H.; Lara, A.; Davenport, J. L.; Hellier, K.; Taniguchi, T.; Watanabe, K.; Carter, S.; Ramirez, A. P.; Velasco, J. Persistent and Reversible Electrostatic Control of Doping in

Graphene/Hexagonal Boron Nitride Heterostructures. *J. Appl. Phys.* **2020**. https://doi.org/10.1063/1.5127770.

(28) Epping, A.; Banszerus, L.; Güttinger, J.; Krückeberg, L.; Watanabe, K.; Taniguchi, T.; Hassler, F.; Beschoten, B.; Stampfer, C. Quantum Transport through MoS2 Constrictions Defined by Photodoping. *J. Phys. Condens. Matter* **2018**. https://doi.org/10.1088/1361-648X/aabbb8.

(29) Volmer, F.; Ersfeld, M.; Rathmann, L.; Heithoff, M.; Kotewitz, L.; Watanabe, K.; Taniguchi, T.; Stampfer, C.; Beschoten, B. How the Dynamic of Photo-Induced Gate Screening Complicates the Investigation of Valley Physics in 2D Materials. *arxiv* **2020**.

(30) Pinto, H.; Markevich, A. Electronic and Electrochemical Doping of Graphene by Surface Adsorbates. *Beilstein Journal of Nanotechnology*. 2014. https://doi.org/10.3762/bjnano.5.195.

(31) Watanabe, K.; Taniguchi, T.; Kanda, H. Direct-Bandgap Properties and Evidence for Ultraviolet Lasing of Hexagonal Boron Nitride Single Crystal. *Nat. Mater.* **2004**. https://doi.org/10.1038/nmat1134.

(32) Taniguchi, T.; Watanabe, K. Synthesis of High-Purity Boron Nitride Single Crystals under High Pressure by Using Ba-BN Solvent. *J. Cryst. Growth* **2007**. https://doi.org/10.1016/j.jcrysgro.2006.12.061.

(33) Museur, L.; Feldbach, E.; Kanaev, A. Defect-Related Photoluminescence of Hexagonal Boron Nitride. *Phys. Rev. B - Condens. Matter Mater. Phys.* **2008**. https://doi.org/10.1103/PhysRevB.78.155204.

(34) Alem, N.; Erni, R.; Kisielowski, C.; Rossell, M. D.; Gannett, W.; Zettl, A. Atomically Thin Hexagonal Boron Nitride Probed by Ultrahigh-Resolution Transmission Electron Microscopy. *Phys. Rev. B - Condens. Matter Mater. Phys.* **2009**. https://doi.org/10.1103/PhysRevB.80.155425.

(35) Alem, N.; Yazyev, O. V.; Kisielowski, C.; Denes, P.; Dahmen, U.; Hartel, P.; Haider, M.; Bischoff, M.; Jiang, B.; Louie, S. G.; Zettl, A. Probing the Out-of-Plane Distortion of Single Point Defects in Atomically Thin Hexagonal Boron Nitride at the Picometer Scale. *Phys. Rev. Lett.* **2011**. https://doi.org/10.1103/PhysRevLett.106.126102.

(36) Velasco, J.; Lee, J.; Wong, D.; Kahn, S.; Tsai, H. Z.; Costello, J.; Umeda, T.; Taniguchi, T.; Watanabe, K.; Zettl, A.; Wang, F.; Crommie, M. F. Visualization and Control of Single-Electron Charging in Bilayer Graphene Quantum Dots. *Nano Lett.* **2018**. https://doi.org/10.1021/acs.nanolett.8b01972.

(37) Frenkel, J. On Pre-Breakdown Phenomena in Insulators and Electronic Semi-Conductors. *Phys. Rev.* **1938**, *54* (8), 647–648. https://doi.org/10.1103/PhysRev.54.647.

(38) Zeghbroeck, B. Van. *Principles of Semiconductor Devices and Heterojunctions*; 2009.

(39) Chang, C. Y.; Hsu, W. C.; Wang, S. J.; Hau, S. S. Capture-Emission Process in Double Poole-Frenkel Well Traps: Theory and Experiments. *J. Appl. Phys.* **1986**. https://doi.org/10.1063/1.337395.

(40) Zaidi, M. A.; Bourgoin, J. C.; Maaref, H. Poole-Frenkel-Assisted Emission from Deep Levels in Electron-Irradiated Germanium. *Semicond. Sci. Technol.* **1989**. https://doi.org/10.1088/0268-1242/4/9/006.

(41) Girolami, M.; Bellucci, A.; Calvani, P.; Flammini, R.; Trucchi, D. M. Radiation-Assisted Frenkel-Poole Transport in Single-Crystal Diamond. *Appl. Phys. Lett.* **2013**. https://doi.org/10.1063/1.4818904.

(42) Oh, T. Poole-Frenkel Behavior in Amorphous Oxide Thin-Film Transistors Prepared on SiOC. *J. Korean Phys. Soc.* **2014**. https://doi.org/10.3938/jkps.64.1519.

(43) Schroeder, H. Poole-Frenkel-Effect as Dominating Current Mechanism in Thin Oxide Films - An Illusion?! *J. Appl. Phys.* **2015**. https://doi.org/10.1063/1.4921949.

(44) Ganichev, S. D.; Prettl, W.; Yassievich, I. N. Deep Impurity-Center Ionization by Far-Infrared Radiation. *Phys. Solid State* **1997**. https://doi.org/10.1134/1.1130157.

(45) Greenaway, M. T.; Vdovin, E. E.; Ghazaryan, D.; Misra, A.; Mishchenko, A.; Cao, Y.; Wang, Z.; Wallbank, J. R.; Holwill, M.; Khanin, Y. N.; Morozov, S. V.; Watanabe, K.; Taniguchi, T.; Makarovsky, O.; Fromhold, T. M.; Patanè, A.; Geim, A. K.; Fal'ko, V. I.; Novoselov, K. S.; Eaves, L. Tunnel Spectroscopy of Localised Electronic States in Hexagonal Boron Nitride. *Commun. Phys.* **2018**. https://doi.org/10.1038/s42005-018-0097-1.

(46) Joucken, F.; Avila, J.; Ge, Z.; Quezada-Lopez, E. A.; Yi, H.; Le Goff, R.; Baudin, E.; Davenport, J. L.; Watanabe, K.; Taniguchi, T.; Asensio, M. C.; Velasco, J. Visualizing the Effect of an Electrostatic Gate with Angle-Resolved Photoemission Spectroscopy. *Nano Lett.* **2019**. https://doi.org/10.1021/acs.nanolett.9b00649.

(47) Nguyen, P. V.; Teutsch, N. C.; Wilson, N. P.; Kahn, J.; Xia, X.; Graham, A. J.; Kandyba, V.; Giampietri, A.; Barinov, A.; Constantinescu, G. C.; Yeung, N.; Hine, N. D. M.; Xu, X.; Cobden, D. H.; Wilson, N. R. Visualizing Electrostatic Gating Effects in Two-Dimensional Heterostructures. *Nature* **2019**. https://doi.org/10.1038/s41586-019-1402-1.

(48) Cadore, A. R.; Mania, E.; Watanabe, K.; Taniguchi, T.; Lacerda, R. G.; Campos, L. C. Thermally Activated Hysteresis in High Quality Graphene/ *h* -

BN Devices. *Appl. Phys. Lett.* **2016**, *108* (23), 233101. https://doi.org/10.1063/1.4953162.

(49) Šiškins, M.; Mullan, C.; Son, S. K.; Yin, J.; Watanabe, K.; Taniguchi, T.; Ghazaryan, D.; Novoselov, K. S.; Mishchenko, A. High-Temperature Electronic Devices Enabled by HBN-Encapsulated Graphene. *Appl. Phys. Lett.* **2019**. https://doi.org/10.1063/1.5088587.

(50) Noh, G.; Choi, D.; Kim, J. H.; Im, D. G.; Kim, Y. H.; Seo, H.; Lee, J. Stark Tuning of Single-Photon Emitters in Hexagonal Boron Nitride. *Nano Lett.* **2018**. https://doi.org/10.1021/acs.nanolett.8b01030.

(51) Vogl, T.; Campbell, G.; Buchler, B. C.; Lu, Y.; Lam, P. K. Fabrication and Deterministic Transfer of High-Quality Quantum Emitters in Hexagonal Boron Nitride. *ACS Photonics* **2018**. https://doi.org/10.1021/acsphotonics.8b00127.

(52) Ziegler, J.; Klaiss, R.; Blaikie, A.; Miller, D.; Horowitz, V. R.; Alemán, B. J. Deterministic Quantum Emitter Formation in Hexagonal Boron Nitride via Controlled Edge Creation. *Nano Lett.* **2019**. https://doi.org/10.1021/acs.nanolett.9b00357.

Chapter 6 - Comprehensive Electrostatic Modeling of Exposed Quantum Dots in Graphene/Hexagonal Boron Nitride Heterostructures

6.1 Introduction

Recent experimental advancements have enabled the creation of tunable localized electrostatic potentials in graphene/hexagonal boron nitride (hBN) heterostructures without concealing the graphene surface.[1–6] These potentials corral graphene electrons yielding systems akin to electrostatically defined quantum dots (QDs). Spectroscopic characterization of these exposed QDs with the scanning tunneling microscope (STM) has revealed intriguing resonances that are consistent with a tunneling probability of 100% across the QD walls. This effect, known as Klein tunneling, is emblematic of relativistic particles, underscoring the uniqueness of these graphene QDs. Despite the advancements with electrostatically defined graphene QDs, a complete understanding of their spectroscopic features still remains elusive. In this chapter, we address this lapse in knowledge by comprehensively considering the electrostatic environment of exposed graphene QDs. We then implement these considerations into tight binding calculations to enable simulations of the graphene QD local density of states. We find that the inclusion of the STM tip's electrostatics in conjunction with that of the underlying hBN charges reproduces all of the experimentally resolved spectroscopic features. Our work provides an effective approach for modeling the electrostatics of exposed graphene QDs. The methods

discussed here can be applied to other electrostatically defined QD systems that have exposed surfaces.

6.2 Scanning Tunneling Spectroscopy on MLG

Before discussing the creation and characterization of QD-like circular *p-n* junctions in MLG, we first need to understand MLG's tunneling spectroscopic features as acquired by an STM. As discussed in Ch. 3, scanning tunneling spectroscopy (STS) probes a sample's surface local density of states (LDOS) if we assume a tip with constant density of states and energy independent tunneling matrix elements [see expression (3.16)]. STS is a surface sensitive probe and, conveniently, graphene is a "surface-only" material due to its true 2D nature. Thus, with STS we acquire a dI/dV_S signal that is proportional to graphene's "bulk" LDOS. This complementary relation makes STS an ideal probe for graphene's electronic properties. However, the tunneling picture described in Fig. 3.2.3b needs to be modified to account for the large in-plane momentum of graphene's charge carriers around the K and K' points as calculated in section 2.3.

6.2.1 Inelastic and elastic tunneling processes

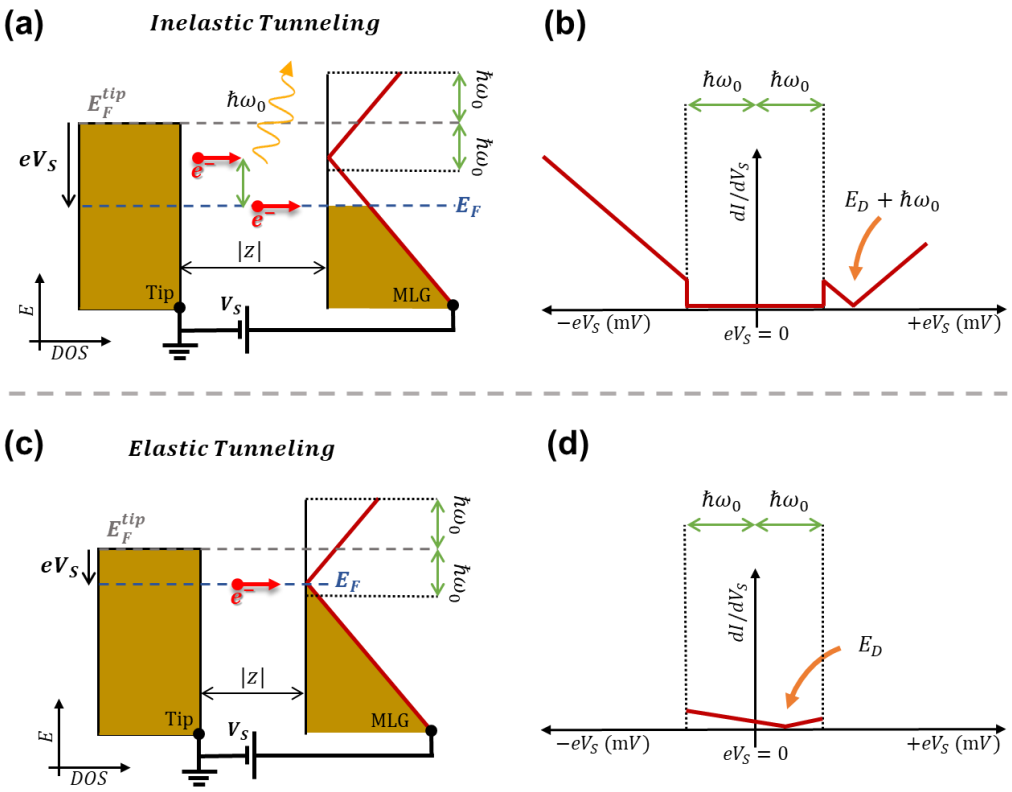

Figure 6.1| Diagrams showing tunneling between an STM tip and MLG in the *inelastic* and *elastic* regimes. (a) Inelastic tunneling of an electron from an STM tip into *p*-doped MLG while applying a bias voltage V_S, such that $|eV_S| > \hbar\omega_0$. In this regime, an electron scatters to a low energy state in MLG by releasing a phonon with energy $\hbar\omega_0$. **(b)** Expected tunneling spectroscopy response of MLG in the inelastic regime. **(c)** Elastic tunneling of an electron from an STM tip into *p*-doped MLG while applying a bias voltage V_S, such that $|eV_S| < \hbar\omega_0$. In this regime, an electron tunnels into a low energy state in MLG of the same energy. **(d)** Expected tunneling spectroscopy response of MLG in the elastic regime.

In Ch. 3 we obtained the following dependence of the tunneling current I on 2D Bloch states tunneling into a spherical tip:

$$I \propto \exp\left(-2\left(\lambda^2 + k_{\parallel}^2\right)^{1/2}|z|\right) \tag{6.1}$$

where λ is the decay factor of the onsite atomic orbitals, $k_{\parallel}$ is the in-plane momentum of the crystal Bloch states, and $|z|$ is the tip-to-sample distance. From this result it is evident that states with large in-plane momentum $k_{\parallel}$ decay rapidly in the vacuum and thus contribute much less to the tunneling current I. Charge carriers in graphene reside near the corners of the Brillouin zone and thus have large in-plane momentum ($\sim 1.7\ \text{Å}^{-1}$). However, graphene has an optical phonon at the K and K' points[7,8] with energy $\hbar\omega_0 \sim 67\ meV$, where ω_0 is the phonon's vibrational frequency. This phonon mode corresponds to out-of-plane vibrations in graphene's lattice and enables charge carriers from graphene's σ^*-band at the Γ point (where $k_{\parallel} = 0$) to scatter into the K point by releasing a K' phonon.[9] In other words, this process can be described as an electron that starts with only initial potential energy, gains momentum by scattering off MLG's lattice, and ends with residual potential energy which is diminished by the energy lost to making MLG's lattice vibrate. Since this process involves the loss of potential energy to vibrational energy it is described as *inelastic*. As a consequence, through this inelastic process, charge carriers with momentum $k_{\parallel} = 0$ are the primary contributors to the tunneling current observed in MLG and BLG.

The schematic in Fig. 6.1a depicts the tunneling process between the STM tip and MLG via the inelastic tunneling process described above. In graphene, inelastic tunneling occurs when electrons with zero momentum have enough energy to scatter into the K and K' points by releasing a phonon, i.e. $|eV_S| > \hbar\omega_0$. In Fig. 6.1a, this process is depicted by an electron with energy at the Dirac point releasing a phonon with energy $\hbar\omega_0$ and tunneling into the highest unoccupied MLG state. The release of

energy via the electron-phonon scattering manifest as a $2\hbar\omega_0$ wide suppression around $V_S = 0$ in the differential conductance (dI/dV_S) signal obtained during STS (see Fig. 6.1b). We refer to this dI/dV_S suppression region as the "phonon gap".[9] Additionally, spectroscopic features from MLG's DOS such as the Dirac point E_D, appear shifted by $+\hbar\omega_0$ and $-\hbar\omega_0$ to the right and left of the phonon gap, respectively.

The use of hBN as a substrate for graphene provides the mechanical stability not accessible to previous STS studies that used SiO_2 substrates.[9,10] This mechanical stability enables us to reduce the distance between the tip and graphene's surface in order to access MLG states within the *elastic* tunneling regime.[11] As indicated in (6.1), the rapid decay of large $k_\parallel$ states in MLG can be counteracted by reducing the tip-to-sample distance $|z|$. The schematic in Fig. 6.1c depicts the tunneling process in the elastic regime, $|eV_S| < \hbar\omega_0$. In this regime, probing of MLG's electronic features leads to finite values for dI/dV_S inside the phonon gap. Generally, the suppression of the dI/dV_S signal inside the phonon gap does not enable a clear observation of the Dirac point E_D, as depicted in Fig. 6.1c. However, in section 6.4 we will probe pseudo-confined states of circular *p-n* junctions that display clear resonances inside the phonon gap.

6.2.2 STS on backgated MLG

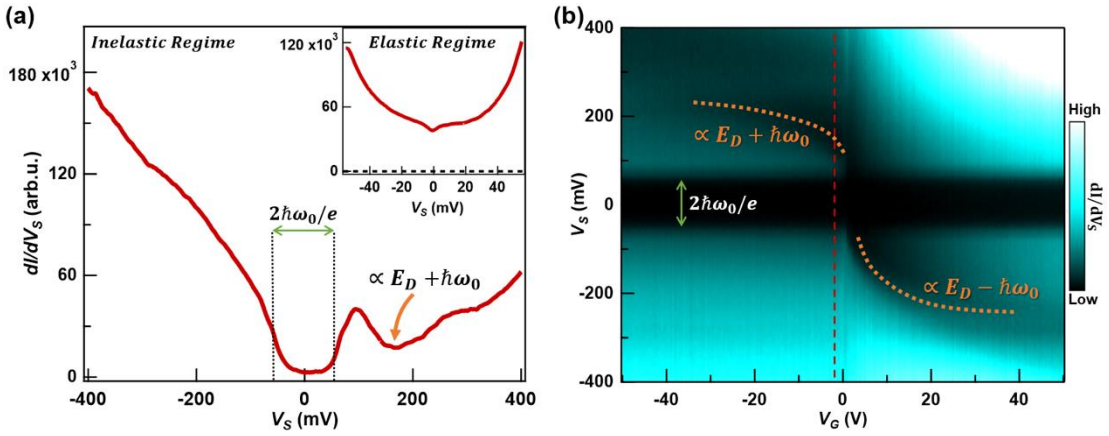

Figure 6.2| Tunneling spectroscopy and backgate-tunability of MLG. (a) Differential conductance $dI/dV_S(V_S)$ of MLG in the inelastic regime showing the $2\hbar\omega_0$ wide suppression centered at $V_S = 0$ and dip due to the Dirac point (E_D) as indicated in Fig. 6.1b. Tunneling parameters: $V_S = -500$ mV; $I = 1$ nA; $V_{ac} = 2$ mV; $f_{ac} = 400$ Hz. Inset: $dI/dV_S(V_S)$ of MLG in the elastic regime showing finite differential conductance. Tunneling parameters: $V_S = -55$ mV; $I = 1$ nA; $V_{ac} = 1.5$ mV; $f_{ac} = 400$ Hz. **(b)** $dI/dV_S(V_S)$ spectra of MLG stacked horizontally for different values of V_G. The V_G-independent suppression due to electron-phonon coupling appears as a dark band centered at $V_S = 0$. The inverted "S" suppression traced by the dashed orange curves corresponds to the shifted Dirac point E_D of MLG that changes with the backgate as $\sqrt{|V_G|}$.

After gaining some familiarity with the elastic and inelastic tunneling processes, we are equipped to discuss the backgate tunability of MLG as characterized by STS. First, in Fig. 6.2a we show an experimentally acquired dI/dV_S curve as a function of sample bias (V_S) for p-doped graphene. This spectrum was acquired by sweeping V_S starting from $V_S = -500$ mV and using a setpoint tunneling current of $I = 1$ nA. This curve displays the primary features depicted in Fig. 6.1b: (1) a dip in conductance corresponding to the shifted Dirac point energy (orange arrow) and (2) a clear dI/dV_S suppression of width ~130 mV centered at $V_S = 0$. The fact that the K

point phonons have energy $\hbar\omega_0 \sim 67$ meV verifies this suppression to be the aforementioned phonon gap. Additionally, we are able to probe MLG's states inside the phonon gap, i.e. in the elastic regime. The inset of Fig. 6.2a shows a dI/dV_S close-up acquired by sweeping V_S starting from $V_S = -55$ mV and using a setpoint tunneling current of $I = 1$ nA. This smaller starting V_S value translates to a $\sim 30\%$ shorter tip-to-sample distance during the STS measurement,[9,11–13] which enhances the tunneling contribution from large $k_{\parallel}$ states. Additionally, from the inset in Fig. 6.2a we see that the dI/dV_S signal within the elastic regime does not completely bottom at zero dI/dV_S. The ability to maintain a stable and finite conductance inside the phonon gap (unlike conventional semiconductors)[14–17] indicates that it does not originate from an electronic bandgap.

The spectrum in Fig. 6.2a was obtained after *p*-doping graphene using a backgate voltage V_G to bring the Dirac point outside of the phonon gap. We can further exploit the gate tunability provided by graphene's 2D nature and map the dependence of tunneling spectra on a variable backgate V_G. In Fig. 6.2b we show a plot where dI/dV_S spectra taken at different V_G have been stacked along the x-axis with bright and dark regions representing high and low values of dI/dV_S intensity, respectively. The application of V_G enables the tunability of the charge carrier density n in graphene. As we saw in Ch. 5, modelling the backgate and graphene as a parallel plate capacitor leads to $n \propto V_G$. Additionally, graphene's linear density of states[18] leads to $n \propto |E|^2$. Thus, we expect that the applied backgate V_G and the Fermi energy E_F in graphene will follow the relation:

$$E_F \propto \mathrm{sgn}[V_G] \times \sqrt{|V_G|} \tag{6.2}$$

This result confirms that the dI/dV_S suppression in Fig. 6.2b corresponds to a DOS feature in MLG that changes along with E_F—namely the Dirac point E_D. In Fig. 6.2b we account for the shifts introduced by the inelastic tunneling process by indicating that the actual energies for E_D need to be shifted by $\hbar\omega_0$. Finally, the presence of the phonon gap across all V_G values, further confirms that the origin of this feature is not from graphene's band structure.

In section 6.2.2, we will approximate the charge carrier density induced by the STM tip on graphene by looking closely at a $dI/dV_S(V_G, V_S)$ plot that displays tip-induced charging features due to charge carrier pseudo-confinement in MLG. These features originate from a secondary tunneling channel not visible on plots with wide V_G and V_S ranges like the one shown in Fig. 6.2b. First, however, we will motivate and discuss the background of charge carrier confinement in MLG.

6.3 Overview of Confinement and Pseudo-Confinement in MLG

The endeavor to corral graphene's massless Dirac fermions has led to the development of multiple techniques and novel procedures for charge carrier confinement. These techniques include the use of lithographic patterning,[19–22] ultra-high vacuum chemical synthesis,[23–26] controlled deposition of adatoms,[27] and the application of perpendicular magnetic fields.[28–30] However, such techniques require either complicated fabrication procedures or rely on rigid material synthesis schemes.

Recently, a flexible procedure was developed to corral graphene charges that employs an STM and a graphene/ hBN heterostructure.[1,31] This procedure works by using an STM tip to locally induce charges in the underlying hBN, thus creating persistent and embedded local gates in the hBN by a similar mechanism to that explored in Ch. 5. These local gates enable the pseudo-confinement of electrons in an exposed circular *p-n* junction, which effectively behaves as a quantum dot (QD).[1] Such QDs have been used to develop novel electronic devices such as Berry phase switches[4] and enabled the unprecedented visualization of correlated relativistic charges under large magnetic fields.[5] Despite the widespread progress on these exposed graphene QDs, their spatially resolved spectroscopic characterization still remains not well understood.

An important commonality in the existing works on exposed graphene QDs is that the influence of the STM tip has been excluded in the theoretical modeling of QD states. This is despite several experiments that show the STM tip itself can induce a small QD,[2] and even create coulomb-like confinement.[3] In this chapter, we address the influence of the STM tip on exposed graphene QDs by comparing our visualization of QD states with tight-binding (TB) calculations that include the electrostatics of the STM tip and underlying charged hBN. Our results demonstrate that accounting for the influence of the STM tip is necessary to reproduce key features seen in the experimental data. Additionally, we use the insight from our study to show how the tip's influence can be mitigated.

6.4 MLG Quantum Dot Creation Using STM

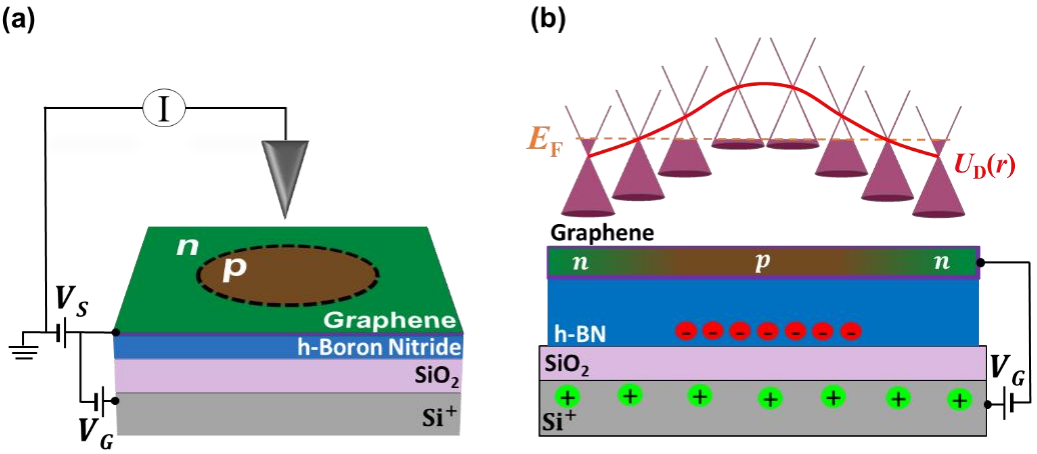

Figure 6.3| Schematic layout of characterization and potential of an exposed graphene Quantum Dot (QD). (a) Schematic showing the STM circuit and graphene/hBN heterostructure. The circular *p*-doped region outlines the QD created by applying a V_S pulse between the tip and graphene/hBN while holding V_G constant. **(b)** Top: $U_D(r)$ (red curve) is the potential of the QD which is outlined by tracing along the Dirac point in each cone. Bottom: Side-view schematic of the QD in a graphene/hBN heterostructure for $V_G > 0$. The application of a high electric field by the STM tip induces a localized net charge accumulation after exciting defects in hBN.[32] Applying V_G with opposite polarity to charges in hBN induces the spatial variation in doping on graphene which forms the QD boundaries.

The experiments we present here were performed on heterostructures composed of graphene on hBN resting on a SiO_2/*p*-doped Si (Si^+) substrate as depicted in Fig. 6.3a. The graphene/hBN heterostructure was assembled using a standard polymer-based transfer technique.[33] Following this assembly, the surface of graphene was cleared of debris and polymer residue using an atomic force microscope while in contact mode[34] as discussed in Ch. 4. We perform this step to ensure the absence of

contaminants that could affect the electronic properties of our QDs. The creation and characterization of graphene QDs were performed at 4.8 K.

Figure 6.3a shows a schematic of the STM circuit used. V_S is applied between graphene and the grounded STM tip to induce a tunneling current between them and enable probing of electronic states. V_G is connected to Si^+ to remotely tune graphene's Fermi level (E_F). We use these control voltages to create a graphene QD by applying a V_S pulse between graphene and the STM tip while maintaining V_G at a constant value.[1,4–6,31,35] For detailed steps on this tip pulsing process see the Appendix section. During the application of this pulse, defects in hBN underneath the tip become ionized with opposite polarity to V_G. The end result of this process is depicted in Fig. 6.3b for the case where $V_G > 0$. At a fixed positive value of V_G, graphene becomes globally *n*-doped except for the circular region where the pulse was applied. In this region, an excess of negative charges embedded in the hBN act as a local backgate that *p*-dopes graphene. The resulting spatial variation of the Dirac point in graphene with respect to E_F (dashed orange line) gives rise to a smooth electrostatic potential $U_D(r)$. A profile of this electrostatic potential is outlined in Fig. 6.3b (red curve) and specifies the boundary of the exposed graphene QD.

6.5 MLG Quantum Dot Characterization Using STM

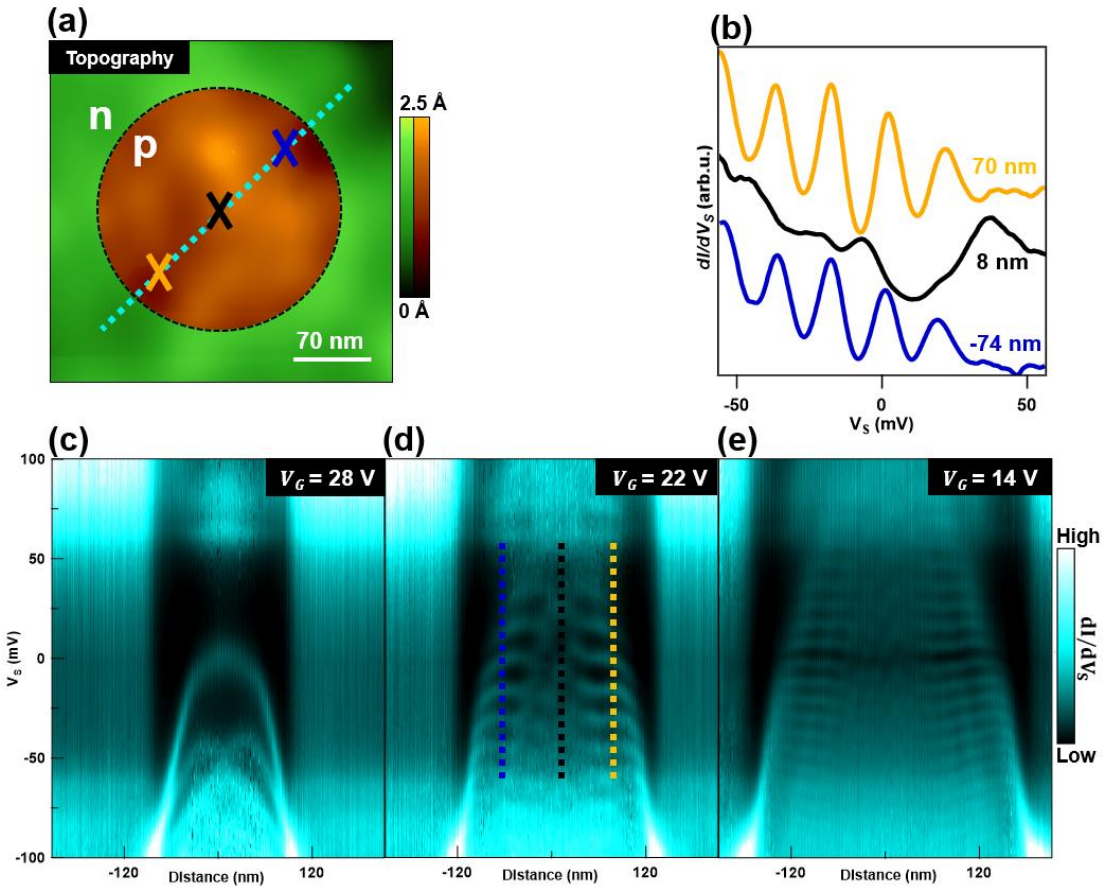

Figure 6.4| Scanning Tunneling Spectroscopy (STS) of an exposed graphene QD. (a) Topography of graphene acquired by STM. Regions where graphene is *n* and *p*-doped are indicated with green and brown color scales respectively. **(b)** $dI/dV_S(V_S)$ spectra obtained at the corresponding crosses indicated in (a). Each spectrum is offset for clarity and was taken with $V_G = 22$ V. **(c-e)** Spatial dependence of dI/dV_S spectra with different V_G values indicated in each panel. These images map the spatial dependence of graphene QD states obtained along the dashed cyan line in (a). Dashed vertical lines in (d) correspond to spectra displayed in (b). Tunneling parameters: $V_S = -100$ mV; $I = 1$ nA; $V_{ac} = 2$ mV; $f_{ac} = 400$ Hz.

To map and visualize the electronic properties of the states in the exposed graphene QD, we use scanning tunneling microscopy (STM) and spectroscopy (STS). Figure 6.4a shows an STM topographic map of graphene's ultra-flat surface after the

creation of a QD. For the case where $V_G > 0$, the approximate regions where graphene is p and n-doped have been colored brown and green, respectively. With STS we can obtain the differential conductance (dI/dV_S) at a specific point on graphene underneath the STM tip. From the tunneling theory discussion in Ch. 3, we recall that this dI/dV_S signal is proportional to graphene's LDOS.[36,37] By performing this measurement at different points within the QD, we reveal the coarse spatial dependence of the QD states. In Fig. 6.4b we plot dI/dV_S as a function of V_S taken at the center (black curve) and boundaries (blue and orange curves) of the QD at points corresponding to the colored crosses in Fig. 6.4a. These curves clearly display differences between the signals recovered at the center and edges of the QD. At the edges, the dI/dV_S curves have prominent peaks while at the center, these peaks are suppressed and broadened.

To attain a more comprehensive understanding of the spatial dependence of the exposed graphene QD's LDOS, we obtain $dI/dV_S(V_S)$ curves at multiple points along the dashed cyan line in Fig. 6.4a. Figures 6.4c-e show the compiled $dI/dV_S(V_S)$ curves plotted as a function of distance, where the origin is defined at the center of the graphene QD. Additionally, each of these image plots are taken at different values of V_G which offsets the global graphene doping. Following the schematic in Fig. 6.3b, as V_G changes, E_F also changes relative to the QD's potential $U_D(r)$. For Fig. 6.4c, E_F is near the top of the potential $U_D(r)$ which creates a shallow QD. From the image plots in Figs. 6.4d-e, it is apparent that as V_G decreases (hole density increases), the QD gains depth and width as the difference between E_F and $U_D(r)$ increases. Finally, we note that signal contributions from the inelastic tunneling channel discussed previously may

be ignored since we probe graphene's LDOS primarily inside the phonon gap. In fact, the image plots in Fig. 6.4c-e clearly display the outer regions of the phonon gap ($|V_S| > 67$ mV) where some resonant states replicas can be observed.

The patterns and features observed in Figs. 6.4b-e can be explained by considering the behavior of massless Dirac fermions corralled within a circular and harmonic electrostatic potential. From our discussion in Ch. 2 regarding Klein tunneling, recall that a *p*-*n* junction on graphene perfectly transmits quasiparticles at normal incidence to the junction but reflects them at larger incident angles.[38–40] We note that the *p*-*n* junction we have created has a smoothly varying profile, unlike the sharp profile discussed in section 2.3.2. In the case of a smoothly varying potential, incident charge carriers deflect their trajectories as they move through the *p*-to-*n* transition region.[41,42] This leads to a narrower transmission probability which means that charges require a smaller incident angle θ_i to achieve total internal reflection (see Fig. 2.3.3b). Therefore, in a circular potential, electrons with high enough angular momentum have oblique incidence with the barrier and become internally reflected. This leads to partial charge carrier trapping and the formation of quasibound states[43–47] with pronounced intensities near the boundary of the circular potential, in agreement with Fig. 6.4b. Additionally, in Fig. 6.4b we also see evidence of the internal reflection due to Klein tunneling. This can be seen in the manifestation of differing peak widths between the dI/dV_S curve taken at the QD's center and curves taken at the QD's edges. As electrons with high angular momenta get trapped near the edges, these states exhibit longer trapping times and thus narrower spectroscopic peaks.[1,2] Moreover, the bright

nodal features in Figs 6.4c-e can be attributed to the eigenstates of the exposed graphene QD.[1] The profile of the confinement potential in this QD is parabolic, akin to that of a harmonic oscillator. However, unlike Schrödinger fermions in a harmonic potential, these nodal patterns are unevenly spaced in energy. Instead, the nodal patterns formed by these massless Dirac fermions become more closely packed as V_S decreases (see. Fig. 6.4d).[1,2,45–47]

In addition to the well understood features described above, there are some features that lack explanation. For example, all three of the plots in Figs. 6.4c-e show a bright skirt-like feature around the edges of the QD ($\sim V_S = -100$ mV). A clear downward bending of the QD states is also visible near the QD boundaries for all values of V_G. This bending effect is particularly pronounced in Fig. 6.4c, where the strong distortion of states creates an envelope-like feature. As we will soon show, these features can be reproduced after comprehensive consideration of the QD electrostatic environment.

6.6 Electrostatic Modeling of Exposed Graphene QDs

To study the effect of the STM tip on the exposed graphene QDs, we use simplified electrostatics and a numerical tight binding model. We first discuss our considerations for the electrostatics. In our experiments, spatial variations in doping across graphene originate from localized hBN defect charges (see Fig. 6.3b) and inadvertent gating from the STM tip. To a first approximation, the localized hBN defect charges will create a fixed spatially varying doping profile. On the other hand, the STM tip will create a mobile spatially varying doping profile that changes its influence as the STM tip's position changes. An exact solution for the charge density in graphene would require inaccessible experimental parameters such as the spatial distribution of hBN defect charges as well as the *in-situ* STM tip's geometry. We proceed by making a set of simple approximations for the doping profiles due to the hBN defects and the geometry of the STM tip.

6.6.1 Extracting the QD potential due to charged hBN defects

We first focus on the doping profile due to charged defects in the underlying hBN. The electrostatic potential profile of a graphene QD can be extracted by tracking the spatial evolution of the region with reduced dI/dV_S intensity. This region corresponds to the spatially varying Dirac point and can be seen in a measurement similar to those shown in Figs. 6.4c-e. Figure 6.5a shows an example of an extracted potential profile $U_D(r)$ (red curve). $U_D(r)$ is then converted to a doping profile $n(r)$ by the relation:

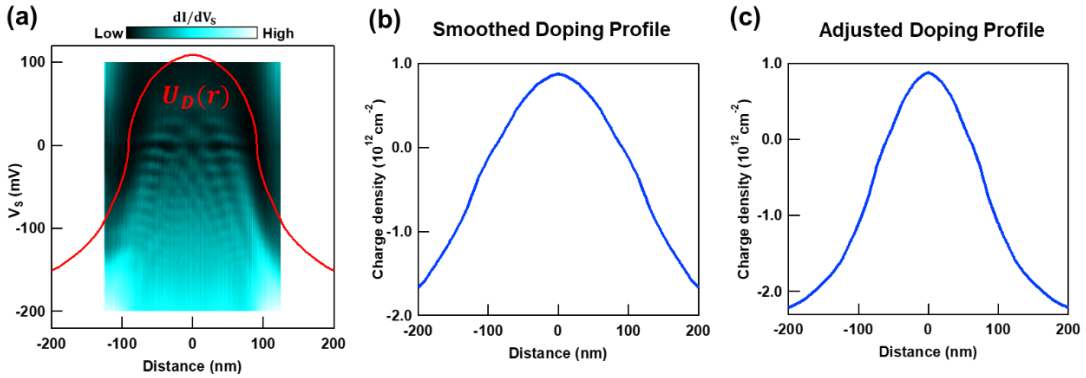

Figure 6.5| Charge density profile induced on graphene by charged hBN defects. **(a)** Experimentally approximated QD potential profile. The underlying 2D plot shows the spatial dependence of QD states (similar to Figs. 6.4c-e). The red line (same as $U_D(r)$ in Fig. 6.3b) represents the extracted potential profile of the graphene QD. **(b)** QD's charge density profile converted and smoothed from the extracted potential profile in (a). **(c)** QD's charge density profile used in our tight binding (TB) calculation after adjustment. This profile's x-axis is reduced to 65% of the profile in (b) to account for the widening effect of the tip-induced electrostatic potential.

$$n(r) = \mathrm{sgn}[U_D(r)] * \frac{U_D(r)^2}{\hbar^2 v_F^2 \pi} \tag{6.3}$$

with $v_F = 1 \times 10^6$ m/s, where $U_D(r)$ replaces the energy term.[48] The resulting plot after smoothing is shown in Fig. 6.5b. We note that the STM data in Fig 6.5a, which is the source of our estimate for the hBN defect potential, necessarily includes the effect of the STM tip. To remove this effect so that we may treat it separately, we preemptively reduce the lateral extent of the potential profile in Fig. 6.5b to 65% while leaving the energy scale unchanged. The resulting adjusted charge density profile is shown in Fig. 6.5c. The similarities displayed by our final simulated (Fig. 6.8) and experimental (Fig. 6.4c-e) results will validate the lateral reduction of the hBN defect potential we applied here.

6.6.2 Approximating the STM tip's top gating effect on MLG

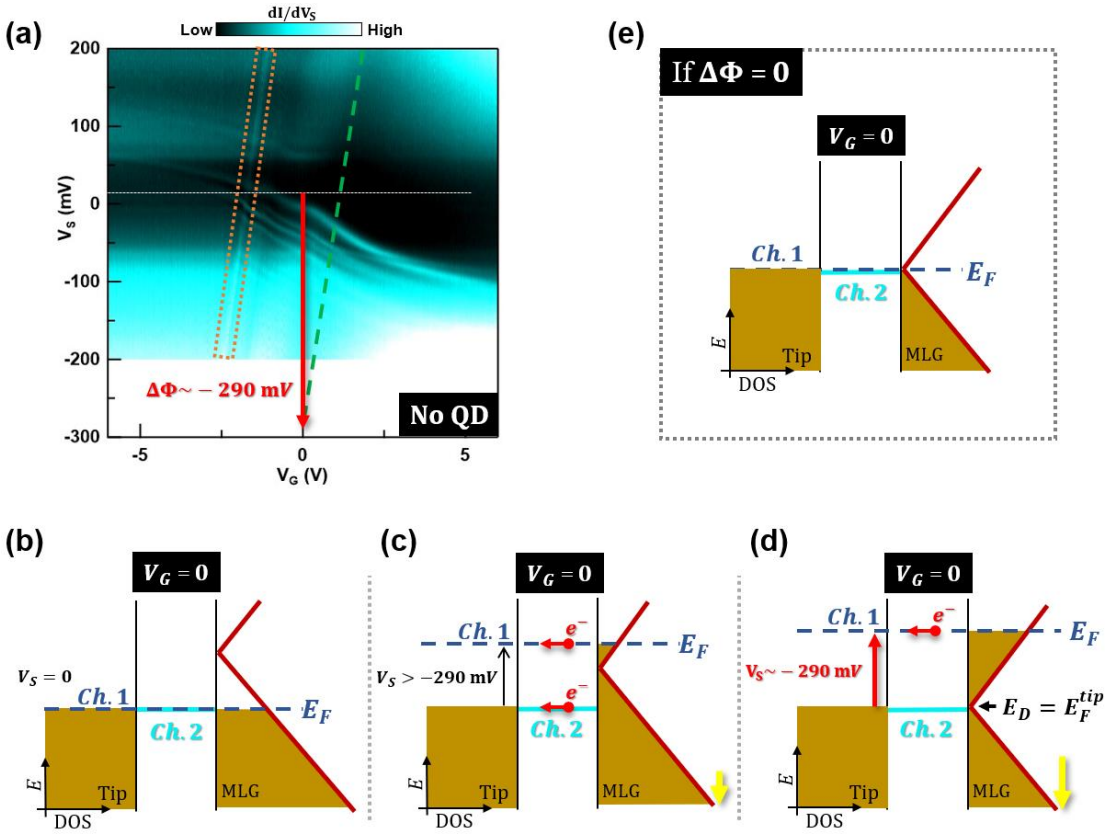

Figure 6.6| Estimate of the work function mismatch between the STM tip and MLG. (a) Experimentally determined $dI/dV_S(V_S, V_G)$ on pristine graphene without a QD. This 2D plot is used to determine the magnitude of the STM tip's band shifting effect on graphene. The inverted "S" shaped features correspond to direct tunneling into tip-induced confined states. Diagonal features correspond to the charging of spectroscopic features as they coincide with the tip's Fermi level E_F^{tip}. Namely, the dashed orange box encloses a charging feature due to a tip-induce state and the green dashed line outlines a dI/dV_S suppression belonging to graphene's Dirac point E_D. The dashed white line indicates where $V_S = 0$. Tunneling parameters: $V_S = -0.2$ V; $I = 1$ nA; $V_{ac} = 2$ mV; $f_{ac} = 400$ Hz. **(b-d)** Tunneling diagrams highlighting the channels responsible for the features in (a) at $V_G = 0$. Both $Ch.1$ and $Ch.2$ contribute to the dI/dV_S signal when $0 > V_S > -290$ mV. The work function mismatch $\Delta\Phi$ is determined by tracking the dI/dV_S suppression in $Ch.2$ that occurs when $eV_S \sim \Delta\Phi$ in (d). **(e)** Hypothetical tunneling diagram if $\Delta\Phi = 0$ at $V_S = V_G = 0$.

Now that we have obtained the induced charge density profile on graphene due to the charged hBN defects alone, we proceed to estimate the induced charge profile due to the STM tip. In our experiments, we use a tip made of tungsten that is likely coated with gold (see Ch. 4). The differing materials (metals and graphene) in close proximity and the indeterminacy of the STM tip's shape lead to a finite work function mismatch ($\Delta\Phi$) between the STM tip and graphene. In the tunneling regime, the STM tip remains at a distance $\sim$7.5 Å from the graphene surface. Because of the finite $\Delta\Phi$, there is shift of the graphene bands even when V_S = 0 and V_G = 0. This effect is depicted in Fig. 6.6b. For $|\Delta\Phi| \gg |V_S|$, the polarity and intensity of the tip induced doping is dominated by $\Delta\Phi$. Therefore, in this regime we can acquire an estimate for the doping profile induced by the STM tip by obtaining an approximation of $\Delta\Phi$.

To get an estimate of $\Delta\Phi$ and ultimately the top gating effect of the STM tip, we measure and plot the dependence of dI/dV_S as function of V_S and V_G on pristine MLG prior to creating the QD (see Fig. 6.6a). As discussed in earlier sections, the resulting 2D image plot displays changes in the tunneling current between the tip and graphene as we vary their relative band alignments. In Fig. 6.6a we observe several confined states appearing as a result of the STM tip's local top gating effect.[2] As we vary V_S for different values of V_G we obtain a dI/dV_S signal that includes the contribution from two channels during the tunneling process, a common occurrence for low dimensional systems with low charge density.[49,50]

The tunneling schematics in Figs. 6.6b-d illustrate these two channels ($Ch.1$ and $Ch.2$) as V_S decreases to negative values. As a side note, when $V_S > 0$ the

conventions for $Ch.1$ and $Ch.2$ we discuss here need to be interchanged. For $V_S < 0$, the first channel ($Ch.1$) corresponds to the differential tunneling current between the topmost occupied states in graphene and unoccupied states in the STM tip at an energy determined by the sample bias V_S. Note, inelastic tunneling is present in $Ch.1$ but is ignored in the schematics for simplicity. From expression (6.2), LDOS features in MLG follow E_F with $\sqrt{|V_G|}$ dependence. Thus, tip-induced resonant states manifest as inverted "S"-shape fans[2] in $Ch.1$. These features are clearly visible in Fig. 6.6a. To obtain an estimate for $\Delta\Phi$, we focus on the second channel ($Ch.2$). As depicted in Fig. 6.6c, this channel corresponds to the differential tunneling current between the lowest unoccupied states of the STM tip and states in graphene at the same energy. Thus, inelastic tunneling does not contribute to the signal of $Ch.2$. Consequently, signal traces in $Ch.2$ will manifest as lines along which MLG retains a constant charge density n.[35,51] These lines have a finite slope due to the capacitive couplings in the tip-MLG and MLG-backgate system.[52] One such line appears in Fig. 6.6a enclosed by an orange box. This feature results from the charging of a tip-induced confined state as it aligns with the tip's Fermi level (E_F^{tip}).

Now that we have identified the origin of the tunneling features in Fig. 6.6a for different band alignment configurations, we are ready to obtain an estimate for $\Delta\Phi$. First, as depicted in Fig. 6.6e, we note that for pristine MLG and assuming $\Delta\Phi = 0$, the Dirac point E_D should cross the Fermi level E_F at $V_S = V_G = 0$. However, because $\Delta\Phi \neq 0$, E_D will be shifted away from E_F at $V_S = V_G = 0$ (see Fig. 6.6b). To this end, we find the value of V_S at which E_D crosses the tip's Fermi level $E_F^{tip} = E_F - eV_S$ at

$V_G = 0$ in $Ch.2$. In summary, applying this V_S voltage counters the STM tip's top gating effect due to $\Delta\Phi$ on the surface of graphene as depicted by the downward shift of MLG's DOS profile in Figs. 6.6b-d (see yellow arrows). In the absence of gating from below, finding this value for V_S allows us to estimate $\Delta\Phi$. Next, we follow the slope of the charging feature inside the orange box and trace a green dashed line with the same slope along the furthest dark fringe on the right (see Fig. 6.6a). The suppression of dI/dV_S along this dark fringe indicates where E_D crosses E_F^{tip} as depicted in Fig. 6.6d. Finally, we extend this green dashed line downward and find that it crosses $V_G = 0$ at $V_S \sim -290$ mV. We note that this value for V_S is greater in magnitude than the V_S range in our measurements (-100 mV $< V_S <$ 100 mV). Thus, we can reasonably assume that the effect of $\Delta\Phi$ dominates within the experimental V_S range we used to map the QD states.

6.6.3 Modeling the charge-induced profile on MLG by the STM tip

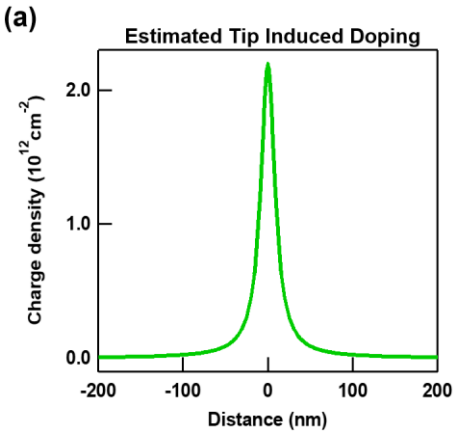

Figure 6.7| Determination of the charge density profile induced by the STM tip on MLG. (a) Charge density profile induced on graphene by the STM tip. The induced charge density intensity is extracted from the extrapolation in (a). The shape of this density profile is determined by assuming the tip to be a charged sphere with a radius of 80 nm.

Finally, with an estimate for the band shift of MLG due to $\Delta\Phi$, we can approximate the profile for the charge induced on graphene by the STM tip. If we assume the STM tip's apex and graphene act as a parallel plate capacitor with a 7.5 Å separation, then the $V_S \sim -290$ mV offset corresponds to a maximum tip induced charge density of $\sim 2.14 \times 10^{12}$ cm^{-2}. We calculated the shape of the tip's doping profile by using a standard Poisson solver where the tip is represented by a charged 80 nm radius sphere placed 7.5 Å away from a metal surface. The tip radius and distance to graphene that we used are both consistent with values found in the literature.[3,9,53] With this analysis we acquire the tip-induced doping profile shown in Fig. 6.7a.

6.6.4 Simulating the STM tip's effect on an exposed graphene QD

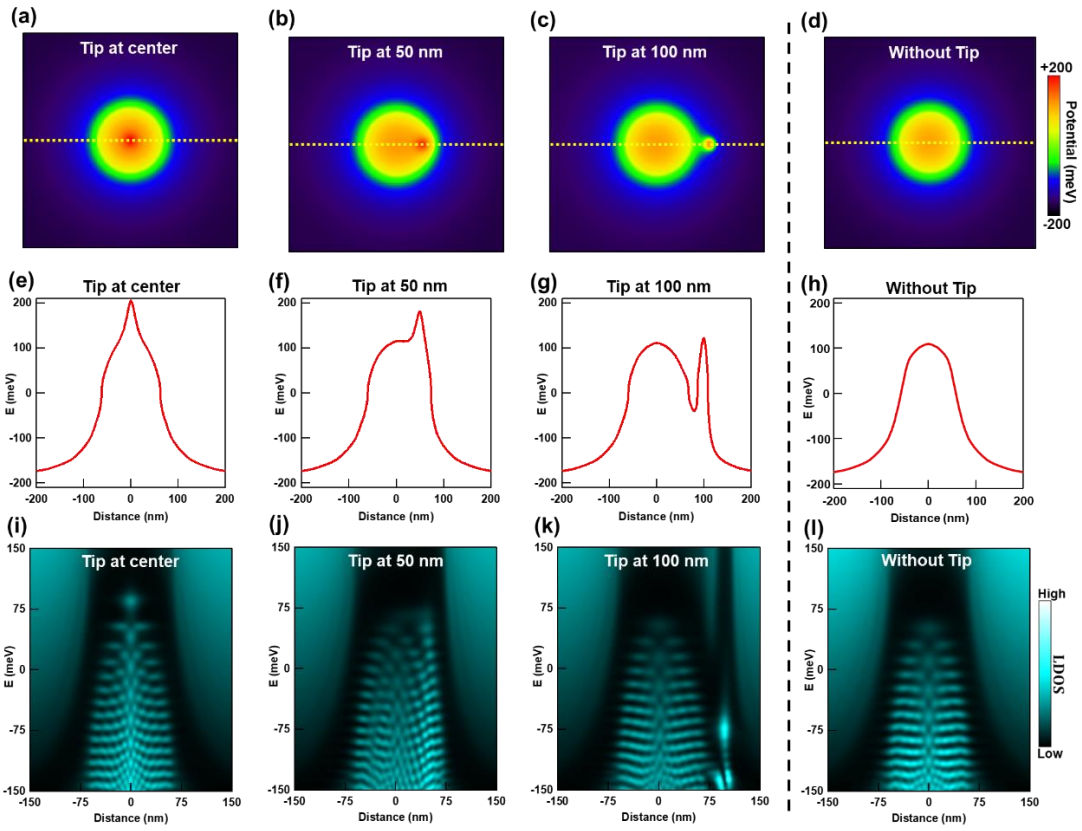

Figure 6.8| Simulation of the local density of states (LDOS) of an exposed graphene QD with an STM tip at a fixed position. (a-c) Spatial 2D map of graphene's Dirac point energy E_D with respect to E_F after adding the contributions from hBN defects (Fig. 6.5c) and the STM tip (Fig. 6.7a). The STM tip's location varies for each of these maps. **(d)** Spatial 2D map of the E_D with respect to E_F determined by only considering the contribution from hBN defects (Fig. 6.5c). **(e-h)** Respective potential profile line cuts along the yellow dashed lines in (a-d). **(i-l)** Calculated LDOS distributions for each corresponding potential map. These simulations reveal the effect of the STM tip on the QD states for tip positions placed at different distances from the QD's center.

We have thus far obtained approximations for the charge density profiles induced on graphene due to charged defects in the underlying hBN and the STM tip.

We proceed by adding these contributions and obtain a potential profile resulting from the summation of the induced charge densities. After adding the charge densities induced on graphene from Figs. 6.5c and 6.7a, we convert the resulting charge density $n(r)$ into a potential profile

$$U_D(r) = \mathrm{sgn}[n(r)] * \hbar v_F \sqrt{\pi |n(r)|} \tag{6.4}$$

Figures 6.8a-c show 2D maps of the potentials resulting from the cumulative charge densities of the hBN defects and STM tip. The color scale corresponds to the potential value, where red and blue indicate high and low values, respectively. Notably, each of the potential maps differ because the position of the tip changes between them. As a comparison, we also show a 2D potential map without the effect of the STM tip (Fig. 6.8d). When the STM tip is at the center (Fig. 6.8a) or 50 nm away from the center (Fig. 6.8b), the potential map has the highest value at the STM tip's location, as indicated by the red dot at the corresponding locations. Additionally, we plot line cuts of the potential maps in Figs. 6.8e-g. Here the QD's potential reveals a distorted profile with a prominent peak. For maps with the STM tip 100 nm away from the center (Fig. 6.8c), the potential profile has two separate peaks (Fig. 6.8g), effectively becoming an asymmetric double QD system.

We now discuss our numerical TB calculations, which use the potential profiles from Figs. 6.8a-d. These calculations allow us to simulate the QD's LDOS in the presence of a fixed STM tip. Figure 6.8i shows the calculated LDOS distribution of a graphene QD when the STM tip is fixed at the center. In this image we note several

distinct nodes that correspond to graphene QD states.[43–47] In Figs. 6.8j and 6.8k we show the calculated LDOS distributions when the STM tip is fixed 50 nm and 100 nm away from the QD's center. As a comparison we also show the calculated LDOS of a QD that excludes the effect of the STM tip (Fig. 6.8l). When the tip is fixed at the QD's center (Fig. 6.8i) or 50 nm away from the center (Fig. 6.8j), several new states with higher LDOS appear at the tip's location. We also note that the LDOS distribution and intensities away from the tip's location (in Figs. 6.8i-j) are similar to the calculated LDOS that excludes the tip's effect (Fig. 6.8l). When the tip is fixed 100 nm away from the QD's center, we observe a new state with a much higher LDOS at the tip's position (Fig. 6.8k). Similar to the previous cases, the LDOS distribution and intensities away from the tip's location remains unaffected.

6.6.5 Simulating spatial STS characterization of an exposed MLG QD

Now that we have demonstrated that graphene QD states are affected by an STM tip at a fixed position with our simulations, we study the case for a movable STM tip, which is more akin to our experiment. In measurements such as those shown in Figs. 6.4c-e, each vertical array of pixels in the image corresponds to a dI/dV_S curve acquired at the location of the STM tip. Consequently, to compare our experimental results with our simulations, we calculate the QD's LDOS with the STM tip located at each position along a line that crosses the QD. After obtaining the LDOS distribution from each profile (similar to those in Figs. 6.8e-g), we compile the individual dI/dV_S curves calculated specifically at the STM tip's location for each point within the QD

and along the line that crosses the QD. In Fig. 6.9a we show the result of this compilation process.

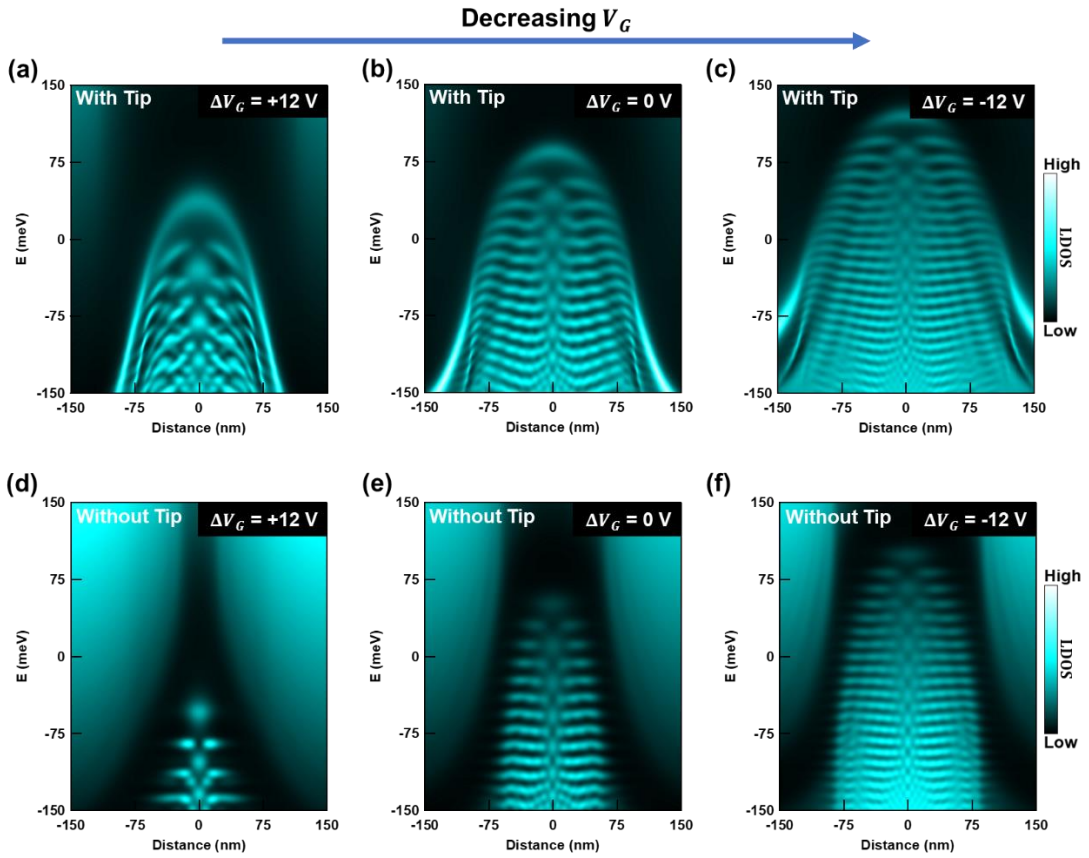

Figure 6.9| Simulation of the LDOS in a graphene QD with a moving STM tip for different V_G configurations. (a-c) Simulated LDOS spectra along a line that crosses the center of a graphene QD. This simulation includes the influence of the STM tip. The LDOS spectra at each position is calculated with the tip fixed at that location. **(d-f)** Simulated LDOS spectra along a line that crosses the center of the graphene QD without considering the effect of the STM tip. The potentials induced by hBN defects used in (a), (b), and (c) are the same as those used in (d), (e), and (f), respectively. By comparing our results that include the effect of the STM tip (a-c) with those that exclude it (d-f), we find that a comprehensive treatment of the QD electrostatic environment is necessary to achieve agreement between theory and the experimental results from Figs. 6.4c-e.

We now consider how varying V_G affects the QD states in our calculation. By changing V_G the global electron and hole densities in graphene are offset. We simulate this effect by shifting the charge density profile due to the hBN defects (see Fig. 6.5c). Specifically, this profile is shifted up to simulate an increase in hole density in graphene. Onto this shifted profile we add the unchanged STM tip's charge density profile (Fig. 6.7a) and perform the sequence of calculations as described for Fig. 6.9a. Figures 6.9b-c show the complete results for two additional simulated values of V_G.

To highlight the importance of the STM tip's influence on our exposed graphene QDs, we show LDOS calculations at different V_G values that omit the tip's presence (Figs. 6.9d–f). Clearly, by comparing these simulations with measurements from Figs. 6.4c–e and the simulations in Figs. 6.9a–c, it is evident that a tip-inclusive model achieves better agreement with our experimental results. Similar agreement can be seen with other experimental results as well.[1,4,5] Specifically, the model that omits the STM tip (Figs. 6.9d–f) lacks several key features from our experiment. For example, the deflection of states near the edges of the QD are missing in Figs. 6.9d–f, but the tip-inclusive model captures this feature consistently. In addition, we note that the presence of a continuous bright line that wraps around the edge of the QD's profile for higher V_G values is shared by the experiment (Fig. 6.4c) and the comprehensive model (Fig. 6.9a), but absent in the model that ignores the tip (Fig. 6.9a). Finally, for the graphene QD from the experiment we note that the QD states are less distorted at higher values of V_G, see for example Fig. 6.4e. This insightful trend is also displayed

in the comprehensive model indicating that the effect of the tip can be mitigated when a sufficiently large QD is achieved.

6.7 Conclusion

In conclusion, we showed that incorporating the STM tip's electrostatics in conjunction with that of the underlying hBN charges enables a more complete understanding of the experimental spectroscopic features of exposed graphene QDs. We compared experimental STM data obtained on graphene QDs with simulations that include the tip-induced potential as well as with simulations that neglect this potential. The agreement between experiments and simulations is greater when the simulations include the influence of the tip. In particular, the experimentally observed bright envelope of the potential and the deflection of states close to the QD edge are only reproduced when the tip-induced potential is included. Our results highlight the importance of considering the effect of the STM tip when interpreting spectroscopic characterization of exposed graphene QD states. Our analysis also reveals the intriguing possibility of studying the interplay between states confined by the potential due to hBN defects and the potential due to the STM tip (see Fig. 6.8k). Studies that seek to reduce such interplay may use insights from our simulations to mitigate the tip's effect by tuning V_G. Additionally, the interaction between these two QDs could potentially be used to emulate relativistic molecular behavior or other complex coupled QD systems.[6]

Chapter 6 - References

(1) Lee, J.; Wong, D.; Velasco, J.; Rodriguez-Nieva, J. F.; Kahn, S.; Tsai, H. Z.; Taniguchi, T.; Watanabe, K.; Zettl, A.; Wang, F.; Levitov, L. S.; Crommie, M. F. Imaging Electrostatically Confined Dirac Fermions in Graphene Quantum Dots. *Nat. Phys.* **2016**. https://doi.org/10.1038/nphys3805.

(2) Zhao, Y.; Wyrick, J.; Natterer, F. D.; Rodriguez-Nieva, J. F.; Lewandowski, C.; Watanabe, K.; Taniguchi, T.; Levitov, L. S.; Zhitenev, N. B.; Stroscio, J. A. Creating and Probing Electron Whispering-Gallery Modes in Graphene. *Science (80-.).* **2015**. https://doi.org/10.1126/science.aaa7469.

(3) Jiang, Y.; Mao, J.; Moldovan, D.; Masir, M. R.; Li, G.; Watanabe, K.; Taniguchi, T.; Peeters, F. M.; Andrei, E. Y. Tuning a Circular P-n Junction in Graphene from Quantum Confinement to Optical Guiding. *Nat. Nanotechnol.* **2017**. https://doi.org/10.1038/nnano.2017.181.

(4) Ghahari, F.; Walkup, D.; Gutiérrez, C.; Rodriguez-Nieva, J. F.; Zhao, Y.; Wyrick, J.; Natterer, F. D.; Cullen, W. G.; Watanabe, K.; Taniguchi, T.; Levitov, L. S.; Zhitenev, N. B.; Stroscio, J. A. An on/off Berry Phase Switch in Circular Graphene Resonators. *Science (80-.).* **2017**. https://doi.org/10.1126/science.aal0212.

(5) Gutiérrez, C.; Walkup, D.; Ghahari, F.; Lewandowski, C.; Rodriguez-Nieva, J. F.; Watanabe, K.; Taniguchi, T.; Levitov, L. S.; Zhitenev, N. B.; Stroscio, J. A. Interaction-Driven Quantum Hall Wedding Cake–like Structures in Graphene Quantum Dots. *Science (80-.).* **2018**. https://doi.org/10.1126/science.aar2014.

(6) Walkup, D.; Ghahari, F.; Gutiérrez, C.; Watanabe, K.; Taniguchi, T.; Zhitenev, N. B.; Stroscio, J. A. Tuning Single-Electron Charging and Interactions between Compressible Landau Level Islands in Graphene. *Phys. Rev. B* **2020**. https://doi.org/10.1103/PhysRevB.101.035428.

(7) Mohr, M.; Maultzsch, J.; Dobardžić, E.; Reich, S.; Milošević, I.; Damnjanović, M.; Bosak, A.; Krisch, M.; Thomsen, C. Phonon Dispersion of Graphite by Inelastic X-Ray Scattering. *Phys. Rev. B - Condens. Matter Mater. Phys.* **2007**. https://doi.org/10.1103/PhysRevB.76.035439.

(8) Jung, S.; Park, M.; Park, J.; Jeong, T. Y.; Kim, H. J.; Watanabe, K.; Taniguchi, T.; Ha, D. H.; Hwang, C.; Kim, Y. S. Vibrational Properties of H-BN and h-BN-Graphene Heterostructures Probed by Inelastic Electron Tunneling Spectroscopy. *Sci. Rep.* **2015**. https://doi.org/10.1038/srep16642.

(9) Zhang, Y.; Brar, V. W.; Wang, F.; Girit, C.; Yayon, Y.; Panlasigui, M.; Zettl, A.; Crommie, M. F. Giant Phonon-Induced Conductance in Scanning Tunnelling Spectroscopy of Gate-Tunable Graphene. *Nat. Phys.* **2008**. https://doi.org/10.1038/nphys1022.

(10) Brar, V. W. Scanning Tunneling Spectroscopy of Graphene and Magnetic Nanostructures. PhD Thesis, University fo California, Berkeley, 2010.

(11) Geringer, V.; Subramaniam, D.; Michel, A. K.; Szafranek, B.; Schall, D.; Georgi, A.; Mashoff, T.; Neumaier, D.; Liebmann, M.; Morgenstern, M. Electrical Transport and Low-Temperature Scanning Tunneling Microscopy of Microsoldered Graphene. *Appl. Phys. Lett.* **2010**. https://doi.org/10.1063/1.3334730.

(12) Lagoute, J.; Joucken, F.; Repain, V.; Tison, Y.; Chacon, C.; Bellec, A.; Girard, Y.; Sporken, R.; Conrad, E. H.; Ducastelle, F.; Palsgaard, M.; Andersen, N. P.; Brandbyge, M.; Rousset, S. Giant Tunnel-Electron Injection in Nitrogen-Doped Graphene. *Phys. Rev. B - Condens. Matter Mater. Phys.* **2015**. https://doi.org/10.1103/PhysRevB.91.125442.

(13) Joucken, F.; Henrard, L.; Lagoute, J. Electronic Properties of Chemically Doped Graphene. *Phys. Rev. Mater.* **2019**. https://doi.org/10.1103/PhysRevMaterials.3.110301.

(14) Feenstra, R. M. A Prospective: Quantitative Scanning Tunneling Spectroscopy of Semiconductor Surfaces. *Surface Science*. 2009. https://doi.org/10.1016/j.susc.2009.08.002.

(15) Lu, C. P.; Li, G.; Mao, J.; Wang, L. M.; Andrei, E. Y. Bandgap, Mid-Gap States, and Gating Effects in MoS2. *Nano Lett.* **2014**. https://doi.org/10.1021/nl501659n.

(16) Koós, A. A.; Vancsó, P.; Magda, G. Z.; Osváth, Z.; Kertész, K.; Dobrik, G.; Hwang, C.; Tapasztó, L.; Biró, L. P. STM Study of the MoS2 Flakes Grown on Graphite: A Model System for Atomically Clean 2D Heterostructure Interfaces. *Carbon N. Y.* **2016**. https://doi.org/10.1016/j.carbon.2016.04.069.

(17) Vancsó, P.; Magda, G. Z.; Peto, J.; Noh, J. Y.; Kim, Y. S.; Hwang, C.; Biró, L. P.; Tapasztó, L. The Intrinsic Defect Structure of Exfoliated MoS2 Single Layers Revealed by Scanning Tunneling Microscopy. *Sci. Rep.* **2016**. https://doi.org/10.1038/srep29726.

(18) Wallace, P. R. The Band Theory of Graphite. *Phys. Rev.* **1947**. https://doi.org/10.1103/PhysRev.71.622.

(19) Ponomarenko, L. A.; Schedin, F.; Katsnelson, M. I.; Yang, R.; Hill, E. W.; Novoselov, K. S.; Geim, A. K. Chaotic Dirac Billiard in Graphene Quantum Dots. *Science (80-.).* **2008**. https://doi.org/10.1126/science.1154663.

(20) Schnez, S.; Güttinger, J.; Huefner, M.; Stampfer, C.; Ensslin, K.; Ihn, T. Imaging Localized States in Graphene Nanostructures. *Phys. Rev. B - Condens. Matter Mater. Phys.* **2010**. https://doi.org/10.1103/PhysRevB.82.165445.

(21) Todd, K.; Chou, H. T.; Amasha, S.; David, G. G. Quantum Dot Behavior in Graphene Nanoconstrictions. *Nano Lett.* **2009**. https://doi.org/10.1021/nl803291b.

(22) Han, M. Y.; Özyilmaz, B.; Zhang, Y.; Kim, P. Energy Band-Gap Engineering of Graphene Nanoribbons. *Phys. Rev. Lett.* **2007**. https://doi.org/10.1103/PhysRevLett.98.206805.

(23) Subramaniam, D.; Libisch, F.; Li, Y.; Pauly, C.; Geringer, V.; Reiter, R.; Mashoff, T.; Liebmann, M.; Burgdörfer, J.; Busse, C.; Michely, T.; Mazzarello, R.; Pratzer, M.; Morgenstern, M. Wave-Function Mapping of Graphene Quantum Dots with Soft Confinement. *Phys. Rev. Lett.* **2012**. https://doi.org/10.1103/PhysRevLett.108.046801.

(24) Hämäläinen, S. K.; Sun, Z.; Boneschanscher, M. P.; Uppstu, A.; Ijäs, M.; Harju, A.; Vanmaekelbergh, D.; Liljeroth, P. Quantum-Confined Electronic States in Atomically Well-Defined Graphene Nanostructures. *Phys. Rev. Lett.* **2011**. https://doi.org/10.1103/PhysRevLett.107.236803.

(25) Phark, S. H.; Borme, J.; Vanegas, A. L.; Corbetta, M.; Sander, D.; Kirschner, J. Direct Observation of Electron Confinement in Epitaxial Graphene Nanoislands. *ACS Nano* **2011**. https://doi.org/10.1021/nn2028105.

(26) Lu, J.; Yeo, P. S. E.; Gan, C. K.; Wu, P.; Loh, K. P. Transforming C 60 Molecules into Graphene Quantum Dots. *Nat. Nanotechnol.* **2011**. https://doi.org/10.1038/nnano.2011.30.

(27) Wang, Y.; Wong, D.; Shytov, A. V.; Brar, V. W.; Choi, S.; Wu, Q.; Tsai, H. Z.; Regan, W.; Zettl, A.; Kawakami, R. K.; Louie, S. G.; Levitov, L. S.; Crommie, M. F. Observing Atomic Collapse Resonances in Artificial Nuclei on Graphene. *Science (80-.).* **2013**. https://doi.org/10.1126/science.1234320.

(28) Jung, S.; Rutter, G. M.; Klimov, N. N.; Newell, D. B.; Calizo, I.; Hight-Walker, A. R.; Zhitenev, N. B.; Stroscio, J. A. Evolution of Microscopic Localization in Graphene in a Magnetic Field from Scattering Resonances to Quantum Dots. *Nat. Phys.* **2011**. https://doi.org/10.1038/nphys1866.

(29) Freitag, N. M.; Chizhova, L. A.; Nemes-Incze, P.; Woods, C. R.; Gorbachev, R. V.; Cao, Y.; Geim, A. K.; Novoselov, K. S.; Burgdörfer, J.; Libisch, F.; Morgenstern, M. Electrostatically Confined Monolayer Graphene Quantum Dots with Orbital and Valley Splittings. *Nano Lett.* **2016**. https://doi.org/10.1021/acs.nanolett.6b02548.

(30) Freitag, N. M.; Reisch, T.; Chizhova, L. A.; Nemes-Incze, P.; Holl, C.; Woods, C. R.; Gorbachev, R. V.; Cao, Y.; Geim, A. K.; Novoselov, K. S.; Burgdörfer, J.; Libisch, F.; Morgenstern, M. Large Tunable Valley Splitting in Edge-Free Graphene Quantum Dots on Boron Nitride. *Nat. Nanotechnol.* **2018**. https://doi.org/10.1038/s41565-018-0080-8.

(31) Velasco, J.; Ju, L.; Wong, D.; Kahn, S.; Lee, J.; Tsai, H. Z.; Germany, C.; Wickenburg, S.; Lu, J.; Taniguchi, T.; Watanabe, K.; Zettl, A.; Wang, F.; Crommie, M. F. Nanoscale Control of Rewriteable Doping Patterns in Pristine Graphene/Boron Nitride Heterostructures. *Nano Lett.* **2016**. https://doi.org/10.1021/acs.nanolett.5b04441.

(32) Quezada-Lopez, E. A.; Joucken, F.; Chen, H.; Lara, A.; Davenport, J. L.; Hellier, K.; Taniguchi, T.; Watanabe, K.; Carter, S.; Ramirez, A. P.; Velasco, J. Persistent and Reversible Electrostatic Control of Doping in Graphene/Hexagonal Boron Nitride Heterostructures. *J. Appl. Phys.* **2020**. https://doi.org/10.1063/1.5127770.

(33) Zomer, P. J.; Dash, S. P.; Tombros, N.; Van Wees, B. J. A Transfer Technique for High Mobility Graphene Devices on Commercially Available Hexagonal Boron Nitride. *Appl. Phys. Lett.* **2011**. https://doi.org/10.1063/1.3665405.

(34) Goossens, A. M.; Calado, V. E.; Barreiro, A.; Watanabe, K.; Taniguchi, T.; Vandersypen, L. M. K. Mechanical Cleaning of Graphene. *Appl. Phys. Lett.* **2012**. https://doi.org/10.1063/1.3685504.

(35) Velasco, J.; Lee, J.; Wong, D.; Kahn, S.; Tsai, H. Z.; Costello, J.; Umeda, T.; Taniguchi, T.; Watanabe, K.; Zettl, A.; Wang, F.; Crommie, M. F. Visualization and Control of Single-Electron Charging in Bilayer Graphene Quantum Dots. *Nano Lett.* **2018**. https://doi.org/10.1021/acs.nanolett.8b01972.

(36) Tersoff, J.; Hamann, D. R. Theory of the Scanning Tunneling Microscope. *Phys. Rev. B* **1985**. https://doi.org/10.1103/PhysRevB.31.805.

(37) Chen, C. J. *Introduction to Scanning Tunneling Microscopy: Second Edition*; 2007. https://doi.org/10.1093/acprof:oso/9780199211500.001.0001.

(38) Katsnelson, M. I.; Novoselov, K. S.; Geim, A. K. Chiral Tunnelling and the Klein Paradox in Graphene. *Nat. Phys.* **2006**. https://doi.org/10.1038/nphys384.

(39) Cheianov, V. V.; Fal'ko, V. I. Selective Transmission of Dirac Electrons and Ballistic Magnetoresistance of N-p Junctions in Graphene. *Phys. Rev. B - Condens. Matter Mater. Phys.* **2006**. https://doi.org/10.1103/PhysRevB.74.041403.

(40) Shytov, A. V.; Rudner, M. S.; Levitov, L. S. Klein Backscattering and Fabry-Pérot Interference in Graphene Heterojunctions. *Phys. Rev. Lett.* **2008**. https://doi.org/10.1103/PhysRevLett.101.156804.

(41) Allain, P. E.; Fuchs, J. N. Klein Tunneling in Graphene: Optics with Massless Electrons. *Eur. Phys. J. B* **2011**. https://doi.org/10.1140/epjb/e2011-20351-3.

(42) Rickhaus, P. S. Electron Optics in Ballistic Graphene. PhD Thesis., University

of Basel, Switzerland, 2015.

(43) Wu, J. S.; Fogler, M. M. Scattering of Two-Dimensional Massless Dirac Electrons by a Circular Potential Barrier. *Phys. Rev. B - Condens. Matter Mater. Phys.* **2014**. https://doi.org/10.1103/PhysRevB.90.235402.

(44) Schulz, C.; Heinisch, R. L.; Fehske, H. Scattering of Two-Dimensional Dirac Fermions on Gate-Defined Oscillating Quantum Dots. *Phys. Rev. B - Condens. Matter Mater. Phys.* **2015**. https://doi.org/10.1103/PhysRevB.91.045130.

(45) Chen, H. Y.; Apalkov, V.; Chakraborty, T. Fock-Darwin States of Dirac Electrons in Graphene-Based Artificial Atoms. *Phys. Rev. Lett.* **2007**. https://doi.org/10.1103/PhysRevLett.98.186803.

(46) Matulis, A.; Peeters, F. M. Quasibound States of Quantum Dots in Single and Bilayer Graphene. *Phys. Rev. B - Condens. Matter Mater. Phys.* **2008**. https://doi.org/10.1103/PhysRevB.77.115423.

(47) Bardarson, J. H.; Titov, M.; Brouwer, P. W. Electrostatic Confinement of Electrons in an Integrable Graphene Quantum Dot. *Phys. Rev. Lett.* **2009**. https://doi.org/10.1103/PhysRevLett.102.226803.

(48) Zhang, Y.; Brar, V. W.; Girit, C.; Zettl, A.; Crommie, M. F. Origin of Spatial Charge Inhomogeneity in Graphene. *Nat. Phys.* **2009**. https://doi.org/10.1038/nphys1365.

(49) Rutter, G. M.; Jung, S.; Klimov, N. N.; Newell, D. B.; Zhitenev, N. B.; Stroscio, J. A. Microscopic Polarization in Bilayer Graphene. *Nat. Phys.* **2011**. https://doi.org/10.1038/nphys1988.

(50) LeRoy, B. J.; Kong, J.; Pahilwani, V. K.; Dekker, C.; Lemay, S. G. Three-Terminal Scanning Tunneling Spectroscopy of Suspended Carbon Nanotubes. *Phys. Rev. B - Condens. Matter Mater. Phys.* **2005**. https://doi.org/10.1103/PhysRevB.72.075413.

(51) Chae, J.; Jung, S.; Young, A. F.; Dean, C. R.; Wang, L.; Gao, Y.; Watanabe, K.; Taniguchi, T.; Hone, J.; Shepard, K. L.; Kim, P.; Zhitenev, N. B.; Stroscio, J. A. Renormalization of the Graphene Dispersion Velocity Determined from Scanning Tunneling Spectroscopy. *Phys. Rev. Lett.* **2012**. https://doi.org/10.1103/PhysRevLett.109.116802.

(52) Davenport, J. L.; Ge, Z.; Joucken, F.; Eberth A. Quezada-Lopez, T. T.; Watanabe, K.; Jr., J. V. Unraveling the Tunneling Spectrum of Bernal-Stacked Bilayer Graphene.

(53) Holdman, G. R.; Krebs, Z. J.; Behn, W. A.; Smith, K. J.; Watanabe, K.; Taniguchi, T.; Brar, V. W. Dynamic Band Structure and Capacitance Effects in Scanning Tunneling Spectroscopy of Bilayer Graphene. *Appl. Phys. Lett.* **2019**.

https://doi.org/10.1063/1.5127078.

Chapter 7 - Nanospot Angle Resolved Photoemission Study of Bernal-Stacked Bilayer Graphene on Hexagonal Boron Nitride: Band Structure and Local Variation of Lattice Alignment

7.1 Introduction

Hexagonal boron nitride (hBN) is the supporting substrate of choice for two-dimensional material devices because it is atomically flat and chemically inert.[1] However, due to the small lateral size of mechanically exfoliated hBN flakes (∼30 μm), electronic structure studies of two-dimensional materials supported by hBN using angle-resolved photoemission spectroscopy (ARPES) are challenging. Here we investigate the electronic band structure of a Bernal-stacked bilayer graphene sheet on a hBN (BLG/hBN) flake using nanospot ARPES (nanoARPES).[2–5] By fitting high-resolution energy vs momentum electronic band spectra, we extract the tight-binding parameters for BLG on hBN. In addition, we reveal spatial variations of the alignment angle between BLG and hBN lattices via inhomogeneity of the electronic bands near the Fermi level. We confirmed these findings by scanning tunneling microscopy (STM) measurements obtained on the same device. Our results from spatially resolved nanoARPES measurements of BLG/hBN heterostructures are instrumental for understanding experiments that utilize spatial averaging techniques such as electronic transport and optical spectroscopy.

7.2 ARPES with Nanometer-Scale Spatial Resolution

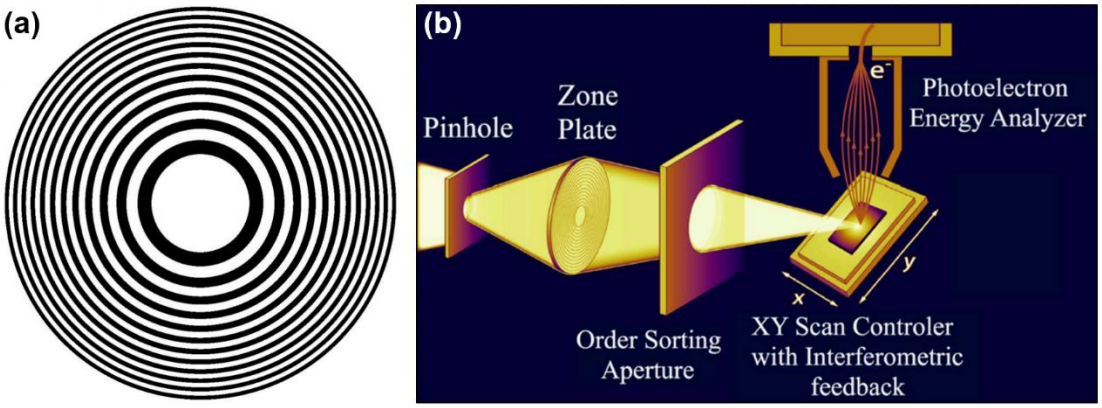

Figure 7.1| Nanospot angle-resolved photoemission spectroscopy (nanoARPES) enabled by advanced optics and translational control. (a) Design outline of a Fresnel zone plate (FZP) showing the alternating opaque (black) and transparent (white) rings. This alternating pattern acts as a diffraction grating component which coaxially focuses an incident monochromatic beam of light. [Image credit: NASA]. **(b)** Schematic of the nanoARPES setup used for the experiments in this chapter. An incident beam of light ($h\nu \sim 100$ eV) from a synchrotron source gets projected by a pinhole onto the FZP. An order sorting aperture filters out higher diffracted modes from the FZP so that the beam is focused down to a ~ 120 nm spot on the sample's surface. A photoelectron analyzer collects the sample's emitted electrons as the stage moves along the xy-plane of the sample to spatially map photoemission intensities. [Image adapted from Chen *et al*].[6]

The fundamental principle and theory of ARPES was discussed in Ch. 3. However, it is necessary to discuss the additional experimental features that enable the novelty of the results presented in this chapter.

Conventional ARPES shines light on a sample's surface with a beam spot size of $50 - 100$ μm in diameter.[2] This spot size is larger than the size of most exfoliated graphene/hBN samples. Thus, the application of ARPES on such samples tends to average over large areas and even include photoemission from the surrounding

substrate.[4,6] To address this lack in spatial resolution, the experiments discussed in this chapter apply an additional optical component to the incident beam. This component is a Fresnel zone plate and its alternating opaque and transparent pattern is depicted in Fig. 7.1a. This zone plate acts as a diffraction grating component that focuses monochromatic light down to a much smaller spot size via constructive interference. The transparent zones are arranged in such a way that the optical path difference through the sequential zones arriving at the focus is exactly one wavelength, and therefore light coming through these zones undergoes positive interference at the focal point.[6] The nanoARPES setup used for the experiments in this chapter can focus this beam down to ~ 120 nm in diameter.

In addition to a conveniently small beam size, this nanoARPES system includes fine spatial control of the substrate stage that uses eight axes of motion.[6] Three linear translators enable the positioning of the sample near the beam spot. Two rotation axes enable probing of different region on the Brillouin zone (BZ) as we will see in the upcoming sections. The last three axes are the piezo-electric controlled translations in xyz that enable the nanometer-scale scanning and focusing of the beam spot along a sample's surface. Figure 7.1b depicts the primary components of the nanoARPES system which includes order sorting aperture to filter out higher order diffracted modes and a photoelectron analyzer that collects the photoemitted charges to map a sample's band structure.

7.3 Background of Spatially Resolved ARPES on 2D Materials

The recent development of nanoARPES allows unprecedented spatial mapping of the electronic band structure of 2D material heterostructures.[7–11] In particular, by applying this spatially resolved technique to heterostructures that use hBN as a supporting substrate, reliable, direct, and insightful visualization of top-lying 2D material band structures can be achieved.[7–11] Recent spatially resolved ARPES studies on monolayer graphene/hBN and WS_2/hBN have carefully examined the band structure of the top-lying 2D materials and found evidence for polarons[8] and bandgap renormalization.[10] BLG that is supported on hBN is also of fundamental interest because of the peculiar physics that has been recently revealed in this system such as excitons with pseudospin texture[12] and indications of non-Abelian excitations.[13] However, direct spatially resolved electronic structure investigation of BLG/hBN heterostructures with ARPES is lacking.

We present in this chapter a direct spatial mapping of the electronic structure of a BLG/hBN heterostructure using nanoARPES in combination with STM. We extract tight-binding parameters from high-resolution ARPES spectra. This allows the comparison of BLG/hBN parameters with those from previous measurements on BLG resting on different substrates and acquired *via* different techniques. In addition, we show that direct access to the band structure with submicron spatial resolution offered by nanoARPES reveals small spatial variations of lattice alignment between BLG and the supporting hBN. Our results provide important fundamental insight on band

structure parameters and nanoscale alignment between 2D materials. This insight can be used for improved modeling and further understanding of the interesting physics hosted in BLG/hBN heterostructures.

7.4 NanoARPES and STM on BLG/hBN

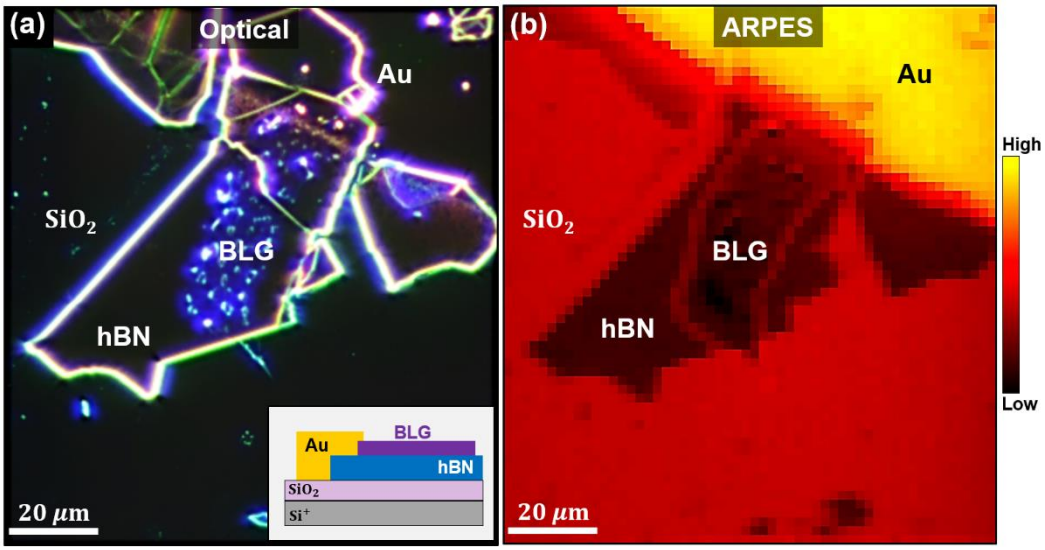

Figure 7.2| Optical and photoemission imaging of the heterostructure used for the experiment. (a) Dark-field optical image of the sample which consists of a Bernal-stacked bilayer graphene/hexagonal boron nitride (BLG/hBN) heterostructure resting upon a SiO_2/Si^+ substrate and is grounded via a gold electrode. This is schematized in the inset with gold electrode in yellow, BLG in purple, hBN in blue, SiO_2 in faded purple, and Si^+ in gray. **(b)** Photoemission image of the same heterostructure as (a). Pixel intensities are assigned after integrating an ARPES $E(\boldsymbol{k})$ spectrum at each pixel position. The components of the device are labeled accordingly in (a) and (b). [Images were adapted from the published article].[14]

Our study was composed of two different characterization techniques (nanoARPES and STM) that were applied to our BLG/hBN heterostructure. The

nanoARPES experiments were carried out at the ANTARES beam line of synchrotron SOLEIL. As described in section 6.2, this beam line is equipped with a Fresnel zone plate (FZP) to focus the beam down to a ~ 120 nm diameter spot. The sample was mounted on a nano-positioning stage which was placed at the coincident focus point of the electron analyzer and the FZP (see Fig. 7.1b). The photoelectron spectra were obtained using a hemispherical analyzer (MBS A1) equipped with electrostatic lenses. These lenses are able to electrostatically deflect the photoemitted electrons so that they hit a screen at different locations depending on their momenta, thus enabling Fermi surface measurements without rotating the sample. All photoemission measurements were performed at a temperature of ~ 100 K, at a photon energy of 100 eV, and with an overall energy and momentum resolution better than 35 meV and 0.01 Å^{-1}, respectively. The sample was annealed at ~ 300 °C for two hours before performing measurements. The STM characterization was conducted in ultrahigh vacuum (UHV) at a pressure below 2×10^{-10} mbar and at a temperature of 4.8 K in a Createc STM. The bias was applied to the sample with respect to the STM tip. The tips were electrochemically etched tungsten tips calibrated against the Shockley surface state of Au(111), as discussed in Ch. 4. The sample was exposed to atmosphere between the two UHV setups. The sample was also annealed at ~ 300 °C for two hours before STM characterization.

A dark-field optical image of the device is shown in Fig. 7.2a, with a schematic in the inset. The BLG flake (purple) rests onto the hBN flake (blue) lying on the SiO_2/Si^+ substrate and is grounded via a gold/chromium electrode (yellow). These

components are labeled in the darkfield optical image. A nanoARPES image of the same region is displayed in Fig. 7.2b. Each pixel of this image is assigned an intensity level by integrating the ARPES energy vs. momentum $E(\boldsymbol{k})$ spectrum obtained at the corresponding positions (for additional details on nanoARPES imaging, see the discussion below and references)[4,8,15,16]. There is a clear correspondence between the optical and nanoARPES image. This enables identification of device components in the nanoARPES image as indicated by the labels in Fig. 7.2b.

7.4.1 Determination of BLG/hBN tight-binding parameters using nanoARPES

We first focus on the electronic structure of our BLG flake supported by hBN. Figure 7.3a displays an ARPES $E(\boldsymbol{k})$ spectrum acquired in the direction indicated in the inset. The measurement direction makes an angle of $\sim 9°$ with the Γ-K direction. Because of matrix element effects[17,18] (also see Ch. 3), only the part of the band corresponding to $\kappa_x < K$ is resolved, where $K \sim 1.7$ Å^{-1}. Note that κ is used (instead of k) to denote small excursions in reciprocal space around the K point as done in Ch. 2. Given that photoemission only probes occupied states and the sample's lack of doping, only the valence bands of BLG are visible in the spectrum[19,20] (also see Ch. 3). We refer to the band closest to the Fermi level as the low-energy band (LEB) and the band below it as the high energy band (HEB). We show in Figs. 7.3b and 7.3c ARPES constant energy cuts acquired around the K point at binding energies (BE) of -1 and -2 eV, respectively. These constant energy cuts allow another visualization of the

matrix element effects.[17,18] We note that the threefold symmetry of the bands around the K point becomes clearly visible at a high binding energy Fig. 7.3c. This is expected because of the threefold symmetry of BLG's reciprocal space around the K point.[21]

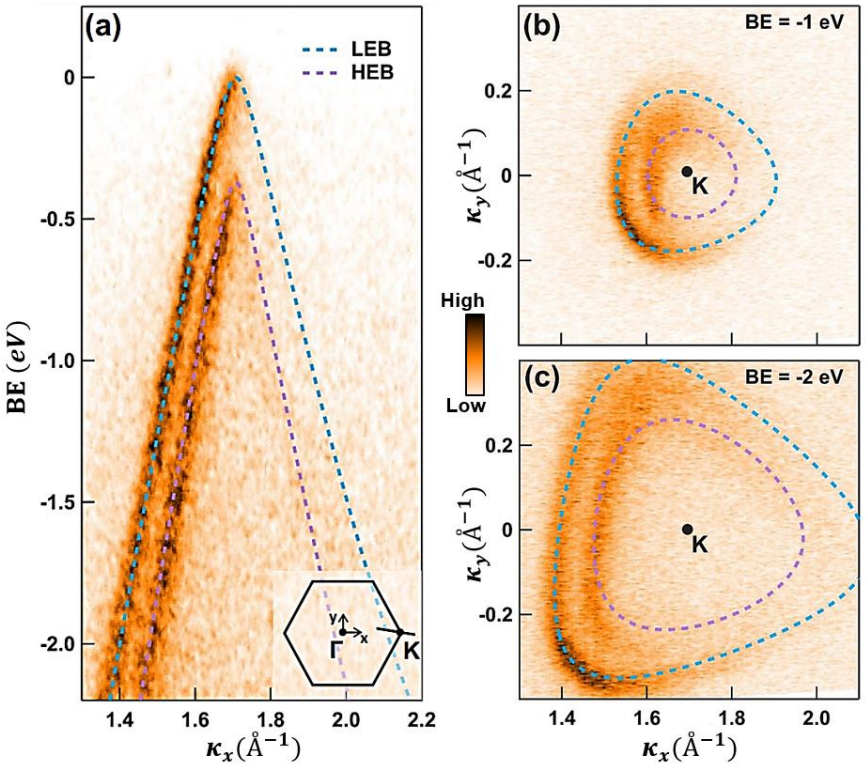

Figure 7.3| ARPES characterization and associated tight-binding (TB) fits of BLG/hBN. (a) Experimental ARPES $E(\boldsymbol{k})$ spectrum acquired along the direction indicated in the BZ shown in the inset. **(b)** Experimental ARPES constant energy cut at a binding energy: BE $= -1$ eV. **(c)** Experimental ARPES constant energy cut at BE $= -2$ eV. Each panel contains superimposed best-fit TB bands following the conventions of McCann and Koshino.[21] Tight-binding parameters used for the fits are: $\gamma_0 = 3.3$ eV, $\gamma_1 = 0.42$ eV, $\gamma_3 = 0.07$ eV, $\gamma_4 = 0.22$ eV, and $\Delta' = 0.02$ eV. [Plots were adapted from the published article].[14]

The direct visualization of BLG's bands in conjunction with the quality of our data enable facile quantitative analysis using a tight binding (TB) model to extract band structure parameters. Fits from such a model are superimposed onto the ARPES $E(\boldsymbol{k})$ spectrum of Fig. 7.3a and the ARPES constant energy cuts in Figs. 7.3b-c. The conventions we used to compute the TB bands follow McCann and Koshino.[21] Specifically, the TB bands are obtained by solving numerically, at each point in reciprocal space, the following Hamiltonian:

$$H = \begin{pmatrix} 0 & -\gamma_0 f(\boldsymbol{k}) & \gamma_4 f(\boldsymbol{k}) & -\gamma_3 f^*(\boldsymbol{k}) \\ -\gamma_0 f^*(\boldsymbol{k}) & \Delta' & \gamma_1 & \gamma_4 f(\boldsymbol{k}) \\ \gamma_4 f^*(\boldsymbol{k}) & \gamma_1 & \Delta' & -\gamma_0 f(\boldsymbol{k}) \\ -\gamma_3 f(\boldsymbol{k}) & \gamma_4 f^*(\boldsymbol{k}) & -\gamma_0 f^*(\boldsymbol{k}) & 0 \end{pmatrix} \qquad (7.1)$$

where $f(\boldsymbol{k})$ is given by equation (2.42). Note that this is a more complete Hamiltonian for BLG than that discussed in Ch. 2. Additionally, we do not consider the Hamiltonian for gapped BLG (2.51) given that layer symmetry is preserved by the lack of a perpendicular electric field or charged contaminants on BLG's surface. Thus, for undoped non-gated BLG, there are five independent TB parameters to determine: the hopping energies ($\gamma_0, \gamma_1, \gamma_3, \gamma_4$) and Δ', which is the energy difference between dimer and non-dimer sites.[21] Briefly, the four hopping energies determine the overall velocity of the bands (γ_0) [see (2.23)], the energy difference between the tops of the LEB and the HEB (γ_1), the trigonal warping effect (γ_3), and the electron-hole asymmetry (γ_4). Because we do not have access to the unoccupied states with ARPES, we assumed that $\gamma_4 = 0.22$ eV, as found from STS studies on a similar sample as ours (BLG/hBN).[22] Also following previous results, we let $\Delta' = 0.02\ eV$ (an average of the values found

in the literature).[23–25] The remaining parameters were determined by our fits, which yielded $\gamma_0 = 3.3 \pm 0.15$ eV, $\gamma_1 = 0.42 \pm 0.05$ eV, and $\gamma_3 = 0.07 \pm 0.1$ eV. The uncertainty of these values is determined by the range of the fitting parameters γ_i in our simulations that agree with our experimental results (for further details see the supplement of the published article).[14] The hopping energies γ_i lead to a band velocity of $v_F = (3/2\hbar)\gamma_0 a_0 = 1.07 \pm 0.05 \times 10^6$ m/s and an effective mass $m = \gamma_1/(2v_F^2) = 0.032 \pm 0.05\, m_e$, where m_e is the bare electron mass. For details regarding the fitting procedure, see the supplement of the published article.[14]

In Table I, we compare our results to previously reported tight binding parameters for BLG. A comparison of our TB results to the values reported in the literature is intricate because of the disparity among definitions for TB parameters, which are not always explicit,[18,19,21–32] as discussed by Jung and MacDonald.[34] The signs of the entries in Table I marked by an asterisk have been corrected following Table III in Jung and MacDonald,[34] which matches the convention used by McCann and Koshino.[21] Our value for γ_0 is slightly higher than the value reported for BLG on hBN by Yankowitz *et al.*[22] However, compared to Yankowitz's result,[22] we probed the bands down to much larger binding energies without applying an effective low-energy Hamiltonian. For γ_1, ARPES analyses for BLG on SiC[27] and on SiO_2[20] led to substantially higher values. The larger value found for BLG on SiC ($\gamma_1 \sim 0.48$ eV)[27] can be explained by an enhancement in substrate interaction as evidenced by strong electron doping. The value of $\gamma_1 \sim 0.61$ eV found for BLG on SiO_2[20] is intriguing and might be explained by the difficulty in extracting γ_1 due to the suppressed intensity at

the top of the HEB. Finally, the disparity between our value for γ_3 and other groups' may be explained by the possibility of γ_3 being negative. In a recent quasiparticle interference experiment[35] we determined that $\gamma_3 = -0.3$ eV, which agrees in magnitude to other groups' results. We also noted that the choice in γ_4 did not appreciably influence the fit value for γ_3.

Reference	γ_0 **(eV)**	γ_1 **(eV)**	γ_3 **(eV)**	γ_4 **(eV)**	Δ' **(eV)**	**Technique/ Substrate**
Malard *et al.*[26] *	2.9	0.30	−0.10	0.12		Raman/SiO_2
Ohta *et al.*[19]		0.41-0.46	0.12			ARPES/SiC
Ohta *et al.*[27]	3.24	0.48				ARPES/SiC
Zhang *et al.*[23]		0.40		0.15	0.018	IR/SiO_2
Lauffer *et al.*[28]	3.27	0.46				STM/SiC
Henriksen *et al.*[29]		0.43-0.52				Cycl. Reso./ SiO_2
Yan *et al.*[30]		0.35				Raman/SiO_2
Kuzmenko *et al.*[24]*	3.16	0.381	−0.38	0.14	0.022	IR/SiO_2
Li *et al.*[25]	3.1-3.4	0.404		0.16	0.018	IR/SiO_2
Zou *et al.*[31]	3.43			0.216		SdH/SiO_2
Mayorov *et al.*[32]			0.435			E-transport/ suspended
Mallet *et al.*[36]	3.7[a]	0.38				STM/SiC
Yankowitz *et al.*[22]	3.1			0.22		STM/hBN
Cheng *et al.*[20]	−3.21	0.61	0.39	0.15		ARPES/SiO_2
Lee *et al.*[33]	3.1-3.3	0.35-0.42		0.06-0.12		E-transport/ hBN
Min *et al.*[37]	2.6	0.34	0.3			DFT/none
This work	**3.3**	**0.42**	**0.07**			**ARPES/hBN**

[a]Mallet *et al*. determined $v_F = 1.21 \times 10^6$ m/s by directly determining the slope of the bands they measured, we translated this value for v_F using $v_F = (3/2\hbar)\gamma_0 a_0$.

Table I| Literature values for the TB parameters of BLG. The signs of the entries in Table I marked by an asterisk have been corrected (using Table III in Jung and MacDonald)[34] to match the convention we used, which is the one from McCann and Koshino.[21] [The table was adapted from the published article][14].

7.4.2 Spatially resolved nanoARPES on BLG/hBN

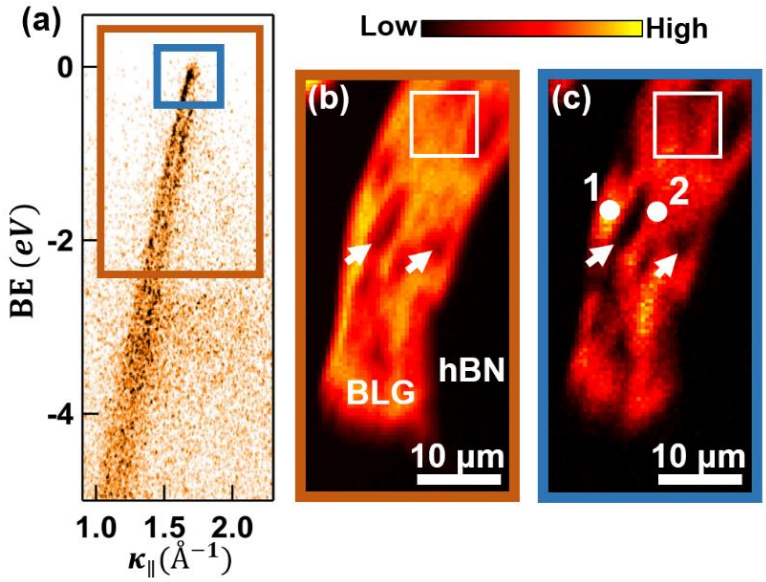

Figure 7.4| Spatial variation of the photoemission intensity across the surface of BLG/hBN. (a) Representative ARPES $E(\boldsymbol{k})$ spectrum from which the photoemission images shown in (b) and (c) are made. **(b)** Photoemission image of the BLG flake in which each pixel level is the integrated intensity within the brown rectangle depicted in (a). **(c)** Photoemission image of the BLG flake in which each pixel level is the integrated intensity within the blue rectangle depicted in (a). Arrows on (b) and (c) indicate areas where BLG is absent (topographic holes). The region boxed by the white frames in both images illustrates the greater intensity modulation for image (c), compared to (b). [Plots and images were adapted from the published article][14].

We now discuss spatial mapping of our BLG/hBN heterostructure via nanoARPES. Figures 7.4b-c depict images constructed from a nanoARPES map of the BLG flake. For each pixel on this map, an ARPES $E(\boldsymbol{k})$ spectrum similar to the one displayed in Fig. 7.4a was recorded. During the map acquisition, the sample position was scanned in the xy-plane, while its rotation axes and the photoelectron analyzer were fixed. From this map, we constructed two different images (Figs. 7.4b and 7.4c) by integrating over the pixel intensities in the $E(\boldsymbol{k})$ regions outlined with brown (Fig.

7.4b) and blue (Fig. 7.4c) frames in Fig. 7.4a. Both images show dark spots, with close to zero intensity (two of which are indicated by white arrows in Figs. 7.4b and 7.4c).

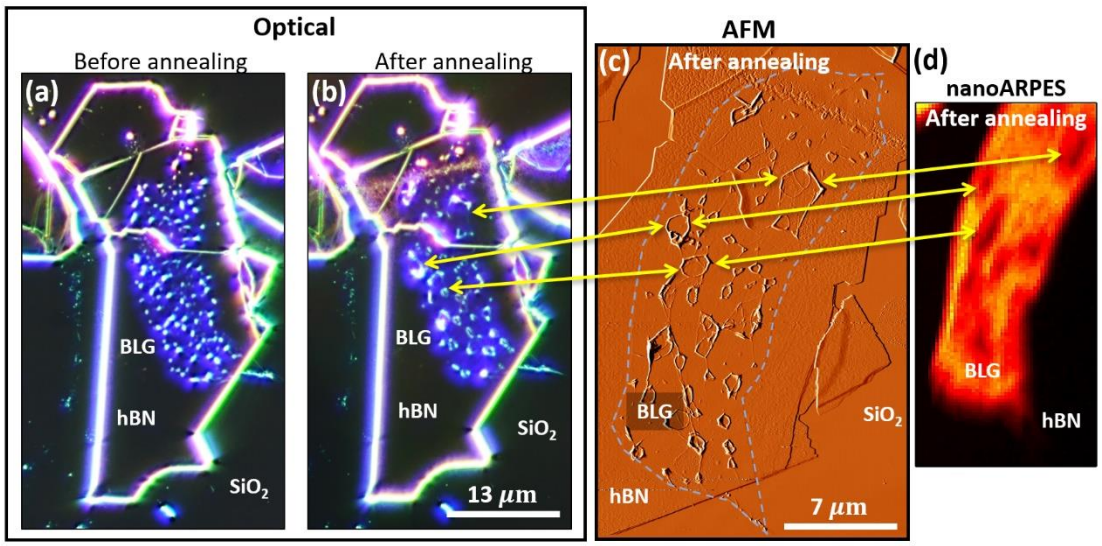

Figure 7.5| Comparison between optical, atomic force, and ARPES images of BLG/hBN. (a) and **(b)** are dark-field optical images before and after UHV annealing at ~300 ℃. **(c)** AFM image of the BLG/hBN region from (b). **(d)** is a nanoARPES image that corresponds to the same region from (c). Yellow arrows are used in (b)-(d) to indicate the same regions between all three images. Because the indicated regions in (d) display a suppression in photoemission intensity, we identify them as holes (exposed hBN) on the BLG flake that arise after UHV annealing. [Images were adapted from the published article][14].

To complement the spatial characterization acquired by nanoARPES, we use optical and atomic force microscopy (AFM) images of our BLG/hBN heterostructure. Figures 7.5a and 7.5b are dark-field optical images of our sample acquired before and after undergoing UHV annealing of up to 300 ℃. The image acquired before UHV annealing (Fig. 7.5a) shows numerous bright blue spots. These features correspond to bubbles that arise from trapped contaminants between 2D materials within a

heterostructure.[38] The image taken after UHV annealing (Fig. 7.5b) shows similar features but with different arrangement, shape, and density than those from Fig. 7.5a. Further insight on these new features can be obtained by comparing the optical images to an AFM image as shown in Fig. 7.5c. This AFM image reveals that these new features correspond to tall ridges that surround flat plateaus. Some of these areas are indicated by yellow arrows which link to corresponding locations in Fig. 7.5b.

To clarify our comparisons, we show the nanoARPES image from Fig. 7.4b in Fig. 7.5d. Yellow arrows are used to indicate the same regions on the three images (Figs 7.5b-d). Because these common regions in Fig. 7.5d display a suppression in integrated $E(\boldsymbol{k})$ intensity, we identify these features as holes in the BLG flake that arise after UHV annealing. Such holes could have been created during the annealing process in UHV,[39] which is a required sample preparation step for nanoARPES experiments. Besides the shared presence of these dark spots on both images in Figs. 7.4b and 7.4c, there are also noticeable differences. Specifically, there is a greater intensity modulation in the region outlined by the white frame in Fig. 7.4c when compared to the same region in Fig. 7.4b.

To gain further insight into this intensity fluctuation, we acquired high-resolution ARPES $E(\boldsymbol{k})$ spectra at various locations on the investigated sample. Figures 7.6a and 7.6b show two typical ARPES $E(\boldsymbol{k})$ spectra obtained at the regions labeled "spot 1" and "spot 2", indicated by white dots in Fig. 7.4c. Notably, the intensity close to the Fermi level ($\mathrm{BE} = 0$ eV) is greater in Fig. 7.6a than in Fig. 7.6b. We attribute this difference to a variation of the BLG lattice alignment with the analyzer

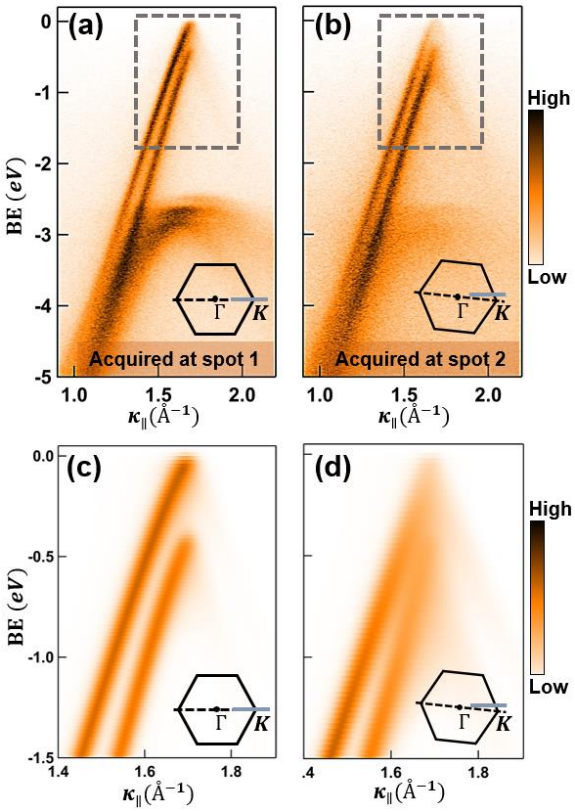

Figure 7.6| Variation of the BLG/hBN alignment as evidenced by nanoARPES. (a) High resolution ARPES $E(\boldsymbol{k})$ spectrum obtained at "spot 1" on Fig. 7.4c for which the analyzer entrance slit is parallel to the Γ-K direction, as indicated in the inset. **(b)** High resolution ARPES $E(\boldsymbol{k})$ spectrum obtained at "spot 2" on image Fig. 7.4c, for which the analyzer entrance slit is slightly misaligned with the Γ-K direction, as indicated in the inset. **(c)** and **(d)** Calculated $E(\boldsymbol{k})$ spectra with simulated slit alignment at 0° and 3° with respect to the Γ-K direction as indicated by the insets. The dashed gray boxes in (a)-(b) indicate the simulated regions in (c)-(d). [Plots and images were adapted from the published article][14].

entrance slit, which is fixed. Indeed, the high intensity close to the Fermi level in Fig. 7.6a indicates that the analyzer entrance slit is aligned with the Γ-K direction for this spectrum, as indicated in the inset. On the other hand, this is not the case for the spectrum of Fig. 7.6b, where the intensity reduction at the Fermi level corresponds to a rotational misalignment between the analyzer entrance slit and the Γ-K direction (see the inset). To support this interpretation, ARPES $E(\boldsymbol{k})$ spectra was simulated for a BLG/analyzer misalignment of 0° and 3° with respect to the Γ-K direction. These simulations reproduced the spectra of Figs. 7.6a and 7.6b and are shown in Figs. 7.6c and 7.6d, respectively. For details on the calculation see the supplement of the published article.[14]

Using this insight, we now explain the intensity modulation differences between the images of Figs. 7.4b and 7.4c. The blue box in Fig. 7.4a (from which the image of Fig. 7.4c is generated) corresponds to the very top of the LEB of BLG. Small misalignment between the probed BLG area and the electron analyzer decreases the integrated intensity in this area significantly, as shown by the difference between Figs. 7.6a and 7.6b. On the other hand, the brown box in Fig. 7.4a is much larger and the corresponding integrated intensity is therefore less dependent on the lattice orientation of the probed BLG area. This explains the intensity modulation difference between the two images. Notably, because the supporting hBN flake is a single crystal, its orientation is the same throughout the entire device. Thus, an alignment variation between the BLG and the electron analyzer equates to an alignment variation between the BLG and the hBN substrate.

7.4.3 Crystallographic misalignment of BLG on hBN determined by STM

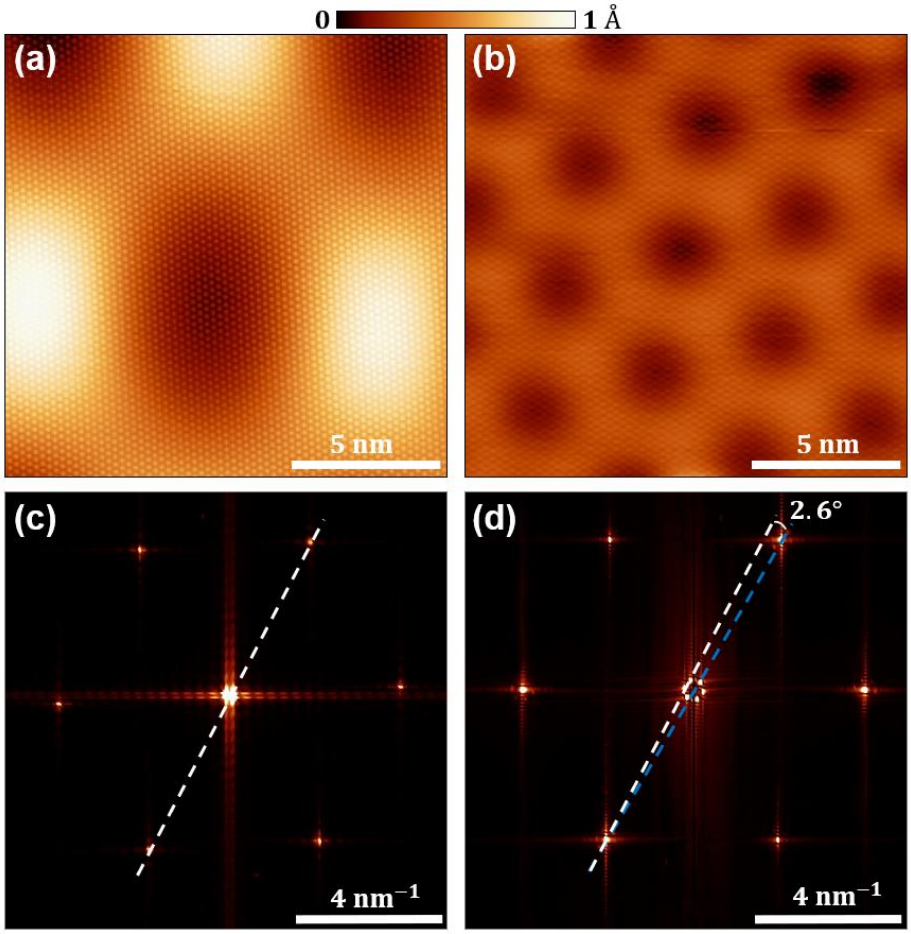

Figure 7.7| Real space STM imaging revealing different BLG/hBN crystallographic alignment on the same device. (a) and **(b)** STM images obtained at two different locations on the same BLG/hBN heterostructure discussed in Figs. 7.2–7.6. The periodicities of the Moiré patterns observed are $\lambda_{(a)} = 11.6$ nm and $\lambda_{(b)} = 4.1$ nm, respectively, corresponding to a BLG/hBN alignment angle of $\phi_{(a)} = 0.7°$ and $\phi_{(b)} = 3.3°$. Tunneling parameters for (a): $I = 0.3$ nA and $V_S = 80$ mV, and (b): $I = 0.1$ nA and $V_S = 75$ mV. **(c)** and **(d)** are the fast Fourier transforms of images (a) and (b), respectively. The white dashed line on (c) serves as a guide to the eye for the graphene lattice orientation of image (a) and is reproduced in (d). The blue dashed line in (d) indicates the orientation of the graphene lattice of image (b). The angle between these two lines is $\sim 2.6°$, as expected from their Moiré wavelengths. [Images were adapted from the published article][14].

To confirm our interpretation of the spatial variation in nanoARPES signal, we acquired STM data on the same device studied in Figs. 7.2–7.6. Figures 7.7a and 7.7b show STM images obtained at two different locations on our sample and their respective fast Fourier transforms (FFTs) are presented in Figs. 7.7c and 7.7d. We observe Moiré periodicities in the images of Figs. 7.7a and 7.7b of $\lambda_{(a)} = 11.6$ and $\lambda_{(b)} = 4.1$ nm, respectively. The relation between the Moiré periodicity λ and the misorientation angle ϕ is given by:

$$\lambda = \frac{(1+\delta)\sqrt{3}a_0}{\sqrt{2(1+\delta)(1-cos\,\phi)+\delta^2}} \tag{7.2}$$

where $\delta = 1.8\%$ is the lattice mismatch between graphene and hBN.[31] Applying (7.2) to the images from Figs. 7.7a and 7.7b yields misorientation angles between the hBN and the BLG of $\phi_{(a)} = 0.7°$ and $\phi_{(b)} = 3.3°$, respectively. These misalignments can also be observed on the FFTs of our topographic data. The white (blue) dashed line in Fig. 7.7c (Fig. 7.7d) indicates the BLG lattice orientation from the image in Fig. 7.7a (Fig. 7.7b). In Fig. 7.7d, we also reproduce the white dashed line from Fig. 7.7c to enable comparison between the lattice orientations. The $\phi_{(b)} - \phi_{(a)} = 2.6°$ mismatch determined by the Moiré wavelength comparison is confirmed by the direct comparison of the lattice orientation in the FFTs. Furthermore, we observed intermediate crystallographic misalignments at eight different locations on the sample with angles $\phi = 3.3°$, 3.1°, 2.8°, 2.4°, 2.1°, 0.7°. The observed variation in Moiré periodicities

confirms our interpretation of the ARPES data in terms of BLG/hBN lattice alignment inhomogeneity.

We believe that the rotational disorder seen in our experiment appears during the annealing procedure because of the heat-induced self-alignment mechanism reported by Woods *et al.*[40,41] These authors have shown that it is energetically favorable for graphene to be macroscopically aligned within $\pm 0.7°$ with hBN, and that mild heating (~ 200 °C in an Ar/H_2 environment) can provide the energy necessary for self-alignment of regions that are misaligned by angles near 1°. In particular, they demonstrated quasi-homogeneous rotation by $\sim 0.3°$ for flakes with characteristic size of ~ 30 μm. In their experiment, they did not observe self-alignment for samples displaying more than a few bubbles. This was attributed to the contaminants within bubbles decoupling graphene from hBN or acting as pinning centers.[41] In our experiment, we believe the misalignment between the BLG and the hBN was $\sim 3.3°$ after transfer and was reduced in a spatially inhomogeneous fashion by the UHV annealing, down to $\sim 0.7°$ in certain regions. The self-rotation we observed ($> 2.5°$) is thus much larger than what was reported by Woods *et al*. and is inhomogeneous across our sample. We attribute this inhomogeneity to the fact that our sample contained numerous bubbles that burst during the UHV annealing as demonstrated by Fig. 7.5. This process most likely segmented our flake into smaller domains loosely attached to one another, making them able to rotate more easily.

7.5 Conclusion

In conclusion, we have presented the results from a nanoARPES investigation of a BLG/hBN heterostructure. We have directly extracted TB parameters with nanoARPES for BLG on hBN, the standard insulating supporting substrate for 2D material heterostructures. We have also shown that nanoARPES can reveal variations in crystallographic alignment between BLG and hBN. These latter findings were confirmed by STM imaging, which showed areas with different Moiré periodicities due to numerous domains with various orientations. We attribute this variation of lattice alignment to an inhomogeneous BLG/hBN alignment induced by standard UHV heating used to prepare samples for ARPES and STM characterization. These results substantially improve our understanding of the BLG/hBN heterostructure and provide researchers using this heterostructure with a direct picture of the electronic bands resolved in reciprocal space with nanoscale resolution. In addition, the spatial variation of lattice alignment between the BLG and the supporting hBN that we evidenced here is important for researchers investigating these samples with spatially averaging probes such as electronic transport or optical spectroscopy.

Chapter 7 - References

(1) Dean, C. R.; Young, A. F.; Meric, I.; Lee, C.; Wang, L.; Sorgenfrei, S.; Watanabe, K.; Taniguchi, T.; Kim, P.; Shepard, K. L.; Hone, J. Boron Nitride Substrates for High-Quality Graphene Electronics. *Nat. Nanotechnol.* **2010**. https://doi.org/10.1038/nnano.2010.172.

(2) Dudin, P.; Lacovig, P.; Fava, C.; Nicolini, E.; Bianco, A.; Cautero, G.; Barinov, A. Angle-Resolved Photoemission Spectroscopy and Imaging with a Submicrometre Probe at the SPECTROMICROSCOPY-3.2L Beamline of Elettra. *J. Synchrotron Radiat.* **2010**. https://doi.org/10.1107/S0909049510013993.

(3) Bostwick, A.; Rotenberg, E.; Avila, J.; Asensio, M. C. Zooming in on Electronic Structure: NanoARPES at SOLEIL and ALS. *Synchrotron Radiat. News* **2012**. https://doi.org/10.1080/08940886.2012.720162.

(4) Avila, J.; Asensio, M. C. First NanoARPES User Facility Available at SOLEIL: An Innovative and Powerful Tool for Studying Advanced Materials. *Synchrotron Radiat. News* **2014**. https://doi.org/10.1080/08940886.2014.889549.

(5) Hoesch, M.; Kim, T. K.; Dudin, P.; Wang, H.; Scott, S.; Harris, P.; Patel, S.; Matthews, M.; Hawkins, D.; Alcock, S. G.; Richter, T.; Mudd, J. J.; Basham, M.; Pratt, L.; Leicester, P.; Longhi, E. C.; Tamai, A.; Baumberger, F. A Facility for the Analysis of the Electronic Structures of Solids and Their Surfaces by Synchrotron Radiation Photoelectron Spectroscopy. *Rev. Sci. Instrum.* **2017**. https://doi.org/10.1063/1.4973562.

(6) Chen, C.; Avila, J.; Asensio, M. C. Chemical and Electronic Structure Imaging of Graphene on Cu: A NanoARPES Study. *Journal of Physics Condensed Matter*. 2017. https://doi.org/10.1088/1361-648X/aa6487.

(7) Wang, E.; Chen, G.; Wan, G.; Lu, X.; Chen, C.; Avila, J.; Fedorov, A. V.; Zhang, G.; Asensio, M. C.; Zhang, Y.; Zhou, S. Electronic Structure of Transferred Graphene/h-BN van Der Waals Heterostructures with Nonzero Stacking Angles by Nano-ARPES. *J. Phys. Condens. Matter* **2016**. https://doi.org/10.1088/0953-8984/28/44/444002.

(8) Chen, C.; Avila, J.; Wang, S.; Wang, Y.; Mucha-Kruczyński, M.; Shen, C.; Yang, R.; Nosarzewski, B.; Devereaux, T. P.; Zhang, G.; Asensio, M. C. Emergence of Interfacial Polarons from Electron-Phonon Coupling in Graphene/h-BN van Der Waals Heterostructures. *Nano Lett.* **2018**. https://doi.org/10.1021/acs.nanolett.7b04604.

(9) Wilson, N. R.; Nguyen, P. V.; Seyler, K.; Rivera, P.; Marsden, A. J.; Laker, Z. P. L.; Constantinescu, G. C.; Kandyba, V.; Barinov, A.; Hine, N. D. M.; Xu,

X.; Cobden, D. H. Determination of Band Offsets, Hybridization, and Exciton Binding in 2D Semiconductor Heterostructures. *Sci. Adv.* **2017**. https://doi.org/10.1126/sciadv.1601832.

(10) Katoch, J.; Ulstrup, S.; Koch, R. J.; Moser, S.; McCreary, K. M.; Singh, S.; Xu, J.; Jonker, B. T.; Kawakami, R. K.; Bostwick, A.; Rotenberg, E.; Jozwiak, C. Giant Spin-Splitting and Gap Renormalization Driven by Trions in Single-Layer WS 2 /h-BN Heterostructures. *Nat. Phys.* **2018**. https://doi.org/10.1038/s41567-017-0033-4.

(11) Yuan, H.; Liu, Z.; Xu, G.; Zhou, B.; Wu, S.; Dumcenco, D.; Yan, K.; Zhang, Y.; Mo, S. K.; Dudin, P.; Kandyba, V.; Yablonskikh, M.; Barinov, A.; Shen, Z.; Zhang, S.; Huang, Y.; Xu, X.; Hussain, Z.; Hwang, H. Y.; Cui, Y.; Chen, Y. Evolution of the Valley Position in Bulk Transition-Metal Chalcogenides and Their Monolayer Limit. *Nano Lett.* **2016**. https://doi.org/10.1021/acs.nanolett.5b05107.

(12) Ju, L.; Wang, L.; Cao, T.; Taniguchi, T.; Watanabe, K.; Louie, S. G.; Rana, F.; Park, J.; Hone, J.; Wang, F.; McEuen, P. L. Tunable Excitons in Bilayer Graphene. *Science (80-.).* **2017**. https://doi.org/10.1126/science.aam9175.

(13) Li, J. I. A.; Tan, C.; Chen, S.; Zeng, Y.; Taniguchi, T.; Watanabe, K.; Hone, J.; Dean, C. R. Even-Denominator Fractional Quantum Hall States in Bilayer Graphene. *Science (80-.).* **2017**. https://doi.org/10.1126/science.aao2521.

(14) Joucken, F.; Quezada-López, E. A.; Avila, J.; Chen, C.; Davenport, J. L.; Chen, H.; Watanabe, K.; Taniguchi, T.; Asensio, M. C.; Velasco, J. Nanospot Angle-Resolved Photoemission Study of Bernal-Stacked Bilayer Graphene on Hexagonal Boron Nitride: Band Structure and Local Variation of Lattice Alignment. *Phys. Rev. B* **2019**. https://doi.org/10.1103/PhysRevB.99.161406.

(15) Chen, C.; Avila, J.; Wang, S.; Yang, R.; Zhang, G.; Asensio, M. C. Electronic Structure of Graphene/Hexagonal Boron Nitride Heterostructure Revealed by Nano-ARPES. *J. Phys. Conf. Ser.* **2017**, *. 864 0120*.

(16) Chen, C.; Avila, J.; Asensio, M. C. Electronic Structure of Polycrystalline CVD-Graphene Revealed by Nano-ARPES. *J. Phys. Conf. Ser.* **2017**, *J. Phys. C*.

(17) Shirley, E. L.; Terminello, L. J.; Santoni, A.; Himpsel, F. J. Brillouin-Zone-Selection Effects in Graphite Photoelectron Angular Distributions. *Phys. Rev. B* **1995**. https://doi.org/10.1103/PhysRevB.51.13614.

(18) Mucha-Kruczyński, M.; Tsyplyatyev, O.; Grishin, A.; McCann, E.; Fal'ko, V. I.; Bostwick, A.; Rotenberg, E. Characterization of Graphene through Anisotropy of Constant-Energy Maps in Angle-Resolved Photoemission. *Phys. Rev. B - Condens. Matter Mater. Phys.* **2008**. https://doi.org/10.1103/PhysRevB.77.195403.

(19) Ohta, T.; Bostwick, A.; Seyller, T.; Horn, K.; Rotenberg, E. Controlling the Electronic Structure of Bilayer Graphene. *Science (80-.).* **2006**. https://doi.org/10.1126/science.1130681.

(20) Cheng, C. M.; Xie, L. F.; Pachoud, A.; Moser, H. O.; Chen, W.; Wee, A. T. S.; Castro Neto, A. H.; Tsuei, K. D.; Özyilmaz, B. Anomalous Spectral Features of a Neutral Bilayer Graphene. *Sci. Rep.* **2015**. https://doi.org/10.1038/srep10025.

(21) McCann, E.; Koshino, M. The Electronic Properties of Bilayer Graphene. *Reports Prog. Phys.* **2013**. https://doi.org/10.1088/0034-4885/76/5/056503.

(22) Yankowitz, M.; Wang, J. I. J.; Li, S.; Birdwell, A. G.; Chen, Y. A.; Watanabe, K.; Taniguchi, T.; Quek, S. Y.; Jarillo-Herrero, P.; LeRoy, B. J. Band Structure Mapping of Bilayer Graphene via Quasiparticle Scattering. *APL Mater.* **2014**. https://doi.org/10.1063/1.4890543.

(23) Zhang, L. M.; Li, Z. Q.; Basov, D. N.; Fogler, M. M.; Hao, Z.; Martin, M. C. Determination of the Electronic Structure of Bilayer Graphene from Infrared Spectroscopy. *Phys. Rev. B - Condens. Matter Mater. Phys.* **2008**. https://doi.org/10.1103/PhysRevB.78.235408.

(24) Kuzmenko, A. B.; Crassee, I.; Van Der Marel, D.; Blake, P.; Novoselov, K. S. Determination of the Gate-Tunable Band Gap and Tight-Binding Parameters in Bilayer Graphene Using Infrared Spectroscopy. *Phys. Rev. B - Condens. Matter Mater. Phys.* **2009**. https://doi.org/10.1103/PhysRevB.80.165406.

(25) Li, Z. Q.; Henriksen, E. A.; Jiang, Z.; Hao, Z.; Martin, M. C.; Kim, P.; Stormer, H. L.; Basov, D. N. Band Structure Asymmetry of Bilayer Graphene Revealed by Infrared Spectroscopy. *Phys. Rev. Lett.* **2009**. https://doi.org/10.1103/PhysRevLett.102.037403.

(26) Malard, L. M.; Nilsson, J.; Elias, D. C.; Brant, J. C.; Plentz, F.; Alves, E. S.; Castro Neto, A. H.; Pimenta, M. A. Probing the Electronic Structure of Bilayer Graphene by Raman Scattering. *Phys. Rev. B - Condens. Matter Mater. Phys.* **2007**. https://doi.org/10.1103/PhysRevB.76.201401.

(27) Ohta, T.; Bostwick, A.; McChesney, J. L.; Seyller, T.; Horn, K.; Rotenberg, E. Interlayer Interaction and Electronic Screening in Multilayer Graphene Investigated with Angle-Resolved Photoemission Spectroscopy. *Phys. Rev. Lett.* **2007**. https://doi.org/10.1103/PhysRevLett.98.206802.

(28) Lauffer, P.; Emtsev, K. V.; Graupner, R.; Seyller, T.; Ley, L.; Reshanov, S. A.; Weber, H. B. Atomic and Electronic Structure of Few-Layer Graphene on SiC(0001) Studied with Scanning Tunneling Microscopy and Spectroscopy. *Phys. Rev. B - Condens. Matter Mater. Phys.* **2008**. https://doi.org/10.1103/PhysRevB.77.155426.

(29) Henriksen, E. A.; Jiang, Z.; Tung, L. C.; Schwartz, M. E.; Takita, M.; Wang, Y. J.; Kim, P.; Stormer, H. L. Cyclotron Resonance in Bilayer Graphene. *Phys. Rev. Lett.* **2008**. https://doi.org/10.1103/PhysRevLett.100.087403.

(30) Yan, J.; Henriksen, E. A.; Kim, P.; Pinczuk, A. Observation of Anomalous Phonon Softening in Bilayer Graphene. *Phys. Rev. Lett.* **2008**. https://doi.org/10.1103/PhysRevLett.101.136804.

(31) Zou, K.; Hong, X.; Zhu, J. Effective Mass of Electrons and Holes in Bilayer Graphene: Electron-Hole Asymmetry and Electron-Electron Interaction. *Phys. Rev. B - Condens. Matter Mater. Phys.* **2011**. https://doi.org/10.1103/PhysRevB.84.085408.

(32) Mayorov, A. S.; Elias, D. C.; Mucha-Kruczynski, M.; Gorbachev, R. V.; Tudorovskiy, T.; Zhukov, A.; Morozov, S. V.; Katsnelson, M. I.; Fal'ko, V. I.; Geim, A. K.; Novoselov, K. S. Interaction-Driven Spectrum Reconstruction in Bilayer Graphene. *Science (80-.).* **2011**. https://doi.org/10.1126/science.1208683.

(33) Lee, K.; Jung, J.; Fallahazad, B.; Tutuc, E. Transport Spectroscopy in Bilayer Graphene Using Double Layer Heterostructures. *2D Mater.* **2017**, *2D Mater.*

(34) Jung, J.; MacDonald, A. H. Accurate Tight-Binding Models for the π Bands of Bilayer Graphene. *Phys. Rev. B - Condens. Matter Mater. Phys.* **2014**. https://doi.org/10.1103/PhysRevB.89.035405.

(35) Joucken, F.; Ge, Z.; Quezada-López, E. A.; Davenport, J. L.; Watanabe, K.; Taniguchi, T.; Velasco, J. Determination of the Trigonal Warping Orientation in Bernal-Stacked Bilayer Graphene via Scanning Tunneling Microscopy. *Phys. Rev. B* **2020**. https://doi.org/10.1103/PhysRevB.101.161103.

(36) Mallet, P.; Brihuega, I.; Bose, S.; Ugeda, M. M.; Gómez-Rodríguez, J. M.; Kern, K.; Veuillen, J. Y. Role of Pseudospin in Quasiparticle Interferences in Epitaxial Graphene Probed by High-Resolution Scanning Tunneling Microscopy. *Phys. Rev. B - Condens. Matter Mater. Phys.* **2012**. https://doi.org/10.1103/PhysRevB.86.045444.

(37) Min, H.; Sahu, B.; Banerjee, S.; MacDonald, A. H. Ab Initio Theory of Gate Induced Gaps in Graphene Bilayers. *Phys. Rev. B* **2007**, *75* (155115). https://doi.org/10.1103/PhysRevB.75.155115.

(38) Castellanos-Gomez, A.; Buscema, M.; Molenaar, R.; Singh, V.; Janssen, L.; Van Der Zant, H. S. J.; Steele, G. A. Deterministic Transfer of Two-Dimensional Materials by All-Dry Viscoelastic Stamping. *2D Mater.* **2014**. https://doi.org/10.1088/2053-1583/1/1/011002.

(39) Lu, J.; Neto, A. H. C.; Loh, K. P. Transforming Moiré Blisters into Geometric Graphene Nano-Bubbles. *Nat. Commun.* **2012**.

https://doi.org/10.1038/ncomms1818.

(40) Woods, C. R.; Britnell, L.; Eckmann, A.; Ma, R. S.; Lu, J. C.; Guo, H. M.; Lin, X.; Yu, G. L.; Cao, Y.; Gorbachev, R. V.; Kretinin, A. V.; Park, J.; Ponomarenko, L. A.; Katsnelson, M. I.; Gornostyrev, Y. N.; Watanabe, K.; Taniguchi, T.; Casiraghi, C.; Gao, H. J.; Geim, A. K.; Novoselov, K. S. Commensurate-Incommensurate Transition in Graphene on Hexagonal Boron Nitride. *Nat. Phys.* **2014**. https://doi.org/10.1038/nphys2954.

(41) Woods, C. R.; Withers, F.; Zhu, M. J.; Cao, Y.; Yu, G.; Kozikov, A.; Ben Shalom, M.; Morozov, S. V.; Van Wijk, M. M.; Fasolino, A.; Katsnelson, M. I.; Watanabe, K.; Taniguchi, T.; Geim, A. K.; Mishchenko, A.; Novoselov, K. S. Macroscopic Self-Reorientation of Interacting Two-Dimensional Crystals. *Nat. Commun.* **2016**. https://doi.org/10.1038/ncomms10800.

Chapter 8 - Atomically Resolved Mapping of the Van Hove Singularity Enhanced by Pseudospin Ferromagnetism in Bernal Stacked Bilayer Graphene

8.1 Introduction

The emergence of flat bands in 2D materials such as twisted magic angle bilayer graphene has attracted substantial attention in recent years. Close proximity between the Fermi energy (E_F) and a flat band leads to an intensely high density of states (DOS) due to the large number of degenerate states. Such phenomena is known as a Van Hove singularity (VHS).[1] The large number of states present at the VHS are often subject to interact with each other. As a consequence, the VHS may host novel phases of matter such as superconductivity,[2] magnetism,[3] and charge density waves.[4] In graphene, recent efforts to engineer flat bands have heavily relied on modulating graphene's lattice with a periodic potential, which is achieved by twisting two or more graphene layers relative to each other.[5–10] Controlled twisting of graphene layers requires cumbersome micromechanical techniques not yet proven to be scalable. On the other hand, naturally occurring Bernal or AB stacked bilayer graphene (BLG) is scalable[11–13] and can host VHSs near E_F.[14–16] By electrostatically controlling the layer occupation asymmetry in BLG, we provide the first report of a clear tunneling spectroscopic signature of the VHS in Bernal stacked BLG. Using a scanning tunneling microscope (STM) we confirm the expected lattice localization of the VHS by imaging the

atomically resolved distribution of states near and at the VHS energy. Additionally, we note a significant asymmetry in the VHS intensity for different layer polarization arrangements. We propose that pseudospin ferro-magnetization accounts for this observed asymmetry given that a non-interacting model fails to do so. Finally, we apply the same imaging technique to confirm and spatially resolve a subtle spectroscopic feature due to secondary bands in BLG.

8.2 Atomic Localization and Tunneling Spectroscopy of BLG

In these subsections I begin by briefly reviewing the lattice and band structure of gapped BLG near the *K* point. Then, I will show the results of numerical calculations (see section 2.5) for the local density of states (LDOS) for each atom in gapped BLG's unit cell. Knowing the LDOS distributions for specific atoms will enable us to make appropriate predictions regarding the localization of states in gapped BLG's lattice as we perform spatially resolved tunneling spectroscopy maps.

8.2.1 BLG band structure and local density of states (LDOS) near *K*

BLG offers unprecedented band structure control achieved via electrostatic gating. As discussed in Ch. 2, we use Bernal (or AB) stacked BLG where the B_T atom in the top graphene layer is located directly above the A_B atom in the bottom graphene

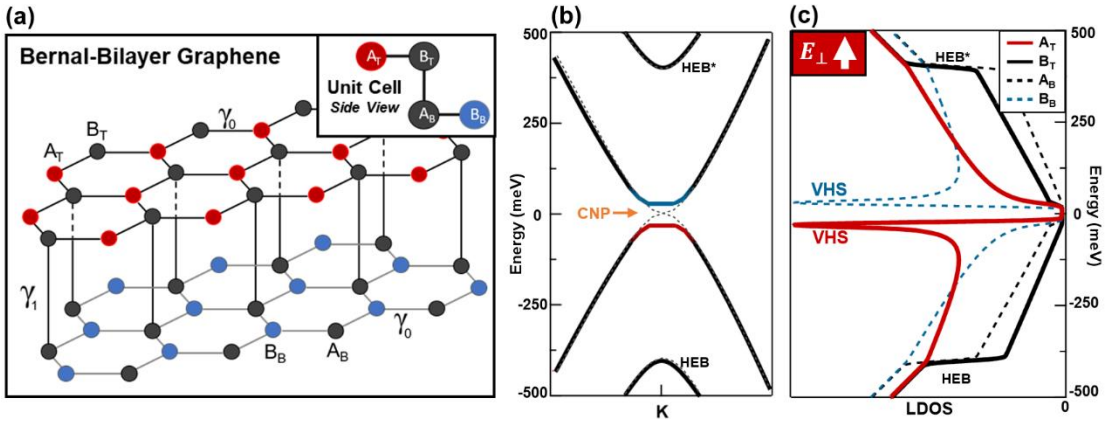

Figure 8.1| Electronic properties of Bernal stacked bilayer graphene (BLG). (a) Schematic of the lattice of Bernal stacked BLG. The inset shows a side view of the unit cell where the A_T and B_T (A_B and B_B) atoms correspond to the top (bottom) graphene layers in BLG. **(b)** Band structure of gapped (solid bands) and non-gapped (dashed bands) BLG calculated using tight binding with $\gamma_0 = 3.0$ eV and $\gamma_1 = 0.4$ eV. **(c)** Calculated local density of states (LDOS) for gapped BLG from (b) at specified atomic sites for each atom in BLG's unit cell. A bandgap of 60 meV is induced with the top and bottom layer's potentials at $\epsilon_{top} = -30$ meV and $\epsilon_{bottom} = +30$ meV, respectively**.** Band structure features such as the charge neutrality point (CNP) and high energy bands (HEBs) are indicated.

layer—forming a "dimer" pair (see Fig. 8.1a). These atoms are considered a dimer pair given that their orbitals have strong interlayer coupling—resembling a 1D dimer in the z-direction. Conveniently, we may refer to the A_T and B_B atoms as "non-dimers". The inset of Fig. 8.1a shows a side view of BLG's unit cell where the dimer pair has been assigned the same gray color. Importantly, BLG has inversion symmetry that can be broken by the application of a perpendicular electric field. Such an electric field unequally alters the potential energy of each layer and induces a bandgap in BLG (see section 2.4.1). The solid lines in Fig. 8.1b correspond to the calculated band structure of BLG around the K point for the case when the top layer is at a lower energy potential than the bottom layer, i.e. the electric field between BLG's layers points in the $+z$

direction. As a comparison, the dashed lines correspond to BLG's band structure when the top and bottom layers have the same energy potential. Evidently, a bandgap centered about the charge neutrality point (CNP) emerges when the top and bottom layers are at different energy potentials.

Unlike non-gapped BLG, the LDOS distribution for gapped BLG displays features which are strongly localized at the atoms in its unit cell. In Fig. 8.1c we plot the LDOS calculated for specific atoms in the unit cell for gapped BLG using the same parameters as the solid bands in Fig. 8.1b. The LDOS at the A_T and B_T atoms from BLG's top layer are represented by the solid red and black curves, respectively. The bottom layer's atoms A_B and B_B are represented by the dashed black and blue curves, respectively. As will be discussed shortly, we have assigned increased visibility (solid instead of dashed lines) to the top layer's LDOS given that STM almost exclusively probes the top layer in BLG. In this plot we have labeled the prominent features discussed in the remainder of this article: VHSs and the onset of the high energy bands (HEB and HEB*). From the LDOS plotted for specific atoms in Fig. 8.1c, it is evident that the valence and conduction VHS peaks are predominantly localized at the A_T and B_B atoms, respectively. Additionally, we see that the dimer site atoms in BLG's unit cell (B_T and A_B) have a significant contribution to BLG's LDOS for energies higher than the onset of the HEB and HEB*.

8.2.2 Scanning tunneling spectroscopy (STS) of BLG on hBN

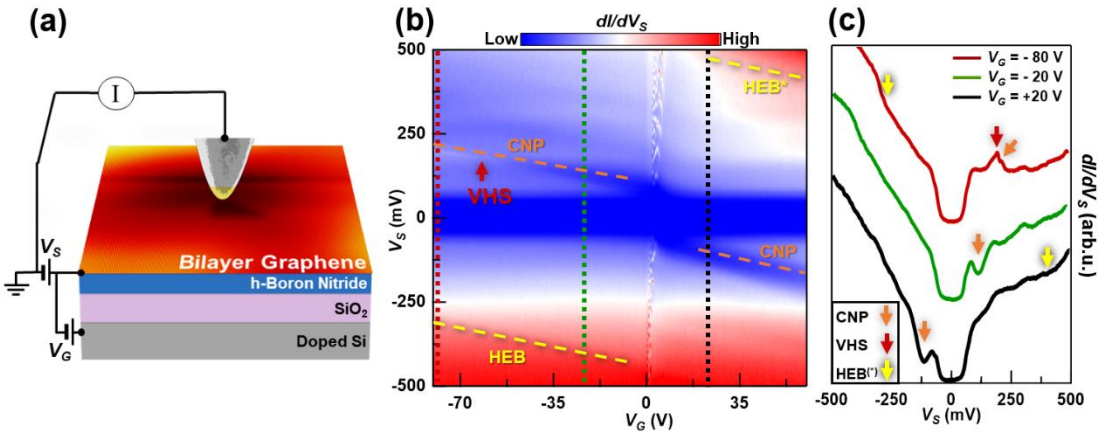

Figure 8.2| Tunneling spectroscopy of BLG. (a) Schematic of the experimental setup showing scanning tunneling microscopy (STM) on a BLG/hexagonal Boron Nitride heterostructure (hBN). The backgate voltage (V_G) applied to *p*-doped Si and the sample bias (V_S) both tune the perpendicular electric field on BLG. Tuning V_S also modulates the tunneling current between the tip and BLG. **(b)** Image plot of the differential conductance (dI/dV_S) of BLG as a function V_S and V_G. Band structure features such as the CNP and HEBs are outlined by the orange and yellow dashed lines, respectively. The onset of the top layer's VHS is noted by the red arrow. **(c)** BLG tunneling spectra taken for different values of V_G corresponding to the vertical dashed lines in (b). Band structure features are indicated with arrows. Tunneling parameters: $V_S = 0.5$ V; $I = 2.5$ nA; $V_{ac} = 5$ mV; $f_{ac} = 400$ Hz.

As detailed in Ch. 4, the experiments presented in this chapter are performed in a low-temperature scanning tunneling microscope (STM). STM enables us to explore BLG's band structure features with atomic scale precision. To achieve high stability, resolution, and spectroscopically reproducible results, the STM tip undergoes careful calibration on Au(111) (see section 4.4 for details). Figure 8.2a shows a schematic of the STM circuit and the BLG on hBN (22 nm thick) heterostructure used in our study. A sample bias voltage (V_S) is applied to tune the tunneling current between states in BLG and the STM tip. A backgate voltage (V_G) is applied to the *p*-doped Si layer at the

bottom of the substrate to tune the perpendicular electric field ($E_\perp$) in BLG. A thermally oxidized layer of 285 nm SiO_2 separates the hBN layer from the *p*-doped Si substrate.

Figure 8.2b shows a differential conductance $dI/dV_S(V_S, V_G)$ measurement performed on pristine BLG/hBN (see Fig. 6.2b for a similar plot of MLG/hBN). From tunneling theory, dI/dV_S is proportional to the LDOS of the substrate material's surface.[17] Thus, the features observed in Fig. 8.2b correspond to band structure features[18–21] like those highlighted in Fig. 8.1b,c. Line cuts for three values of V_G are plotted in Fig. 8.2c, where the relevant band structure features introduced above, the CNP, VHS, and HEBs, are indicated by the orange, red, and yellow arrows, respectively. In Fig. 8.2b we observe that the dI/dV_S suppression centered along the CNP becomes narrower between $V_G = +60$ V and ~ -50 V. This suppression feature outlines BLG's bandgap in the inelastic channel[20–22] which gradually closes as V_G decreases. For $V_G < -51$ V, we see a higher dI/dV_S intensity feature along the CNP which we will show to be BLG's top layer VHS in the upcoming sections.

The secondary bands (HEB and HEB*) in BLG and tip-induced quantum dot charging features can also be observed spectroscopically. The HEB/HEB* bands' onsets are outlined by the dashed yellow lines in Fig. 8.2b and indicated by the yellow arrows in Fig. 8.2c. Additionally, a numerical derivative of the image plot from Fig. 8.2b is shown in Fig. 8.3a with a wider V_S range. In the plot shown in Fig. 8.3a, we have enclosed the boundaries that outline the onsets for the HEB and HEB* with

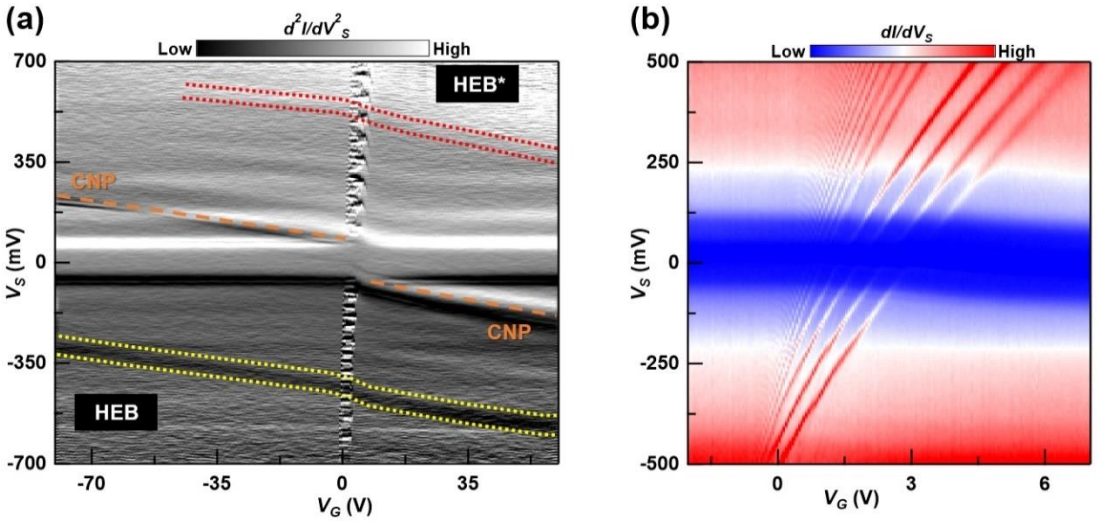

Figure 8.3| Tunneling spectroscopy highlighting the high energy bands (HEBs) and tip-induced quantum dot (QD) charging states in BLG. (a) Numerical derivative of the $dI/dV_S(V_G, V_S)$ plot from Fig. 8.2b plotted within a wider V_S range. The onset boundaries for the HEB and HEB* follow the dispersion of the CNP and are enclosed by the yellow and red dashed lines, respectively. **(b)** $dI/dV_S(V_G, V_S)$ image plot taken within a narrow V_G range to display the charging features originating from a tip-induced QD.

dashed yellow and red lines, respectively. We note that these features follow the same trend as the CNP which is linear in V_G due to the quadratic dispersion relation near the K points. As discussed in Ch. 6, dI/dV_S features that disperse with E_F correspond to band structure features. This further verifies that the dark and bright boundaries labeled HEB and HEB* in Fig. 8.3a are band structure features.

Figures 8.2b and 8.3a also display clear and strong vertical features parallel to the $V_G = 0$ line. These striking features in the dI/dV_S signal are due to STM tip-induced single electron charging effects.[23] A $dI/dV_S(V_S, V_G)$ image plot with a narrower V_G range is shown in Fig. 8.3b. Similar to our discussion in Ch. 6, the STM

tip's top gating effect creates a circular region below the tip's apex that is *p*-doped relative to the surrounding bulk. As a consequence, strong single electron charging peaks appear within certain values of V_G. These charging features display a distinctive four-fold grouping that accounts for spin and valley degeneracies.[23] These spectroscopic features are observed in BLG but not in MLG given that BLG's low energy bands are gapped at the boundaries of the circular *p*-*n* junction formed by the tip. Thus, charges become trapped in a similar manner to conventional quantum dots, unlike pseudo-confined charges in MLG. Finally, it is important to mention that the dI/dV_S plots in Figs. 8.2b, 8.3a-b clearly display the "phonon gap"[20,23,24] akin to the case for MLG. For a detailed discussion of the origin of this feature see section 6.2.1.

8.3 Atomic Localization of the Van Hove Singularity in BLG

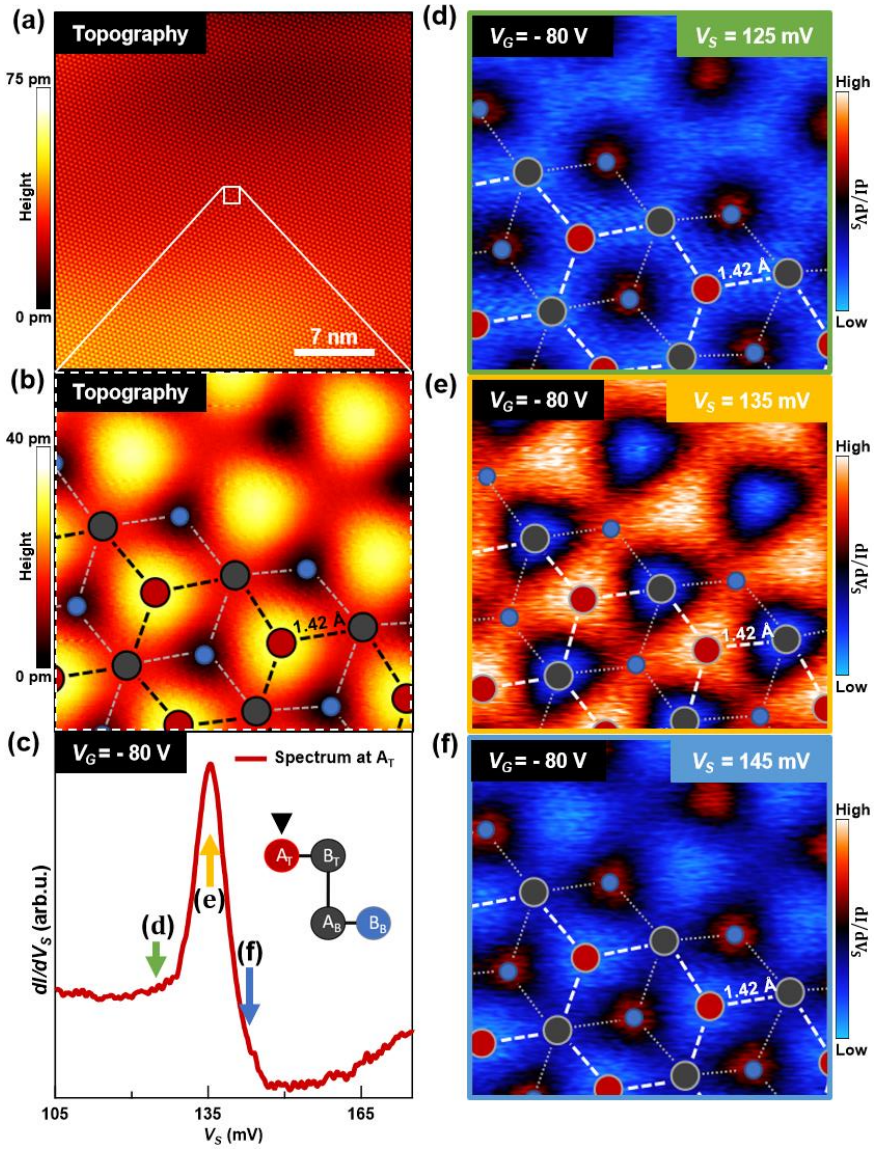

Figure 8.4| Atomically resolved localization of the Van Hove singularity (VHS) in Bernal stacked BLG. (a) STM topography of ultra-flat pristine BLG/hBN. **(b)** Topography map of white box in (a). Schematic of BLG's lattice overlays the image. The top layer's atoms A_T (B_T) are represented by the red (gray) circles. The blue circles represent B_B atoms. **(c)** Tunneling spectroscopy of BLG taken over an A_T atom with $V_G = -80$ V. Tunneling parameters: $V_S = 0.1$ V, $I = 1.2$ nA, $V_{ac} = 2$ mV. **(d-f)** Spatial dI/dV_S maps of BLG taken for energies at ($V_S = 135$ mV) and near ($V_S = 125$ mV, $V_S = 145$ mV) the top layer's VHS as noted by the arrows in (c). For energies below (d) and above (f) the VHS, A_T and B_T atoms display similar dI/dV_S intensities. At the VHS (e), there is a clear increase in dI/dV_S intensity localized at A_T.

In this study we explore features in BLG's band structure that lack spatially resolved examination. Specifically, we are interested in the high intensity feature observed for $V_G < -51$ V (see Fig. 8.2b-c). In previous tunneling spectroscopy studies on gated Bernal stacked BLG, this feature has been largely ignored,[20,22] attributed to impurities,[18] or fallen outside the experimental V_G range.[19,21] A differential capacitance study attributed electrode-induced disorder to their observation of a strongly suppressed VHS.[25] We demonstrate below that this feature corresponds to BLG's top layer VHS.

Before we explore the spatial dependence of the dI/dV_S peak in the red curve ($V_G = -80$ V) of Fig. 8.2c, we first identify BLG's atomically resolved topographic features. Figure 8.4a shows a constant-current STM topographic map of pristine BLG on hBN. From this image, it is evident that the ultra-flat region used in our study does not contain defects or impurities that could alter the electronic properties of BLG. We also note the absence of a moiré superlattice which indicates that BLG and hBN are properly decoupled by a large mismatch angle.[6,26–28] To map the atomically resolved distribution of the LDOS in BLG, we scan over a 6×6 Å region shown in Fig. 8.4b. A schematic of BLG's lattice is overlaid onto the topographic scan to highlight the location of the atoms probed.[29,30] The high elevation points in the scan correspond to the A_T atoms depicted by the red circles. The saddle points in the scan correspond to the B_T atoms (grey circles) which sit right above the A_B atoms. The lowest elevation points in Fig. 8.4b align with the location of the B_B atoms. However, given that the interlayer separation (~ 3 Å) is considerably larger than the tunneling current decay

length on graphene ($0.25 - 0.5$ Å),[24,31] we do not expect dI/dV_S signal contributions by A_B nor B_B. As a result, STM probes electronic states exclusively from BLG's top layer.

Next, we use the STM's atomically resolved spectroscopic capabilities to determine that the dI/dV_S peak in the red curve ($V_G = -80$ V) of Fig. 8.2c is strongly localized at the A_T atom and thus corresponds to a VHS in BLG. Figure 8.4c shows a $dI/dV_S(V_S)$ spectrum taken at the location of an A_T atom within a V_S range around the CNP. The spectrum in Fig. 8.4c appears shifted to lower V_S when compared to the spectrum in Fig. 8.2c because the former is taken at a higher setpoint, which suppresses the inelastic tunneling channel[32] (see also section 6.2.1). Figures 8.4d-f show spatial dI/dV_S maps plotted using the same relative dI/dV_S scale. Simultaneously acquired constant-current topographic maps enable us to overlay BLG's lattice on them. The dI/dV_S map in Fig. 8.4d (8.4f) was obtained at a V_S voltage 10 mV below (above) the prominent peak at $V_S = 135$ mV (see Fig. 8.4c). The maps in Fig. 8.4d and 8.4f display small variations in dI/dV_S signal intensity which we attribute to artefacts due to tip height variations (see section 8.3.1). In contrast, the dI/dV_S map in Fig. 8.4e acquired at the energy of the prominent peak in Fig. 8.4c ($V_S = 135$ mV), shows a drastic increase in dI/dV_S intensity localized at the A_T atoms (red circles). With this consideration, it is evident that the spectrum in Fig. 8.1c shows that the intense LDOS peak obtained at A_T corresponds to BLG's top layer VHS. The localization of the dI/dV_S intensity peak at the A_T atoms in Fig. 8.4e agrees with our LDOS calculations

in Fig. 8.1c. Thus, we attribute this localization in dI/dV_S intensity to BLG's top layer VHS.

8.3.1 Height variation artefact in dI/dV_S intensity on MLG/hBN

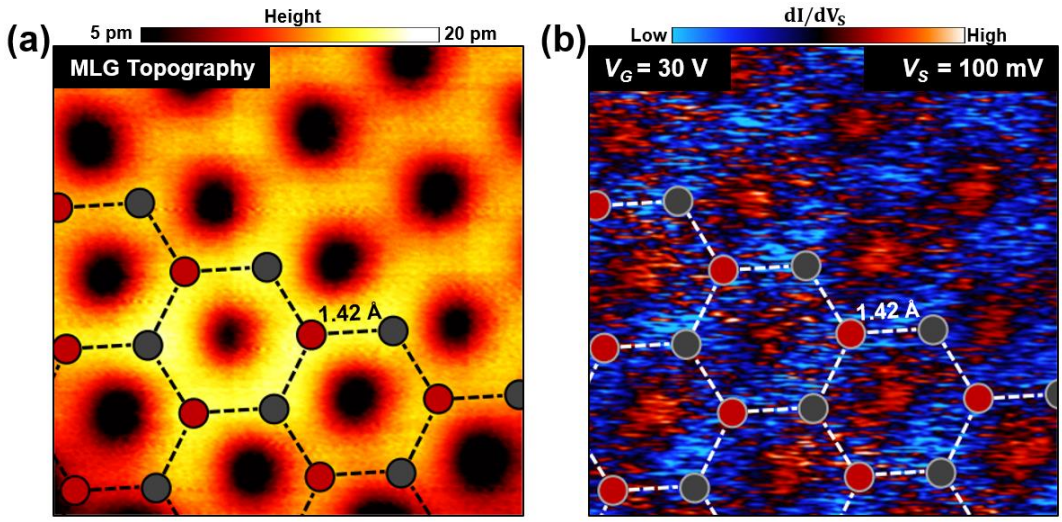

Figure 8.5| Observation of height variation dI/dV_S artefact on monolayer graphene (MLG). (a) STM constant-current topographic map of MLG with its lattice schematic overlaid. **(b)** Spatial dI/dV_S map of the same region as (a) taken at $V_G = 30$ V. The regions of low elevation in (a) correspond to regions of higher dI/dV_S intensity in (b). The region centered on the honeycombs are not expected to contribute to the LDOS. Thus, the apparent higher intensity in (b) suggests contribution to the dI/dV_S signal from neighboring $2p_z$ orbitals as the STM tip gets closer to graphene's surface. Tunneling parameters: $V_S = 0.1$ V; $I = 1.5$ nA; $V_{ac} = 2.5$ mV; $f_{ac} = 400$ Hz.

The spatial dI/dV_S maps in Fig. 8.4d-f display an artefact we attribute to variations in height during the constant-current topographic scan. To further investigate this artefact, we performed a similar spatial dI/dV_S map on MLG/hBN. A constant-current topographic map with overlaid MLG lattice is shown in Fig. 8.5a. Figure 8.5b

shows the spatial dI/dV_S map of MLG acquired at the same time as the map in Fig. 8.5a. By comparing these two images, we see that a higher dI/dV_S intensity region appears at the center of the carbon honeycombs. Since we do not expect the middle of the honeycombs to have a significant contribution to graphene's LDOS, we attribute the higher intensity on these regions to an enhancement of the dI/dV_S signal due to a decrease in tip-sample distance. As discussed above, this artefact is observed in BLG. The B_B atoms in BLG display the highest dI/dV_S intensities in Figs. 8.4d and 8.4f and second highest dI/dV_S intensity in Fig. 8.4e despite being at the lowest topographic points.

8.4 Backgate Modulated Pseudospin Ferromagnetic Transitions in BLG

We electrostatically tune BLG's band structure near the bandgap minimum ($V_G \sim -51$ V $\equiv V_G^0$) and find that the top layer VHS displays considerably different intensities for $V_G < V_G^0$ and $V_G > V_G^0$. Figure 8.6a shows a $dI/dV_S(V_G, V_S)$ map taken within narrower V_G and V_S values than the map in Fig. 8.2b. This image plot displays a suppression in the dI/dV_S signal centered near the CNP which corresponds to BLG's bandgap. We clearly see the evolution of BLG's bandgap as it narrows from $V_G = -20$ V to V_G^0, and widens from V_G^0 to $V_G = -80$ V. As previously noted, the strip with high dI/dV_S intensity (colored yellow) corresponds to BLG's top layer VHS. Remarkably, a feature of similar intensity does not appear on either valence or

conduction band edges for $V_G > V_G^0$. This is a surprising result given that differential capacitance studies in dual gated Bernal stacked BLG predicted and observed layer polarized VHS peaks adjacent to BLG's bandgap minimum.[25,33]

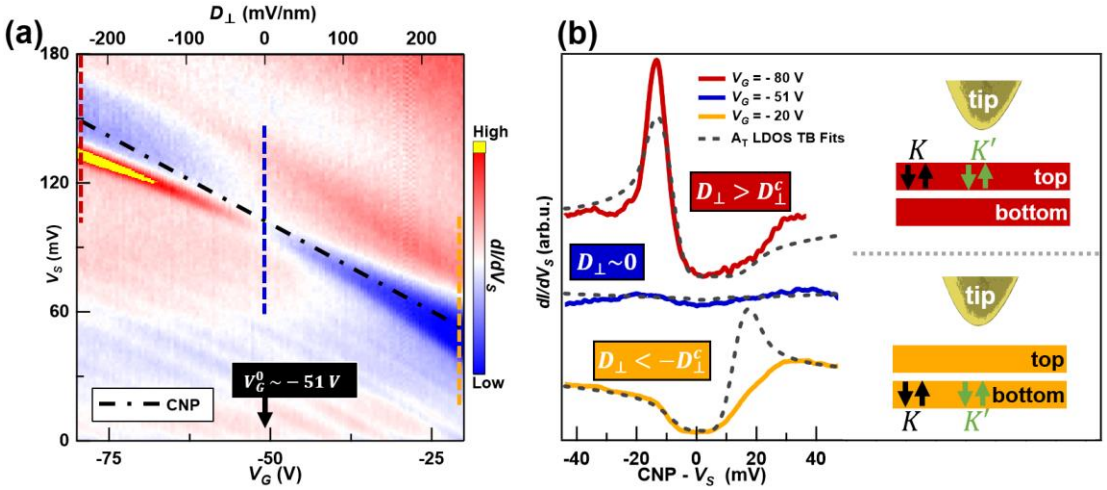

Figure 8.6| Asymmetry in VHS intensities due to layer polarization enhanced by pseudospin ferromagnetism in BLG. (a) $dI/dV_S(V_G, V_S)$ image plot of BLG for values near BLG's bandgap minimum ($V_G^0 \sim -51$ V). The peak corresponding to the top layer VHS has been saturated in yellow to allow for better visibility of surrounding features. **(b)** dI/dV_S spectra taken at $V_G = -80$ V (red), $V_G = V_G^0$ (blue), and $V_G = -20$ V (yellow) corresponding to the vertical dashed lines in (a) and centered at BLG's CNP. Tunneling parameters: $V_S = 0.18$ V; $I = 1.2$ nA; $V_{ac} = 2$ mV; $f_{ac} = 400$ Hz. The dashed gray curves are fitted with the A_T atom's calculated LDOS using TB.[34] The TB fit for the red curve uses layer energies: $\epsilon_{top} = -13.5$ meV and $\epsilon_{bottom} = +13.5$ meV. The TB fit for the blue curve uses layer energies: $\epsilon_{top} = \epsilon_{bottom} = 0$. And, the TB fit for the yellow curve uses layer energies: $\epsilon_{top} = +10\,meV$ and $\epsilon_{bottom} = -10$ meV. All three fits use $\gamma_0 = 3.0$ eV, $\gamma_1 = 0.4$ eV, $\gamma_3 = 0.3$ eV, and $\gamma_4 = 0.15$ eV. Insets: Diagrams of the layer polarization enhanced by pseudospin ferromagnetism (as described by Jung *et al)*[35] in BLG corresponding to values of $V_G < V_G^0$ and $V_G > V_G^0$ depicted by the red and yellow schematics, respectively. The layer polarization in red shows a high intensity dI/dV_S peak corresponding to the VHS; whereas the layer polarization in yellow shows no peak.

By comparing the A_T atom's calculated LDOS with our experimental results we infer that a change in layer polarization and direction of the perpendicular

displacement field ($D_\perp$) between BLG's layers occurs around V_G^0. Figure 8.6b shows dI/dV_S spectra taken at $V_G = -80\ \mathrm{V} < V_G^0$ (red curve), V_G^0 (blue curve), and $V_G = -20\ \mathrm{V} > V_G^0$ (yellow curve), corresponding to the vertical dashed lines in Fig. 8.6a. A recent analysis on the top gating effect of the STM tip on MLG yields a work-function mismatch displacement field[36] of $D_\perp^{tip} \sim +0.44 \pm 0.15\ \mathrm{V/nm}$ for a tip-sample separation between 5 and 10 Å. By using a screening-inclusive dielectric constant[35] $\varepsilon_r \sim 5/2$ for our substrates, we expect a backgate displacement field of $D_\perp^{gate} \sim -0.42\ \mathrm{V/nm}$ at V_G^0. From these observations we infer that the total displacement field $D_\perp$ vanishes near V_G^0 (i.e. $D_\perp = D_\perp^{tip} + D_\perp^{gate} \sim 0$) Additionally, given that the bandgap narrows and then widens as V_G decreases monotonically from -20 to -80 V, we expect a reversal in the sign of layer potential energy between the top and bottom layers. With this in mind, we calculate the A_T atom's LDOS with opposite top and bottom layer potentials. In Fig. 8.6b we include the tight-binding (TB) fits for the $V_G < V_G^0$, $V_G \sim V_G^0$ and $V_G > V_G^0$ cases. For $V_G = -80$ V, we assume top and bottom layer potentials of $\epsilon_{top} = -13.5$ meV and $\epsilon_{bottom} = +13.5$ meV, repectively. For $V_G = V_G^0$, we assume $\epsilon_{top} = \epsilon_{bottom} = 0$. And for $V_G = -20$ V, we assume $\epsilon_{top} = +10$ meV and $\epsilon_{bottom} = -10$ meV. We also note that the estimated bandgap values corresponding to the displacement fields (see top axis in Fig. 8.6a) obtained in Fig. 8.6b reasonably agree with previous estimates for BLG's bandgap.[20,37]

By comparing our TB fits and spectra in Fig. 8.6b, we observe the expected transition in layer energy polarization but we also note a disagreement between VHS

intensities for the $V_G < V_G^0$ and $V_G > V_G^0$ cases. In Fig. 8.1c we showed the LDOS distribution for the case of the displacement field pointing up ($D_\perp > 0$). For this case, the VHS at A_T appears at the valence band edge. For the case of the displacement field pointing down ($D_\perp < 0$), the VHS at A_T should appear at the conduction band edge. The band edge localization of the top layer VHS for both $D_\perp > 0$ and $D_\perp < 0$ cases is captured by the TB fits. In both cases, the simulated LDOS display reasonable agreement with the spectra's dip and shoulder regions. However, there is a clear disagreement between the expected VHS intensity from TB and the spectrum for the $D_\perp < 0$ case. It has been shown that the presence of disorder may suppress and smear the VHS in BLG.[25,33,38] However, we rule out disorder as the cause for the VHS suppression due to the following reasons: (1) the use of hBN as an intermediary substrate decouples BLG from oxide substrate effects,[19] (2) we showed in Fig. 8.4a that we are probing exposed BLG on a clean, flat, and defect-free region, and (3) the VHS for the $D_\perp > 0$ case (red curve in Fig. 8.6b) does not become suppressed or smeared.

To explain the observed asymmetry in VHS intensities between the $D_\perp < 0$ and $D_\perp > 0$ cases, we propose that we are resolving a transition between pseudospin ferromagnetic states in BLG,[35] where pseudospin refers to the layer degree freedom. The lattice Hartree-Fock model for BLG proposed by Jung *et al.*[35] describes the energetics for various competing broken-symmetry layer occupation arrangements in BLG. These competing states include six antiferromagnetic (AF) states [where both layers are occupied evenly], eight ferrimagnetic (Fi) states [where one of the layers has a $1/4$ occupation], and two ferromagnetic (F) states [where a single layer becomes fully

occupied]. Among the predictions made by this model is the existence of insulating states at $D_\perp = 0$ which has been experimentally verified.[39,40] We will not make any claims regarding the $D_\perp \sim 0$ case given that our spectroscopic data does not show distinctive features for $|V_G - V_G^0| < 1.5$ V and the temperature used in our experiments is higher than the previous experimental studies. However, considering a parallel plate capacitor system with a dielectric constant $\varepsilon_r \sim 5/2$,[35] this backgate voltage range translates into a displacement field range of $|D_\perp| < 12\ \mathrm{mV/nm} \equiv D_\perp^c$. Here we define $D_\perp^c$ as the critical perpendicular displacement field magnitude that coincides with the boundary between the AF/Fi and F regimes predicted by Jung *et al.*[35] Thus, for $|V_G - V_G^0| > 1.5$ V (or equivalently $|D_\perp| > D_\perp^c$), the pseudospin ferromagnetic states become the most favorable configurations.

In Fig. 8.6b we have included schematics that show the two BLG ferromagnetic states for the $D_\perp > D_\perp^c$ and $D_\perp < -D_\perp^c$ cases. When $D_\perp < -D_\perp^c$, the bottom layer atoms A_B and B_B in the unit cell get fully occupied by charge carriers with both valley and spin indices as depicted in the yellow schematic in Fig. 8.6b. In a similar but opposite manner, the top layer atoms A_T and B_T become fully occupied when $D_\perp > D_\perp^c$ (see red schematic in Fig. 8.6b).

The drastic accumulation of states onto specific layers predicted using a many-body approach reasonably accounts for our experimental observations. A strong suppression of the VHS for the $D_\perp < -D_\perp^c$ case should be expected given that states accumulate in the bottom layer and are thus not immediately accessible to the STM tip.

Additionally, the VHS intensity for the $D_\perp > D_\perp^c$ case generally appears higher than predicted by TB which can be explained by the accumulation of states on the top layer.

We suspect that our observation of the VHS intensity asymmetry has evaded previous tunneling studies of gated Bernal stacked BLG due to limitations in electrostatic gating ranges,[19,21,30] presence of defects,[41] or lack of highly resolved spectroscopic characterization.[18,20,22] Additionally, with STM we probed BLG's surface with an electrode-to-sample distance an order of magnitude smaller than that achieved by a differential capacitance study on BLG.[25] This study claims to observe a faint signature of the VHS for both $D_\perp > D_\perp^c$ and $D_\perp < -D_\perp^c$ cases. In our experiments, we expect the close proximity of the STM tip to BLG's surface to result in a larger near layer capacitance enhancement.[20,33] This consideration and the absence of substrate-induced disorder can account for the fact that we observed a clear contrast between the two pseudospin ferromagnetic states.

8.5 Atomic Localization of the High Energy Bands in BLG

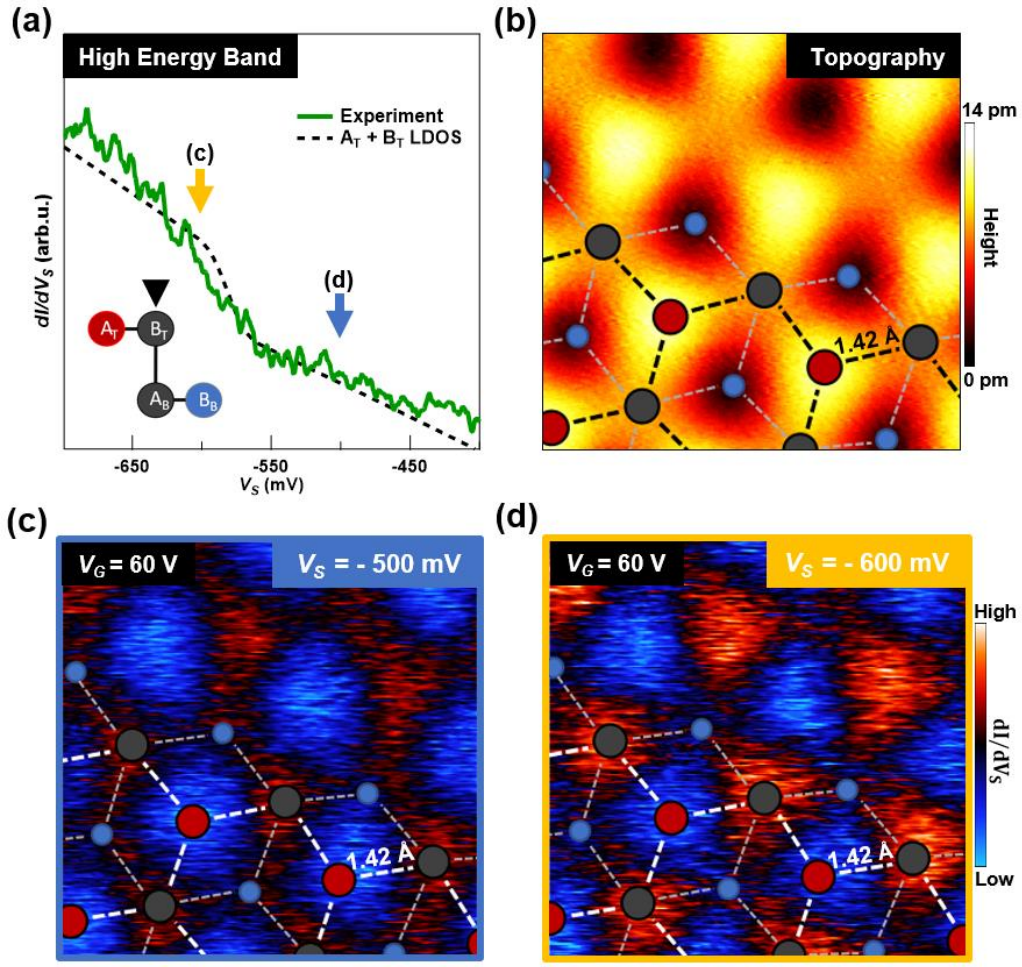

Figure 8.7| Atomically resolved localization of the high energy band (HEB) in BLG. (a) dI/dV_S of BLG near the onset of the HEB plotted in green. The added calculated LDOS for the A_T and B_T atoms is given by the dashed black curve. Tunneling parameters: $V_S = -0.4$ V; $I = 2.5$ nA; $V_{ac} = 5$ mV; $f_{ac} = 400$ Hz. **(b)** Atomically resolved topography of BLG with overlaid lattice schematic. **(c)** and **(d)** Spatial dI/dV_S maps of BLG taken at energies below ($V_S = -500$ mV) and above ($V_S = -600$ mV) the onset of the HEB in BLG corresponding to the blue and orange arrows in (a), respectively. A schematic of BLG's lattice overlays each image. Below the onset of the HEB (c), dI/dV_S intensities between the B_T and B_B sites are similar. Above the onset of the HEB (d), the dI/dV_S signal is more localized at the B_T atom as predicted in Fig. 8.1c.

The procedure to spatially map the evolution of BLG's top layer VHS can also be applied to a more subtle spectroscopic feature such as the HEBs in BLG. Figure 8.1c displays a clear increase in LDOS from the A_B and B_T atoms once the edges of the second set of bands (HEB and HEB*) have been crossed. In our experimental data, these features manifest as shoulders in dI/dV_S curves such as those highlighted by the black arrows in Fig. 8.2c. Figure 8.7a shows a $dI/dV_S(V_S)$ spectrum measured with the STM tip positioned above the B_T atom. Here, the shoulder around $V_S = -550$ mV corresponds to the edge of the HEB. The calculated LDOS of the top layer atoms (A_T and B_T) is shown by the black dashed curve. Figure 8.7b shows a topographic STM map of BLG's lattice. This map is similar to that in Fig. 8.4b, but with a significantly smaller height range. Figures 8.7c and 8.7d show spatial dI/dV_S maps of the same region in Fig. 8.7b taken at V_S biases below (blue arrow in Fig. 8.7a) and above (yellow arrow in Fig. 4a) the onset of the HEB, respectively. Before the onset of the HEB (Fig. 8.7c), the regions of higher dI/dV_S intensity appear similarly distributed between the B_T (grey circles) and B_B (blue circles) atom locations. After the onset of the HEB (Fig. 8.7d), the regions of higher dI/dV_S intensity are clearly localized at the B_T (grey circles) atoms. This behavior is consistent with the enhanced LDOS contribution by the B_T atom depicted in Fig. 8.1c.

We observe a similar localization behavior on the HEB*. We perform a similar analysis as done above but with the upper secondary bands labeled HEB* in Fig. 8.2b. Figure 8.8a shows a $dI/dV_S(V_S)$ spectrum measured with the STM tip positioned above the B_T atom. The shoulder around $V_S = 550$ mV corresponds to the edge of the HEB*.

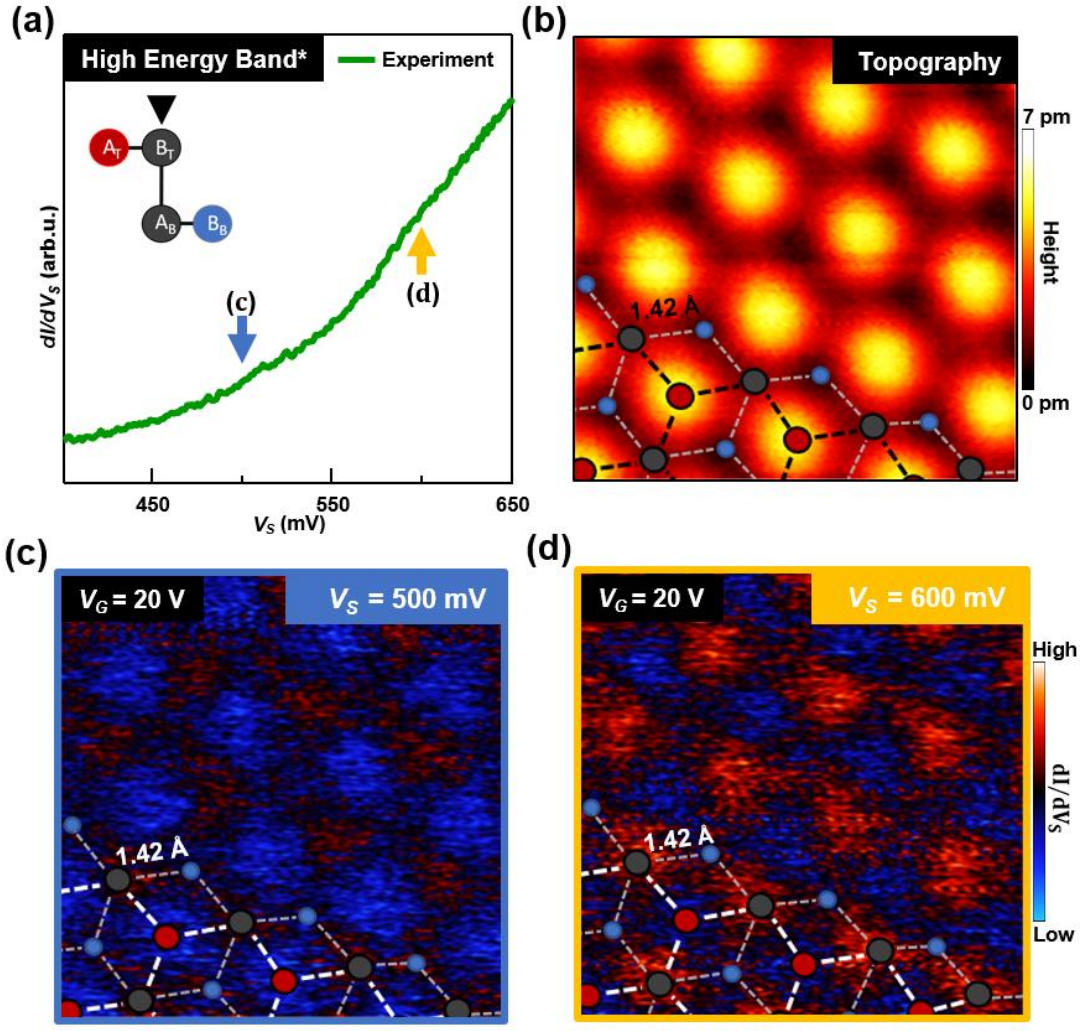

Figure 8.8| Atomically resolved localization of the HEB* in BLG. (a) dI/dV_S of BLG near the onset of the HEB* plotted in green. Tunneling parameters: $V_S = 0.4$ V; $I = 2$ nA; $V_{ac} = 5$ mV; $f_{ac} = 400$ Hz. **(b)** Atomically resolved topography of BLG with overlaid lattice schematic. **(c)** and **(d)** Spatial dI/dV_S maps of BLG taken at energies below ($V_S = 500$ mV) and above ($V_S = 600$ mV) the onset of the HEB in BLG corresponding to the blue and orange arrows in (a), respectively. A schematic of BLG's lattice overlays each image. Below the onset of the HEB (c), dI/dV_S intensities between the B_T and B_B sites are similar. Above the onset of the HEB (d), the dI/dV_S signal is localized at the B_T atom as predicted in Fig. 8.1c.

Figure 8.8b shows a topographic STM map of BLG, similar to Fig. 8.7b. Figures 8.8c and 8.8d show spatial dI/dV_S maps of the same region in Fig. 8.8b taken at V_S biases

below (blue arrow in Fig. 8.8a) and above (yellow arrow in Fig. 8.8a) the onset of the HEB*, respectively. Before the onset of the HEB* (Fig. 8.8c), the regions of higher dI/dV_S intensity appear similarly distributed between the B_T (grey circles) and B_B (blue circles) atoms. After the onset of the HEB* (Fig. 8.8d), the regions of higher dI/dV_S intensity appear localized near the B_T (grey circles) atoms. Again, similar to the case for the HEB, this behavior is consistent with the enhanced LDOS contribution by the B_T atom depicted in Fig. 8.1c.

8.6 Conclusion

In conclusion we have shown that an enhancement in layer polarization attributed to pseudospin ferromagnetism in Bernal stacked BLG, leads to a clear spectroscopic signature of the VHS. As predicted by our localized LDOS calculations, we used spatially and atomically resolved STS to demonstrate that BLG's top layer VHS is localized at a single atom (A_T) in the unit cell. Additionally, we employed the same atomically resolved imaging technique to study the HEBs in BLG. Similarly, we verified our LDOS calculations by experimentally determining that states localize at the overlapping atom (B_T) in the unit cell at the onset of the HEBs. Future studies may focus on the modification of the STM tip's work function[42] to bring the band edges in BLG closer to E_F. Additionally, BLG is expected to host various competing layer occupation states near the bandgap minimum ($V_G \sim -51$ V)[35,43,44] and the energy cost

of some of these states can be tuned via the application of a perpendicular magnetic field. As a consequence, the asymmetry in VHS intensity observed in our experiment could display different behavior when a magnetic field as small as 4 mT is applied.[35] This field should vary the energy costs of different spin occupation states between the top and bottom layer in BLG.

Chapter 8 - References

(1) Van Hove, L. The Occurrence of Singularities in the Elastic Frequency Distribution of a Crystal. *Phys. Rev.* **1953**. https://doi.org/10.1103/PhysRev.89.1189.

(2) Kohn, W.; Luttinger, J. M. New Mechanism for Superconductivity. *Phys. Rev. Lett.* **1965**. https://doi.org/10.1103/PhysRevLett.15.524.

(3) Fleck, M.; Oleś, A. M.; Hedin, L. Magnetic Phases near the Van Hove Singularity In- and-Band Hubbard Models. *Phys. Rev. B - Condens. Matter Mater. Phys.* **1997**. https://doi.org/10.1103/PhysRevB.56.3159.

(4) Rice, T. M.; Scott, G. K. New Mechanism for a Charge-Density-Wave Instability. *Phys. Rev. Lett.* **1975**. https://doi.org/10.1103/PhysRevLett.35.120.

(5) Li, G.; Luican, A.; Lopes Dos Santos, J. M. B.; Castro Neto, A. H.; Reina, A.; Kong, J.; Andrei, E. Y. Observation of Van Hove Singularities in Twisted Graphene Layers. *Nat. Phys.* **2010**. https://doi.org/10.1038/nphys1463.

(6) Wong, D.; Wang, Y.; Jung, J.; Pezzini, S.; Dasilva, A. M.; Tsai, H. Z.; Jung, H. S.; Khajeh, R.; Kim, Y.; Lee, J.; Kahn, S.; Tollabimazraehno, S.; Rasool, H.; Watanabe, K.; Taniguchi, T.; Zettl, A.; Adam, S.; Macdonald, A. H.; Crommie, M. F. Local Spectroscopy of Moiré-Induced Electronic Structure in Gate-Tunable Twisted Bilayer Graphene. *Phys. Rev. B - Condens. Matter Mater. Phys.* **2015**. https://doi.org/10.1103/PhysRevB.92.155409.

(7) Cao, Y.; Fatemi, V.; Fang, S.; Watanabe, K.; Taniguchi, T.; Kaxiras, E.; Jarillo-Herrero, P. Unconventional Superconductivity in Magic-Angle Graphene Superlattices. *Nature* **2018**. https://doi.org/10.1038/nature26160.

(8) Chen, G.; Jiang, L.; Wu, S.; Lyu, B.; Li, H.; Chittari, B. L.; Watanabe, K.; Taniguchi, T.; Shi, Z.; Jung, J.; Zhang, Y.; Wang, F. Evidence of a Gate-Tunable Mott Insulator in a Trilayer Graphene Moiré Superlattice. *Nat. Phys.* **2019**. https://doi.org/10.1038/s41567-018-0387-2.

(9) Yuan Cao, 1, ∗ Daniel Rodan-Legrain, 1 Oriol Rubies-Bigorda, 1 Jeong Min; Park, 1, 2 Kenji Watanabe, 3 Takashi Taniguchi, 3 and Pablo Jarillo-Herrero. Electric Field Tunable Correlated States and Magnetic Phase Transitions in Twisted Bilayer-Bilayer Graphene. **2019**.

(10) Chen, G.; Sharpe, A. L.; Gallagher, P.; Rosen, I. T.; Fox, E. J.; Jiang, L.; Lyu, B.; Li, H.; Watanabe, K.; Taniguchi, T.; Jung, J.; Shi, Z.; Goldhaber-Gordon, D.; Zhang, Y.; Wang, F. Signatures of Tunable Superconductivity in a Trilayer Graphene Moiré Superlattice. *Nature* **2019**. https://doi.org/10.1038/s41586-019-1393-y.

(11) Liu, W.; Kraemer, S.; Sarkar, D.; Li, H.; Ajayan, P. M.; Banerjee, K. Controllable and Rapid Synthesis of High-Quality and Large-Area Bernal Stacked Bilayer Graphene Using Chemical Vapor Deposition. *Chem. Mater.* **2014**. https://doi.org/10.1021/cm4021854.

(12) Qi, Z.; Shi, H.; Zhao, M.; Jin, H.; Jin, S.; Kong, X.; Ruoff, R. S.; Qin, S.; Xue, J.; Ji, H. Chemical Vapor Deposition Growth of Bernal-Stacked Bilayer Graphene by Edge-Selective Etching with H2O. *Chem. Mater.* **2018**. https://doi.org/10.1021/acs.chemmater.8b03393.

(13) Pablo Solís-Fernández*, Yuri Terao, Kenji Kawahara, Wataru Nishiyama, Teerayut Uwanno, Yung-Chang Lin, Keisuke Yamamoto, Hiroshi Nakashima, Kosuke Nagashio, Hiroki Hibino, Kazu Suenaga, and H. A. Isothermal Growth and Stacking Evolution in Highly Uniform Bernal-Stacked Bilayer Graphene. *ACS Nano Artic. ASAP* **2020**. https://doi.org/https://doi.org/10.1021/acsnano.0c00645.

(14) Malard, L. M.; Nilsson, J.; Elias, D. C.; Brant, J. C.; Plentz, F.; Alves, E. S.; Castro Neto, A. H.; Pimenta, M. A. Probing the Electronic Structure of Bilayer Graphene by Raman Scattering. *Phys. Rev. B - Condens. Matter Mater. Phys.* **2007**. https://doi.org/10.1103/PhysRevB.76.201401.

(15) Mkhitaryan, V. V.; Raikh, M. E. Disorder-Induced Tail States in Gapped Bilayer Graphene. *Phys. Rev. B - Condens. Matter Mater. Phys.* **2008**. https://doi.org/10.1103/PhysRevB.78.195409.

(16) McCann, E.; Koshino, M. The Electronic Properties of Bilayer Graphene. *Reports Prog. Phys.* **2013**. https://doi.org/10.1088/0034-4885/76/5/056503.

(17) Tersoff, J.; Hamann, D. R. Theory of the Scanning Tunneling Microscope. *Phys. Rev. B* **1985**. https://doi.org/10.1103/PhysRevB.31.805.

(18) Deshpande, A.; Bao, W.; Zhao, Z.; Lau, C. N.; Leroy, B. J. Mapping the Dirac Point in Gated Bilayer Graphene. *Appl. Phys. Lett.* **2009**. https://doi.org/10.1063/1.3275755.

(19) Rutter, G. M.; Jung, S.; Klimov, N. N.; Newell, D. B.; Zhitenev, N. B.; Stroscio, J. A. Microscopic Polarization in Bilayer Graphene. *Nat. Phys.* **2011**. https://doi.org/10.1038/nphys1988.

(20) Holdman, G. R.; Krebs, Z. J.; Behn, W. A.; Smith, K. J.; Watanabe, K.; Taniguchi, T.; Brar, V. W. Dynamic Band Structure and Capacitance Effects in Scanning Tunneling Spectroscopy of Bilayer Graphene. *Appl. Phys. Lett.* **2019**. https://doi.org/10.1063/1.5127078.

(21) Davenport, J. L.; Ge, Z.; Joucken, F.; Eberth A. Quezada-Lopez, T. T.; Watanabe, K.; Jr., J. V. Unraveling the Tunneling Spectrum of Bernal-Stacked Bilayer Graphene.

(22) Yankowitz, M.; Wang, J. I. J.; Li, S.; Birdwell, A. G.; Chen, Y. A.; Watanabe, K.; Taniguchi, T.; Quek, S. Y.; Jarillo-Herrero, P.; LeRoy, B. J. Band Structure Mapping of Bilayer Graphene via Quasiparticle Scattering. *APL Mater.* **2014**. https://doi.org/10.1063/1.4890543.

(23) Velasco, J.; Lee, J.; Wong, D.; Kahn, S.; Tsai, H. Z.; Costello, J.; Umeda, T.; Taniguchi, T.; Watanabe, K.; Zettl, A.; Wang, F.; Crommie, M. F. Visualization and Control of Single-Electron Charging in Bilayer Graphene Quantum Dots. *Nano Lett.* **2018**. https://doi.org/10.1021/acs.nanolett.8b01972.

(24) Zhang, Y.; Brar, V. W.; Wang, F.; Girit, C.; Yayon, Y.; Panlasigui, M.; Zettl, A.; Crommie, M. F. Giant Phonon-Induced Conductance in Scanning Tunnelling Spectroscopy of Gate-Tunable Graphene. *Nat. Phys.* **2008**. https://doi.org/10.1038/nphys1022.

(25) Young, A. F.; Dean, C. R.; Meric, I.; Sorgenfrei, S.; Ren, H.; Watanabe, K.; Taniguchi, T.; Hone, J.; Shepard, K. L.; Kim, P. Electronic Compressibility of Layer-Polarized Bilayer Graphene. *Phys. Rev. B - Condens. Matter Mater. Phys.* **2012**. https://doi.org/10.1103/PhysRevB.85.235458.

(26) Xue, J.; Sanchez-Yamagishi, J.; Bulmash, D.; Jacquod, P.; Deshpande, A.; Watanabe, K.; Taniguchi, T.; Jarillo-Herrero, P.; Leroy, B. J. Scanning Tunnelling Microscopy and Spectroscopy of Ultra-Flat Graphene on Hexagonal Boron Nitride. *Nat. Mater.* **2011**. https://doi.org/10.1038/nmat2968.

(27) Freitag, N. M.; Chizhova, L. A.; Nemes-Incze, P.; Woods, C. R.; Gorbachev, R. V.; Cao, Y.; Geim, A. K.; Novoselov, K. S.; Burgdörfer, J.; Libisch, F.; Morgenstern, M. Electrostatically Confined Monolayer Graphene Quantum Dots with Orbital and Valley Splittings. *Nano Lett.* **2016**. https://doi.org/10.1021/acs.nanolett.6b02548.

(28) Kim, H.; Leconte, N.; Chittari, B. L.; Watanabe, K.; Taniguchi, T.; Macdonald, A. H.; Jung, J.; Jung, S. Accurate Gap Determination in Monolayer and Bilayer Graphene/ h-BN Moiré Superlattices. *Nano Lett.* **2018**. https://doi.org/10.1021/acs.nanolett.8b03423.

(29) Lauffer, P.; Emtsev, K. V.; Graupner, R.; Seyller, T.; Ley, L.; Reshanov, S. A.; Weber, H. B. Atomic and Electronic Structure of Few-Layer Graphene on SiC(0001) Studied with Scanning Tunneling Microscopy and Spectroscopy. *Phys. Rev. B - Condens. Matter Mater. Phys.* **2008**. https://doi.org/10.1103/PhysRevB.77.155426.

(30) Kim, K. S.; Kim, T. H.; Walter, A. L.; Seyller, T.; Yeom, H. W.; Rotenberg, E.; Bostwick, A. Visualizing Atomic-Scale Negative Differential Resistance in Bilayer Graphene. *Phys. Rev. Lett.* **2013**. https://doi.org/10.1103/PhysRevLett.110.036804.

(31) Lagoute, J.; Joucken, F.; Repain, V.; Tison, Y.; Chacon, C.; Bellec, A.; Girard, Y.; Sporken, R.; Conrad, E. H.; Ducastelle, F.; Palsgaard, M.; Andersen, N. P.; Brandbyge, M.; Rousset, S. Giant Tunnel-Electron Injection in Nitrogen-Doped Graphene. *Phys. Rev. B - Condens. Matter Mater. Phys.* **2015**. https://doi.org/10.1103/PhysRevB.91.125442.

(32) Néel, N.; Steinke, C.; Wehling, T. O.; Kröger, J. Inelastic Electron Tunneling into Graphene Nanostructures on a Metal Surface. *Phys. Rev. B* **2017**. https://doi.org/10.1103/PhysRevB.95.161410.

(33) Young, A. F.; Levitov, L. S. Capacitance of Graphene Bilayer as a Probe of Layer-Specific Properties. *Phys. Rev. B - Condens. Matter Mater. Phys.* **2011**. https://doi.org/10.1103/PhysRevB.84.085441.

(34) Moldovan, D.; Anđelković, M.; Peeters Francois. pybinding v0.9.4: a Python package for tight-binding calculations http://doi.org/10.5281/zenodo.826942.

(35) Jung, J.; Zhang, F.; MacDonald, A. H. Lattice Theory of Pseudospin Ferromagnetism in Bilayer Graphene: Competing Interaction-Induced Quantum Hall States. *Phys. Rev. B - Condens. Matter Mater. Phys.* **2011**. https://doi.org/10.1103/PhysRevB.83.115408.

(36) Quezada-López, E. A.; Ge, Z.; Taniguchi, T.; Watanabe, K.; Joucken, F.; Velasco, J. Comprehensive Electrostatic Modeling of Exposed Quantum Dots in Graphene/Hexagonal Boron Nitride Heterostructures. *Nanomaterials* **2020**. https://doi.org/10.3390/nano10061154.

(37) Zhang, Y.; Tang, T. T.; Girit, C.; Hao, Z.; Martin, M. C.; Zettl, A.; Crommie, M. F.; Shen, Y. R.; Wang, F. Direct Observation of a Widely Tunable Bandgap in Bilayer Graphene. *Nature* **2009**. https://doi.org/10.1038/nature08105.

(38) Nilsson, J.; Castro Neto, A. H. Impurities in a Biased Graphene Bilayer. *Phys.*

Rev. Lett. **2007**. https://doi.org/10.1103/PhysRevLett.98.126801.

(39) Velasco, J.; Jing, L.; Bao, W.; Lee, Y.; Kratz, P.; Aji, V.; Bockrath, M.; Lau, C. N.; Varma, C.; Stillwell, R.; Smirnov, D.; Zhang, F.; Jung, J.; MacDonald, A. H. Transport Spectroscopy of Symmetry-Broken Insulating States in Bilayer Graphene. *Nat. Nanotechnol.* **2012**. https://doi.org/10.1038/nnano.2011.251.

(40) Freitag, F.; Trbovic, J.; Weiss, M.; Schönenberger, C. Spontaneously Gapped Ground State in Suspended Bilayer Graphene. *Phys. Rev. Lett.* **2012**. https://doi.org/10.1103/PhysRevLett.108.076602.

(41) Chandni, U.; Watanabe, K.; Taniguchi, T.; Eisenstein, J. P. Signatures of Phonon and Defect-Assisted Tunneling in Planar Metal-Hexagonal Boron Nitride-Graphene Junctions. *Nano Lett.* **2016**. https://doi.org/10.1021/acs.nanolett.6b04369.

(42) Zhao, Y.; Wyrick, J.; Natterer, F. D.; Rodriguez-Nieva, J. F.; Lewandowski, C.; Watanabe, K.; Taniguchi, T.; Levitov, L. S.; Zhitenev, N. B.; Stroscio, J. A. Creating and Probing Electron Whispering-Gallery Modes in Graphene. *Science (80-.).* **2015**. https://doi.org/10.1126/science.aaa7469.

(43) Kharitonov, M. Canted Antiferromagnetic Phase of the N=0 Quantum Hall State in Bilayer Graphene. *Phys. Rev. Lett.* **2012**. https://doi.org/10.1103/PhysRevLett.109.046803.

(44) Kharitonov, M. Antiferromagnetic State in Bilayer Graphene. *Phys. Rev. B - Condens. Matter Mater. Phys.* **2012**. https://doi.org/10.1103/PhysRevB.86.195435.

Chapter 9 – Conclusion

As one of my adviser's first graduate students working to set up a new 2D materials lab, I was tasked with benchmarking some of the latest (at the time) results in the field. When I began my graduate studies, this field had vastly studied (among other things) the electrical properties of graphene and was in the midst of exploring ways to apply and enhance these properties by interfacing graphene with other 2D materials such as hexagonal boron nitride (hBN). As a result, I was able to gather and apply knowledge from a mature and still active field. This enabled me to pay closer attention to experimental peculiarities as I assembled and characterized the graphene/hBN heterostructure from the bottom up. The experiments presented in Ch.5-8 are, therefore, a byproduct of a global scientific effort started in 2004 which continues to actively further our understanding of the physical world as well as to provide viable solutions for current and future challenges.

9.1 What We Learned Through Our Journey from the Bottom to the Top

We started our journey at the **bottom** in Ch. 5, where silicon oxide (SiO_2) meets hBN. There we learned that electric fields on the order of $\sim 1\,\mathrm{V/nm}$ lead to the accumulation of charged defects at the SiO_2/hBN interface. By exposing graphene/hBN field effect transistors (FETs) to such high electric fields we demonstrated reversible

changes in our graphene FETs' electronic properties. A range of electric field intensities and different temperatures were examined in Ch. 5. We found that shifts in graphene's charge neutrality point (CNP) increase as both the electric field intensity and temperature are increased. Due to the similarities between CNP shifts in our study and prior works on Poole-Frenkel emissions, we applied the Poole-Frenkel model to explain the mechanism by which high electric fields induce persistent doping in our graphene/hBN FETs. Using insight from our proposed mechanism, we assembled an FET heterostructure that eliminates persistent unintended doping. This FET contains an additional layer of graphite underneath the graphene/hBN stack. Here, graphite acts as a backgate and, importantly, prevents charge buildup in the hBN. The suppression of charge buildup in hBN is important for ARPES and high temperature electrical transport studies because it recovers controllable device doping.[1–3] Nonetheless, studies that utilize doping in 2D materials can incorporate the doping technique we presented in Ch.5 to enhance *n*-doping in a given 2D material. Finally, this doping technique can be used to quantify deliberate defect incorporation in hBN, which has been employed by several quantum emitter studies.[4–6] Synthesis processes that deliberately increase defect densities in hBN may utilize high exposure to high electric fields to attain an approximate measure of defect densities based on the magnitude of CNP shifts.

Then, in Ch. 6 and Ch. 7, our journey progressed to the **interface** between graphene and hBN. In Ch. 6 we learned how to corral graphene charges using an scanning tunneling microscope (STM) on a graphene/hBN heterostructure by creating a persistent and embedded local gate in the hBN[7–10] by a similar mechanism to that in

Ch. 5. This embedded local gate enables the pseudo-confinement of graphene charge carriers *via* Klein tunneling—creating a structure resembling a quantum dot (QD). In particular, we showed that incorporating the STM tip's electrostatics in conjunction with that of the underlying hBN charges enables a more complete understanding of the experimental spectroscopic features of exposed graphene QDs. We compared experimental STM data obtained on graphene QDs with simulations that include the tip-induced potential as well as with simulations that neglect this potential. The agreement between experiments and simulations is greater when the simulations include the influence of the tip. Our analysis also reveals the intriguing possibility of studying the interplay between states confined by the potential due to hBN defects and the potential due to the STM tip. Studies that seek to reduce such interplay may use insights from our simulations to mitigate the tip's effect by tuning a backgate voltage. Additionally, the interaction between these two QDs could potentially be used to emulate relativistic molecular behavior or other complex coupled QD systems.[10]

Still at the **interface**, in Ch.7 we looked at the interplay between bilayer graphene (BLG) and hBN in regard to their relative crystallographic alignment. We performed a spatially resolved investigation of a BLG/hBN heterostructure using an advanced photoemission spectroscopy technique—nanoARPES. With this technique, we were able to directly extract tight-binding parameters for BLG on hBN. We showed that nanoARPES can reveal variations in crystallographic alignment between BLG and hBN. These latter findings were confirmed by STM imaging, which showed areas with different Moiré periodicities due to numerous domains with various orientations. We

attributed this variation of lattice alignment to an inhomogeneous BLG/hBN alignment induced by standard ultra-high vacuum heating used to prepare samples for ARPES and STM characterization. These results substantially improve our understanding of the BLG/hBN heterostructure and provide researchers using this heterostructure with a direct picture of the electronic bands resolved in reciprocal space with nanoscale resolution. In addition, the spatial variation of lattice alignment between the BLG and the supporting hBN that we evidenced here is important for researchers investigating these samples with spatially averaging probes such as electronic transport or optical spectroscopy.

Finally, we reached the **top** in Ch.8, where BLG is decoupled from and yet is still supported by hBN. In Ch.8 we primarily focused on the intricate and tunable electronic behavior of BLG down to the atomic scale. Such an achievement was realized partly due to hBN's ultra-flat and inert properties that make it an ideal substrate for graphene—leading to unprecedented STM probe stability. We showed that an enhancement in layer polarization due to pseudospin ferromagnetism in Bernal stacked BLG can lead to a clear spectroscopic signature of BLG's Van Hove singularity (VHS). As predicted by our local density of states (LDOS) calculations, we used spatially and atomically resolved scanning tunneling spectroscopy (STS) to demonstrate that such VHS is localized at a single atom in BLG's top layer. Additionally, we employed the same atomically resolved imaging technique to study the higher energy bands in BLG. Similarly, we verified our LDOS calculations by experimentally determining that states localize at the dimer site in the unit cell at the onset of their band edges. Future studies

may focus on the modification of the STM tip's work function[11] to bring the band edges in BLG even closer to the Fermi level (E_F), providing further insights into many-body phenomena in BLG. Additionally, the application of a perpendicular magnetic field and temperature variability should enable the exploration of the pseudospin ferromagnetic transitions in BLG[12–14] for small electric field intensities.

9.2 Prospects for Future Investigations

An intriguing direction for further studying the phenomena explored in Ch. 6 and Ch. 8 involves tuning the work function of the STM tip. The STM tip's work function could possibly be changed by exposure to deuterium gas as done by Zhao *et al*[11] or by calibrating the STM tip onto a crystalline surface with a different work function than gold. By modifying the work function difference between graphene and the STM tip ($\Delta\Phi$) such that $\Delta\Phi \geq 0$, could provide different results for the spatially resolved spectroscopic characterization of circular *pn* junctions as done in Ch. 6. Furthermore, having $\Delta\Phi \geq 0$ opens up the possibility of bringing the bandgap minimum in BLG close to $V_G = 0$. This would bring the observed VHS in Ch. 8 closer to E_F which could enable the partial filling of the flat bands at the VHS, as was done in twisted graphene studies.[15–17]

In Ch. 8, I showed that many body effects are present near the VHS in BLG. This result may be explored further. For example, BLG is expected to host various competing layer occupation states near the bandgap minimum ($V_G \sim -51$ V).[12–14] The

energy cost of some of these states can be tuned via the application of a perpendicular magnetic field. As a consequence, the asymmetry in VHS intensity observed in Ch. 8 should display different behavior after a magnetic field as small as 4 mT is applied.[12] Additionally, the technique for creating quasibound states in Ch. 6 may be applied to create circular regions in BLG such that the inner circle has a different top layer occupation than the surrounding bulk. This could possibly lead to the observation of a new kind of confined states in BLG subject to interaction effects.

Chapter 9 - References

(1) Cadore, A. R.; Mania, E.; Watanabe, K.; Taniguchi, T.; Lacerda, R. G.; Campos, L. C. Thermally Activated Hysteresis in High Quality Graphene/ *h* - BN Devices. *Appl. Phys. Lett.* **2016**, *108* (23), 233101. https://doi.org/10.1063/1.4953162.

(2) Joucken, F.; Avila, J.; Ge, Z.; Quezada-Lopez, E. A.; Yi, H.; Le Goff, R.; Baudin, E.; Davenport, J. L.; Watanabe, K.; Taniguchi, T.; Asensio, M. C.; Velasco, J. Visualizing the Effect of an Electrostatic Gate with Angle-Resolved Photoemission Spectroscopy. *Nano Lett.* **2019**. https://doi.org/10.1021/acs.nanolett.9b00649.

(3) Volmer, F.; Ersfeld, M.; Rathmann, L.; Heithoff, M.; Kotewitz, L.; Watanabe, K.; Taniguchi, T.; Stampfer, C.; Beschoten, B. How the Dynamic of Photo-Induced Gate Screening Complicates the Investigation of Valley Physics in 2D Materials. *arxiv* **2020**.

(4) Noh, G.; Choi, D.; Kim, J. H.; Im, D. G.; Kim, Y. H.; Seo, H.; Lee, J. Stark Tuning of Single-Photon Emitters in Hexagonal Boron Nitride. *Nano Lett.* **2018**. https://doi.org/10.1021/acs.nanolett.8b01030.

(5) Vogl, T.; Campbell, G.; Buchler, B. C.; Lu, Y.; Lam, P. K. Fabrication and Deterministic Transfer of High-Quality Quantum Emitters in Hexagonal Boron Nitride. *ACS Photonics* **2018**. https://doi.org/10.1021/acsphotonics.8b00127.

(6) Ziegler, J.; Klaiss, R.; Blaikie, A.; Miller, D.; Horowitz, V. R.; Alemán, B. J. Deterministic Quantum Emitter Formation in Hexagonal Boron Nitride via Controlled Edge Creation. *Nano Lett.* **2019**. https://doi.org/10.1021/acs.nanolett.9b00357.

(7) Lee, J.; Wong, D.; Velasco, J.; Rodriguez-Nieva, J. F.; Kahn, S.; Tsai, H. Z.; Taniguchi, T.; Watanabe, K.; Zettl, A.; Wang, F.; Levitov, L. S.; Crommie, M. F. Imaging Electrostatically Confined Dirac Fermions in Graphene Quantum Dots. *Nat. Phys.* **2016**. https://doi.org/10.1038/nphys3805.

(8) Ghahari, F.; Walkup, D.; Gutiérrez, C.; Rodriguez-Nieva, J. F.; Zhao, Y.; Wyrick, J.; Natterer, F. D.; Cullen, W. G.; Watanabe, K.; Taniguchi, T.; Levitov, L. S.; Zhitenev, N. B.; Stroscio, J. A. An on/off Berry Phase Switch in Circular Graphene Resonators. *Science (80-.).* **2017**. https://doi.org/10.1126/science.aal0212.

(9) Gutiérrez, C.; Walkup, D.; Ghahari, F.; Lewandowski, C.; Rodriguez-Nieva, J. F.; Watanabe, K.; Taniguchi, T.; Levitov, L. S.; Zhitenev, N. B.; Stroscio, J. A. Interaction-Driven Quantum Hall Wedding Cake–like Structures in Graphene Quantum Dots. *Science (80-.).* **2018**. https://doi.org/10.1126/science.aar2014.

(10) Walkup, D.; Ghahari, F.; Gutiérrez, C.; Watanabe, K.; Taniguchi, T.; Zhitenev, N. B.; Stroscio, J. A. Tuning Single-Electron Charging and Interactions between Compressible Landau Level Islands in Graphene. *Phys. Rev. B* **2020**. https://doi.org/10.1103/PhysRevB.101.035428.

(11) Zhao, Y.; Wyrick, J.; Natterer, F. D.; Rodriguez-Nieva, J. F.; Lewandowski, C.; Watanabe, K.; Taniguchi, T.; Levitov, L. S.; Zhitenev, N. B.; Stroscio, J. A. Creating and Probing Electron Whispering-Gallery Modes in Graphene. *Science (80-.).* **2015**. https://doi.org/10.1126/science.aaa7469.

(12) Jung, J.; Zhang, F.; MacDonald, A. H. Lattice Theory of Pseudospin Ferromagnetism in Bilayer Graphene: Competing Interaction-Induced Quantum Hall States. *Phys. Rev. B - Condens. Matter Mater. Phys.* **2011**. https://doi.org/10.1103/PhysRevB.83.115408.

(13) Kharitonov, M. Canted Antiferromagnetic Phase of the N=0 Quantum Hall State in Bilayer Graphene. *Phys. Rev. Lett.* **2012**. https://doi.org/10.1103/PhysRevLett.109.046803.

(14) Kharitonov, M. Antiferromagnetic State in Bilayer Graphene. *Phys. Rev. B - Condens. Matter Mater. Phys.* **2012**. https://doi.org/10.1103/PhysRevB.86.195435.

(15) Cao, Y.; Fatemi, V.; Fang, S.; Watanabe, K.; Taniguchi, T.; Kaxiras, E.; Jarillo-Herrero, P. Unconventional Superconductivity in Magic-Angle Graphene Superlattices. *Nature* **2018**. https://doi.org/10.1038/nature26160.

(16) Lu, X.; Stepanov, P.; Yang, W.; Xie, M.; Aamir, M. A.; Das, I.; Urgell, C.; Watanabe, K.; Taniguchi, T.; Zhang, G.; Bachtold, A.; MacDonald, A. H.; Efetov, D. K. Superconductors, Orbital Magnets and Correlated States in Magic-Angle Bilayer Graphene. *Nature* **2019**. https://doi.org/10.1038/s41586-019-1695-0.

(17) Li, G.; Luican, A.; Lopes Dos Santos, J. M. B.; Castro Neto, A. H.; Reina, A.; Kong, J.; Andrei, E. Y. Observation of Van Hove Singularities in Twisted Graphene Layers. *Nat. Phys.* **2010**. https://doi.org/10.1038/nphys1463.

Appendix Section

Appendix A: Polymer Substrate Preparation

The following steps outline the process of preparing a polymer substrate for use in the graphene/hBN heterostructure assembly discussed in Ch. 4.

Steps:

1. Cut a glass slide into squares using a diamond-tip pen and carefully snap them with your hands (see Fig. A.1). **Discard** any glass squares that have nicks or other significant damage on the edges as these may increase the chances of cracking and braking during the assembly process.

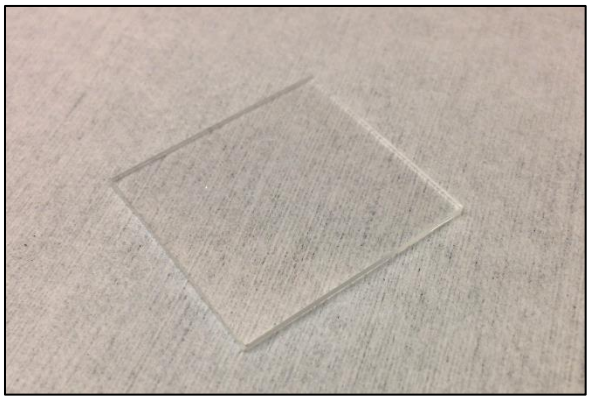

Figure A.1| Cut glass slide.

2. Blow clean nitrogen gas onto the cut slide to remove any shards or dust. Rinse the glass square with acetone and isopropanol. Immediately after, dry the glass square with nitrogen gas.
3. Gently and slowly place Clear Tape™ onto the clean glass square (see Fig. A.2). Then, with your index finger press the tape onto the glass with a steam-rolling motion to minimize the amount of bubbles formed. Finally, remove the excess tape from the edges with a clean razor blade.

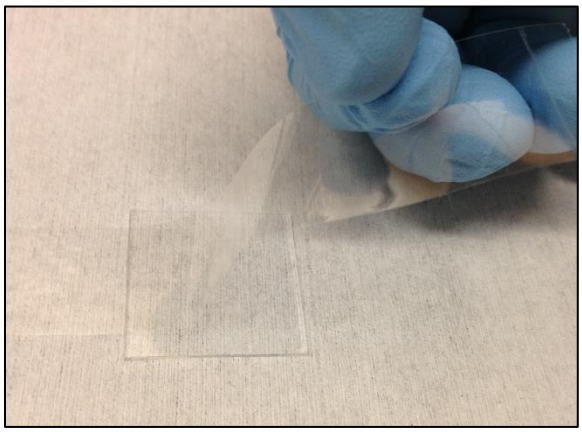

Figure A.2| Placing tape on glass slide.

4. Before spin coating the slide with MMA solution (10: 1 MIBK:MMA by mass) onto the glass slide and tape, do the following:
   - Squirt some acetone onto the tape, wait ~5 seconds.
   - Run the spinner at ~3000 RPM for 4 seconds and squirt a small amount of IPA as the square spins to rinse the Acetone off. Letting the acetone dry creates groves on the PVC side of the tape which allows for better polymer adhesion.

- Turn the spinner off.
- To apply the MMA place 9 drops of MMA solution using the glass dropper bottle in a 3×3 array (see Fig. A.3).
- **Immediately** after, turn on spinner and increase the speed from $\sim$500 RPM to 1300 RPM in about 3 to 4 seconds.
- Let spinner run for 1 minute before reducing the spinner's rotation speed down to $\sim$500 RPM.
- After a few seconds, turn the spinner off.

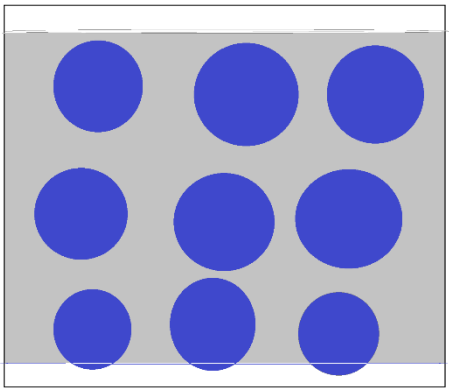

Figure A.3| MMA solution droplets on a tape/glass slide. The blue circles represent the MMA droplets. The gray area represents the tape which sits on the clear glass.

Appendix B: Electron Beam Lithography Parameters

The following screenshots show the parameters used in patterning with the NPGS program (https://www.jcnabity.com). There are two run files “e” and “b” for small and large electrodes, respectively (see the top “File” label on each screenshot). We consider small electrodes those with widths between a few micrometers to a few tens of micrometers. Large electrodes are features between a few tens to a few hundred micrometers. The right column of the images below contain the exposure, magnification, and line density parameters.

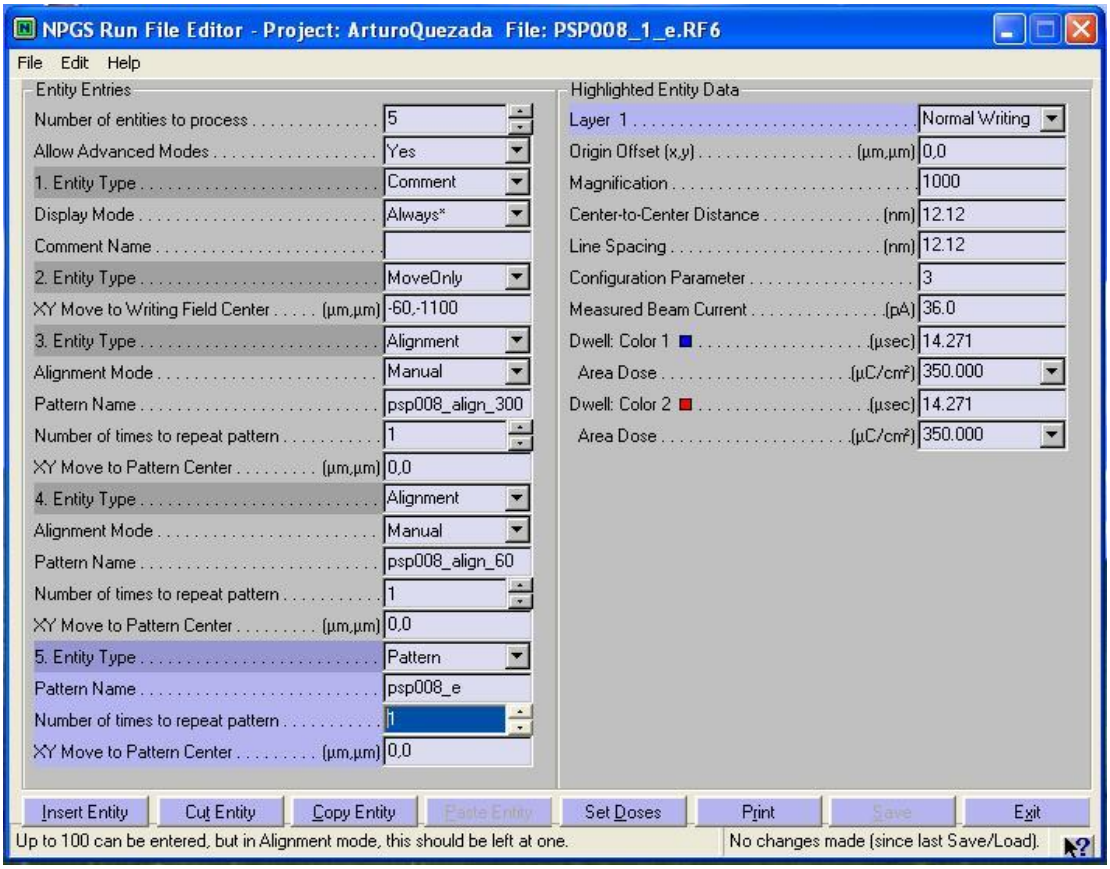

Figure B.1| NPGS parameters for small electrodes.

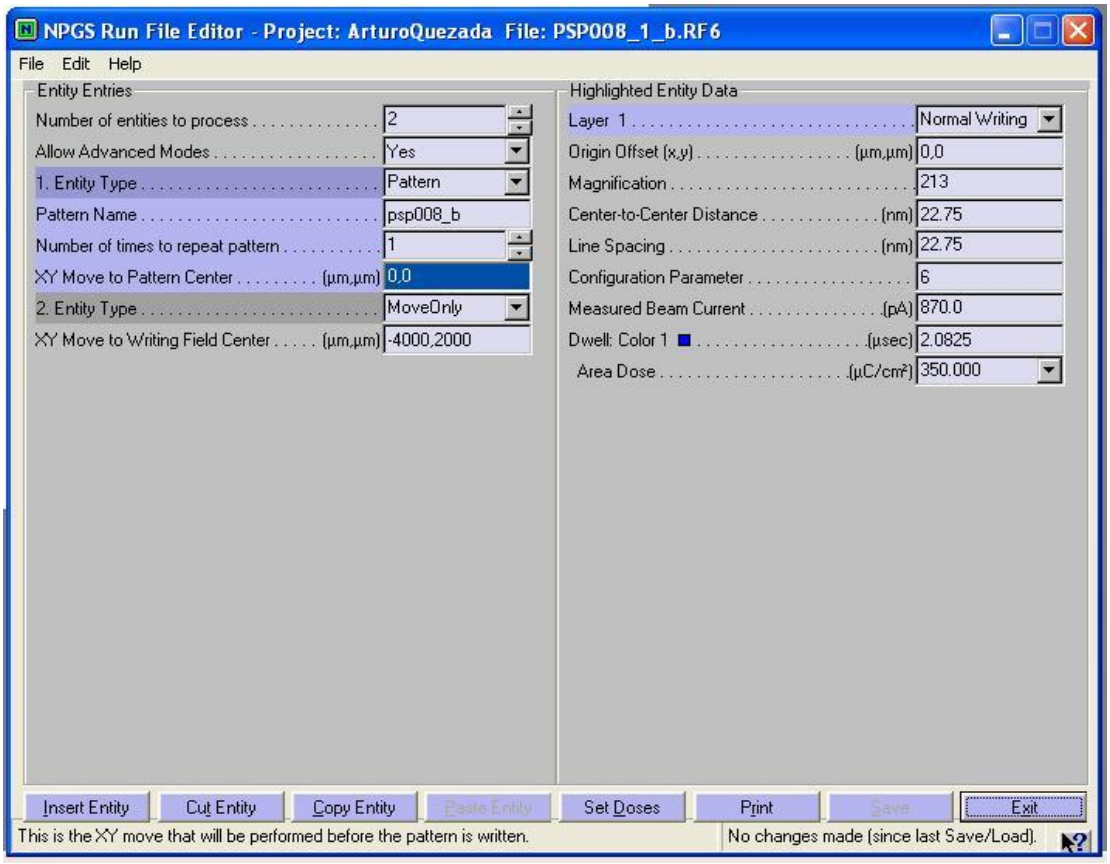

Figure B.2| NPGS parameters for large electrodes.

Appendix C: Making a Circular *p*-*n* Junction with the STM

The following steps outline the process of creating a circular *p*-*n* junction or quantum dot (QD) on the surface of monolayer graphene (MLG) in order to probe quasibound states as done in Ch. 6. These steps assume that the STM tip has been properly calibrated on the surface of Au(111) as outlined in Ch. 4.

Part 1. Locate a clean region on the surface of MLG

After landing the STM tip on the surface of MLG, perform topographic scans on small windows ($\sim 2 \times 2$ nm) on a square grid with an area of about 200×200 nm. About 16 windows will suffice during this small-window sampling process. The QDs are generally ~ 150 nm in diameter. Therefore, the grid must be large enough to contain the QD while ensuring that there are no contaminants present on the surface. After ensuring that the windows sampled only contain pristine and flat graphene, proceed to scanning the entire 200×200 nm area.

Part 2. Create a *p*-doped QD

- Move the STM tip over the center of the clean region found in Part 1 and set the current (I) to 500 pA and the sample bias (V_S) to $+500$ mV while the tunneling current feedback is engaged.

- Change the backgate voltage (V_G) to an arbitrary positive value. A typical value used is $V_G = +30$ V.
- Lift the STM tip 2 nm off the surface of MLG and immediately change V_S to $+5$ V.
- After one minute, switch V_S back to $+500$ mV and bring the tip back down by 2 nm (the same height the tip was lifted by).

Part 2.5. (Alternatively) Create an *n*-doped QD

- To create an *n* doped QD you must follow the same steps as in Part 2 but use a negative value for V_G. A typical value used is $V_G = -30$ V.

Part 3. Characterize the *p*-doped QD

- Change the setpoint to values used for QD characterization. The typical values used are $I = 1$ nA and $V_S < -100$ mV.
- Change V_G to some value between zero and the V_G value used in Part 2 (e.g. $V_G = +15$ V for a *p* doped QD or $V_G = -15$ V for a *n* doped QD). Perform a spatial dI/dV_S map along a line that crosses the center of the QD (see Ch. 6). We call this type of spatial sampling a "line scan". You do not need a high-resolution line scan here. You may perform a scan that takes ~ 20 minutes.

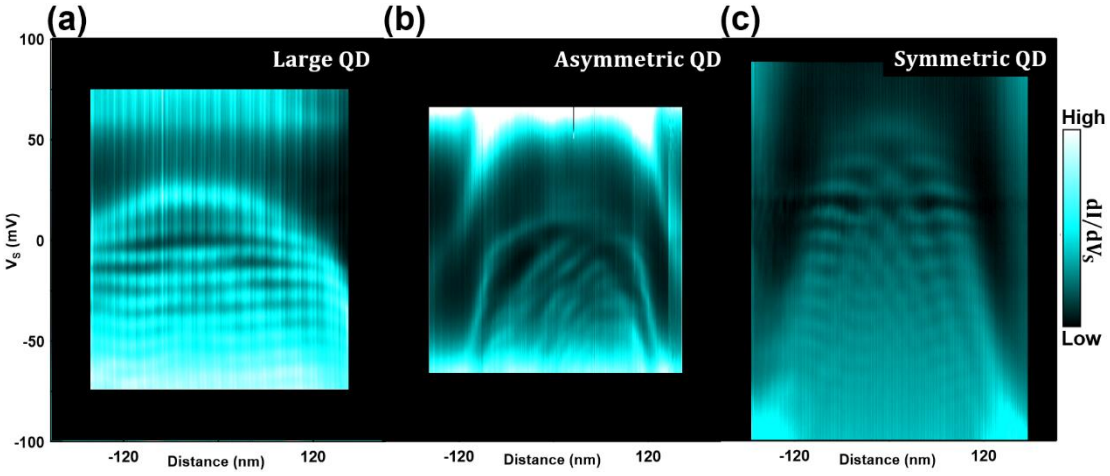

Figure C.1| Examples of QDs. (a) Shows a QD too large to resolve the typical intermittent nodal pattern attributed to quasibound states. **(b)** Shows an asymmetric QD. Asymmetry in a QD may arise due to a highly asymmetric macroscopic STM tip or contaminant(s) on the surface of graphene near or on the QD area. **(c)** Shows an example of an ideal QD that symmetrically displays the nodal patterns expected in an MLG QD.

- Verify that the QD created is symmetric and that the nodal patterns that indicate quasibound states in MLG are present. For example, Fig. C.1a shows a QD that is too large. A QD that extends too far laterally tends to suppress the intermittent nodal patterns associated with QD states. If the QD is too large, you may try to use a larger tip-to-sample distance than that used in Part 2 (e.g. 2.2 nm). Fig. C.1b shows an example of a quantum dot with strong asymmetry. It is very rare to find a QD with near perfect symmetry. However, a QD that shows strong asymmetry such as that shown in Fig. C.1b should not be used. At this point you may attempt to create a QD again after resetting the area (see Part 4). If the strong asymmetry persists, the shape of the macroscopic tip is likely asymmetric. If this is the

case, you must recalibrate the tip on Au(111). Finally, Fig. C.1c shows an example of an ideal MLG QD. If the QD appears shallow or deep (see Ch. 6 for examples) but still displays the intermittent nodal patterns, then you may try to use different values of V_G during the line scan to obtain a scan like that shown in Fig. C.1c

Part 4. Reset the QD

In the event that the QD created does not have the ideal qualities discussed in Part 3, you are able to reset the QD and attempt to create a new QD. To reset the QD follow these steps:

- Place the STM tip at the center of the QD and change the setpoint to I = 500 pA and $V_S = +500$ mV while in tunneling mode.
- Lift the STM tip 1.2 nm off the surface of MLG and immediately change V_S to $+5$ V.
- After two minutes, switch V_S back to $+500$ mV and bring the tip back down by 1.2 nm.